

Final Technical Report

USGS Award #: G19AP00052

May 1, 2019 – July 31, 2021

Seismotectonics and Seismic Potential of Three Intraplate Seismic Zones

Charles A. Langston, P.I.
Christine A. Powell, Co-P.I.

Center for Earthquake Research and Information
The University of Memphis
3876 Central Ave., Suite 1
Memphis, TN 38152

(901) 678-4869 (W - CAL), (901) 678-4734 (Fax)
clangstn@memphis.edu

(901) 678-8455 (W – CAP), (901) 678-4734 (Fax)
capowell@memphis.edu

Acknowledgement: This material is based upon work supported by the U.S. Geological Survey under Grant No. G19AP00052.

Disclaimer: The views and conclusions contained in this document are those of the authors and should not be interpreted as representing the opinions or policies of the U.S. Geological Survey. Mention of trade names or commercial products does not constitute their endorsement by the U.S. Geological Survey.

November 28, 2021

Abstract

The New Madrid Seismic Zone (NMSZ), Eastern Tennessee Seismic Zone (ETSZ), and Charlevoix Seismic Zone (CSZ) are the source of most of the earthquake hazard for the Central and Eastern United States. The NMSZ and CSZ are source zones with Repeating Large Magnitude Earthquakes (RLMEs) in the USGS earthquake hazard model and all seismic zones are associated with tectonic regionalizations that further quantify the hazard model through background seismicity rates. We have relocated the highest quality seismicity in each seismic zone through joint inversion of earthquake hypocenters and three-dimensional velocity structure using traveltimes tomography. In addition, relative locations in the New Madrid Seismic Zone for the entire New Madrid catalog from 2000 to 2019 were determined using the HypoDD algorithm.

Focal mechanisms for 455 relocated earthquakes in the CSZ were determined using P, SV, and SH wave amplitudes. Inversion for the stress field in partitioned areas show significant variations in the direction of the maximum principal stress with an implied regional direction that is nearly EW. The maximum principal stress is also seen to rotate in a clockwise direction with depth, an intriguing but unexplained observation that merits further study. The relocated seismicity in the CSZ was also used to determine suites of fault models based on modifications of the Optimal Anisotropic Dynamic Clustering (OADC) algorithm that included focal mechanism data as fault plane orientation seeds. Faulting in the CSZ is complex but consists of near vertical faults along the northwestern boundary, southwest dipping faults probably associated with Appalachian thrust sheets on the southwest side, and cross faults associated with the ring structure of the La Malbaie impact structure. Fault models suggest that the future earthquakes could be as large as Mw7.2 in the CSZ.

The OADC technique was used to develop fault models for the NMSZ using the seismicity relocated with HypoDD. NMSZ faults are seen to be largely continuous but segmented. In particular, the Northern and Southern segments of the Reelfoot fault are cut by a SE dipping fault. Work is ongoing to incorporate focal mechanisms into the clustering analysis and to apply the OADC method to the earthquake tomography relocations of the highest quality seismicity.

Results from the EarthScope program were integrated into an interpretation of the seismotectonic zonation that we proposed be used in the National Seismic Hazards Map. In particular, we suggest that the western limit of the rifted Iapetan crust is east of the Blue Ridge province at the Appalachian gravity gradient. Ongoing work for the ETSZ include both focal mechanism determinations, stress modeling, and OADC cluster analysis using the relocated earthquake tomography seismicity.

Table of Contents (page number upper left)

Abstract	2
Investigations	8
Problems Encountered	9
Publications and Presentations to Date	11
Other References Cited	11
The Western Limit of Iapetan Rifting in the Eastern United States:	
A New Assessment.....	13
Abstract.....	14
Introduction.....	15
Evidence for the currently mapped western limit of Iapetan rifting.....	17
New estimates of crustal thickness and basement tectonic features in the southeastern United States.....	19
The western margin of extended continental crust.....	20
Implications for the newly recognized western limit of Iapetan extended crust.....	21
Intraplate seismicity in the craton west of the extended crust.....	21
Conclusions.....	23
Data and Resources.....	24
Acknowledgements.....	24
References.....	24
Figure 1.....	30
Figure 2.....	31
Figure 3.....	33
Figure 4.....	34
Figure 5.....	35
Figure 6.....	36
Figure 7.....	37
Focal Mechanisms of Relocated Earthquakes and Stress Orientation in the Charlevoix Seismic Zone.....	
Key Points.....	39
Abstract.....	39
Plain Language Summary.....	39
Introduction.....	40
Figure 1.....	40
Figure 2.....	42
Materials and Methods.....	42
Focal Mechanism Determination.....	42
Grid Search Using Wave Polarities.....	43
Grid Search Using Wave Amplitude Ratios.....	44
Combining Wave Polarity and Wave Amplitude Ratios.....	45
Preferred Focal Mechanism.....	45
Effect of Error in Focal Depth.....	45
Stress Inversion Using Focal Mechanisms.....	45
Results.....	46

Synthetic Data.....	46
Figure 3.....	47
Charlevoix Seismic Zone Earthquakes.....	47
Data and Data Processing.. ..	47
Figure 4.....	48
Figure 5.....	50
Focal Mechanisms of Relocated Earthquakes ($M > 2$)	51
Figure 6.....	52
Figure 7.....	53
Distribution of the P-, I-, and T-axes and faulting styles for CSZ	
Earthquakes.....	54
Figure 8.....	54
Stress Inversion of the Focal Mechanisms.....	54
Stress Inversion of All Earthquakes.....	55
Figure 9.....	55
Stress Inversion for Different Earthquake Clusters.....	56
Table 1.....	56
Figure 10.....	57
Figure 11.....	58
Variation of σ_1 Orientation with Depth.....	58
Figure 12.....	59
Figure 13.....	60
Effect of Temporal Subsets of the Focal Mechanisms	
on the Observed Spatial and Depth Variations in	
σ_1 Orientations.....	60
Discussion.....	60
Conclusions.....	62
Acknowledgements.....	63
References.....	64
Supporting Information.....	67
Proof for the relation between the trace of T and the	
dot product of all observed and calculated	
amplitude ratio vectors.....	67
Effect of the free surface on the displacement of an	
incident SV wave.....	67
Figure S1.....	68
Figure S2.....	70
Figure S3.....	70
Figure S4.....	71
Figure S5.....	72
Table S1.....	73
Table S2.....	73
Table S3.....	74
Fault Geometry for the Charlevoix Seismic Zone.....	92
Key Points.....	92
Abstract.....	92

Plain Language Summary.....	92
Introduction.....	93
Figure 1.....	94
Materials and Methods.....	96
Declustering Analyses.....	96
Modified OADC Algorithm.....	97
Results.....	98
Declustering Analyses.....	98
Figure 2.....	99
Figure 3.....	100
Fault Plane Geometry of the CSZ using the Clustered Hypocenters.....	100
Figure 4.....	102
Faults Associated with the Gouffre Northwest Fault (GNF).....	103
Figure 5.....	103
Table 1.....	105
Faults Associated with the Saint-Laurent Fault (SLF).....	106
Faults Associated with the Charlevoix Fault (CHF).....	106
Figure 6.....	107
Figure 7.....	108
Figure 8.....	109
Faults Associated with the Impact Structure (IM).....	110
Combined Fault Model for the CSZ.....	110
Figure 9.....	111
Figure 10.....	112
Figure 11.....	113
Discussion.....	114
Clustered Seismicity.....	114
Figure 12.....	115
Fault Planes of the Modified OADC Algorithm.....	116
Conclusions.....	117
Acknowledgements.....	118
References.....	118
Supporting Information.....	121
Figure S1.....	121
Figure S2.....	122
Figure S3.....	123
Figure S4.....	124
Figure S5.....	125
Figure S6.....	125
Figure S7.....	126
Table S1.....	126
A New Madrid Seismic Zone Fault System Model from Relative Event	
Locations and Application of Optimal Anisotropic Dynamic Clustering.....	127
Key Points.....	127
Abstract.....	127
Plain Language Summary.....	127

Introduction.....	128
Figure 1.....	129
Tectonic History.....	130
Methods.....	131
Double-Difference (DD) Relocation.....	131
LSQR Inversion.....	131
Figure 2.....	132
Table 1.....	133
Table 2.....	133
SVD Inversion.....	133
Optimal Anisotropic Dynamic Clustering.....	134
Declustering Analysis.....	135
Data.....	135
Results.....	136
Relocation.....	136
Figure 3.....	137
Figure 4.....	138
OADC fault models.....	138
Figure 5.....	139
Figure 6.....	140
Figure 7.....	141
Table 3.....	142
Figure 8.....	143
Figure 9.....	144
Figure 10.....	145
Final Fault Model for the NMSZ.....	146
Figure 11.....	146
Figure 12.....	147
Discussion.....	147
Conclusions.....	149
Data and Resources.....	149
Acknowledgements.....	149
References.....	149
Supporting Information.....	153
Contents.....	153
Introduction.....	154
Figure S1.....	155
Figure S2.....	156
Figure S3.....	157
Figure S4.....	158
Figure S5.....	160
Figure S6.....	160
Figure S7.....	161
Figure S8.....	162
Figure S9.....	163
Figure S10.....	164

Figure S11.....	165
Table S1.....	166
References.....	167

Investigations

The problem addressed in this research is inferring the size, orientation, and style of faulting in three major intraplate seismic zones in the Central and Eastern U.S. (CEUS), the New Madrid Seismic Zone (NMSZ), Eastern Tennessee Seismic Zone (ETSZ), and Charlevoix Seismic Zone (CSZ), responsible for much of the seismic hazard in the CEUS. There has been considerable progress in developing fault models for the NMSZ that are currently included in the USGS seismic hazard model (Petersen et al, 2014), but specific seismogenic faults are largely unknown for the ETSZ and CSZ. Refining the fault system in the NMSZ and determining faults in the ETSZ and CSZ can directly affect the U.S. seismic hazard model by reducing the uncertainty in source zone models and, possibly, defining source zones for the ETSZ that could be added to the hazard logic tree. In addition to improving the hazard model, knowledge of possible fault planes and stress orientations in all seismic zones will place significant constraints on tectonic mechanisms giving rise to the seismicity leading to significant improvements in scientific understanding of each seismic zone.

We employed two basic hypotheses in this work. The first was that modern, instrumentally-located seismicity indicates the location and geometry of active faults. The second was that focal mechanisms for the seismicity also define fault geometry and style (e.g., strike-slip vs thrust). These are reasonable hypotheses that are standard approaches to understanding seismicity all over the world in diverse tectonic environments. However, their use in defining source zones for earthquake hazards assessments in the CEUS depend on additional assumptions such as spatial stationarity (CEUS-SSC, 2012) where repeating large magnitude earthquakes (RLMEs) are expected to occur in roughly the same area over time. In addition, it has only been in the last 15 years or so where regional network seismic data in the CEUS have been good enough to produce high-resolution spatial images of seismicity.

Our plan was to merge the data from two different seismological techniques in order to refine fault models for the NMSZ and develop fault models for the ETSZ and CSZ. Over the past two decades 3D velocity tomography for developing 3D velocity models and relocating network seismicity in the NMSZ, ETSZ, and CSZ have produced high-resolution hypocenter locations that can be used to image the geometry of faults (Powell et al, 2010; Dunn et al, 2010; Vlahovic et al, 1998; Powell et al, 2014; Vlahovic et al, 2003; Powell and Lamontagne, 2017). We incorporated seismicity data up to 2019 to produce a new 3D tomography velocity model for the CSZ and up to 2021 for the NMSZ and ETSZ and relocated the highest quality seismicity in each zone.

Charlevoix Seismic Zone

The student initially working on this project, Oluwaseun Fadugba, had developed a geodynamic model for the CSZ (Fadugba et al., 2019) and was the ideal candidate to continue working on fault plane solutions and clustering analysis for the CSZ at the start of the project. Fadugba and the PI's developed algorithms for fault plane solutions using body wave amplitudes and extended the OADC technique for including focal mechanisms as seed planes. Results of these extensive studies for the CSV are given in this report in the form of two papers. The first paper (Fadugba et al., 2021) has been submitted to the *Journal of Geophysical Research, Solid Earth*, and is being revised for publication. The second (Fadugba et al., 2022) will be submitted to *JGR* when the first is accepted based on *JGR* policy of requiring published results, here the

focal mechanisms, to be available to reviewers since the second paper requires these vetted results. Results for the CSZ formed a large part of Fadugba's PhD thesis (Fadugba, 2021).

New Madrid Seismic Zone

PStomo work was set back by about 4 months in the second year because of an unavoidable change in computer systems (moving from SUN to Mac) while simultaneously installing an updated version of the program and updating existing scripts to use GMT-6 from GMT-5. A second graduate student, Yixin Zhang, also became interested in analysis of NMSZ seismicity so she was recruited for the NMSZ aspect of the project while largely being supported by University of Memphis funds. To avoid the PStomo and computer upgrade problem, we used HypoDD (Waldhouser and Ellsworth, 2000) to perform relative locations of the New Madrid catalog. These relocations were then modeled using OADC to produce a multi-segment fault model for the seismic zone. Details of this model are given in this report in the last section. Even though the grant was over July 31st, Zhang has been working on and will be completing focal mechanism analysis and stress inversion for the NMSZ for her PhD thesis. The USGS will be acknowledged in this project.

In addition, the P.I.'s completed a new earthquake tomography model that includes relocation of the best hypocenters in the New Madrid catalog. This work occurred after the technical end of the grant (July 31, 2021) but is a direct result of grant funding because of the effort made in software and hardware upgrades. The relocated seismicity refines the interpretation of fault structure in the NMSZ as produced by Zhang et al. (2021). Results of this study are presently being prepared for publication with acknowledgement of USGS support.

ETSZ

Likewise, after July 31st, the catalog for seismicity in the ETSZ was updated with hypocenters through to mid-2021. PStomo was used to relocate the expanded catalog and produce an updated velocity model for the seismic zone. The P.I.s are examining hypocenter clustering will be producing new focal mechanisms for the ETSZ. ETSZ work will also acknowledge USGS support.

In the first year of the grant, Powell, et al., (2021) considered the seismo-tectonic framework of the eastern-most U.S. that includes the ETSZ based on results obtained by many field experiments that were performed in the area during the NSF EarthScope program. They suggest that the regionalization used in the National Seismic Hazards Maps that includes a relatively large area of Iapetan rifted crust throughout the Appalachians and to the west is not appropriate since there is no evidence from EarthScope that the crust is thin there. Instead, they suggest that the western limit of Iapetan rifting is associated with the Appalachian gravity gradient, east of the Blue Ridge province. This paper is included in the first section of the report.

Problems Encountered

The grant started on 1 May 2019. Work on the CSZ had started during the previous year when this project was recommended for funding but put on hold by the USGS program and ultimately rejected. Fadugba et al. (2019) had produced a stress model for the CSZ and we had started collecting waveform data from the Canadian DRM system. A code for producing focal mechanisms using ray theoretical amplitudes in a vertically inhomogeneous structure was

developed during the first year of the grant. In addition, the OADC method was modified to include seed planes in the clustering analysis.

Presentations were given at the SSA Spring meeting on some interesting wave propagation effects seen in the seismogram data (Fadugba et al., 2019A) and at the Fall AGU meeting on clustering analysis (Fadugba et al., 2019b). Reports on the focal mechanisms for the CSZ were given at the SSA and AGU meetings in 2020 (Fadugba et al., 2020a; 2020b). Although manuscripts were prepared on these results, we recognized that we had an incomplete catalog for the CSZ. The catalog was expanded from events occurring in 1988-2011 to 2020. The additional 9 years of data were vetted and relocated using the new version of PStomo. Results did not change significantly with the additional data. However, inclusion of the new results caused a delay in submitting the manuscript for publication.

Zhang started working on the NMSZ catalog and fault models at the beginning of the project. Her support came from the University of Memphis as valued-added for the grant. Initial work was presented at the 2019 Eastern Section of the SSA meeting (Zhang et al., 2019) using HypoDD relocations of the New Madrid catalog. Zhang also worked with Christos Kyriakopoulos at CERI to produce a 3D printed version of her fault model. Work during the second year continued to refine the OADC methods to be appropriate for the large extent of New Madrid seismicity. Zhang is currently processing waveform data from the New Madrid Cooperative Network to obtain new focal mechanism for the seismic zone. This work will appear in her PhD thesis.

After updating the PStomo and GMT codes, we produced velocity models and new locations for the best earthquakes in the catalogs for all three seismic zones. Although the grant ended in on 31 July, the P.I.s are investigating fault models for the NMSZ and ETSZ using these new catalogs of relocated seismicity.

In summary, work is continuing on both NMSZ and ETSZ seismicity since each region is of high interest to the P.I.s and their students. Work on the CSZ is complete. In hindsight, the P.I.s under-estimated the amount of time involved in gathering and processing the data from thousands of earthquakes over the three major seismic zones of eastern North America. We suspected that this would be a problem last year in preparing the annual technical report and asked for a no-cost extension until 31 July 2021. The purpose of the three-month, no-cost extension was primarily to be able to cover page charges from Fadugba's CSZ paper using first year publication charges. However, technical problems with computer hardware delayed us in the effort to have velocity models and catalogs that were most current so we delayed submittal of the paper to include events from the updated CSZ catalog.

We found it impossible to use the publication portion of our proposed budget because of the timing of research work and lack of flexibility of extending the annual budget simply to cover publication costs. We recommend that the USGS NEHRP program look into this problem to see if it is a common experience for P.I.s across the small grants program and come up with a solution for publication expenses. Afterall, an expressed goal of the program is that work be published in the refereed literature. Submission and reviews of manuscripts often take 3 to 6 months in most journals. This means that research work needs to be complete 6 months in for an annual award. Two-year awards have the same problem since unused portions of the first-year budget cannot be continued into year 2.

Publications and Presentations to Date

- Fadugba, O. I., C. A. Langston, and C. A. Powell (2019a). Wave propagation analysis of the SP headwave observed in the Charlevoix seismic zone and its application for constraining source depth, *Seism. Res. Lett.*, 90, no. 2B, p. 950, Annual meeting of the S.S.A. Seattle, WA.
- Fadugba, O. I., C. A. Langston, and C. A. Powell (2019b). Better constraining the geometry of faults in the Charlevoix seismic zone, abstract S52C-08, Fall meeting of the AGU, San Francisco, CA.
- Fadugba, O. I., C. A. Langston, and C. A. Powell (2020a). Focal mechanisms of relocated earthquakes and new stress orientations in the Charlevoix seismic zone, *Seism. Res. Lett.*, 91, 2B, page 1229. Annual meeting of the Seismological Society of America, Albuquerque, New Mexico, April 27-30, 2020.
- Fadugba, O. I., C. A. Langston, and C. A. Powell (2020b). Focal mechanisms of relocated earthquakes and stress orientation in the Charlevoix seismic zone, paper S041-05, AGU annual meeting (online), 1-17 December 2020.
- Fadugba, O. I., C. A. Langston, and C. A. Powell (2021). Focal mechanisms of relocated earthquakes and stress orientation in the Charlevoix seismic zone, submitted to *Jour. Geophys. Res.: Solid Earth*, in review.
- Fadugba, O. I., C. A. Langston, and C. A. Powell (2022). Fault geometry for the Charlevoix seismic zone, to be submitted to *Jour. Geophys. Res.: Solid Earth*, preprint.
- Powell, C.A., W. A. Thomas, R. D. Hatcher, Jr. (2021). The western limit of Iapetan rifting in the Eastern United States: A new assessment, *Seismol. Res. Lett.*, 91, 3483-3495, doi: 10.1785/02202000042.
- Zhang, Y., S. Horton, C. Langston, C. Powell (2019). A statistical study of the New Madrid Seismic Zone, meeting of the Eastern Section of the Seismological Society of America, 3 November 2019, Columbus, Ohio.
- Zhang, Y., S. Horton, C. Langston, C. Powell (2021). A New Madrid seismic zone fault system model from relative event locations and application of optimal anisotropic dynamic clustering, preprint.

Other References Cited

- Central and Eastern United States Seismic Source Characterization for Nuclear Facilities, Technical Report (2012). EPRI, Palo Alto, CA, U.S. DOE, and U.S. NRC.
- Dunn, M., S. Horton, H. DeShon, and C. Powell (2010), High-resolution earthquake relocation in the New Madrid seismic zone, *Seism. Res. Lett.*, 81, 406-413.
- Fadugba, O. I., Choi, E., & Powell, C. A. (2019). Effects of preexisting structures on the seismicity of the Charlevoix Seismic Zone. *Journal of Geophysical Research: Solid Earth*, 124, 7370– 7386. <https://doi.org/10.1029/2019JB017831>.
- Fadugba, O. I. (2021). Waveform and geodynamic modeling of seismicity associated with the Charlevoix Seismic Zone, Ph.D., University of Memphis, Memphis, TN.
- Petersen, M.D., M. P. Moschetti, P. M. Powers, C. S. Mueller, K. M. Haller, A. D. Frankel, Y. Zeng, S. Rezaeian, S. C. Harmsen, O. S. Boyd, N. Field, R. Chen, K. S. Rukstales, N. Luco,

- R. L. Wheeler, R. A. Williams, and A. H. Olsen, (2014). Documentation for the 2014 Update of the United States National Seismic Hazard Maps, Open-File Report 2014-1091, U.S. Department of the Interior, U.S. Geological Survey.
- Powell, C.A., M. Withers, H. Deshon, and M. Dunn (2010). Intrusions and anomalous Vp/Vs ratios associated with the New Madrid seismic zone, *Jour. Geophys. Res.*, v.115, B08311, doi:10.1029/2009JB007107.
- Powell, C.A., Withers, M., Cox, R.T., Vlahovic, G., and Arroucau, P. (2014). Crustal velocity structure associated with the eastern Tennessee seismic zone: Vp and Vs images based upon local earthquake tomography: *Journal of Geophysical Research: Solid Earth*, v. 119, p. 464–489, doi:10.1002/2013JB010433.
- Powell, C. A., and M. Lamontagne (2017). Velocity models and hypocenter relocations for the Charlevoix seismic zone, *Jour. Geophys. Res. Solid Earth*, 122, 6685-6702, doi:10.1002/2017JB014191..
- Vlahovic, G., Powell, C.A., Chapman, M.C., and Sibol, M.S. (1998). ET1D: New one dimensional P- and S-wave velocity models for the eastern Tennessee seismic zone: *Seismological Research Letters*, v. 69, p. 441–449, doi:10.1785/gssrl.69.5.441.
- Vlahovic, G., Powell, C., and M. Lamontagne (2003). A three-dimensional P wave velocity model for the Charlevoix seismic zone, Quebec, Canada, *J. Geophys. Res.*, 108, B9, 2439, doi:10.1029/2002JB002188.
- Waldhauser, F., & Ellsworth, W. L. (2000). A double-difference earthquake location algorithm: Method and application to the northern Hayward fault, California. *Bulletin of the Seismological Society of America*, 90(6), 1353-1368.

The Western Limit of Iapetan Rifting in the Eastern United States: A New Assessment

Christine A. Powell^{1*}

William A. Thomas²

Robert D. Hatcher Jr.³

*Corresponding Author

¹Center for Earthquake Research and Information

University of Memphis,

3876 Central Ave., Suite 1

Memphis, Tennessee 38057, USA

capowell@memphis.edu; (901) 678-8455

²Emeritus University of Kentucky

Geological Survey of Alabama

Tuscaloosa, Alabama 35487, USA

³Department of Earth and Planetary Sciences

Emeritus University of Tennessee

1621 Cumberland Avenue, Room 602

Knoxville, Tennessee 37996, USA

Submitted to

Seismological Research Letters

Abstract

Specifying the extent and location of rifted, crystalline Precambrian crust in the eastern United States is important for seismic hazard evaluation and for models that relate upper mantle structure to ancient tectonic features and ongoing tectonism. As currently depicted in the National Seismic Hazard Maps (NSHM), the western limit of Iapetan rifted crust is beneath the Appalachian Plateau physiographic province, west of the Valley and Ridge province. New estimates of crustal thickness using EarthScope Transportable Array and other data do not support the presence of rifted crust beneath the Blue Ridge, Valley and Ridge, and Appalachian Plateau physiographic provinces. Crustal thicknesses exceed 45 km throughout most of this region. The crust thins to the southeast beneath the southeastern part of the Piedmont physiographic province and is only 36 km thick near the edge of the Atlantic Coastal Plain. We suggest that the western limit of Iapetan rift-extended crust is east of the Blue Ridge province and is associated with the prominent Appalachian gravity gradient. This location coincides with palinspastic reconstructions based on geologic data for the Iapetan rifted margin. Recognition of thick crust beneath the Blue Ridge and Valley and Ridge provinces, unextended by Iapetan rifting, will support more robust modeling of the effects of mantle structure (such as delamination and abrupt changes in lithospheric thickness) on ongoing tectonism and earthquake activity in the eastern United States and will provide more accurate seismotectonic zonation in the NSHM.

Introduction

Specifying the extent and location of rifted and extended continental crust within the stable continental region (SCR, as defined by Johnston and Kanter (1990) and Johnston (1994)) is essential for seismic hazard evaluation in the eastern United States (U.S.) and for models that relate upper mantle structure to ancient tectonic processes and ongoing seismicity. In eastern North America, the SCR includes the continental craton and extends eastward to the passive margin along the Atlantic Ocean (Johnston and Kanter, 1990; Johnston, 1994). Rifted and extended continental crust within the SCR is a result of the breakup of supercontinent Rodinia and the opening of the Iapetus Ocean (referred to herein as “Iapetan rifting” or the “Iapetan rift”) by about 530 Ma (summary in Thomas, 2006, 2019), as well as the breakup of supercontinent Pangaea and the opening of the Atlantic Ocean (“Atlantic rift”) by about 180 Ma.

The process of continental rifting and breakup of a supercontinent leaves rifted margins around the newly separated continents, which become bounded by newly generated oceanic crust as the ocean basin opens at an evolving mid-ocean ridge (e.g., Berk, 2011). The structural expression of the rifted margin in the form of extensional faults varies in accord with factors such as the direction of dip of the low-angle-detachment fault. The detachment fault dips beneath the upper plate and away from the lower plate (Figure 1) (Wernicke, 1985; Lister et al., 1986, 1991; Svartman Dias et al., 2015). The width of transitional continental crust between the new oceanic crust and the full-thickness (not extended) continental crust ranges from relatively narrow with few down-to-ocean faults along upper-plate margins to wide with multiple oceanward-dipping listric faults that bound rift grabens along lower-plate margins (Figure 1). Transform margins are steep and have near-vertical faults (Lister et al., 1986, 1991; Thomas, 1991). Subsequent to rifting, a passive margin forms as a result of thermal subsidence caused by cooling of the lithosphere adjacent to the rifted margin (Buck et al., 1988; Thomas and Astini, 1999). Passive-margin sedimentary rocks, most commonly shallow-marine carbonate rocks and mature sandstones, cover the faulted basement rocks near the rift margin and extend to the interior of the continent. In general, the rifted continental margin contains a variable number of normal faults that may be reactivated in subsequent stress fields. For this reason, specifying the location and geometry of an ancient rifted margin is important for the assessment of seismic hazard in the SCR (Wheeler, 1995; Wheeler and Frankel, 2000).

In eastern North America, the location of the Iapetan rift margin, as well as the western limit of extended continental crust associated with opening of the Iapetus Ocean, is difficult to determine because the rifted crust has been covered by post-rift sedimentary deposits and modified by subsequent tectonic events, especially by late Paleozoic Appalachian thrusting (i.e. the Appalachian thrust belt). The shape of the margin can be palinspastically reconstructed using data from outcrop geology, stratigraphic thicknesses, data from deep wells, and geophysical surveys such as seismic reflection profiles (Thomas, 1991, 2006). Palinspastic reconstruction (Figures 1 and 2) of the Iapetan rifted margin of North America outlines the trace of the rift, distinguishes between upper-plate and lower-plate rifts, and identifies the location of transform faults along the rifted margin (Thomas, 1991, 1993; Allen et al., 2009, 2010). For example, the trace of the rifted margin of continental crust (Figures 1 and 2) is based on the palinspastic location of shelf-edge facies in a restoration of shortening in the Appalachian sedimentary thrust

belt (Thomas, 1991). Along the rifted margin in the Tennessee embayment, a wide expanse of thick, laterally variable, synrift sedimentary and volcanic rocks (now in the Blue Ridge province) records accumulation in rotated half-grabens in the hanging walls of multiple listric extensional faults and transform offsets, indicating a wide zone of oceanward thinning crust in a lower-plate extensional setting (Figures 1 and 2) (Thomas, 1993; Hatcher et al., 2007).

Inboard from the extended and rifted crust (i.e. to the west), the craton is broken by rift-parallel and transform-parallel fault systems (Figures 1 and 2) (Thomas, 1991, 1993, 2006, 2014, 2019); however, the magnitude of extension on these intracratonic structures is too small to significantly reduce crustal thickness. Some intracratonic structures host large earthquakes under special conditions, in which the structure has been overprinted by concentrated crustal deformation (Thomas and Powell, 2017). Examples include the New Madrid, Eastern Tennessee, and Charlevoix seismic zones.

The extended and faulted crust along the rifted margin differs with respect to seismic hazard from the crust inboard from the rift in the SRC. Indeed, a global survey found that large intraplate earthquakes preferentially occur in extended crust such as intra-continental grabens and passive margins (Johnston and Kanter, 1990; Johnston, 1994). The observed preference for large SCR earthquakes in Phanerozoic extended crust forms the basis for using geology to delineate separate source zones for the central Precambrian core and a more seismogenic rim of Phanerozoic rifted margins in the United States Geological Survey (USGS) National Seismic Hazard Maps (NSHM) (Wheeler and Frankel, 2000). The cratonward (western) limit of normal faults associated with continental rifting and the opening of the Iapetus Ocean is a critical boundary for seismic hazard assessment.

Wheeler (1995) developed a framework for rifted crust associated with opening of the Iapetus Ocean to improve seismic hazard assessment in eastern North America. On the basis of limited information about basement structure available at the time, Wheeler (1995) determined that the most logical location for the cratonward edge of major Iapetan rift faults extends below the northwestern edge of the Appalachian thrust sheets and adjacent parts of the craton (Figure 3). The western limit determined by Wheeler (1995) is used in the NSHM to separate the relatively aseismic Precambrian craton to the west and northwest from more seismogenic, extended crust to the east and southeast. The division allows development of a background source model with different uniform average seismicity rates and maximum magnitudes for the craton and the extended crust.

Knowledge of crustal structure in the eastern U.S. has improved dramatically since the pioneering work of Wheeler (1995), particularly with passage of the EarthScope Transportable Array (TA) through the region. New determinations of crustal thickness using TA and additional broadband stations allow a reassessment of the westward extent of Iapetan extension. In this article, we summarize the current knowledge of crustal thickness in the southeastern U.S. and suggest that the western limit of successful Iapetan rifting is located far to the east of the Blue Ridge physiographic province (note that physiographic provinces, as labeled in Figure 4, are used herein only for a geographic reference frame and do not reflect crustal structure), in accordance with palinspastic reconstructions (Thomas, 1991, 2006), Bouguer gravity and aeromagnetic anomalies (e.g., Hatcher and Zietz, 1980).

Evidence for the currently mapped western limit of Iapetan rifting

Wheeler's boundary

Before suggesting a modification to the currently mapped western limit of Iapetan rifting, it is instructive to review the evidence amassed by Wheeler (1995) that led to his interpretation (Figure 3). According to Wheeler (1995), the most compelling evidence for the western limit of rifted and extended crust comes from two intraplate seismic zones, Charlevoix and Giles County. The Charlevoix seismic zone is located along the St. Lawrence River in eastern Canada, northeast of Québec City, beneath the leading edge of the Appalachian sedimentary thrust belt. The Giles County seismic zone is located in southwestern Virginia, southeast of the leading edge beneath the Appalachian thrust belt (roughly the Valley and Ridge physiographic province). At the time, enough seismic instruments were located in these intraplate seismic zones to support a detailed study of the hypocenter distribution and focal mechanisms of recorded earthquakes.

Wheeler (1995) noted that earthquake hypocenters in the Charlevoix seismic zone (CSZ) cluster into two NE-trending, steeply dipping tabular zones in Precambrian basement rocks. Within each group, hypocenters are aligned along planar surfaces, and upward projections of these surfaces coincide with mapped Iapetan normal faults (Rondot, 1971, 2000; Anglin, 1984). Many studies following the work of Wheeler (1995) support the presence of reactivated Iapetan extensional faults in Charlevoix (e.g. Lamontagne, 1999; Lamontagne et al., 2000; 2004; Yu et al., 2016; Powell and Lamontagne, 2017); however, these are rift-parallel basement faults inboard from the rifted margin of continental crust (Allen et al., 2009, 2010; Thomas and Powell, 2017). The inboard location is based on structural and stratigraphic evidence presented in Allen et al. (2009, 2010).

The Giles County seismic zone (GCSZ) is approximately 40 km long and was the location of an estimated magnitude 5.8 (m_b) earthquake in 1897 (Bollinger and Wheeler, 1988). Iapetan rift faults, if present, are buried under the Appalachian thin-skinned thrust sheets emplaced during the late Paleozoic Alleghanian orogeny. Munsey and Bollinger (1985) located 35 Giles County earthquakes and determined 11 focal mechanism solutions. The earthquakes occur in the depth range 7 to 20 km on one or more closely spaced, N-NE-trending, near vertical faults. The focal mechanisms display some variation but indicate right-lateral strike-slip motion on N-NE-trending, near vertical planes. Bollinger and Wheeler (1988) investigated the Late Proterozoic and Phanerozoic structural history of the region and concluded that the earthquakes represent reactivation of Iapetan normal faults, because no other plausible explanation could be found for basement faults with the observed orientation and vertical dimension.

Additional evidence used by Wheeler (1995) to delineate the western limit of Iapetan rifting is not as conclusive as the evidence derived from the Charlevoix and Giles County seismic zones. Locations where additional evidence was found are shown in Figure 3. The interpretation of reactivated Iapetan faults was extended to the Eastern Tennessee seismic zone (ETSZ) on the basis of structural position with respect to the Giles County seismic zone and similarity of focal mechanism solutions (Davison, 1988). In a similar way, seismic activity in the St. Lawrence River seismic zone was attributed to reactivation of Iapetan faults on the basis of diffuse alignments of seismicity that trend parallel to faults in the Charlevoix seismic zone. Seismic activity in the lower St. Lawrence River and shallow induced earthquake activity on or near the Clarendon-

Linden fault system in New York was used to extend the northwestern boundary of large Iapetan normal faults along a line from Labrador to Alabama (Figure 3). Less conclusive support for the location of the boundary between the seismically active areas includes seismic reflection profiles, well logs, geologic mapping, and magnetic mapping (Figure 3). Further support for the location of the boundary put forth by Wheeler (1995) was that the width of the Iapetan margin was comparable to the width of the Atlantic Ocean extended margin.

Some modification to the original boundary determined by Wheeler (1995) has occurred for use in the USGS seismic hazard maps. The revised boundary extends farther inland in Canada to include the seismically active Saguenay and Ottawa-Bonnechere grabens (Figure 3). With the exception of the later inclusion of the Rome trough in eastern Kentucky, Wheeler's (1995) boundary has remained unchanged in seismic hazard maps for the eastern U.S. (i.e., northern New York to northeastern Alabama).

Cratonward extension of the boundary

The boundary between the craton and the Phanerozoic rifted margin used in the seismotectonic zonation map (Figure 3) extends cratonward beyond the boundary established by Wheeler (1995). We do not discuss the validity of this boundary but mention the observations used to establish it. A detailed description is given in Wheeler and Frankel (2000). The extended boundary forms a south-facing concave arc from the Mississippi-Alabama border, through central Arkansas and into Texas, and was drawn on the basis of gravity and aeromagnetic gradients that were thought to indicate the cratonward limit of Late Proterozoic and Cambrian (Iapetan) extensional faults (Frankel, 1995; Frankel et al., 1996, Wheeler and Frankel, 2000). Three large Iapetan transform-parallel intracratonic fault systems (Southern Oklahoma, Ottawa-Bonnechere, and Saguenay) and one rift-parallel intracratonic fault system (Mississippi Valley graben) extend at a high angle into the craton and are included in the craton-rim boundary (Figure 3). Intracratonic fault systems completely inboard from the rift margin include two rift-parallel grabens (Rome and Birmingham) and one transform-parallel graben (Rough Creek). The Mississippi Valley graben (also called the Reelfoot Rift), Southern Oklahoma fault system, Ottawa-Bonnechere graben, and Saguenay graben are seismogenic and/or have paleoseismic evidence for large Holocene earthquakes; however, the Rough Creek graben, Rome trough, and Birmingham graben are no more seismically active than other parts of the craton (Figure 3) (Wheeler and Frankel, 2000).

Additional studies

The Central and Eastern United States Seismic Source Characterization for Nuclear Facilities (CEUS-SSC) Project (Coppersmith, 2012) determined several versions of the western limit of Iapetan rifting in a 2012 study (Figure 5). In the seismotectonic model deemed to have the most convincing structural and seismological evidence, the western limit of Iapetan rifting was modified to follow the trace of the New York-Alabama (NY-AL) aeromagnetic lineament, and the limit was placed to the east of the Clarendon-Linden fault system in New York (Figure 5). This is the "narrow extended Paleozoic crust" model. The NY-AL aeromagnetic lineament (Figures 2, 4, and 5) is indicative of a major basement structural boundary beneath sedimentary strata of the Appalachian

foreland basin and thin-skinned thrust belt (e.g., King and Zietz, 1978). The Clarendon-Linden faults are now recognized as regional basement structure related to the Grenville orogeny; these faults may have undergone reactivation during subsequent Iapetan extension but do not represent rift faults (e.g., Jacobi and Fountain, 2002). Another model, called “wide extended Paleozoic crust,” is represented by the green area shown in Figure 5 and is closer to Wheeler’s western limit of extended crust; the only difference between the western limit of Iapetan rifted crust between the two models in the U.S. occurs in northern Pennsylvania and western New York (compare Figures 3 and 5). In the CEUS-SSC models, Paleozoic extended crust associated with the Iapetan rifting is distinguished from Mesozoic extended crust produced by opening of the Atlantic Ocean (Figure 5). The boundary between the two extended margins follows the Appalachian gravity gradient maximum, inferred to define a fundamental structural boundary representing the western limit of thinned, extended crust lying east of the Appalachian Mountains (e.g. Pratt et al., 1988; Coppersmith et al., 2012). The CEUS-SSC models are used in the 2014 NSHM to assist in the development of maximum magnitude models within the seismicity-based background source model. Wheeler’s model (Figure 3) is referred to as Model A and the CEUS-SSC model (Figure 5) as Model B in the 2014 NSHM documentation (Petersen et al., 2014).

New estimates of crustal thickness and basement tectonic features in the southeastern United States

Crustal thickness estimates beneath the Blue Ridge and Valley and Ridge physiographic provinces in the southeastern U.S. are now available from the TA deployment and other sources (Figure 6), and provide evidence that the basement inboard from the rifted margin did not undergo significant extension during opening of the Iapetus Ocean. Moho depths determined from receiver functions indicate a very consistent crustal thickness of 46 to 49 km beneath the Valley and Ridge province in Tennessee (Parker et al., 2013; Graw et al., 2015; Hopper et al., 2017). Wide-angle reflections (Hawman et al., 2012) and receiver functions (Parker et al., 2013, 2015; Wagner et al., 2012; Hopper et al., 2017) indicate crustal thickness ranging from 46 to 60 km beneath the Blue Ridge province in North Carolina, Tennessee, and Georgia. The crust thins progressively southeastward beneath the southeastern part of the Piedmont province and is only 36 km thick at the northwestern edge of the Atlantic Coastal Plain (Figure 6) (Hawman et al., 2012; Parker et al., 2013, 2015; Hopper et al., 2017). Thick crust below the Blue Ridge and Valley and Ridge provinces is also indicated in a deep reflection COCORP (Consortium for Continental Reflection Profiling) profile (Cook and Vesudevan., 2006).

The Southern Appalachian COCORP profile (Cook and Vesudevan, 2006) also demonstrates that crustal thickening below the Blue Ridge and Valley and Ridge provinces as a result of the Appalachian orogeny is minor. The COCORP transect crosses the entire orogen from the foreland (Valley and Ridge province), across the metamorphosed interior (Blue Ridge and Inner Piedmont provinces), across accreted terranes (AT) within the Piedmont province, and ends in the Atlantic coastal margin (Figure 4). Rocks in the Valley and Ridge, Blue Ridge, and western portion of the Piedmont provinces are separated from non-reflective, Precambrian (Mesoproterozoic age) basement by a shallow and shallow-dipping décollement. Depth to the décollement

along the transect changes from about 4.5 km at the western end below the Valley and Ridge to about 9 km below the middle of the Piedmont, indicating the lack of significant crustal thickening west of the Iapetan rifted margin during the Appalachian orogeny.

Crustal thickness estimates are available for the entire U.S. from studies using the TA and associated FlexArray deployments (e.g. Shen and Ritzwoller, 2016; Buehler and Shearer, 2017). For example, a map of crustal thickness for the eastern and central U.S. is shown in Figure 7. This map was constructed by Wagner et al. (2018) using P-s wavefield migration (e.g. Hopper et al., 2016) and receiver functions for the TA and the Southeastern Suture of the Appalachian Margin Experiment (SESAME) stations. Thick crust is found beneath the Valley and Ridge and Blue Ridge provinces, and in central New York east of the western limit of Iapetan rifting determined by Wheeler (1995).

Thick crust below the Valley and Ridge and Blue Ridge provinces is also suggested by negative Bouguer gravity anomalies (e.g. Hutchinson et al., 1983; Hawman et al., 2012). The Bouguer gravity map for the southern and central Appalachians (Figure 2) is dominated by the northeast-trending Appalachian gravity gradient, an abrupt transition from low values on the northwest to high values on the southeast beneath the eastern part of the Piedmont physiographic province (Figure 6). The gravity low can be explained by thick crust, but the steep gradient and the gravity high are enigmatic. Most explanations attribute the steep gradient and associated gravity high to thinned crust and additional high-density material (e.g., Hatcher and Zietz, 1980; Hutchinson et al., 1983; Wagner et al., 2012). The steep gradient is located far to the west of the Atlantic rift, even west of the Triassic graben faults that are intracratonic, rift-parallel faults of the Atlantic system. As discussed below, we suggest that the steep gradient marks the location of the Iapetan rift.

The western margin of extended continental crust

Along the palinspastically restored Iapetan rifted margin (Thomas, 1991), the distributions and thicknesses of synrift sedimentary and igneous rocks now within the Appalachian orogenic belt provide insights into the tectonic framework of the rifted margin, and age dates provide earliest and latest bounds on the age of rifting in many locations (summary in Thomas, 2014). The transition from an active rift to a passive margin is indicated by a well-documented unconformity below Lower Cambrian strata (Thomas, 1977; Wehr and Glover, 1985; Fichter and Diecchio, 1986). A transgressive sequence from basal alluvial-fan deposits to marine deposits at the top marks post-rift thermal subsidence of the passive margin. Thomas (1991) made use of all available geologic, deep well, and seismic reflection information to construct balanced structural cross sections that constrain a palinspastic reconstruction of the rift margin (Figure 2). Along the northern Blue Ridge, a long, straight rift segment and few extensional faults indicate an upper-plate setting; but, south of the Virginia-Tennessee transform, multiple rift and transform segments produce a more complicated, distributed pattern in a lower-plate setting (Figure 1) (Thomas, 1991, 1993).

The palinspastic location of the Iapetan rift segments and transform faults (Thomas, 1991, 2019) displays a remarkable correlation with Bouguer gravity anomalies, especially the Appalachian gravity gradient (Figure 2). Significantly, the potential-field maps were not used in making the palinspastic reconstruction (Thomas, 1991); thus, the correlation between the Appalachian gravity gradient and the independently derived palinspastic

trace of the rifted margin is a positive test of the reconstruction. According to the palinspastic reconstruction, the crust below the Blue Ridge and Valley and Ridge provinces was not significantly affected by extensional faulting, an interpretation that agrees with the Bouguer gravity anomalies and with the geophysical evidence discussed above. In summary, we suggest that the western limit of major Iapetan extension and thinning of the crust closely corresponds to the Appalachian gravity gradient maximum (Figure 2), a location that coincides with the division of Paleozoic and Mesozoic rifting determined in the CEUS-SSC study (Figure 5).

Implications for the newly recognized western limit of Iapetan extended crust

The western limit of Iapetan rifting plays an important role in the NSHM because it is used to establish seismotectonic zonation for the CEUS. Throughout most of the CEUS, there is little geologic or geodetic information about the presence or absence of faults capable of generating damaging earthquakes; a background source model is used in the hazard maps to account for earthquakes that are distributed across the region, as well as large earthquakes not associated with identified faults (Petersen et al., 2014). The western boundary established by Wheeler (1995), separating relatively undeformed craton from presumed thinned, extended crust, allowed determination of different uniform average seismicity rates and maximum magnitudes for the two seismotectonic zones within the background source model. Only a lower bound on maximum magnitude in each zone can be determined from prehistoric and historical earthquakes; the desired upper limit relies on observations from other SCRs worldwide in comparable seismotectonic settings. For this reason, correct specification of the seismotectonic models that form the basis of the zonation is important. Adoption of our modification of the western limit of Iapetan rifting in the NSHM will provide a more realistic seismotectonic model for a large part of the eastern U.S. and may impact the maximum magnitude value for the portion of the crust located west of the Appalachian gravity gradient.

Our depiction of the western limit of Iapetan rifting, interpreted to follow the Appalachian gravity gradient maximum, is compatible with palinspastic reconstructions of the rifted margin, Bouguer gravity anomalies, and crustal thickness values determined from seismic investigations (Figures 2, 6, and 7). Our western limit coincides with the boundary separating the Paleozoic and Mesozoic rifted crust determined in the CEUS-SSC study (Figure 5). We suggest that the region labeled as “Mesozoic” rifted crust in Figure 5 actually represents crust that was bounded by the Iapetan rift; the region labeled “Paleozoic” contains thick crust unaffected by major extensional faulting. This has implications for studies involving the strength of the CEUS lithosphere. The presence of thick crust below the Valley and Ridge and Blue Ridge physiographic provinces suggests that the lithosphere in these locations was not thinned and weakened during Iapetan rifting. Changes in lithospheric thickness imaged in recent tomographic inversions are most likely related to other factors such as delamination or inherited structure from past orogenies (e.g. Biryol et al., 2016).

Intraplate seismicity in the craton west of the extended crust

Considering that the crust is not thinned and rifted below the Blue Ridge and Valley and Ridge provinces and farther west requires an explanation other than extended and thinned crust for seismic activity that occurs in this region, including the presence of

distinct intraplate seismic zones (Figures 2 and 4). Thomas and Powell (2017) have suggested that concentrated crustal deformation, which has been focused by a variety of mechanisms, causes the localization of seismicity within the craton. These seismic zones are generally associated with ancient basement structures that have been overprinted by some other deformation.

In the Charlevoix seismic zone (CSZ, Figure 3), earthquake hypocenters in Precambrian basement rocks cluster into two steeply southeast-dipping groups, in which the hypocenters are aligned along planar surfaces that project to the surface along mapped basement faults (Rondot, 1971, 2000; Anglin, 1984; Thomas and Powell, 2017). The majority of CSZ earthquake activity is limited to the area of crustal damage caused by a meteor impact overprinted on the basement faults (e.g. Rondot, 1971; Lamontagne et al., 2004). The basement faults are parallel with and about 100 km northwest of the Iapetan rifted margin (Allen et al., 2010), indicating that these are rift-parallel intracratonic extensional faults (not rift faults) in thick continental crust. A reflection-refraction profile and travel times from controlled sources recorded by the Charlevoix seismic network show that crustal thickness in the Charlevoix area is about 42–45 km (Lyons et al., 1980).

The Eastern Tennessee seismic zone (ETSZ) is located beneath the Valley and Ridge province where the crust is generally >45 km thick (Figures 6 and 7). A recent seismotectonic model developed for the ETSZ provides an explanation that does not involve Iapetan rifting. Powell et al. (2014) and Powell and Thomas (2016) presented evidence that a large-scale shear zone, which originated as a sinistral continental transform fault during the Grenville orogeny and assembly of supercontinent Rodinia, constitutes the framework for ETSZ earthquake activity. The NY-AL aeromagnetic lineament (Figures 2, 4, and 5) is interpreted to mark the trace of the transform fault. Support for this model (summary and references cited in Powell and Thomas, 2016) includes evidence from crustal velocity models, apparent polar-wander curves, isotopic constraints on the growth of southeastern Laurentia during the Grenville orogeny, preferential alignment of hypocenters, and focal mechanism solutions. In particular, the compatible alignments of hypocenters and focal mechanism nodal planes suggest strike-slip motion on steeply dipping fault planes in the basement rocks (Chapman et al., 1997). The orientations of the planes suggest a conjugate set of faults, a characteristic of major strike-slip faults in continental crust (Fossen and Tikoff, 1998). A releasing bend in the sinistral transform (labeled in Figure 4) offers a mechanism for ductile extension and concentrated crustal deformation in the ETSZ (Powell and Thomas, 2016; Thomas and Powell, 2017). The shear zone may extend into eastern Kentucky as suggested by the source parameters of the 2012 M_w 4.2 Perry County earthquake (Carpenter et al., 2014) (Figure 4).

Earthquake source parameters for the Giles County seismic zone (GCSZ) are very similar to those for the ETSZ and the basement faults may be part of the same distributed shear zone. This concept is supported by analysis of a M 3.2 earthquake that occurred in the GCSZ on September 13, 2017; the hypocenter is located at a depth of 17.8 km and the focal mechanism indicates right-lateral, strike-slip motion on a north-south trending, near-vertical plane or left-lateral strike-slip motion on an east-west trending near vertical plane (M. Chapman, written communication).

The active New Madrid seismic zone (NMSZ) lies within the MVG (Figure 3) far to the west of the westernmost boundary of Iapetan extended crust determined by Wheeler (1995) and the boundary delineated in this study. The MVG, however, is identified as extended crust in the NSHM and in the CEUS-SSC project, and we provide a brief discussion of the origin of this graben. The MVG is part of a system of intracratonic faults that resulted from late-stage crustal extension during and immediately following breakup of Rodinia and opening of the Iapetus Ocean in latest Precambrian to Cambrian (~565-495 Ma) time (Thomas, 2014). The magnitude of extension, however, is only about 6% (Thomas and Powell, 2017). Late Paleozoic contraction along the MVG is a far-field response to the Appalachian-Ouachita orogeny and assembly of supercontinent Pangaea (~270 Ma). The northern MVG merges with the east-trending Rough Creek graben that forms a transform-sense oblique strike-slip offset between the rift-parallel MVG and the Rome trough (Figure 1) (Thomas 1993, 2014). Overprint of the successive ancient episodes of extension and contraction produced concentrated crustal deformation along selective fault zones in basement rocks of the northern MVG basement rocks hosting the NMSZ (Thomas and Powell, 2017). Recent discoveries made using TA and other broadband stations suggest that the location of the NMSZ is also influenced by the presence of a pronounced low velocity zone (LVZ) in the upper mantle (Chen et al, 2014; Chen et al., 2016; Nyamwandha et al., 2016). Pollitz and Mooney (2014) demonstrated that the presence of an upper mantle LVZ is unique to the upper MVG and may explain why other CEUS intracratonic grabens (e.g., mid-continent rift, Rome trough, Rough Creek graben) do not host seismic zones. Zhan et al. (2016) used a series of numerical experiments to emphasize the importance of the LVZ for NMSZ earthquake nucleation.

Upper mantle structure may prove to be an important component of seismotectonic models for intraplate seismic zones in SCR regions. Establishing the link between mantle structure and ongoing tectonism will require formulation of accurate mantle and crustal models. For example, Biryol et al. (2016) speculated that stress localization associated with an abrupt change in lithospheric thickness might contribute to reactivation of basement faults in the ETSZ and the GCSZ. The abrupt change in lithospheric thickness approximately coincides with the NY-AL magnetic lineament and may represent the transform boundary established during the assembly of Rodinia. Numerical modeling establishing the influence of the mantle structure on seismogenesis will be more robust if it is recognized that the crust hosting this seismic activity is thick rather than rifted and extended.

Conclusions

New estimates of crustal thickness for the Blue Ridge and Valley and Ridge physiographic provinces indicate that the basement did not undergo extension and thinning during the opening of the Iapetus Ocean. Crustal thickness below these provinces is greater than 45 km and exceeds 55 km in some locations beneath the Blue Ridge. Crustal thickening below the Appalachian and Valley and Ridge provinces during the Appalachian orogeny was only minor as evidenced by the presence of a shallow decollement separating Appalachian thrust sheets from non-reflective basement (Cook and Vesudevan, 2006). These results contradict the model of Iapetan rifted crust developed by Wheeler (1995) and used in the USGS NSHM to establish seismotectonic zonation for the CEUS. We suggest that the western limit of the Iapetan rifted margin

coincides with the prominent Appalachian gravity gradient maximum beneath the central part of the Piedmont physiographic province. This location is compatible with the palinspastic reconstruction of Iapetan rifts. Our modification of the western limit of Iapetan rifting will provide a more realistic separation of the craton from the surrounding rim of rifted margins in the NSHM. A more realistic seismotectonic model for the southeastern U.S. incorporating thick crust below the Blue Ridge and Valley and Ridge provinces unaffected by Iapetan rifting will allow more robust modeling of the effects of mantle structure on ongoing tectonism and seismogenesis.

Data and Resources

All earthquake data are available at the U.S. Geological Survey ANSS Comprehensive Earthquake Catalog (ComCat) and the CERI earthquake catalog.

Acknowledgements

We thank Cheryl Waters-Tormey, Oliver Boyd and an anonymous reviewer for constructive reviews. This material is based upon work supported by the U.S. Geological Survey under Grant No. G19AP00052. The views and conclusions contained in this document are those of the authors and should not be interpreted as representing the opinions or policies of the U.S. Geological Survey. Mention of tradenames or commercial products does not constitute their endorsement by the U.S. Geological Survey.

References

- Allen, J.S., Thomas, W.A., and Lavoie, D. (2009). Stratigraphy and structure of the Laurentian rifted margin in the northern Appalachians: a low angle detachment rift system, *Geology*, 37, 335-338, doi:10.1130/G25371A.1.
- Allen, J.S., Thomas, W.A., and Lavoie, D. (2010). The Laurentian margin of northeastern North America, in Tollo, R.P., Bartholomew, M.J., Hibbard, J.P., and Karabinos, P.M., eds. From Rodinia to Pangea: The Lithotectonic Record of the Appalachian Region: *Geological Society of America Memoir* 206, 71-90, doi:10.1130/2010.1206(04).
- Anglin, F. M. (1984). Seismicity and faulting in the Charlevoix zone of the St. Lawrence Valley, *Bull. Seismol. Soc. Am.*, **74**, 595–603.
- Berk, K. (2011). Plate tectonics, the Wilson cycle, and mantle plumes: geodynamics from the top, *Annual Review of Earth and Planetary Sciences*, 39:1-29, <https://doi.org/10.1146/annurev-earth-040809-152521>.
- Biryol, C. B., Wagner, L. S., Fischer, K. M., and Hawman, R. B. (2016). Relationship between observed upper mantle structures and recent tectonic activity across the Southeastern United States, *J. Geophys. Res. Solid Earth*, **121**, <https://doi.org/10.1002/2015JB012698>.
- Bollinger, G. A., and Wheeler, R. L. (1988). The Giles County, Virginia, seismogenic zone— Seismological results and geological interpretations: *U.S. Geological Survey Professional Paper* 1355, 85 p.
- Buck, W.R., Martinez, F., Steckler, M.S., and Cochran, J.R., (1988). Thermal consequences of lithospheric extension: *Tectonics*, 7, 213-230.
- Buehler, J.S., and Shearer, P.M. (2017). Uppermost mantle seismic velocity structure

- beneath USArray, *J. Geophys. Res. Solid Earth*, 122, doi/10.1002/2016JB013265.
- Carpenter, N. S., Woolery, E. W., and Wang, Z. (2014). The Mw 4.2 Perry County, Kentucky, earthquake of 10 November 2012: Evidence of the Eastern Tennessee seismic zone in southeastern Kentucky: *Seismol. Res. Lett.*, **85**, 931-939, <https://doi/10.1785/0220130221>.
- Chapman, M. C., Powell, C.A., Vlahovic, G., and M. S. Sibol (1997), The nature of faulting in eastern Tennessee inferred from a statistical analysis of focal mechanisms and epicenter locations, *Bull. Seismol. Soc. Am.*, 87, 1522–1536.
- Chen, C., Gilbert, H., Andronicos, C., Hamburger, M.W., Larson, T., Marshak, S., Pavlis, G.L., and Yang, X. (2016). Shear velocity structure beneath the central United States: implications for the origin of the Illinois Basin and intraplate seismicity, *Geochem. Geophys. Geosyst.*, 17, 1020-1041, doi:10.1002/2015GC006206.
- Chen, C., D. Zhao, and Wu, S. (2014). Crust and upper mantle structure of the New Madrid Seismic Zone: Insight into intraplate earthquakes, *Phys. Earth Planet. Inter.*, 230, 1–14.
- Cook, F.A. and Vasudevan, K. (2006). Reprocessing and enhanced interpretation of the initial COCORP Southern Appalachians traverse, *Tectonophysics*, **420**, 161-174, doi:10.1016/j.tecto2006.01.022.
- Coppersmith, K. J. (2012). Technical Report: Central and Eastern United States Seismic Source Characterization for Nuclear Facilities. EPRI, Palo Alto, CA, U.S. DOE, and U.S. NRC: 2012.
- Davison, F. C., Jr. (1988). Stress tensor estimates derived from focal mechanism solutions of sparse data sets—Applications to seismic zones in Virginia and eastern Tennessee [Ph.D. thesis]: Blacksburg, Virginia Polytechnic Institute and State University, 189 p.
- Fichter, L. S., and Diecchio, R. J. (1986). Stratigraphic model for timing the opening of the Proto-Atlantic Ocean in northern Virginia, *Geology*, **14**, 307-309, [https://doi.org/10.1130/0091-7613\(1986\)14<307:SMFTTO>2.0.C\):2](https://doi.org/10.1130/0091-7613(1986)14<307:SMFTTO>2.0.C):2).
- Fossen, H., and Tikoff, B. (1998). Extended models of transpression and transtension, and application to tectonic settings, in Holdsworth, R.E., Strachan, R.A., and, Dewey, J.F. (editors), *Continental Transpressional and Transtensional Tectonics, Geological Society, London, Special Publications*, **135**, 15-33.
- Frankel, A. (1995). Mapping seismic hazard in the central and eastern United States, *Seismol. Res. Lett.*, **66**, 8-21.
- Frankel, A.D., Mueller, C., Barnhard, T., Perkins, D., Leyendecker, E., Dickman, N., Hanson, S., and Hopper, M. (1996). National seismic-hazard maps: documentation June 1996, U.S. Geological Survey Open-File Report 96-532, 110 pp., <http://eqhazmaps.usgs.gov>.
- Graw, J. H., Powell, C. A., and Langston, C. A. (2015). Crustal and upper mantle velocity structure in the vicinity of the eastern Tennessee seismic zone based upon radial P wave transfer functions, *J. Geophys. Res. Solid Earth*, **120**, 243–258, <https://doi/10.1002/2014JB011516>.
- Hatcher, R.D., Jr., and Zietz, I. (1980). Tectonic implications of regional aeromagnetic and gravity data from the southern Appalachians, in Wones, D., ed., *International Geological Correlation Program – Caledonide Orogen Project Symposium*, 235-244.

- Hatcher, R.D., Jr., Lemiszki, P.J., and Whistner, J.B. (2007). Character of rigid boundaries and internal deformation of the southern Appalachian foreland fold-thrust belt, in Sears, J.W., Harms, T.A., and Evenchick, C.A., eds., *Whence the Mountains? Inquiries into the Evolution of orogenic Systems: A Volume in Honor of Raymond A. Price: Geological Society of America Special Paper 433*, p. 243-276, doi:10.1130/2007.2433(12).
- Hawman, R. B., Khalifa, M.O., and Baker, S. (2012). Isostatic compensation for a portion of the Southern Appalachians: Evidence from a reconnaissance study using wide-angle, three-component seismic soundings, *Geol. Soc. Am. Bull.*, 124, 291–317.
- Hopper, E., Fischer, K.M., Rondenay, S., Hawman, R.B., and Wagner, L.S. (2016). Imaging crustal structure beneath the southern Appalachians with wavefield migration, *Geop. Res. Lett.*, 43, <https://doi.org/10.1002/2016GL071005>.
- Hopper, E., Fischer, K. M., Wagner, L. S., and Hawman, R. B. (2017). Reconstructing the end of the Appalachian orogeny, *Geology*, **45**, 15-18, <https://doi/10.1130/G38453.1>.
- Hutchinson, D. R., Grow, J. A., and Klitgord, K. D. (1983). Crustal structure beneath the southern Appalachians: the nonuniqueness of gravity modeling, *Geology*, **11**, 611-615.
- Jacobi, R. D., and Fountain, J. (2002). The character and reactivation history of the southern extension of the seismically active Clarendon-Linden Fault System, western New York State, *Tectonophysics*, **353**, 215-262.
- Johnston, A. C., and Kanter, L. R. (1990). Earthquakes in stable continental crust: *Scientific American* **262**, 68–75.
- Johnston, A. C. (1994). Seismotectonic interpretations and conclusions from stable continental region seismicity database, in *The Earthquakes of Stable Continental Regions*, vol. 1, edited by J. Schneider J. (Editor), Electr. Power Res. Inst., Palo Alto, Calif., pp. 4-1-4-103.
- King, E. R., and Zietz, I. (1978). The New York-Alabama lineament: Geophysical evidence for a major crustal break in the basement beneath the Appalachian basin: *Geology*, **6**, 312–318, [https://doi/10.1130/0091-7613\(1978\)6<312:TNYLGE>2.0.CO;2](https://doi/10.1130/0091-7613(1978)6<312:TNYLGE>2.0.CO;2).
- Lamontagne, M. (1999). Rheological and geological constraints on the earthquake distribution in the Charlevoix Seismic Zone, Québec, Canada [CD-ROM], *Geol. Surv. Can. Open File*, D3778.
- Lamontagne, M., Keating, P., and Toutin T. (2000). Complex faulting confounds earthquake research in the Charlevoix Seismic Zone, Québec, *Eos Trans. AGU*, 81(26), 289–293.
- Lamontagne, M., Beauchemin, M., and Toutin T. (2004). Earthquakes of the Charlevoix Seismic Zone, *Can. Soc. Explor. Geophys. Rec.*, **43**, 41–44.
- Lister, G.S., Etheridge, M.A., Symonds, P.A. (1986). Detachment faulting and the evolution of passive continental margins, *Geology*, 14, 246-250.
- Lister, G.S., Etheridge, M.A., Symonds, P.A. (1991). Detachment models for the formation of passive continental margins, *Tectonics*, 10, 1038-1064.
- Lyons, J.A., Forsyth, D.A., and Mair, J.A. (1980). Crustal studies in the La Malbaie region, Quebec, *Canadian Journal of Earth Sciences*, **17**, 478-490, <https://doi.org/10.1139/e80-044>.

- Munsey, J. W., and Bollinger, G. A. (1985). Focal mechanism analyses for Virginia earthquakes (1978-1984) (1985). *Bull. Seismol. Soc. Am.*, 75, 1613-1636.
- Nyamwandha, C. A., Powell, C. A., and Langston, C. A. (2016). A joint local and teleseismic tomography study of the Mississippi Embayment and New Madrid Seismic Zone, *J. Geophys. Res. Solid Earth*, **121**, <https://doi.org/10.1002/2015JB012761>.
- Parker, E. H., Hawman, R. B., Fischer, K. M., and Wagner, L. S. (2015). Constraining lithologic variability along the Alleghanian detachment in the southern Appalachians using passive-source seismology, *Geology*, <https://doi.org/10.1130/G36517.1>.
- Parker, E. H., Jr., Hawman, R. B., Fischer, K. M., and Wagner, L. S., (2013). Crustal evolution across the southern Appalachians: Initial results from the SESAME broadband array: *Geophysical Research Letters*, **40**, p. 3853–3857, <https://doi.org/10.1002/grl.50761>.
- Petersen, M. D., Moschetti, M. P., Powers, P. M., Mueller, C. S., Haller, K. M., Frankel, A. D., Zeng, Y., Rezaeian, S., Harmsen, S. C., Boyd, O. S., Field, N., Chen, R., Rukstales, K. S., Luco, N., Wheeler, R. L., Williams, R. A., and Olsen, A. (2014). Documentation for the 2014 United States national seismic hazard maps, Open-File Report 2014-1091, U.S. Department of the Interior, U.S. Geological Survey, 243 pp.
- Pollitz, F. F., and W. D. Mooney (2014), Seismic structure of the Central US crust and shallow upper mantle: Uniqueness of the Reelfoot Rift, *Earth Planet. Sci. Lett.*, **402**, 157–166.
- Powell, C. A., and Lamontagne, M. (2017). Velocity models and hypocenter relocations for the Charlevoix Seismic Zone, *J. Geophys. Res. Solid Earth*, **122**, <https://doi.org/10.1002/2017JB014191>.
- Powell, C. A., Withers, M. M., Cox, R. T., Vlahovic, G., and Arroucau, P. (2014). Crustal velocity structure associated with the eastern Tennessee seismic zone: Vp and Vs images based upon local earthquake tomography, *J. Geophys. Res. Solid Earth*, **119**, <https://doi.org/10.1002/2013JB010433>.
- Powell, C. A., and Thomas, W. A. (2016). Grenville basement structure associated with the eastern Tennessee seismic zone, southeastern USA, *Geology*, **44**, 39-42, <https://doi.org/10.1130/G37269.1>.
- Pratt, T.L., Coruh, C., Costain, J.K., and Glover, L.,III (1988). A geophysical study of the Earth's crust in central Virginia: implications for Appalachian crustal structure, *J. Geophys. Res. Solid Earth*, **93**, <https://doi.org/10.1029/JB093iB06p06649>.
- Rondot, J. (1971). Impactite of the Charlevoix structure, Quebec, Canada, *J. Geophys. Res.*, **76**, 5414–5423, <https://doi.org/10.1029/JB076i023p05414>.
- Rondot, J. (2000). Charlevoix and Sudbury as gravity-readjusted impact structures, *Meteorit. Planet. Sci.*, **35**, 707–712.
- Shen, W., and Ritzwoller, M.H. (2016). Crustal and uppermost mantle structure beneath the United States, *J. Geophys. Res. Solid Earth*, **121**, 4306-4342, [doi:10.1002/2016JB012887](https://doi.org/10.1002/2016JB012887).
- Svartman Dias, A. E., Lavier, L. L., and Hayman, N. W. (2015). Conjugate rifted margins width and asymmetry: The interplay between lithospheric strength and

- thermomechanical processes, *J. Geophys. Res. Solid Earth*, **120**, 8672–8700, <https://doi.org/10.1002/2015JB012074>.
- Thomas, W.A. (2014). A mechanism for tectonic inheritance at transform faults of the Iapetan margin of Laurentia, *Geoscience Canada*, 41, 321, 344, <http://dx.doi.org/10.12789/geocanj.2014.41.048>.
- Thomas, W. A. (2006). Tectonic inheritance at a continental margin: *GSA Today*, **16**, 4–11, doi: [https://doi.org/10.1130/1052-5173\(2006\)016\[4:TIAACM\]2.0.CO;2](https://doi.org/10.1130/1052-5173(2006)016[4:TIAACM]2.0.CO;2).
- Thomas, W. A. (1991). The Appalachian-Ouachita rifted margin of southeastern North America, *Geol. Soc. Am. Bull.*, **103**, 415–431, [http://dx.doi.org/10.1130/0016-7606\(1991\)103<0415:TAORMO>2.3.CO;2](http://dx.doi.org/10.1130/0016-7606(1991)103<0415:TAORMO>2.3.CO;2).
- Thomas, W. A. (1977). Evolution of Appalachian–Ouachita salients and recesses from reentrants and promontories in the continental margin, *Am. Jour. Sci.*, **277**, 1233–1278, <https://dx.doi.org/10.2475/ajs.277.10.1233>.
- Thomas, W.A. (1993). Low-angle detachment geometry of the late Precambrian–Cambrian Appalachian–Ouachita rifted margin of the southeastern North America, *Geology*, **21** (10), 921–924, [https://doi.org/10.1130/0091-7613\(1993\)021<0921:LAGOT>2.3.CO;2](https://doi.org/10.1130/0091-7613(1993)021<0921:LAGOT>2.3.CO;2).
- Thomas, W. A. (2019). Tectonic inheritance at multiple scales during more than two complete Wilson cycles recorded in eastern North America, *Geol. Soc. London Spec. Pub.*, **470**, 337–352, doi.org/10.1144/SP470.4.
- Thomas, W. A., and Powell, C. A. (2017). Necessary conditions for intraplate seismic zones in North America. *Tectonics*, **36**, 2903–2917, <https://doi.org/10.1002/2017TC004502>.
- Thomas, W.A., and Astini, R.A. (1999). Simple-shear conjugate rift margins of the Argentine Precordillera and the Ouachita embayment of Laurentia, *Geol. Soc. Am. Bull.*, 111(7), 1069–1079, [https://doi.org/10.1130/0016-7606\(1999\)111<1069:SSCRMO>2.3.CO;2](https://doi.org/10.1130/0016-7606(1999)111<1069:SSCRMO>2.3.CO;2).
- Yu, H., Liu, Y., Harrington, R. M., and, Lamontagne, M. (2016). Seismicity along St. Lawrence paleorift faults overprinted by a meteorite impact structure in Charlevoix, Quebec, eastern Canada, *Bull. Seismol. Soc. Am.*, **106**, <https://doi.org/10.1785/0120160036>.
- Wagner, L. S., Stewart, K., and Metcalf, K. (2012). Crustal-scale shortening structures beneath the Blue Ridge Mountains, North Carolina, USA, *Lithosphere*, <https://doi.org/10.1130/L184.1>.
- Wagner, L.S., Fischer, K.M., Hawman, R., Hopper, E., and Howell, D. (2018). The relative roles of inheritance and long-term passive margin lithosphere evolution on the modern structure and tectonic activity in the southeastern United States, *Geosphere*, 14, doi:10.1130/GES01593.1.
- Wehr, F., and Glover, L., III (1985). Stratigraphy and tectonics of the Virginia–North Carolina Blue Ridge: Evolution of a Late Proterozoic–early Paleozoic hinge zone, *Geol. Soc. Am. Bull.*, **96**, 285–295.
- Wernicke, B. (1985). Uniform-sense normal simple shear of the continental lithosphere: *Canadian Journal of Earth Sciences*, 22, 108–125.
- Wheeler, R. L. (1995). Earthquakes and the western limit of Iapetan rifting in eastern North America, *Geology* **23**, 105–108.

- Wheeler, R. L., and, Frankel, A. (2000). Geology in the 1996 USGS seismic-hazard maps, central and eastern United States, *Seismol. Res. Lett.* **71**, 273-280.
- Zhan, Y., Hou, G., Kusky, T., and Gregg, P.M. (2016). Stress development in heterogenetic lithosphere: insights into earthquake precesses in the New madrid seismic zone, *Tectonophysics*, 671, 56-62,
<https://dx.doi.org/10.1016/j.tecto.2016.01.016>.

Christine A. Powell
 Center for Earthquake Research and Information
 The University of Memphis, Memphis, Tennessee 38057, USA capowell@memphis.edu

William A. Thomas
 Emeritus University of Kentucky, and Geological Survey of Alabama
 Tuscaloosa, Alabama 35486, USA

Robert D. Hatcher Jr.,
 Emeritus Department of Earth and Planetary Sciences
 University of Tennessee
 1621 Cumberland Avenue, Room 602

Knoxville, Tennessee 37996, USA

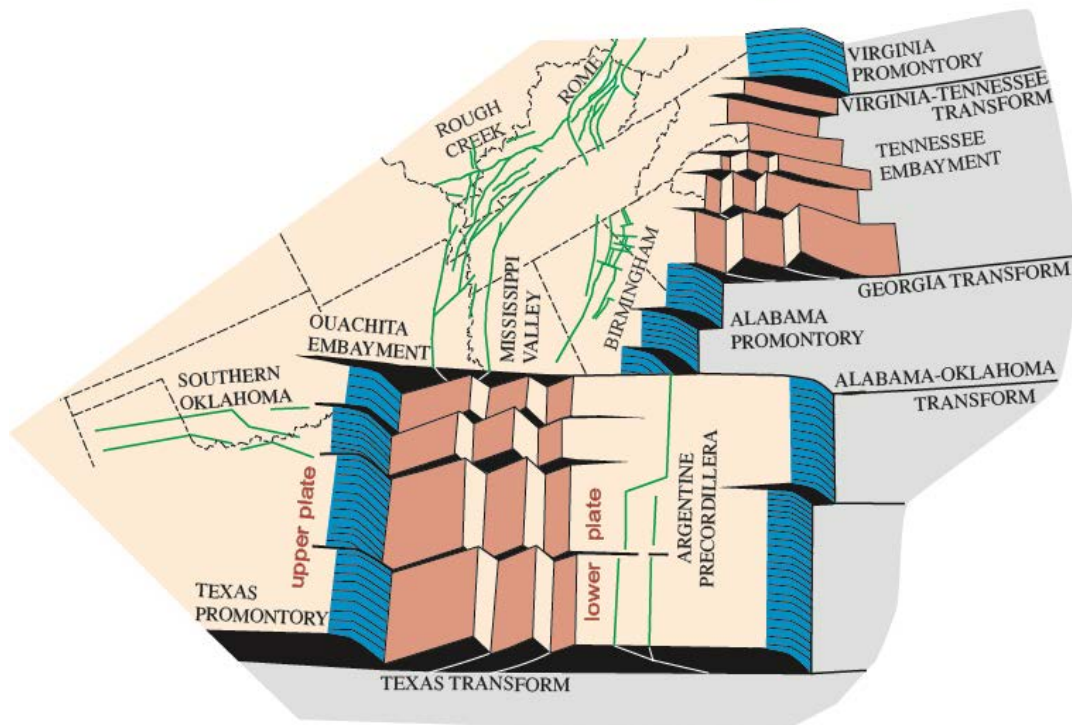


Figure 1. Block diagram illustrating the structure of the Iapetan rifted margin of southeastern Laurentia in present-day southeastern North America (adapted from Thomas, 1991, 1993, 2014, and Thomas and Astini, 1999, which provide further discussion of rift-related structures). The diagram uses a low-angle detachment model for continental rifting, in which the detachment dips beneath the upper-plate margin and multiple oceanward-dipping listric extensional faults bound half grabens along the lower-plate margin (after Lister et al., 1986, 1991; Wernicke, 1985). Upper-plate margins (blue) are narrow and have few down-to-the-ocean normal faults; lower-plate margins (brown) are wide and have multiple faults dipping toward the rift. Transform faults offset the rift and also accommodate along-strike reversals in direction of dip of the detachment. Oceanic crust shown in gray. The diagram includes rifting of the Argentine Precordillera from Laurentia to illustrate the relationship between the conjugate upper-plate and lower-plate rift margins in low-angle-detachment continental rifting. Green lines indicate synrift, intracratonic basement faults.

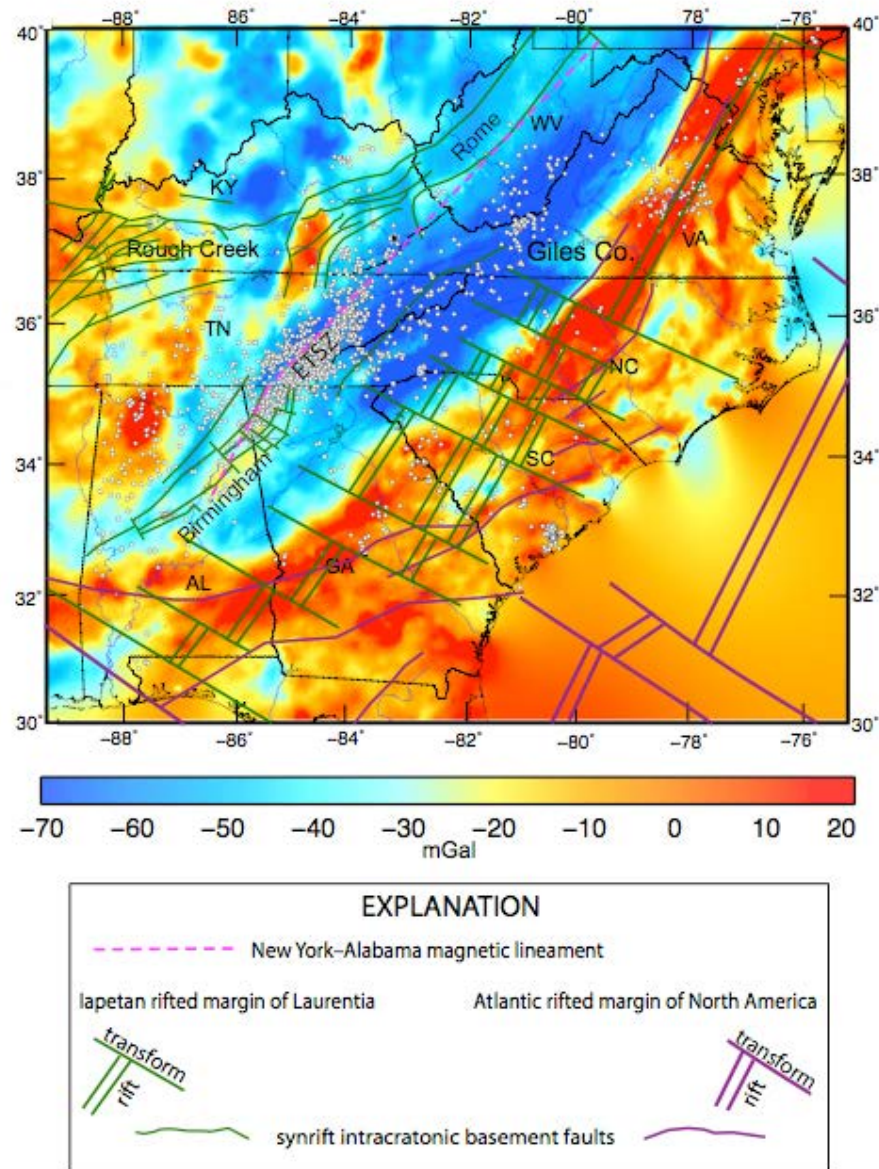


Figure 2. Map of Bouguer gravity anomalies and Iapetan rifted margin of continental crust (shown in palinspastic location; multiple parallel sets of the double-line symbol for rifts schematically show multiple extensional faults in a lower-plate setting). The Iapetan rifted margin formed as a result of breakup of supercontinent Rodinia during early Paleozoic (~530 Ma). The Rough Creek graben, Rome trough and Birmingham graben are intracratonic faults that represent late synrift extension inboard from the Iapetan rifted margin. Note the

correspondence of the western limit of thinned crust at the palinspastically restored Iapetan rift margin with the prominent Appalachian gravity gradient. The New York–Alabama (NY–AL) magnetic lineament is interpreted to represent a continental transform during assembly of supercontinent Rodinia during Mesoproterozoic (~1200 Ma). Exotic Gondwanan terranes were accreted to the Iapetan rifted margin during the assembly of supercontinent Pangaea in late Paleozoic (~270 Ma), and were left attached to Laurentia after Atlantic rifting in the Mesozoic (~170 Ma), which formed the present Atlantic rifted margin some distance outboard from the Iapetan rifted margin. The crust between the Iapetan rifted margin and the Atlantic rifted margin consists of accreted Gondwanan terranes. Mesozoic intracratonic faults, associated with opening of the Atlantic Ocean, are genetically similar to the intracratonic faults formed during Iapetan rifting. Note the clear spatial and temporal separation of Iapetan and Atlantic rifting. Earthquakes shown as white dots taken from the ANSS Comprehensive Earthquake Catalog from 2007-2017. ETSZ—Eastern Tennessee seismic zone.

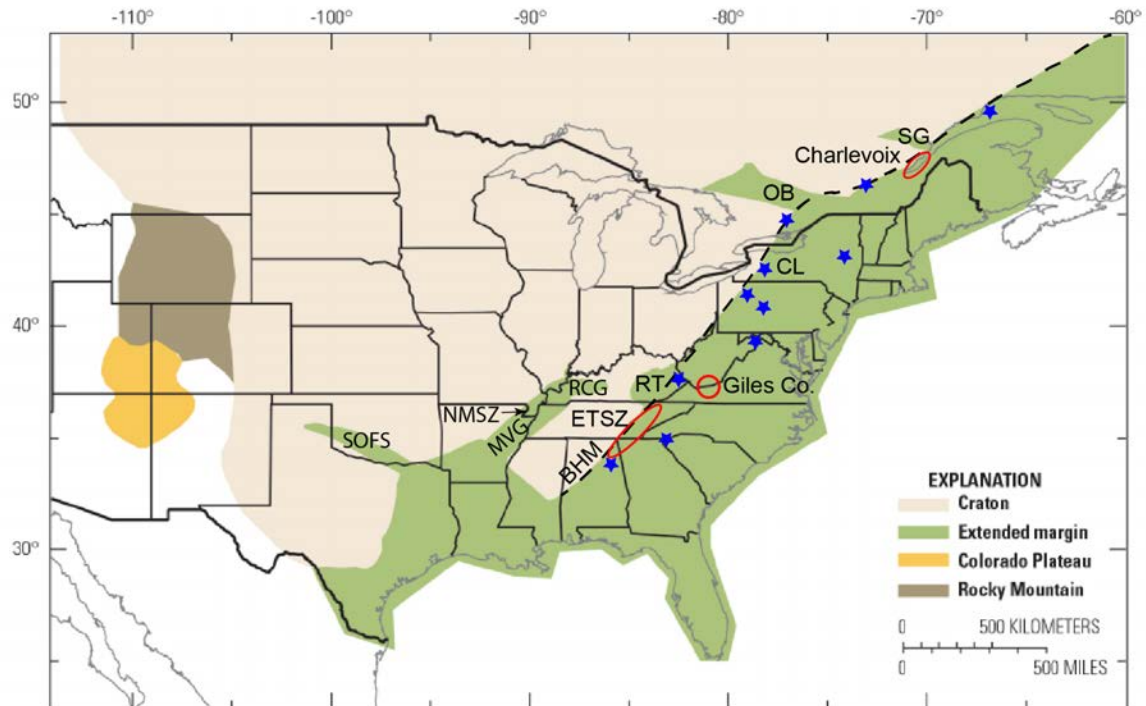


Figure 3. Seismotectonic zonation map for the central and eastern U.S. used in the USGS NSHMP (Model A, modified from Petersen et al., 2014). Area shown in green is interpreted as rifted crust associated with the openings of the Iapetus and Atlantic Oceans. Dashed black line is the western limit of Iapetus rifted crust determined by Wheeler [1995]. Seismic zones used by Wheeler [1995] are circled in red and the blue stars indicate locations where other evidence was used to delineate the boundary. ETSZ: Eastern Tennessee seismic zone, RT: Rome Trough, OB: Ottawa-Bonnechere graben, SG: Saguenay graben, CL: Clarendon-Linden fault system, MVG: Mississippi Valley graben; RCG: Rough Creek graben; SOFS: Southern Oklahoma fault system; NMSZ: New Madrid seismic zone; BHM: Birmingham graben.

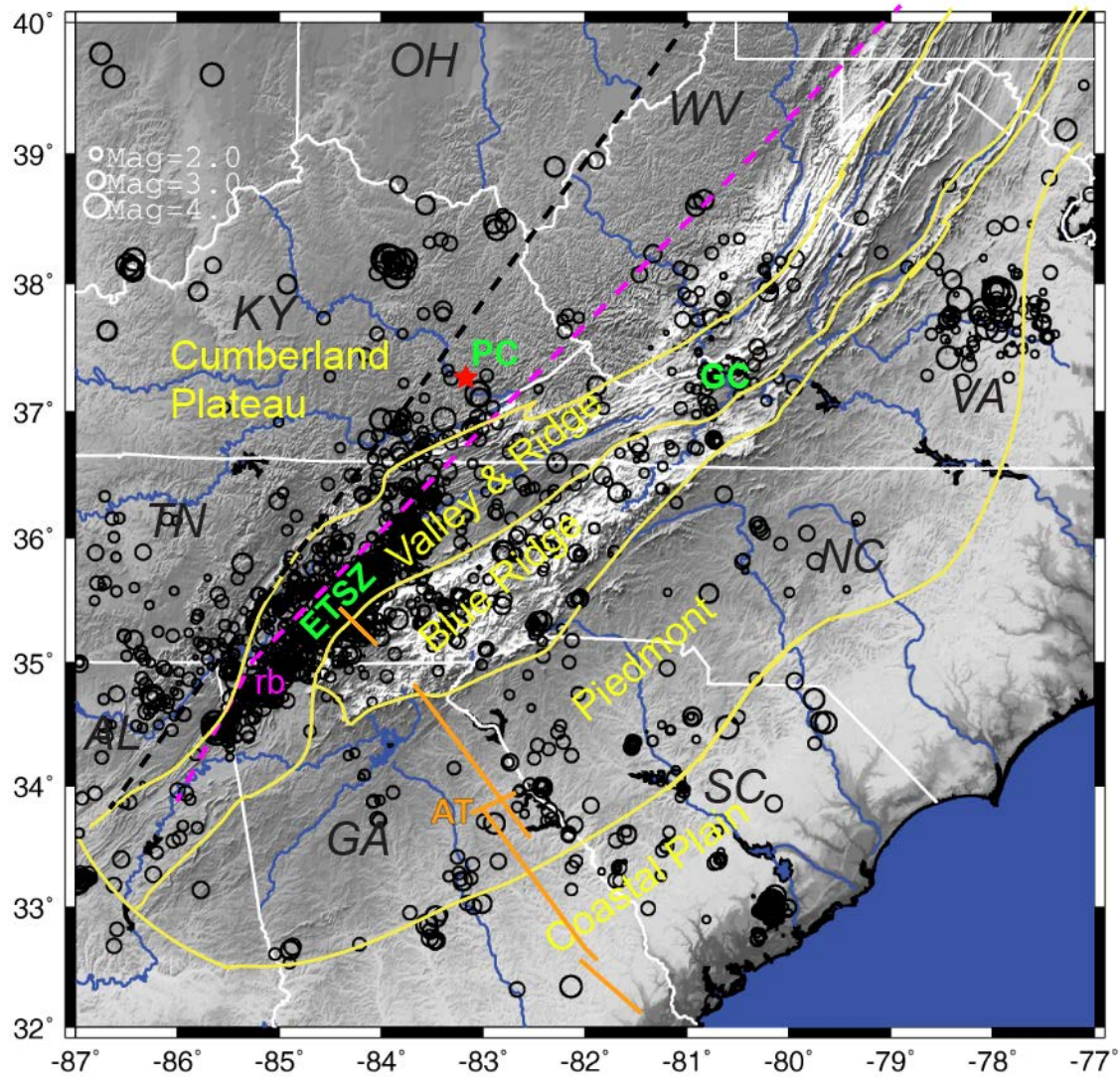


Figure 4. Digital elevation map of the southeastern U.S. with physiographic provinces labeled in yellow (physiographic provinces are used herein only as a geographic reference frame). ETSZ: eastern Tennessee seismic zone, rb: present location of the releasing bend, GC: Giles County seismic zone, PC: Perry County earthquake. Magenta dashed line indicates the location of the NY-AL magnetic lineament. Black dashed line is the western limit of Iapetan rifting determined by Wheeler (1995). Orange line is the COCORP southern Appalachian seismic reflection line. AT marks the location of accreted terrane. Earthquakes for the time period 1984-2017 from the CERI and ANSS earthquake catalogs.

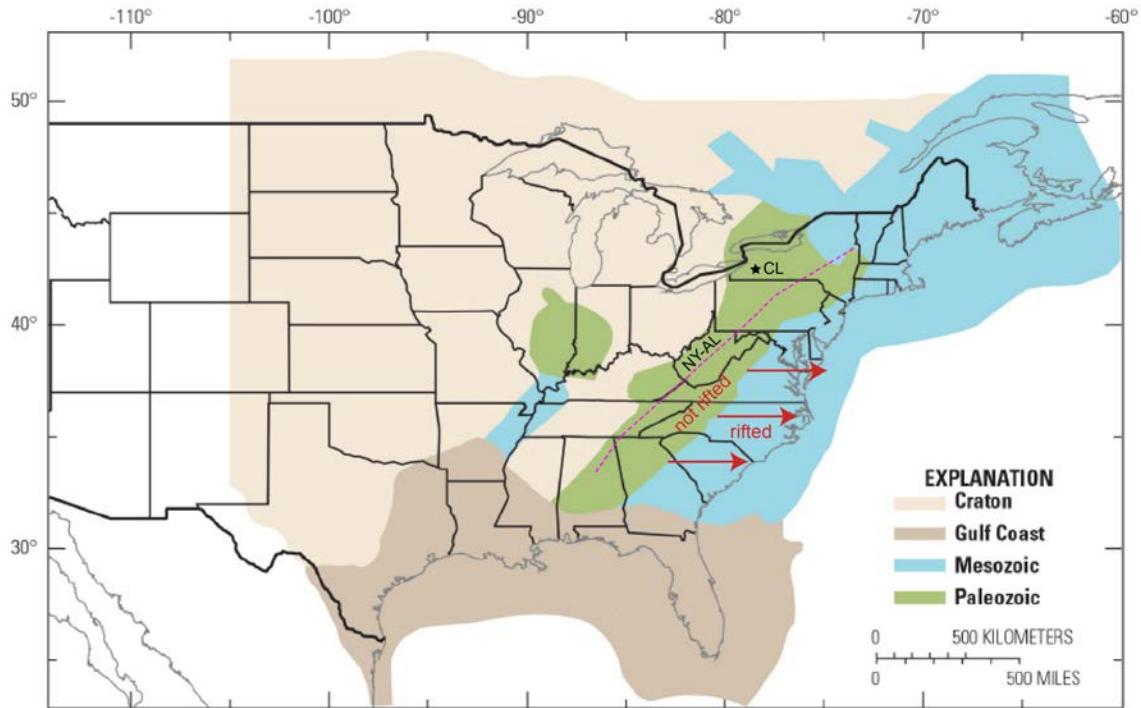


Figure 5. Seismotectonic zonation map for the central and eastern U.S. developed in the CEUS-SSC Project (modified from Coppersmith et al., 2012). This is Model B used in the USGS NSHMP. Rifted crust associated with the opening of the Iapetus Ocean (green area) is differentiated from rifted crust associated with the Atlantic Ocean (blue area) in this map. There are two models for the Paleozoic extended crust. The “wide Paleozoic extended crust” is shown in the figure as the green area. The northwestern margin of the second, and preferred model in the report, the “narrow Paleozoic crust”, coincides with the location of the NY-AL magnetic lineament (dashed line); the narrow model does not contain rifted crust west of the NY-AL magnetic lineament. The boundary between the green and blue areas corresponds to the Appalachian gravity gradient maximum. We suggest that the actual western limit of Iapetan rifted crust corresponds to the division between the green and blue areas. CL - Clarendon-Linden fault system.

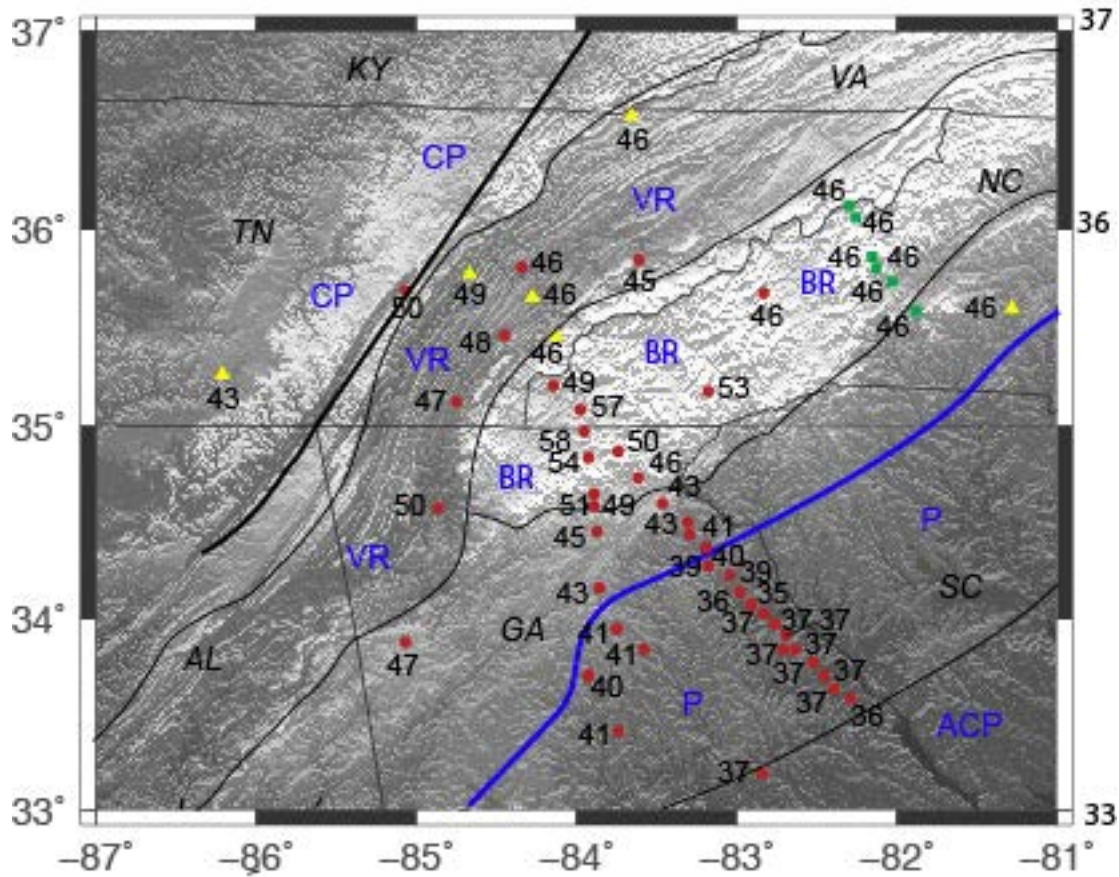


Figure 6. Compilation of Moho depths determined from receiver functions at broadband stations. Red dots: Parker et al. [2013, 2015]; Yellow triangles: Graw et al. [2015]; Green squares: Wagner et al. [2012]. Black line is the western limit of Iapetan rifting determined by Wheeler [1995]. Blue line is the location of the Appalachian gravity gradient maximum. ACP: Atlantic Coastal Plane; BR: Blue Ridge, CP: Cumberland Plateau, P: Piedmont, VR: Valley and Ridge.

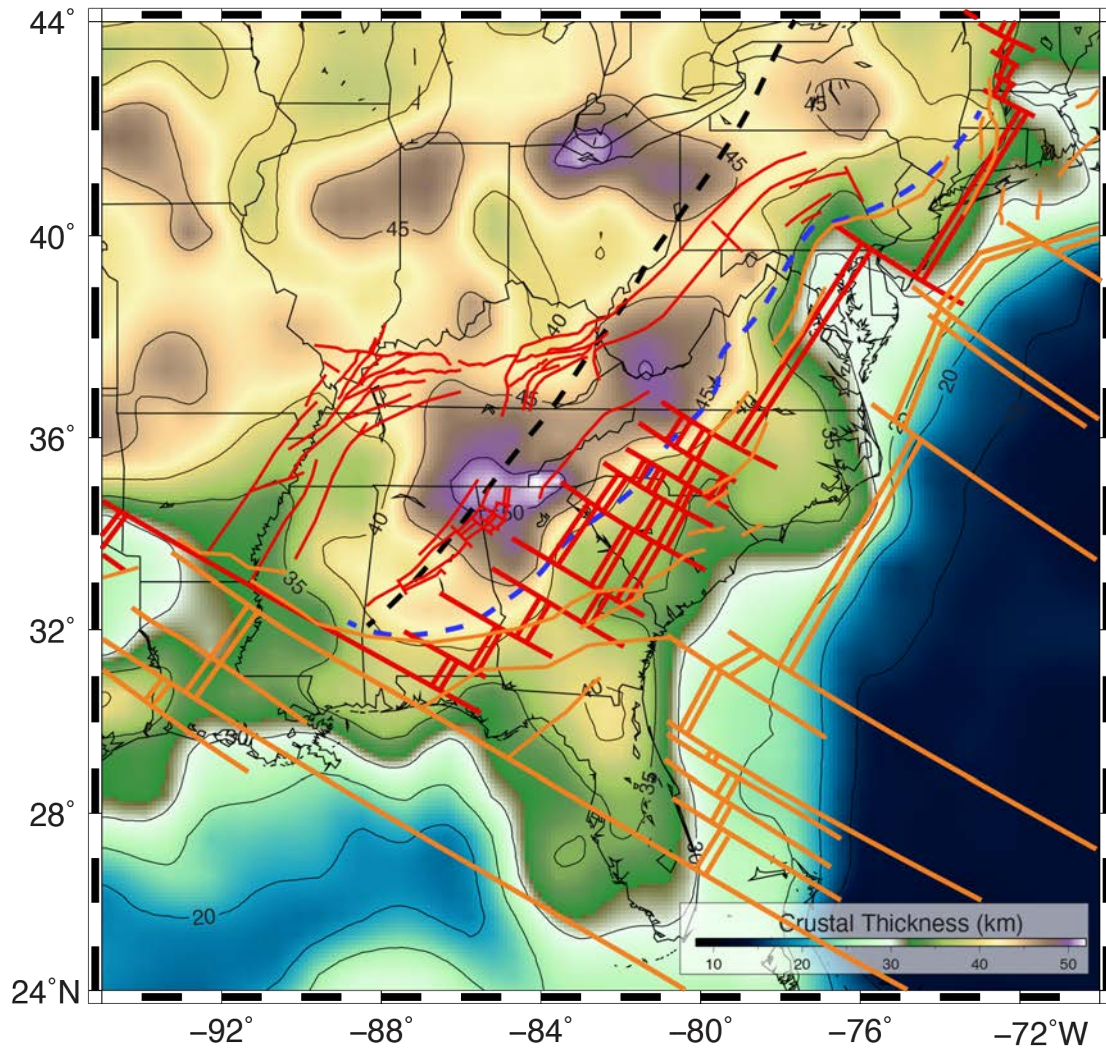


Figure 7. Crustal thickness map based on receiver functions for TA and SESAME stations as well as P-s wavefield migration results (map modified from Wagner et al., 2018). The Iapetan rifted margin and late Iapetan synrift faults, as well as the Atlantic rifted margin, are from Figure 2 (the different line colors are necessary to show a contrast with the background)

map). The Appalachian gravity gradient corresponds to our proposed western limit of crustal extension associated with Iapetan rifting, which contrasts with the western limit of Iapetan rifting determined by Wheeler (1995).

Focal Mechanisms of Relocated Earthquakes and Stress Orientation in the Charlevoix Seismic Zone

Oluwaseun Idowu Fadugba¹, Charles A. Langston¹ and Christine A. Powell¹

¹Center for Earthquake Research and Information, The University of Memphis, Memphis, TN 38152.

Submitted to
Journal of Geophysical Research: Solid Earth

Key Points

- Stress inversion using 455 focal mechanisms in the CSZ shows σ_1 orientation of N103°, in contrast to N86° from previous work.
- σ_1 is N73° within the impact zone compared to N106° outside the zone; σ_1 is N53° for events in the NW half of the impact structure.
- A distinct systematic clockwise change in σ_1 orientation is seen from N83° to N127° as a function of depth from the surface to 20 km.

Abstract

Focal mechanisms for a catalog of 455 relocated earthquakes within the Charlevoix Seismic Zone (CSZ) of eastern Canada are determined using amplitude and polarities of P- and S-wave phases. The large number of earthquakes in the catalog and well-constrained source depths allow us to examine spatial changes in stress within the CSZ. Stress inversion using all focal mechanisms shows that the σ_1 orientation is N103°, in contrast to N86° from previous work, with reverse faulting dominating. The southwestern half of the CSZ contains ring structures produced by the Devonian Malbaie impact; σ_1 is N73° within the impact zone compared to N106° outside the zone. Events that concentrate in the northwestern half of the impact have a more northerly σ_1 average orientation of N53°, suggesting that structures associated with the impact cause major perturbations to the regional stress field. A distinct systematic clockwise change in σ_1 orientation of 44° is observed as a function of source depth from the surface to 20 km, changing from N83° to N127°. The pattern of stress changes correlates with the pattern of velocity anomalies determined from 3D tomography and clustering of seismicity along faults within the St. Lawrence rift zone. This suggests that seismicity and the observed stress rotations of the CSZ are controlled by velocity heterogeneity and rock stiffness, including the impact structure, and pre-existing fault structure within a stress field generated by both plate tectonic forces and glacial rebound.

Plain Language Summary

We determined the fault plane solutions of 455 well-located local earthquakes in the Charlevoix Seismic Zone (CSZ) and used the fault planes to determine the principal compressive stress orientation in the CSZ. The fault plane solutions for the individual earthquakes were grouped into different areas and in depth to investigate the variation of stress within the seismic zone. A common variation of stress in the CSZ is a more northerly stress orientation determined for the earthquakes within the impact zone than those outside the zone. Another notable variation is an increase in the stress orientation, in a clockwise sense, as earthquakes get deeper from the surface to 20 km depth. This pattern of stress change is like the pattern of velocity anomalies determined from 3D tomography and relocations of the earthquakes. Seismicity and the observed stress

rotations are controlled by changes in Earth material properties, damage caused by the meteorite impact, and tectonic faults along the St. Lawrence River.

1.0 Introduction

The Charlevoix Seismic Zone (CSZ) is the most seismically active region in eastern Canada (Figure 1; Anglin 1984). The seismic zone generates over 200 earthquakes per year (Nuttli magnitudes, mN mostly ≤ 3 ; Baird et al., 2010), and has been the location of several large historical earthquakes, such as a magnitude (M) 6.5 in 1925 (Bent, 1992) and a M7.5 in 1663 (Ebel, 2011). The CSZ is located along the St. Lawrence River within the Late Proterozoic-Early

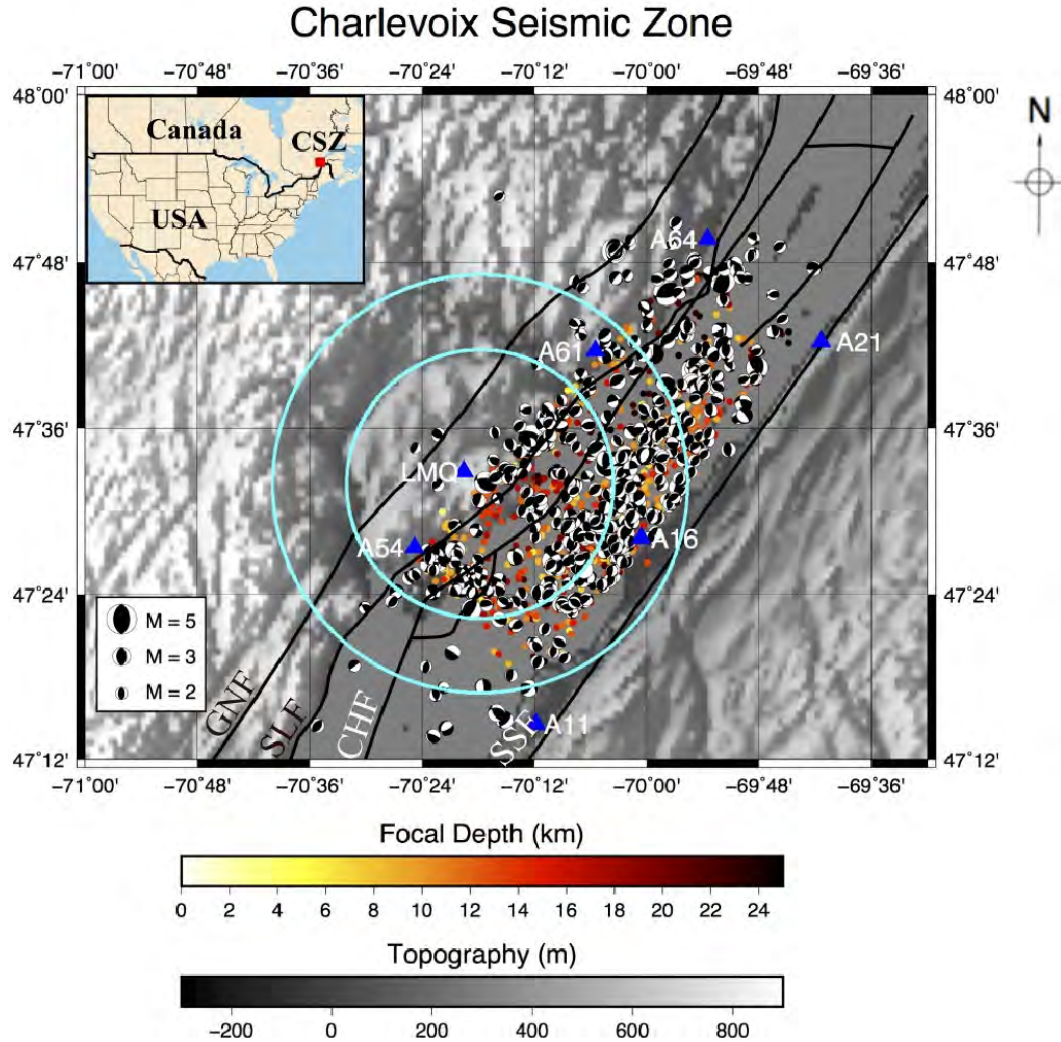


Figure 1: Topography and seismicity of the Charlevoix Seismic Zone (CSZ), locations of the impact structure (outer cyan circle) and the more damaged inner impact structure (inner cyan circle), and the seismic stations. Small circles and stars are relocated epicenters (Powell & Lamontagne, 2017) for the years 1988–2020, and their colors represent focal depth. The focal mechanisms are from this study. Solid black lines mark the rift faults known in the region: GNF, Gouffre Northwest fault; SLF, Saint-Laurent fault; CHF, Charlevoix fault; and SSF, South Shore fault (Lamontagne, 1999; Rondot, 1971). The inset shows the location of the CSZ in eastern Canada. Earthquake data set is from the National Resources Canada catalog.

Cambrian St. Lawrence rift zone. The location was also the site of a Devonian impact structure (Rondot, 1994). The CSZ poses higher seismic risk due to its history of generating M4+ earthquakes compared to the other seismic zones in the area. The CSZ is also close to the densely populated cities of Quebec, Ottawa and Montreal, and contributes to much of the seismic hazard of New England (e.g., Lamontagne, 1999). In other parts of the world, impact structures are not, in general, seismogenic (Solomon and Duxbury, 1987), but the combined effects of the impact structure and the associated rift faults may be responsible for the high occurrence of the seismicity in the CSZ (Fadugba et al., 2019; Thomas and Powell, 2017).

The rift zone is characterized by three main rift-parallel basement faults, inboard from the rifted continental margin associated with the opening of the Iapetus ocean: Gouffre Northwest Fault (GNF), Saint-Laurent fault (SLF), and the Charlevoix Fault (CHF) (Powell and Lamontagne, 2017; Fadugba et al., 2019). The impact structure has a 56-km surface diameter and is thought to be 12 km deep (Rondot, 1994). It has an inner damaged zone with a diameter of 36 km (Figure 1).

Several researchers have been interested in the focal mechanisms of CSZ earthquakes with a view to understanding the stress state of the seismic zone (e.g., Lamontagne, 1998; Bent 1992; Ebel, 2011; Mazzotti and Townend, 2010). Lamontagne (1998) used P- and SH-wave first motions to determine focal mechanisms. Mazzotti and Townend (2010) performed a stress inversion using focal mechanisms from previous published studies (e.g., Adams, 1991; Lamontagne, 1998; Bent, 1992; Bent et al., 2003). They observed a maximum compressive stress orientation of N86°, which represents a 32° clockwise rotation from the regional σ_1 orientation determined from nearby boreholes (i.e., 54°, Mazzotti and Townend, 2010). Mazzotti and Townend (2010) further investigated the stress rotation by dividing the CSZ into two clusters, one northwest of the SLF and one to the southeast. The stress inversion for earthquakes in the GNF (i.e., the NW cluster) and for earthquakes in both the SLF and the CHF (i.e., the SE cluster) yielded σ_1 orientations of N55° and N101°, respectively (Mazzotti and Townend, 2010).

Powell and Lamontagne (2017) determined three-dimensional (3-D) P- and S-wave velocity models using 1328 earthquakes in the CSZ and event relocations. They showed that the relocated earthquakes have small location uncertainties and further constrain the geometry of the rift faults. The hypocenters have horizontal and vertical location errors of 0.15 km and 0.35 km, respectively. They also observed circular arcs of seismicity that follow the edge of the impact structure as defined by velocity contrasts in the 3-D tomographic inversions. The study by Powell and Lamontagne (2017) provided better resolution of a high-velocity body at mid-crustal depths below the CSZ, first detected in a P-wave velocity inversion by Vlahovic et al. (2003). The high-velocity body trends parallel to the St. Lawrence River and most earthquakes occur on either side of the body, forming the two earthquake clusters noted by Mazzotti and Townend (2010). Figure 2 shows the 3-D tomography model determined by Powell and Lamontagne (2017) with the change in P-wave velocity relative to the 1-D starting model. The high-velocity body, labelled H1, increases in size with depth and goes under the impact structure at about 10-12 km depth. Earthquakes in the SE cluster occur within the high-velocity body at depths exceeding 12 km. The high-velocity body is attributed to the presence of commonly observed Grenvillian basement lithologies such as diorite and granulite (Vlahovic et al., 2003; Powell and Lamontagne, 2017). The low-velocity rocks outside the impact structure (labelled L1) are attributed to Appalachian sedimentary sequences (Powell and Lamontagne, 2017).

Event locations determined by Powell and Lamontagne (2017) offer an opportunity to improve knowledge of the state of stress in the CSZ through an analysis of focal mechanisms.

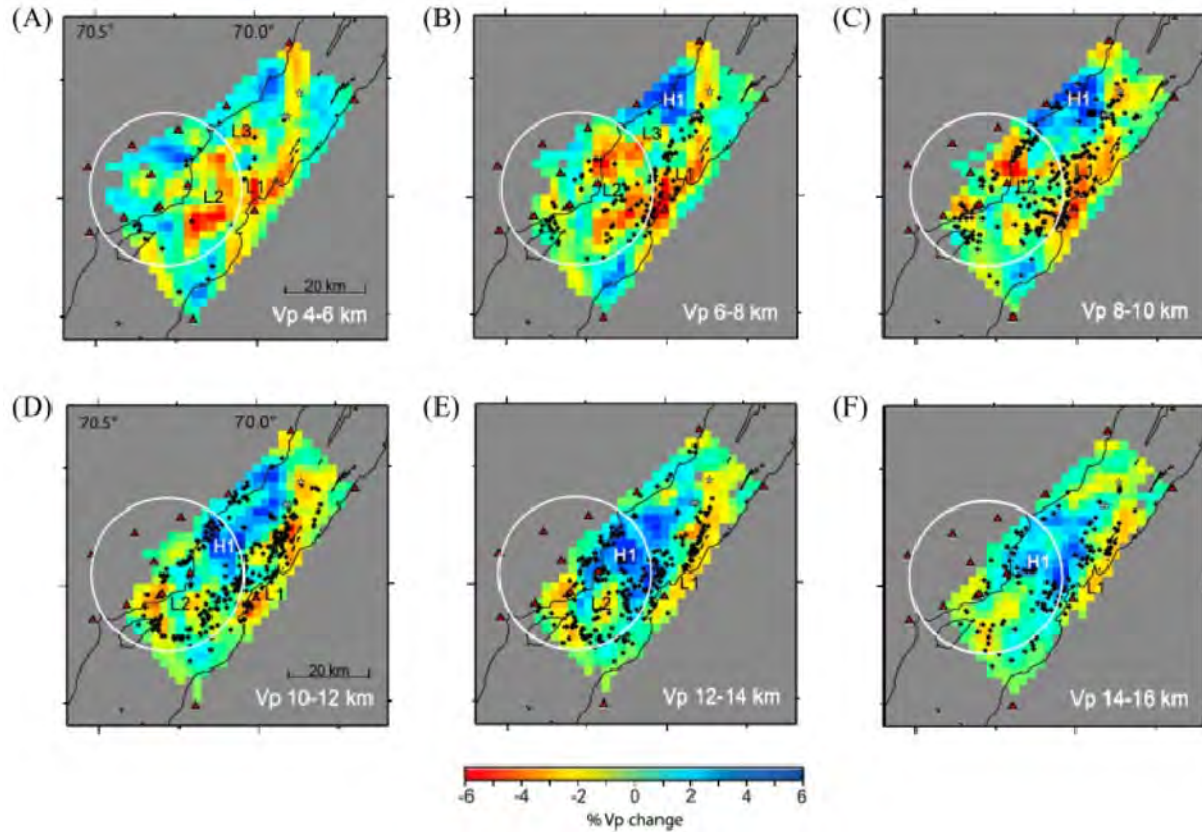


Figure 2: Three-dimensional (3-D) tomography model showing the change in P wave velocity relative to a starting 1-D model at each depth range (Powell and Lamontagne, 2017). The black dots are the earthquakes used in the tomography study.

Accurate locations and the velocity model allow for accurate estimates of take-off angle and azimuth from the earthquake source needed to map first motions and amplitudes back to the reference focal sphere (e.g., Bent et al., 2003). In addition, the CSZ appears to have relatively simple wave propagation properties because the waveforms of the earthquakes are relatively simple and show distinct seismic phases. We experiment with using wave amplitude ratios in the focal mechanism determination to further constrain fault orientations.

In this study, we improve the resolution of the variation in stress orientation in the CSZ in both the horizontal and vertical directions using an updated earthquake catalog from 1988-2020. We determine high-quality focal mechanisms for 455 relocated earthquakes with magnitudes of at least 2.0 using several constraints including P- (vertical) and SH- (tangential) wave polarities, and amplitude ratios ($|SV|/SH$, SH/P and $|SV|/P$). A grid search method is used to determine the fault plane solution that minimizes the mismatch between the observed and calculated wave polarities and amplitude ratios. An averaging algorithm similar to Hardebeck and Shearer (2002) is used to find preferred focal mechanisms. We then present new stress orientations in the CSZ using the focal mechanisms.

2.0 Materials and Methods

2.1 Focal Mechanism Determination

We determine the focal mechanisms of CSZ earthquakes using a grid search algorithm with wave polarities and amplitude ratios as constraints. We check the algorithm using synthetic

amplitudes datasets at hypothetical stations of a known input focal mechanism. The main inputs are wave amplitudes (vertical-P, radial-SV and/or tangential-SH), earthquake parameters including the source depth, the distances and azimuths of each seismic station to the earthquake hypocenter, and the local 1-D velocity model. The absolute value of SV amplitude (i.e., $|SV|$) is used to account for a possible polarity reversal at the free surface.

We estimate the P- and S- wave velocities, and density at the source depth using the input velocity model, and calculate the take-off angle and the direction of wave propagation (either upgoing or downgoing) to each seismic station. We use a travel-time calculation algorithm based on ray theory to determine the take-off angles and the direction of propagation for crustal earthquakes (Shearer, 2009). For upgoing waves, we add 180° to the azimuth of the seismic stations to determine the amplitude of corresponding downgoing waves to be consistent with a lower hemispherical focal sphere. We then determine vertical-P, radial-SV and/or tangential-SH wave amplitudes at each station using ray theory for all possible combinations of strike, dip and rake at each station (Bullen, 1963). We assign weight to each input amplitude from 1 (less confident) to 5 (most confident). Amplitudes with zero weight are not used in the inversion. We extended the algorithm to determine focal mechanisms of teleseisms using a global 1-D velocity model and Tau-p for teleseisms (Crotwell et al., 1999) to determine the take-off angles and direction of propagation.

We perform a grid search algorithm to determine the fault plane solution that minimizes the mismatch between the observed and calculated wave polarities and amplitude ratios. The grid search method is based on three steps: wave polarities, amplitude ratios and the combination of the two grid search methods.

A. Grid Search Using Wave Polarities

Consider the diagonal matrices P_{obs} and P_{calc} that contain observed and calculated polarities in each diagonal, respectively as:

$$\text{diag}P_{\text{obs}} = [p_{\text{obs}_1} \quad \cdots \quad p_{\text{obs}_i} \quad sv_{\text{obs}_1} \quad \cdots \quad sv_{\text{obs}_j} \quad sh_{\text{obs}_1} \quad \cdots \quad sh_{\text{obs}_k}] \quad (1)$$

$$\text{diag}P_{\text{calc}} = [p_{\text{calc}_1} \quad \cdots \quad p_{\text{calc}_i} \quad sv_{\text{calc}_1} \quad \cdots \quad sv_{\text{calc}_j} \quad sh_{\text{calc}_1} \quad \cdots \quad sh_{\text{calc}_k}] \quad (2)$$

Each observed or calculated polarity for a P wave, SV wave, or SH wave can take a value of +1 or -1 and there may be i P waves, j SV waves, and k SH waves.

The observations are also assigned a weight based on assessment of the quality of the polarity. This is given by a diagonal weighting matrix, W_{obs} , where

$$\text{diag}W_{\text{obs}} = \frac{1}{5} \times [wp_{\text{obs}_1} \quad \cdots \quad wp_{\text{obs}_i} \quad wsv_{\text{obs}_1} \quad \cdots \quad wsv_{\text{obs}_j} \quad wsh_{\text{obs}_1} \quad \cdots \quad wsh_{\text{obs}_k}] \quad (3)$$

and each weight (e.g., wp_{obs}) is given a value of 1 for poor quality, to 5 for the highest quality.

A diagonal polarity test matrix, T , is computed through:

$$T = P_{\text{calc}} W_{\text{obs}} P_{\text{obs}} \quad (4)$$

and then separated into positive and negative values:

$$T = T^+ + T^- \quad (5)$$

The accuracy of the fit of polarities is then computed by:

$$\epsilon_{\text{pol}} = 100 \frac{|\text{diag}T^+|}{|\text{diag}T|} \quad (6)$$

since positive diagonal elements of \mathbf{T} mean the polarities are the same between observed and calculated polarities. If all polarities are fit, then ε_{pol} is 100%. The weighting matrix helps insure that poorly determined polarities do not have as much influence in determining the magnitude of $\text{diag}\mathbf{T}$ or $\text{diag}\mathbf{T}^+$.

B. Grid Search Using Wave Amplitude Ratios

Amplitude ratios of P, SV, and SH waves are measured from local seismograms to serve as constraints on focal mechanisms:

$$\mathbf{A}_{obs} = [A_{SH/P_1} \cdots A_{SH/P_l} A_{SV/P_1} \cdots A_{SV/P_m} A_{SV/SH_1} \cdots A_{SV/SH_n}] \quad (7)$$

There may be $l \frac{SH}{P}$, $m \frac{SV}{P}$, and $n \frac{SV}{SH}$ amplitude ratios. The total number of the amplitude ratios is s , where $s = l + m + n$.

Take each amplitude ratio and calculate a unit vector. The unit vector for amplitude ratio of, for example, A_{SV/P_m} , is computed by

$$v_{1m} = \frac{|SV|_{obs_m}}{\sqrt{|SV|_{obs_m}^2 + P_{obs_m}^2}}; v_{2m} = \frac{P_{obs_m}}{\sqrt{|SV|_{obs_m}^2 + P_{obs_m}^2}} \quad (8)$$

$$\text{and } |\vec{v}_m| = 1 \quad (9)$$

Arrange all unit vectors, \vec{v}_i for $i = 1 \dots s$, for the amplitude ratio observations into columns of matrix \mathbf{V}_{obs} :

$$\mathbf{V}_{obs} = \begin{bmatrix} v_{11} & v_{12} & \cdots & v_{1s} \\ v_{21} & v_{22} & \cdots & v_{2s} \end{bmatrix} \quad (10)$$

The quality of the amplitude ratio will vary. Define a weighting matrix as before:

$$\mathbf{W}_{obs} = \frac{1}{5} \begin{bmatrix} w_{11} & \cdots & 0 \\ \vdots & \ddots & \vdots \\ 0 & \cdots & w_{ss} \end{bmatrix} \quad (11)$$

where each weight (e.g., w_{11}) varies as 1 for poor quality, to 5 for the highest quality.

The weighted observed amplitude ratios will be:

$$\mathbf{V}'_{obs} = \mathbf{V}_{obs} \mathbf{W}_{obs} \quad (12)$$

Calculate the theoretical amplitude ratio vectors and form a test matrix, \mathbf{V}_{calc} . Take:

$$\begin{aligned} \mathbf{T} &= \mathbf{V}'_{obs} \mathbf{V}_{calc}^T \\ &= \underbrace{\mathbf{V}_{obs}}_{2 \times s} \underbrace{\mathbf{W}_{obs}}_{s \times s} \underbrace{\mathbf{V}_{calc}^T}_{s \times 2} \end{aligned} \quad (13)$$

2×2

The trace of \mathbf{T} ($\text{tr } \mathbf{T}$) will be related to the dot product of all observed and calculated amplitude ratio vectors (see supporting information for the proof). Now if all calculated amplitude ratios fit the data perfectly, each quantity in the parentheses will be 1 since:

$$v_{11}v''_{11} + v_{21}v''_{21} = v_{11}^2 + v_{21}^2 = \cos^2\theta + \sin^2\theta = 1 \quad (18)$$

Therefore, a perfect fit of all amplitude ratios will be:

$$\text{tr } \mathbf{T}_{\text{PERFECT}} = \sum_{q=1}^s w_{qq} \quad (19)$$

Define a fit parameter

$$\varepsilon_{\text{ratios}} = 100 \frac{\text{tr } \mathbf{T}}{\text{tr } \mathbf{W}_{\text{obs}}} \quad (20)$$

$\varepsilon_{\text{ratios}}$ will vary between -100 and +100. This can be used in conjunction with the polarity quality of fit. The maximum will give the best fit.

C. Combining Wave Polarity and Wave Amplitude Ratios

We determined a global percentage of accuracy (ε) using a weighted average of the accuracy determined from the two grid search methods (ε_{pol} and $\varepsilon_{\text{ratios}}$) for each combination of strike, dip and rake angles. We assigned the focal mechanism to the strike, dip and rake that maximizes ε .

$$\varepsilon = (W_{\text{pol}} \times \varepsilon_{\text{pol}}) + (W_{\text{ratios}} \times \varepsilon_{\text{ratios}}) \quad (21)$$

where W_{pol} and W_{ratios} are the weights for the grid searches using polarity and amplitude ratio, respectively, and $W_{\text{pol}} = 1 - W_{\text{ratios}}$.

D. Preferred Focal Mechanism

We often have many acceptable focal mechanisms that fit the input wave polarities and amplitude ratios. Often the preferred solution is determined by averaging the acceptable solutions using the normal and slip vectors after removing the outliers (Hardebeck and Shearer, 2002). Hardebeck and Shearer (2002) iteratively remove the corresponding focal mechanisms that are more than 30° from the average focal mechanism. They determine the average focal mechanism of the remaining acceptable solutions and repeat the process until all the solutions are within 30° of their average focal mechanism. As a measure of the quality of the preferred focal mechanism, they determine the percentage of acceptable solutions that are within 30° of the preferred solution (Θ) and the root-mean-square of the angle between all acceptable solutions from the preferred solution (1σ).

The Hardebeck and Shearer (2002) averaging algorithm gives a good preferred solution. However, the preferred focal mechanism changes with different starting acceptable solutions whether they are sets of nodal or auxiliary planes. We follow the suggestion of Kraft et al. (2006) by vectorial averaging of the nodal fault and the corresponding auxiliary fault planes separately, and use the preferred solution with the smaller variance i.e., a lower 1σ .

E. Effect of Error in Focal Depth

We perturbed the focal depth to evaluate the stability of the calculated focal mechanisms. The error in focal depth may change the focal mechanisms of an earthquake because it can affect both the take-off angle and direction of propagation (hence, azimuth), especially when the focal depth is close to a layer boundary or less than the epicentral distance.

2.2 Stress Inversion Using Focal Mechanisms

We use the StressInverse 1.1.2 software to determine the principal stress orientation using the focal mechanisms in this study (Vavrycuk, 2014). StressInverse 1.1.2 improves upon the Michael (1984) stress inversion algorithm. We give a brief description of technique but we refer our readers to Vavrycuk (2014) for further description and the comparison of the method to other

stress inversion algorithms (e.g., Michael, 1984; Gephart and Forsyth, 1984; Lund and Slunga, 1999). StressInverse assumes, similar to other stress inversion methods, that the tectonic stress in the area of investigation is uniform (homogeneous), the recorded earthquakes occur on pre-existing faults with varying orientations, the direction of the shear stress on the fault has the same direction as the slip vector (i.e., Wallace-Bott hypothesis; Wallace (1951) and Bott (1959)), the trace of the stress tensor is zero, and the shear stress on activated faults is the same for all earthquakes. Michael (1991) found that as long as the magnitude of the uniform part of the stress field is larger than the magnitude of the variable part, an inversion based on the assumption of homogeneous stress will correctly recover the uniform part of the stress tensor.

The method of Gephart and Forsyth (1984) usually provides more accurate estimates of stress orientation than the method of Michael (1984), especially for high-quality datasets, but the confidence regions are, in most cases, too large (Hardebeck and Hauksson, 2001a). The method of Michael (1984, 1987b) is more accurate for very noisy data sets and provides a more appropriate estimate of uncertainty. The accuracy of both methods improves with increasing data set size with the most improvement occurring between 20 and 50 earthquakes (Hardebeck and Hauksson, 2001a). For a reliable inversion, the orientations of the fault planes must be adequately diverse to sample the entire stress tensor (Hardebeck and Hauksson, 2001a; Vavrycuk, 2014). The diversity of focal mechanisms can be tested qualitatively by displaying P and T axis distributions or by calculating a measure of the mechanism diversity quantitatively using the RMS of the angular difference from the average mechanism. Hardebeck and Hauksson (2001b) found that an RMS angular difference of at least $\sim 40^\circ$ - 45° for focal mechanisms with 10-20 errors is required for a reliable stress inversion.

3.0 Results

3.1 Synthetic Data

We generated a synthetic first-motion dataset using the station parameters in Table S1, patterned on the distribution of stations around a typical hypocenter in the CSZ, to check the performance of the algorithm. We used strike, dip and rake values of 50° , 70° and 90° , respectively, and a focal depth of 12.83 km to generate the synthetic dataset. Our velocity model is the 1-D velocity model for the CSZ (Fig. 3; Lamontagne, 1999) overlying a halfspace mantle velocity model. We used a strike, dip and rake angle increment of 5° . Density (ρ) of the crust was derived using Gardner's principle (Gardner et al., 1974): $\rho = 0.31 \times V_p^{0.25}$, where V_p is the P wave velocity in meters per second and density is given as grams per cubic centimeters. We set the values of W_{pol} and W_{ratio} to 1.0 and 0.0, respectively, for an inversion involving polarity only, and used 0.7 and 0.3, respectively, for an inversion involving polarity and amplitude ratios.

We evaluated the performance of the algorithm using the Kagan angle method to compare the preferred focal mechanism from the synthetic data with the input fault parameters (Kagan, 1991). The Kagan angle is a measure of the similarity between two focal mechanisms, and it gives the angle that one of the focal mechanisms needs to be rotated in 3-D to be the same as the other

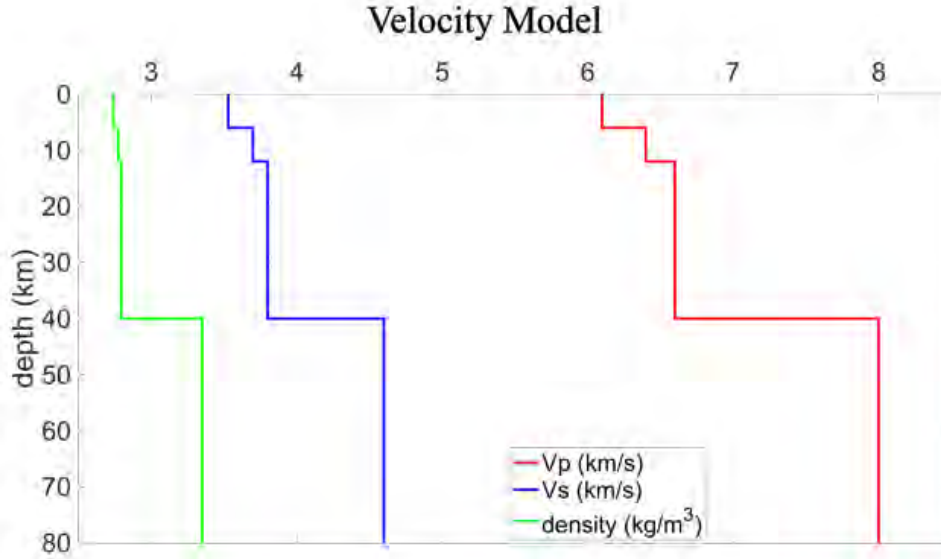


Figure 3: Velocity model for the CSZ (Modified after Lamontagne, 1999).

(Kagan, 1991). Kagan angle is based on the transformation of a focal mechanism using its pressure (P), intermediate (I) and tensional (T) axes into a normalized quaternion ($q = q_0 + q_1i + q_2j + q_3k$; and $q_0^2 + q_1^2 + q_2^2 + q_3^2 = 1$; where i, j, k are complex identities and obey complex identity multiplication rules). The quaternion, similar to the Euler rotation, defines a 3-D rotation with the scalar component corresponding to the rotation angle while the vector part corresponds to the rotation axis (Altmann, 1986, Kagan, 1991). We refer the reader to Kagan (1991) for the details of the transformation. After determining the quaternion of the two focal mechanisms, we can determine a quaternion (q') corresponding to the rotations transforming q_1 into q_2 such that $q_2 = q'q_1$. Due to the symmetry of the double-couple sources assumed in determining the focal mechanisms, there are four ways a focal mechanism can be rotated into another mechanism. The Kagan angle is the smallest of the possible rotations determined from the scalar component of the quaternion (i.e., $\Phi = \cos^{-1}(q_0)$) along a rotation axis described in a spherical coordinate system as azimuth ($\psi = \tan^{-1}\left(\frac{q_2}{q_1}\right)$) and colatitude ($\theta = \cos^{-1}\left(\frac{q_3}{\sin(\Phi/2)}\right)$). The Kagan angle varies from 0° to 120° . Two focal mechanisms with a Kagan angle that is well below 60° are considered to have good correspondence while a Kagan angle that is above 60° means that the focal mechanisms are significantly different (Dahal and Ebel, 2020; D'Amico et al., 2011; Pondrelli et al., 2006, Kubo et al., 2002).

The preferred focal mechanism is similar to the input focal mechanism for different constraint options (Fig. 4). The values of the preferred focal mechanisms and the number of acceptable solutions are presented in Table S2. The preferred focal mechanism has a Kagan angle of 11.8° when only P wave polarity was used as the constraint and 154 acceptable solutions. The angle decreased to 5.4° (with 16 acceptable solutions) when we used P, SV and SH wave polarities, and further decreased to 0° when we introduced amplitude ratios. The percentage of acceptable focal mechanisms that are within 30° of the normal vectors of the preferred solutions for all the solutions is 100%. Figure 5 shows the effect of 1-km error in focal depth for the four constraints.

3.2 Charlevoix Seismic Zone Earthquakes

3.2.1 Data and Data Processing

We focused our study on 455 relocated earthquakes with magnitudes ≥ 2.0 for the time period 1988 to 1999 (Powell and Lamontagne, 2017) and additional relocated earthquakes ($M \geq 2.0$) from 2000 to 2020. The earthquakes were recorded by the Canadian National Seismograph Network (CNSN). More than 68% of the 1329 relocated earthquakes using the 3-D velocity model by Powell and Lamontagne (2017) have horizontal errors ≤ 0.15 km and vertical errors ≤ 0.35 km. We used the Automatic Data Request Manager (AutoDRM) of the National Resources Canada website to download the waveforms from seven of the CNSN stations (i.e., A11, A16, A21, A54, A61, A64 and LMQ) (Fig. 1). The seismic stations have undergone several upgrades in their history. Station LMQ has a broadband seismometer with a sampling frequency of 40 Hz during the period of interest while the other six stations have short period seismometers with a sampling

Synthetic Data Results

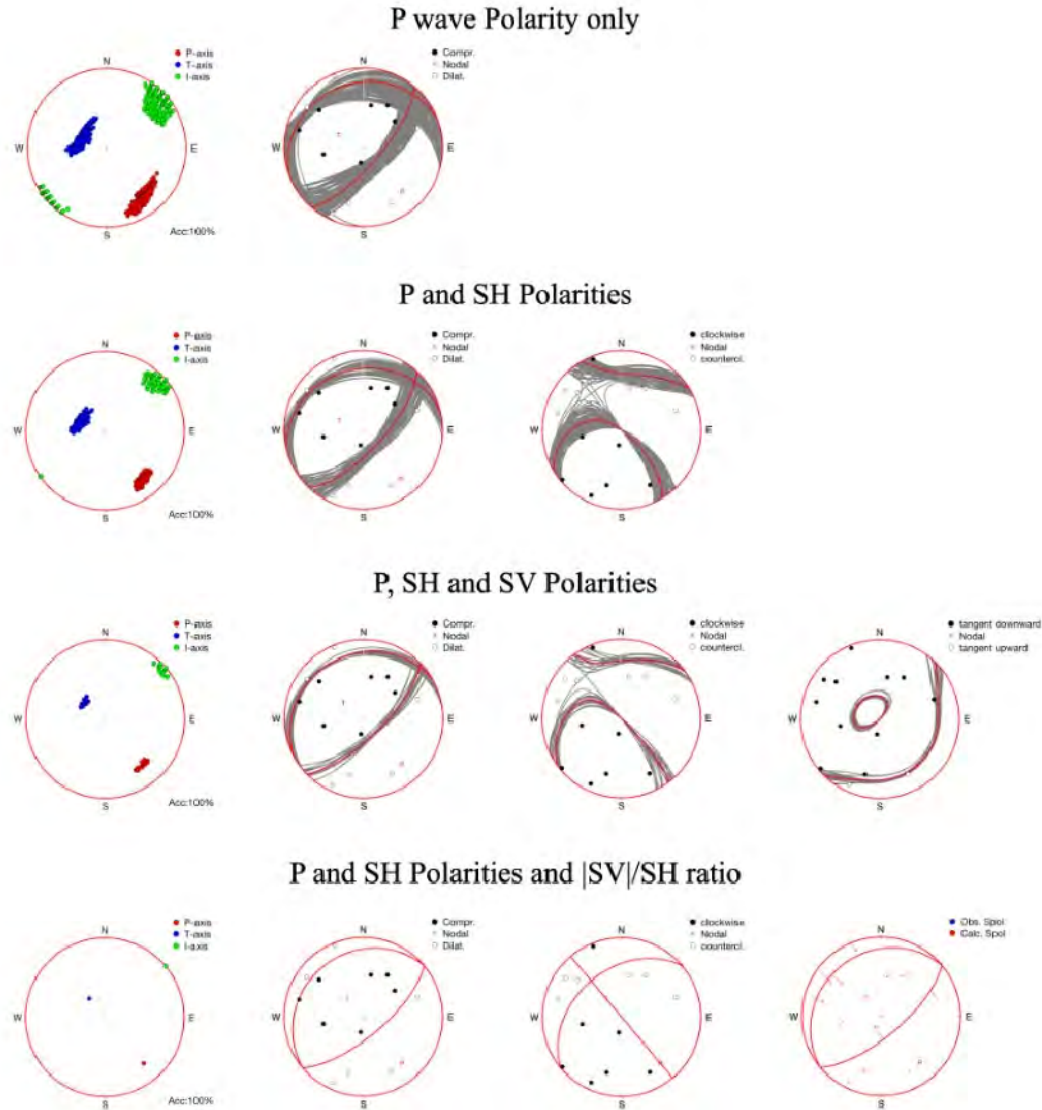


Figure 4: Synthetic data results using different constraints. Values of the preferred focal mechanisms and the number of acceptable solutions are presented in Table S1. The P-, T- and I-axes are the solid red, blue and green circles, respectively. The black and open circles represent positive (compressional) and negative (dilatational) values, respectively. Looking downward, clockwise SH motion is positive while

counterclockwise SH motion is negative. For the SV wave, positive is measured tangentially downward while negative is measured tangentially upward.

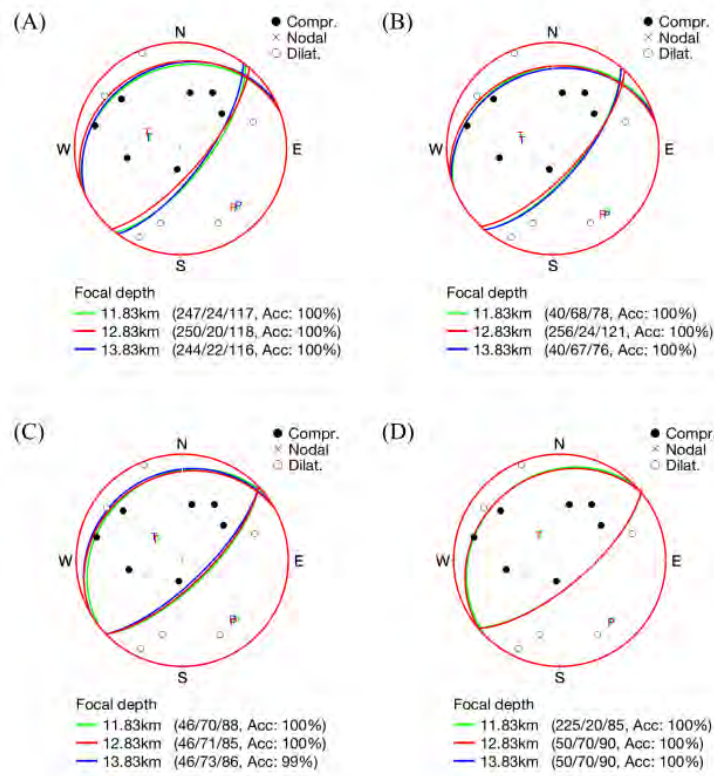


Figure 5: Effect of 1-km error in focal depth for the four constraints. Same scheme as Figure 4.

frequency of 100 Hz. We determined the instrument response of each station to inform the frequency limits in removing the instrument response. We confirmed the correctness of the polarity of the stations using the vertical, radial and tangential component waveforms recorded from a teleseismic earthquake that occurred in South America.

We removed the instrument response from the raw data to obtain wave displacements, rotated the resulting seismic data to the great circle path, and filtered the data using a phaseless Butterworth bandpass filter with corner frequencies of 2 and 10 Hz. We determined P-, SH- and SV- wave amplitudes from the vertical, tangential and radial components, respectively. We used the absolute value of SV amplitude for CSZ earthquakes because of possible polarity reversal at the free surface when the incident angle is higher than a critical value. Figure S2 shows the radial-component synthetic seismograms illustrating the effect of the free surface on the displacement of an incident SV wave as a function of incident angle (See supporting information for a summarized mathematical background).

The SV amplitudes and the corresponding SH amplitudes were determined with caution. We observed a large, secondary P-wave arrival before the S wave with a fairly constant arrival time with respect to the first P wave, and the wave is prominent on the vertical and radial components (Fig. S3). We performed a wave propagation study for a local earthquake (October 28, 1997 at 11:44:19; M4.7; and depth = 9.143 km) in the CSZ using the 1-D velocity model (Fig. 3). The travel time analysis suggests that the secondary wave is a SP headwave propagating near the surface in the relatively homogeneous Charlevoix crust, and overlaps the SV wave when the

epicentral distance is about one focal depth of the earthquake. The travel time analysis also revealed that the SP headwave starts when the ray parameter of the S wave is just above the inverse of the P- wave velocity near the surface, hence the headwave is horizontally propagating near the free surface.

3.2.2 Focal Mechanisms of the Relocated Earthquakes ($M \geq 2$)

Focal mechanisms of the 455 relocated earthquakes were determined using P- and SH-polarities, and SH/P, $|SV|/SH$ and $|SV|/P$ amplitude ratios as data. The SV amplitude was taken from the radial component of the SV wave. We used only seismic stations where P-, SH- and SV-wave amplitudes were picked with high confidence. We used the 1-D velocity model of the CSZ (Fig. 3) with a strike, dip and rake angle increment of 2° for the grid search over the mechanisms.

The focal mechanisms of the relocated earthquakes are presented in the supporting information. We present the focal mechanisms of earthquakes that occurred on 10/28/1997 (Event 1) and 12/8/1991 (Event 2). We used six seismic stations with clear P-, SH- and SV- wave amplitudes for both events. The focal mechanisms of the two events are $310^\circ/52^\circ/24^\circ$ and $354^\circ/46^\circ/52^\circ$ (strike/dip/rake) with an accuracy 98% and 94% for the events, respectively (Fig. 6). The solutions fit both P and SH polarities accurately. The focal mechanisms for both events are stable within a 1-km error in their focal depths. The observed S wave polarization plots are in good agreement with the ratio between the $|SV|$ and SH amplitudes, and with the relative vector length for all the stations.

When only P and SH polarities are used as constraints for Events 1 and 2 using 2° increments of strike and dip values, there are 925 and 14 acceptable solutions, respectively. These acceptable solutions were all within 25.28° and 2.36° of the preferred focal mechanisms, respectively (Fig. 6). The preferred focal mechanisms for the two events using P and SH polarities are $355^\circ/44^\circ/94^\circ$ and $354^\circ/49^\circ/51^\circ$ with an accuracy of 100% and 96%, respectively. These preferred focal mechanisms have Kagan angles of 51.2° and 3.2° compared to the corresponding focal mechanism obtained when both P- and SH- polarities and $|SV|/SH$ and SH/P amplitude ratios were used as constraints.

We compared the focal mechanisms of the 29 relocated earthquakes that are common between this study and those used for the stress inversion by Mazzotti and Townend (2010) (e.g., Adams, 1991; Lamontagne, 1998; Bent, 1992; Bent et al., 2003). The focal mechanisms of 21 out of the 29 earthquakes (about 72%) have Kagan angles that are less than 50° compared to the corresponding focal mechanism used by Mazzotti and Townend (2010), hence they are not considerably different. However, the observed difference could slightly change and may further constrain the stress orientation determined from the stress inversion of the new focal mechanisms. As an example, Figures 7A and 7B compare the P wave nodal planes of the solutions from the two studies for earthquakes that occurred on 10/28/1997 and 12/8/1991 with Kagan angles of 74.4°

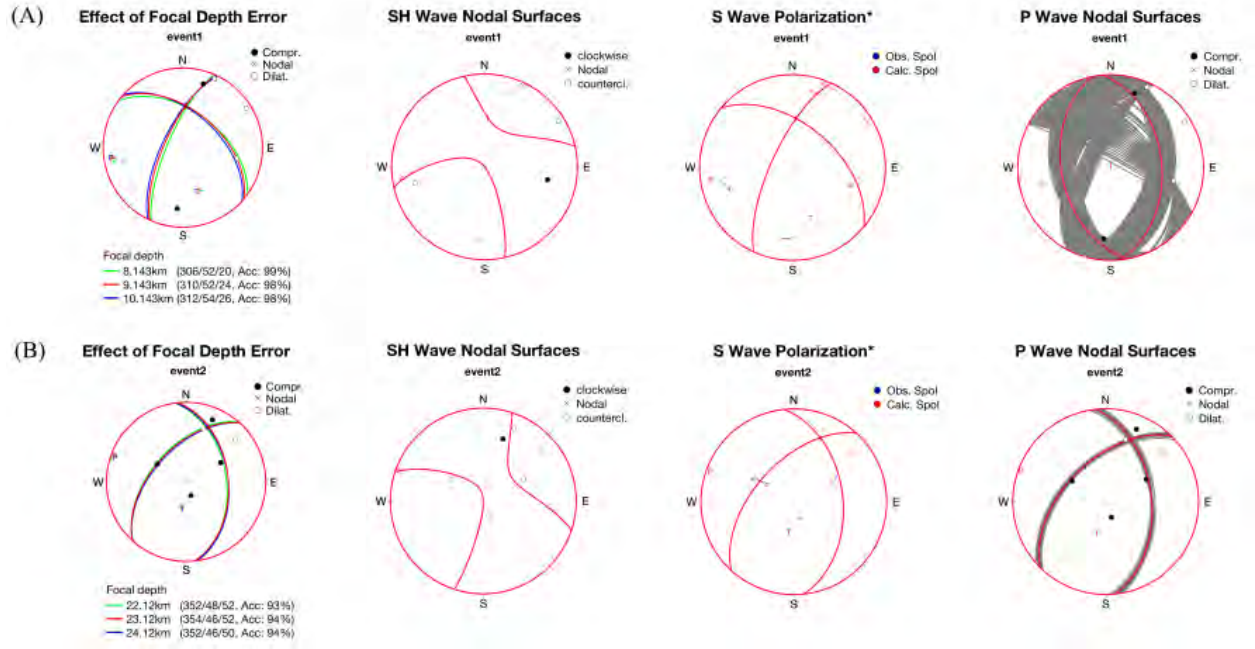


Figure 6: Focal mechanisms for earthquakes on (A) 10/28/1997 and (B) 12/8/1991. The figure shows the P wave nodal planes, the SH wave nodal plane, S wave polarization, and the P wave nodal planes of all acceptable solutions (grey nodal planes), and the preferred focal mechanism (red nodal plane) when only P and SH polarities are used as constraints. The green and blue nodal planes are P wave nodal planes for -1- and 1-km error in the focal depth of the earthquakes, respectively.

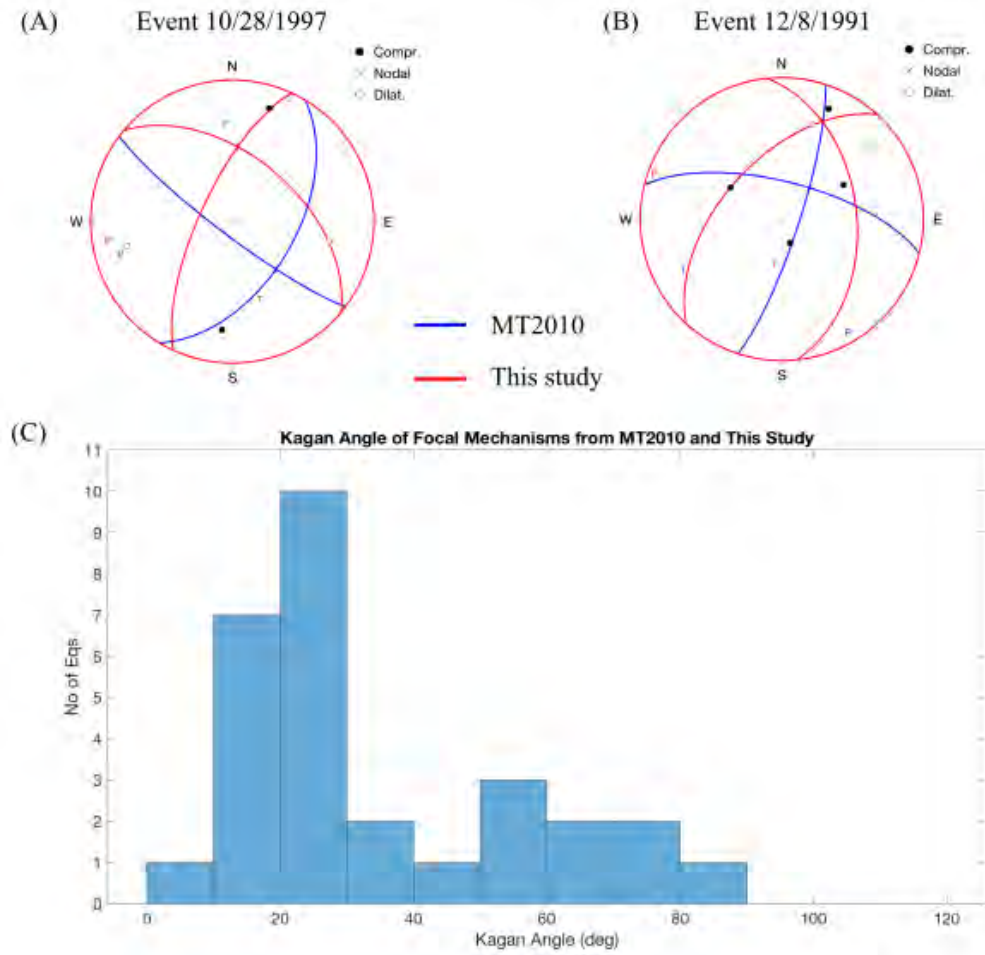


Figure 7: Comparison of focal mechanisms determined in this study with those used by Mazzotti and Townend (2010). (A-B) The P wave nodal planes for earthquakes occurring on 10/28/1997 and 12/8/1991. (C) Distribution of the Kagan angles between the 29 focal mechanisms common to this study and Mazzotti and Townend (2010).

and 56.9° , respectively. Figure 7C shows the distribution of the Kagan angles between the 29 focal mechanisms and those determined by Mazzotti and Townend (2010).

3.3 Distribution of the P-, I- and T- axes and faulting styles for CSZ Earthquakes

We examined the distribution of the stress axes directions to understand the stress state and faulting styles in the CSZ. We determined the P, I and T axes of 455 earthquakes whose focal mechanisms were determined using at least four seismic stations (Fig. 8A-C). The P and I axes were distributed over a wide range of azimuths with plunge angles that are generally less than 30° but some I axes were near vertical. The T axis is generally near vertical. The distribution of the P axis azimuths showed three distinct trends of about 80° , 105° and 120° (Fig. 8D).

We classified the earthquakes into different faulting styles using the FMC1.01 software (Fig. 8E; Álvarez-Gómez, 2015). The classification scheme revealed that 83.1% of the earthquakes occurred on reverse and reverse-strike slip faults (R and R-SS), and increase slightly

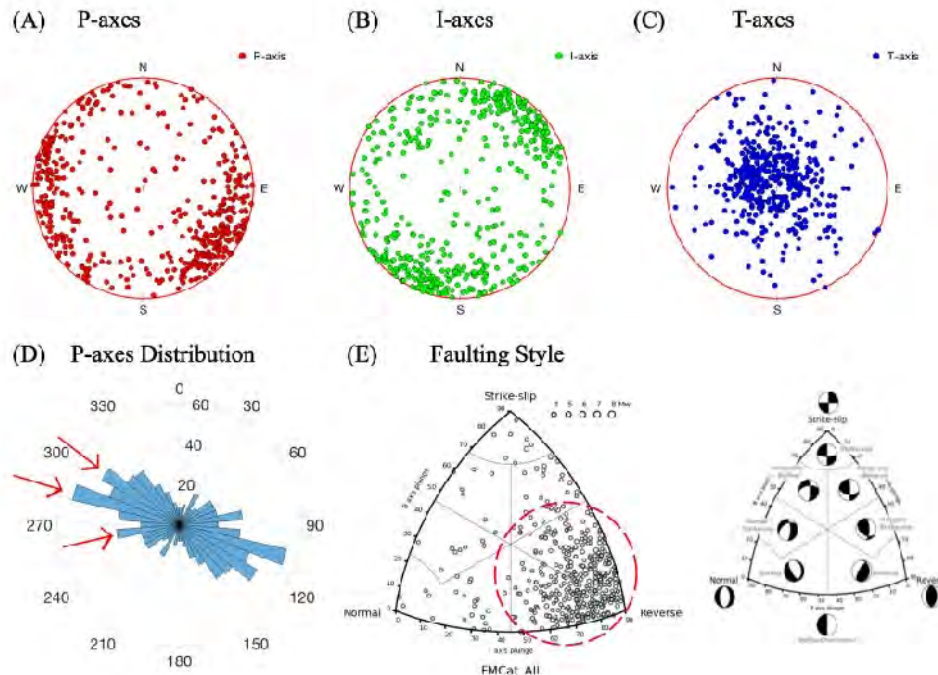


Figure 8: (A-C) P-, I- and T- axes of the earthquakes in this study. (D) Rose diagram of the azimuth of the P axes. (E) Faulting style using the classification scheme of Álvarez-Gómez (2015).

to 89.7% if we include the strike slip-reverse faults (i.e., R, R-SS and SS-R). These high percentages confirmed that the P axes are horizontal.

3.4 Stress Inversion of the Focal Mechanisms

We performed a stress inversion of the focal mechanisms using StressInverse 1.1.2 (Vavrycuk, 2014) to determine the orientation of the maximum principal stress (σ_1) in the CSZ. Noisy focal mechanisms were generated in two steps: by perturbing the fault normals and slip directions with random noise generated from a normal distribution with a mean deviation of 10° , and then inverting the noisy normals and slip directions to determine the noisy focal mechanisms. We also tested the effect of a mean deviation value of 15° , on stress orientation. We ran the stress inversion using 100 random noise realizations of the input focal mechanisms to evaluate the

stability of the stress solution, and set the friction value range from 0.3 to 0.8. We quantified focal mechanism diversity in the stress inversion using the RMS of the angular difference of each mechanism from the average mechanism.

3.4.1 Stress Inversion of All Earthquakes

The orientation and plunge of σ_1 for all earthquakes are N103.1° and 5.6°, respectively (Fig. 9). The 100 random noise realizations of the input focal mechanisms give a σ_1 orientation that varies between N99.9° and N109.3° showing that the orientation is well-constrained. The shape ratio, $R=(\sigma_1 - \sigma_2)/(\sigma_1 - \sigma_3)$, is between 0.32 and 0.46, and peaks at 0.39. The specific values of the σ_1 orientations and the corresponding orientations ranges from the 100-random noise realization are presented in Table 1. The plunge of σ_2 and σ_3 are 7.0° and 81.1°, respectively. The plunge of the principal stresses shows that σ_1 and σ_2 are near horizontal while σ_3 is near vertical, as expected for a predominantly thrust faulting stress regime. Thus, the orientation of σ_1 is the same as the orientation of the maximum horizontal stress (SH_{max}).

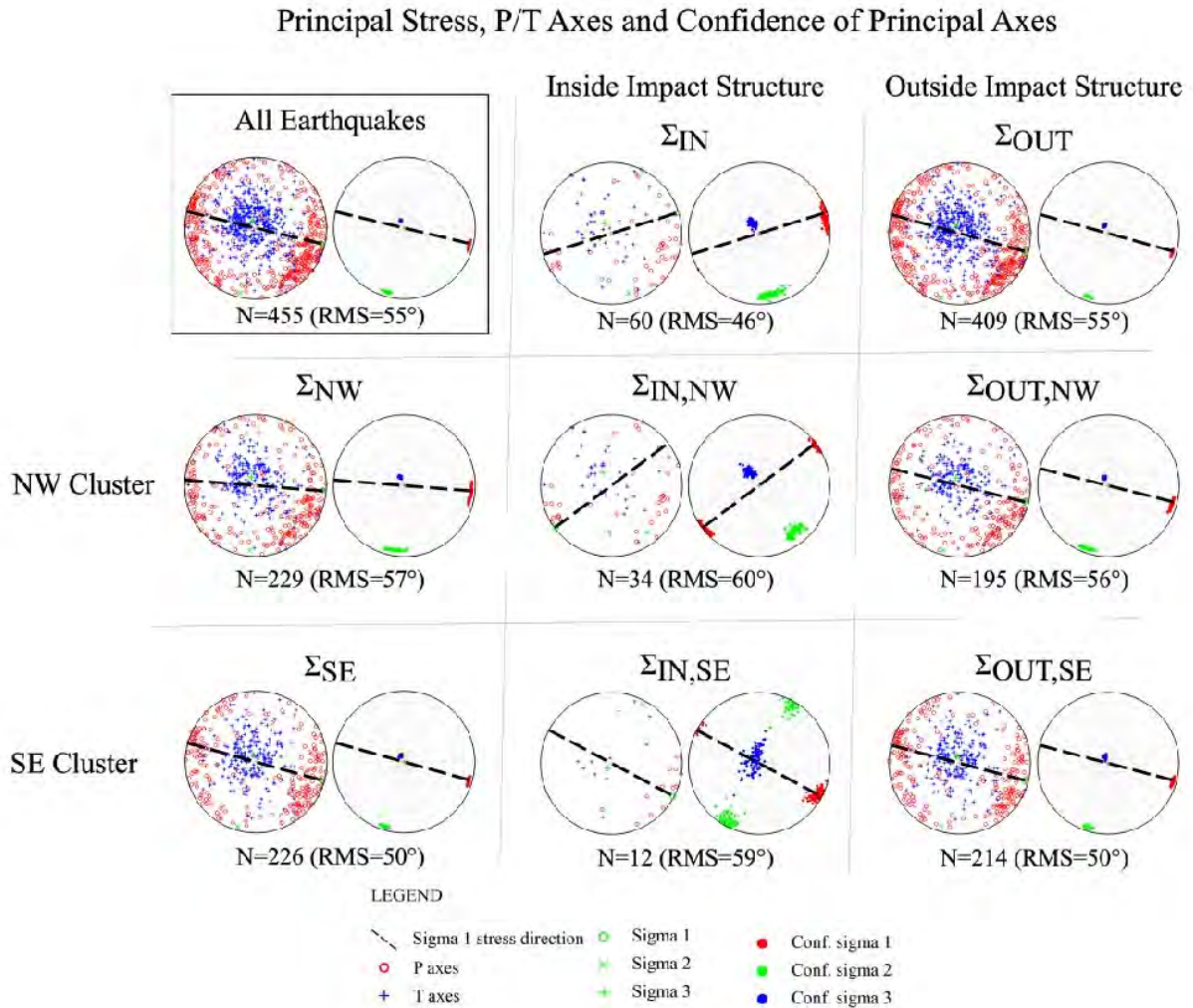


Figure 9: Stress inversion of the CSZ earthquakes showing σ_1 orientation of all earthquakes and the different clusters. Stress solution for each cluster is represented in two focal spheres. The left focal sphere shows the P- and T- axes of the earthquakes in the corresponding cluster and the inverted σ_1 , σ_2 and σ_3 directions. The right focal sphere shows the distribution of the σ_1 orientation for the 100 noise realizations

of the input focal mechanisms in the cluster. We determined the range of σ_1 direction as the confidence interval. The dashed line represents the σ_1 direction for each cluster. N represents the number of earthquakes in the cluster while RMS is a measure of focal mechanism diversity and it represents the RMS value of the angular difference between each focal mechanism and the average focal mechanism in the cluster.

3.4.2 Stress Inversion for Different Earthquake Clusters

We partitioned the earthquakes in a systematic way to investigate the spatial distribution of the σ_1 orientation. We divided the earthquakes based on whether they were inside or outside the impact structure (Σ_{IN} and Σ_{OUT}) and whether they were on the northwest or southeast side of the seismic gap between the Gouffre Northwest and the Saint-Laurent faults (Σ_{NW} and Σ_{SE}) (Fig. 10). We also analyzed the σ_1 orientation for different combinations of the two partition schemes (i.e., $\Sigma_{IN,NW}$, $\Sigma_{IN,SE}$, $\Sigma_{OUT,NW}$ and $\Sigma_{OUT,SE}$). The impact structure was modeled as a hemispherical bowl with a 28-km surface radius and maximum depth of 12 km (Rondot, 1994). We present the results in Figure 9.

The orientation of σ_1 for all of the earthquakes in Σ_{IN} is N72.9° and ranges between N64.2° and N97.2° using the 100 random noise realizations of the input focal mechanisms (Fig. 9). This orientation changes significantly when the earthquakes are partitioned into NW and SE counterparts. The σ_1 direction of the earthquakes inside the impact structure on the NW side ($\Sigma_{IN,NW}$) is N53.1° which is a smaller azimuth relative to all earthquakes in the Σ_{IN} cluster. However, the σ_1 orientation for the earthquakes in $\Sigma_{IN,SE}$ is a larger azimuth, though less constrained, relative to all earthquakes in Σ_{IN} , with an orientation of N118.0°.

The orientation of σ_1 for all earthquakes in Σ_{OUT} is N105.6° which is similar to the orientation for all of the earthquakes. This orientation does not change significantly when partitioned into NW and SE counterparts; the σ_1 for the group of earthquakes outside the impact structure on the NW ($\Sigma_{OUT,NW}$) is N103.6° while the σ_1 orientation for the earthquakes in $\Sigma_{OUT,SE}$ is N105.1°.

The σ_1 orientation for all earthquakes in the NW cluster (Σ_{NW}) is N94.2°. This orientation is significantly different than the σ_1 orientation of N53.1° for the earthquakes in the NW cluster

Table 1: Summary of stress inversion of focal mechanisms for different clusters.

	Clusters		σ_1 orientation/ plunge	Range of σ_1 orientation for the 100 random noise realizations	σ_2 orientation/ plunge	σ_3 orientation/ plunge	Shape ratio
1	All Earthquakes		103.1° /5.6°	99.9° – 109.3°	13.8° /7.0°	154.4° /81.1°	0.39
4	Inside Impact Structure	All Inside	72.9° /3.8°	64.2° - 97.1°	163.7° /13.1°	147.2° /76.3°	0.40
5		IN_NW	53.1° /1.8°	35.9° - 64.6°	142.5° /17.8°	148.8° /72.1°	0.48
6		IN_SE	118.0° /1.6°	107.4° - 128.4°	27.8° /6.9°	41.0° /82.9°	0.74
7	Outside Impact Structure	All outside	105.6° /5.8°	101.3° - 110.9°	16.4° /7.1°	156.8° /80.8°	0.40
8		OUT_NW	103.6° /6.4°	99.4° - 121.0°	14.4° /7.5°	153.4° /80.2°	0.29
9		OUT_SE	105.1° /5.4°	100.9° - 109.3°	15.7° /6.4°	155.3° /81.7°	0.50
2	NW Cluster		94.2° /5.3°	83.8° - 107.0°	5.1° /8.9°	153.7° /79.6°	0.26
3	SE Cluster		105.7° /5.3°	102.6° - 110.8°	16.3° /6.0°	154.8° /82.0°	0.52
10		5km	82.7° /3.5°	69.0° - 91.5°	173.2° /7.3°	147.1° /81.9°	0.65

11	Depth Slices	10km	95.8° / 5.6°	92.2° - 104.4°	6.1° / 3.6°	128.9° / 83.3°	0.46
12		15km	112.8° / 7.7°	105.0° - 118.3°	24.3° / 11.0°	168.4° / 76.5°	0.39
13		20km	127.0° / 10.4°	115.7° - 139.8°	37.7° / 3.6°	146.4° / 78.9°	0.44
14		25km	83.1° / 3.3°	6.6° - 156.0°	172.8° / 4.4°	30.1° / 84.4°	0.15
15	Depth Ranges	0 - 6km	101.9° / 7.2°	0.3° - 179.9°	11.9° / 0.3°	99.7° / 82.8°	0.05
16		6 - 12km	95.5° / 3.9°	90.1° - 99.8°	5.9° / 5.1°	148.1° / 83.6°	0.56
17		12 - 40km	113.7° / 7.6°	110.4° - 121.8°	24.8° / 7.8°	160.3° / 79.1°	0.32

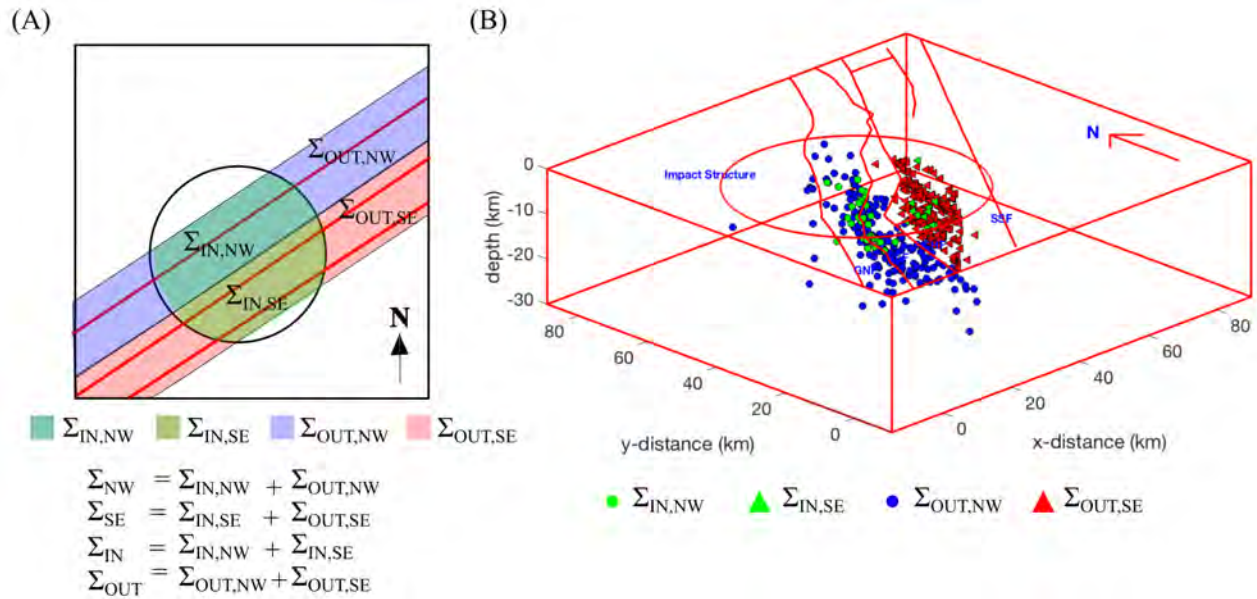


Figure 10: Earthquake partitioning map showing the (A) schematic diagram of the partitioning and (B) the earthquakes in each area group.

within the impact structure ($\Sigma_{IN,NW}$) but only slightly lower in magnitude than the orientation for all of the earthquakes. Earthquakes in the SE cluster (Σ_{SE}) have a σ_1 orientation of N105.7°, similar to all earthquakes.

In summary, the stress inversion of different earthquake clusters shows four distinct groups of σ_1 orientations (Fig. 11A). They are: (1) Σ_{IN} and $\Sigma_{IN,NW}$ with σ_1 orientation values of N72.9° and N53.1°, respectively (much smaller than the σ_1 orientation of all earthquakes), (2) Σ_{NW} with a σ_1 orientation value of N94.2° (slightly lower than the σ_1 orientation of all earthquakes), (3) Σ_{SE} , $\Sigma_{OUT,SE}$, Σ_{OUT} and $\Sigma_{OUT,NW}$ with σ_1 orientation value of N105.7°, N105.6°, N105.1° and N103.6°, respectively (similar to the σ_1 orientation of all earthquakes), and (4) $\Sigma_{IN,SE}$ with a σ_1 orientation value of N118.0° which is less constrained due to a fewer number (12) of earthquakes in the cluster. We tested the effect of a mean deviation value of 15° on stress orientation (Fig. S4). Our results show that the observed spatial and depth variations in the σ_1 orientation are still significant for a mean deviation value of 15°.

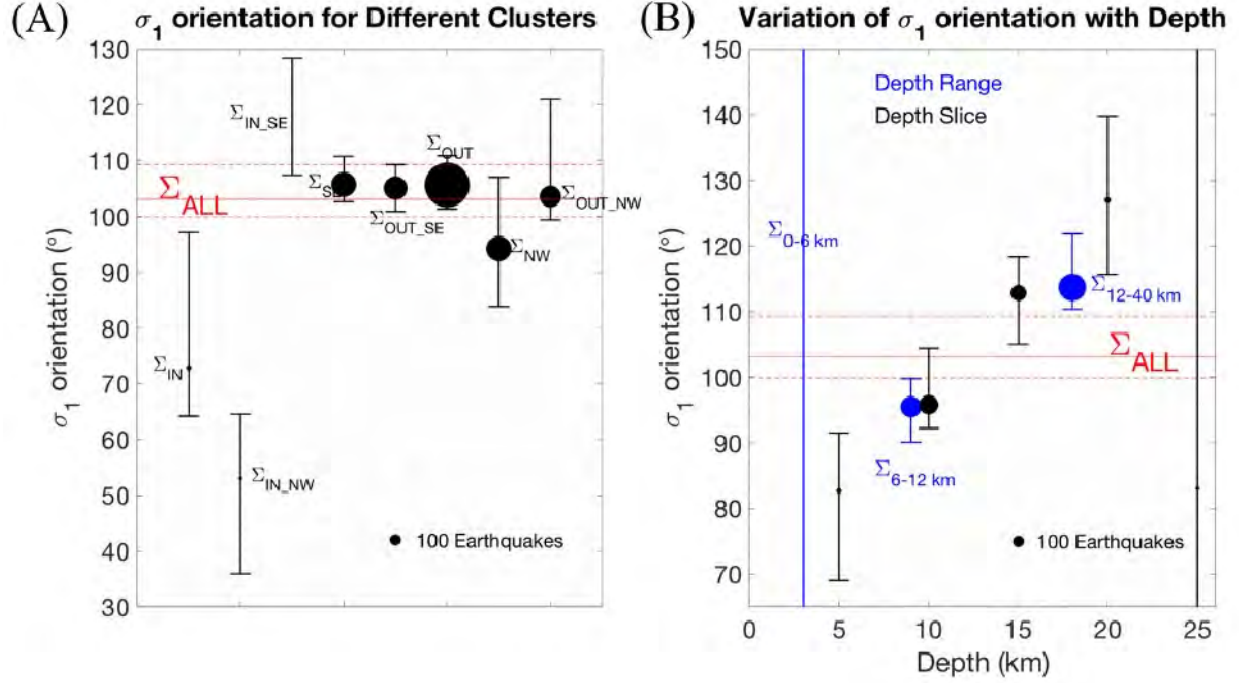


Figure 11: Variation of σ_1 orientation with (A) different clusters and (B) depth slice and depth range.

3.4.3 Variation of σ_1 Orientation with Depth

We investigated the σ_1 orientation of all relocated earthquakes as a function of depth by clustering the earthquakes based on different depth slices and depth ranges irrespective of their lateral position relative to the impact structure. The depth slices are 5, 10, 15, 20 and 25 km, and we clustered the earthquakes that are within 2.5 km of each depth slice. We also considered depth ranges of 0-6 km, 6-12 km and 12-40 km based on the three rock layers in the 1-D velocity model of Lamontagne (1999) (Fig. 3).

The orientation of σ_1 changes in a systematic, clockwise sense with increasing depth (Fig. 11B and 12). The σ_1 orientation changes from N82.7°, to N95.8°, to N112.8°, to N127.0° for depth slices at 5, 10, 15 and 20 km, respectively. The σ_1 orientation is N83.1° at 25-km depth but it is less constrained, ranging from N6.6° and N156.0°. We also observe an increase in σ_1 orientation when considering depth ranges (Fig. 11B and 12). The σ_1 orientation for earthquakes between 0 and 6 km is not well constrained; the σ_1 orientation is N101.9°. The σ_1 orientation changes from N95.5° to N113.7° for the earthquakes that occurred within the depth ranges of 6-12 km and 12-40 km, respectively.

We observe the increase in the degree of clockwise stress orientation with depth for earthquakes located outside the impact structure (Σ_{OUT}) and the trend is similar to the trend when all earthquakes are used for the stress inversion (Fig. 13). However, the orientation of σ_1 for the 5 km depth slice changes from N82.7° to N91.8°. The stress orientation at 10 km (N95.8°) is similar to the orientation when all earthquakes are used (N95.5°) and thus is not affected by the removal of the earthquakes within the impact structure.

We also observe that the increase in the degree of clockwise stress orientation rotation with depth persists for depth slices for the $\Sigma_{OUT,NW}$ and $\Sigma_{OUT,SE}$ clusters (Fig. 12B). However, the ranges of the orientation using the 100 random noise realizations give larger error bars due to the smaller number of earthquakes in each slice. The degree of stress rotation increase for the $\Sigma_{OUT,NW}$ cluster

is higher than that for the $\Sigma_{OUT,SE}$ cluster. The increase in orientation with depth is significant between the 10 and 20 km depth slices for the $\Sigma_{OUT,NW}$ cluster and between 5 and 15 km for the $\Sigma_{OUT,SE}$ cluster.

In summary, the stress inversion for earthquake clusters at different depths and depth ranges show that σ_1 orientation does not only change across the seismic zone, it also changes with depth in systematic ways (Fig. 11B and 12). The σ_1 orientation values increase with depth for both depth- and spatial- partition schemes but the σ_1 orientations for the 25-km depth slice and 0-6 km depth range are not well constrained. In addition, the depth slices and depth ranges are independent

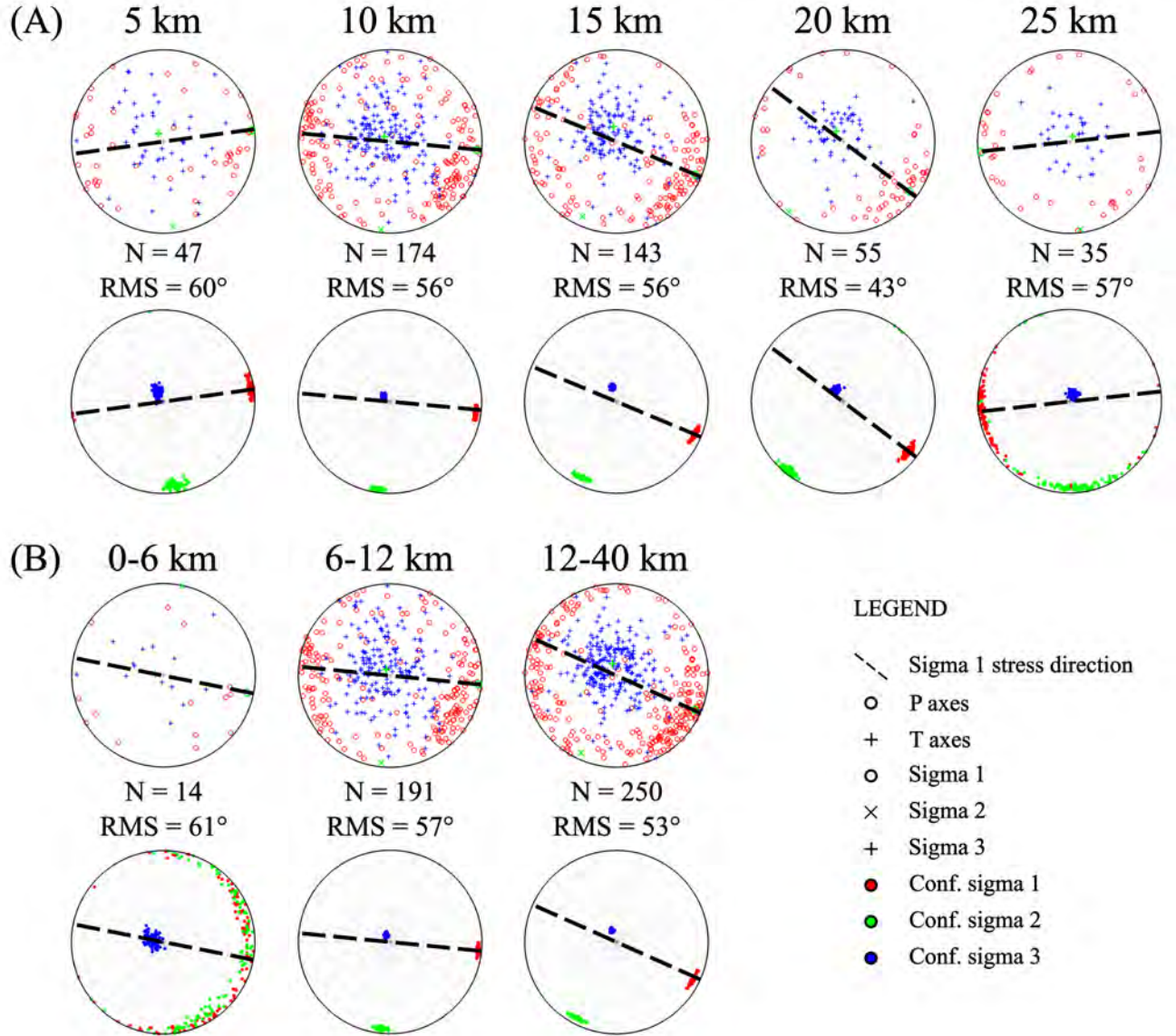


Figure 12: Same as Fig. 9 but showing the variation of σ_1 orientation with clusters at different depths and depth ranges. The 25-km depth slice and 0-6 km depth range solutions are not well constrained.

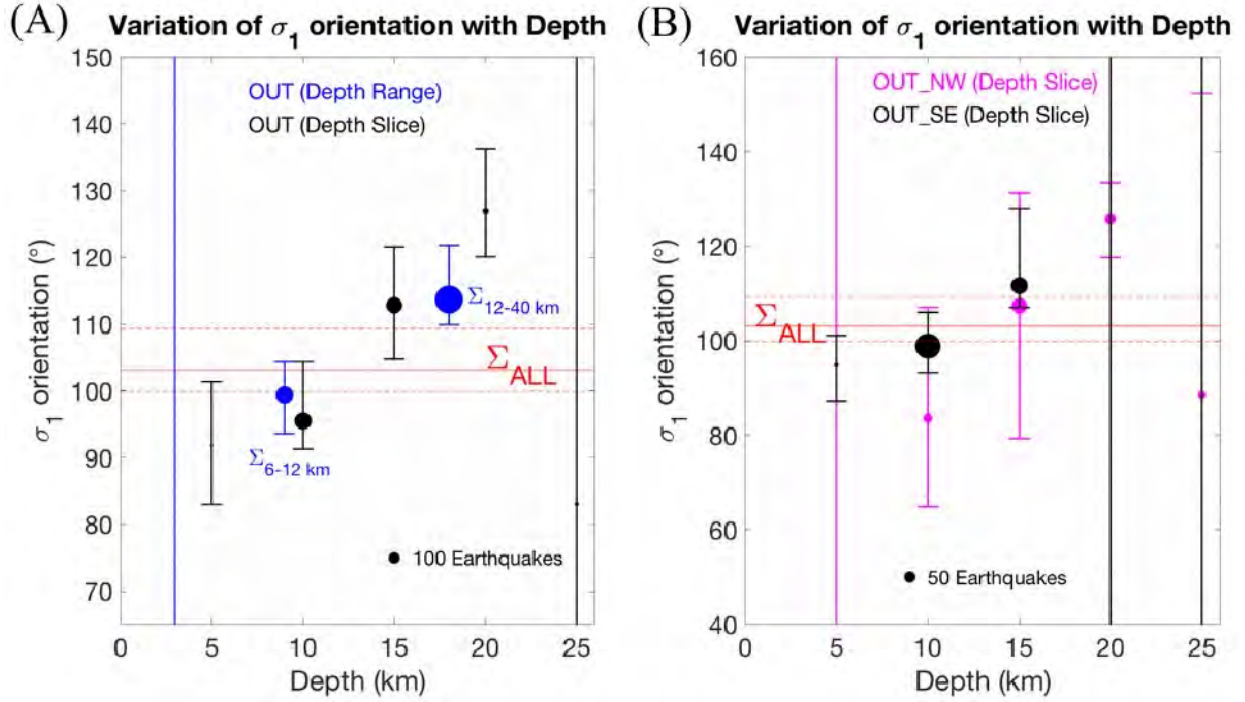


Figure 13: Same as Fig. 11B but for the earthquakes located (A) outside the impact structure and (B) outside the impact structure on the NW and SE clusters.

3.4.4 Effect of Temporal Subsets of the Focal Mechanisms on the Observed Spatial and Depth Variations in σ_1 Orientations

We partitioned the focal mechanisms into three subsets using different time partitions (1988-1999, 2000-2010 and 2011-2020) to access the observed spatial and depth variations in the σ_1 orientation. The results for the different subsets of focal mechanisms show some similarities with the observed σ_1 orientation variations using all focal mechanisms. For example, the σ_1 orientation for earthquakes in Σ_{IN} are consistently smaller than the σ_1 orientation in Σ_{OUT} except for the 2000-2010 partition. Also, the σ_1 orientation for Σ_{OUT} , Σ_{SE} and $\Sigma_{OUT,SE}$ clusters for each subset are similar to the σ_1 orientation for all earthquakes in the corresponding partition. Furthermore, the σ_1 orientation for Σ_{NW} is consistently smaller than the σ_1 orientation for Σ_{SE} except for the 1988-1999 partition where it is slightly higher. Our results support the increase in clockwise rotation in stress orientation with depth for the three time partitions though the error bars are larger in the 2011-2020 partition (Fig. S5).

4.0 Discussion

Our study provides insight into σ_1 partitioning in the CSZ. The orientation of maximum principal stress for all of the relocated earthquakes in the CSZ is about N103.1° and ranges between N99.9° and N109.3° for the 100 random noise realizations (Fig. 9). The minimum principal stress, σ_3 , is near vertical while σ_1 and σ_2 are near horizontal. So, the orientation of σ_1 can be used for maximum horizontal stress orientation for the CSZ. The σ_1 orientation from this study is similar to the network average strain rates involving mostly ESE- WNW shortening determined by Mazzotti et al. (2005) using GPS measurements. However, our σ_1 orientation for all of the

earthquakes differs by about 17° from the σ_1 orientation of $N86^\circ$ determined from the inversion of 60 focal mechanisms (mostly between 1974 and 1997) by Mazzotti and Townend (2010).

Some significant relative rotations of σ_1 determined in previous studies were diminished in our study, probably due to the larger number of available earthquakes. For example, our results show about a 12° clockwise rotation in the SE ($N105.7^\circ$) relative to the NW ($N94.2^\circ$) clusters instead of the 47° relative rotation previously observed by Mazzotti and Townend (2010). Also, the stress orientation in the SE cluster ($N105.7^\circ$) is similar to the orientation obtained when all of the earthquakes were used in the inversion ($N103.1^\circ$) instead of the previously observed 15° clockwise rotation of the SE cluster relative to all earthquakes found by Mazzotti and Townend (2010).

In general, the σ_1 orientation for earthquakes inside the impact structure is smaller than the σ_1 orientation outside the impact structure; the σ_1 orientation within the impact structure is $N72.9^\circ$ while the σ_1 orientation outside the impact structure is $N105.6^\circ$, representing a 32.7° relative rotation (Fig. 9). Also, the σ_1 orientation inside the impact structure has about a 30° anticlockwise stress rotation relative to the $N103.1^\circ$ orientation for all of the earthquakes. We observed a greater anticlockwise stress rotation of about 50° between earthquakes inside the impact structure in the NW cluster (i.e., $\Sigma_{IN,NW}$ with σ_1 orientation of $N53.1^\circ$) relative to the orientation for all of the earthquakes. Note that the σ_1 orientation in the $\Sigma_{IN,NW}$ is similar to the $N55^\circ$ orientation for the NW cluster in Mazzotti and Townend (2010). The similarity between the $N103.6^\circ$ σ_1 orientation for earthquakes in $\Sigma_{OUT,NW}$, the σ_1 orientation of $N105.1^\circ$ in the $\Sigma_{OUT,SE}$ and the σ_1 orientation of $N105.6^\circ$ in the Σ_{OUT} clusters, in contrast to the generally smaller orientations within the impact structure ($\Sigma_{IN} = N72.9^\circ$ and $\Sigma_{IN,NW} = N53.1^\circ$), further suggests a tectonic or geologically related interpretation for the observed spatial variations in the σ_1 orientations. The location of the impact structure coincides with the region of lower P- and S-wave velocities found in the tomography studies (Fig. 2; Vlahovic et al., 2003; Powell and Lamontagne, 2017). Therefore, the variation of σ_1 orientation between the earthquakes within and outside the impact structure could be due to the presence of highly fractured, lower stiffness rocks within the impact structure. We observed about 15° clockwise rotation in $\Sigma_{IN,SE}$ ($N118.0^\circ$) relative to the orientation for all of the earthquakes, but this orientation is not well constrained due to the limited number of earthquakes in the cluster.

The σ_1 orientation increases with increasing depth; the orientation increases systematically from about $N82.7^\circ$ at the 5-km depth slice to about $N127.0^\circ$ at the 20-km slice (Fig. 12; Table 1). The σ_1 orientation changes back to $N83.1^\circ$ at the 25-km depth slice, although the stress inversion for this depth slice is less constrained from the 100 noise realizations. Considering the depth ranges in the starting model, σ_1 orientation changes from about $N92.5^\circ$ between 6-12 km to about $N113.7^\circ$ for 12-40 km. The σ_1 orientation for the 0-6 km depth range is less well constrained. The observed increase in orientation is consistent for different depth slices and depth ranges for different partitions of the earthquakes (e.g., Σ_{All} , Σ_{OUT} , $\Sigma_{OUT,NW}$ and $\Sigma_{OUT,SE}$; Fig. S4 and 13) and temporal subsets of the focal mechanisms (i.e., 1988-1999, 2000-2010 and 2011-2021; Fig. S5). When the earthquakes within the impact structure were not included in the depth slices (i.e., just Σ_{OUT}), the stress orientation for the 5-km depth slice increases to $N91.8^\circ$ from $N82.7^\circ$ but the stress orientation for the 10-km depth slice is not affected (Fig. 11 and 13). This observation supports the idea that the presence of relatively lower velocity and highly fractured rocks within the impact structure are affecting stress orientation.

Several studies have also observed a variation in σ_1 orientation with depth. For example, a stress inversion using the 2011 Mineral, Virginia earthquake aftershock focal mechanisms indicated a change of about 20° in the orientation of the maximum principal stress with depth (Wu

et al., 2015); σ_1 orientation changed from N80° for the subset of focal mechanisms associated with hypocenter depths less than 4 km to N100° for focal mechanisms associated with hypocenters deeper than 6 km. A large variation in σ_1 orientation is found for the depth range 4-6 km, where most of the aftershocks occur, and was attributed to breakage of less optimally oriented fault planes by positive Coulomb stress transfer following the mainshock. Wu et al. (2015) suggested that the difference between focal mechanisms for aftershocks at depths less than 4 km and those greater than 6 km, along with the mainshock, point to the possibility of a depth dependent stress field prior to the occurrence of the mainshock.

Zakharova and Goldberg (2014) observed a decrease in σ_1 orientation with depth in a deep well drilled in the northern Newark Rift Basin while evaluating the risk of induced seismicity for underground fluid injection of CO₂. They observed that the orientation rotates anticlockwise with depth from about N80° in the upper 800 m to about N25° below 1180 m (1180-1400 m). Zakharova and Goldberg (2014) attributed the change in the stress orientation to the presence of faults that penetrated the drilled hole at depths of about 800 m and 1200 m. They also suggested that the stress perturbation could be due to a release of in situ stresses by prior earthquakes on faults tens to hundreds of meters long, similar to the conclusions drawn by Wu et al. (2015).

The variation in stress orientation with depth in seismic zones could be due to different rock stiffness values and mechanical behavior (Valley and Evans, 2009). We observed a significant relative stress rotation between the zone of highly fractured rocks in the impact structure and the relatively stronger surrounding crust. We also find a significant stress rotation between the input velocity model depth ranges 6-12 km and 12-40 km (Fig. 3). This supports the stiffness argument as a cause for the rotation since the depth ranges in the input model are indicative of different rock properties. The depth-dependent clockwise stress rotation in the CSZ could represent the ambient stress field due to an increase in rock stiffness with depth, as noted by Wu et al. (2015) for the Mineral Virginia aftershock zone. Valley and Evans (2009) also observed a 20°-30° change in σ_1 orientation at a depth of 2.5 km, coinciding with the interface between sediment (sandstone with $\sigma_1 = \text{N}115^\circ\text{E} \pm 12^\circ$) and basement rocks ($\sigma_1 = \text{N}144^\circ\text{E} \pm 14^\circ$), using a vertical profile of σ_1 orientation from wellbore failure beneath the Swiss city of Basel. The observed increase in σ_1 orientation in the CSZ between the 15- and 20-km depth slices may be due to the presence of the high velocity body imaged at mid-crustal depths (Fig. 2; Vlahovic et al., 2003; Powell and Lamontagne, 2017).

Another possibility for the change in σ_1 orientation with depth in the CSZ is a change in the friction coefficient of the rift faults with depth. Wesson (1988) observed that the local direction of maximum compression at a depth of 2 km in the Cajon Pass Scientific Drill hole near the San Andreas fault is nearly normal to the fault zone. However, the orientation of the regional maximum compression expected from plate tectonics is about 66°NE from the strike of the fault. Wesson (1988) explained the apparent conflict in the σ_1 orientation with a model in which the fault zone is locked over a depth interval of 2-5 to 15 km but is very weak above and below that interval. They suggest that the sense of stress rotation is due to the relative angle between the regional stress and the strike of the fault, and the variation of the friction coefficient on the fault.

5.0 Conclusions

We determined the focal mechanisms of 455 relocated earthquakes derived from a previous tomography study for the CSZ, using wave polarities and amplitude ratios as constraints, to understand the stress state of the seismic zone. The stress inversion results have some similarities with previous studies. The σ_1 orientation of N103.1° supports the observed maximum horizontal

stress orientation from focal mechanisms in previous studies such as Zoback (1992), Levandowski et al. (2018), and Mazzotti et al. (2005) but differs from the σ_1 orientation of N86° determined by Mazzotti and Townend (2010) using focal mechanisms for 60 CSZ earthquakes. We observed a clockwise σ_1 rotation for the SE earthquake cluster relative to the NW cluster which is similar to, but smaller than, the rotation found by Mazzotti and Townend (2010).

Our results indicate stress changes across the seismic zone. There is significant stress rotation between earthquakes that are inside (N72.9°) versus outside (N105.6°) the impact structure. A greater clockwise rotation is observed between earthquakes inside the impact structure in the NW cluster ($\Sigma_{IN,NW}$) (N53.1°) and earthquakes outside the impact structure (N105.6°). This variation in the σ_1 orientation could be due to the highly fractured rocks within the impact structure, compared to the more competent, higher velocity rocks located outside of the impact structure. We observe about a 15° clockwise rotation in $\Sigma_{IN,SE}$ (N118.0°) relative to the σ_1 orientation (N103.1°) for all of the earthquakes, but the $\Sigma_{IN,SE}$ orientation is not well constrained due to the limited number of earthquakes in the cluster.

Our study also revealed a significant, systematic clockwise principal stress rotation with depth. This increase in orientation angle is consistent using different depth slices and depth ranges for different partitions of the earthquakes (e.g., Σ_{All} , Σ_{OUT} , $\Sigma_{OUT,NW}$ and $\Sigma_{OUT,SE}$) and temporal subsets of the focal mechanisms (e.g., 1988-1999, 2000-2010 and 2011-2020). The increase in σ_1 orientation with depth could be due to increases in rock stiffness and changes in the friction coefficient on the rift faults with depth. The observed increase in σ_1 orientation between the 15- and 20-km depth slices may be due to the presence of the high velocity body imaged at mid-crustal depths.

When the earthquakes within the impact structure were not included in the depth slices (i.e., Σ_{OUT}), the stress orientation for the 5-km depth slice increased to N91.8° from N82.7° but the stress orientation at 10 km was not affected. This observation also suggests that the relatively low velocity rocks (lower rock stiffness) within the impact structure affects the stress orientation in the upper 5 km and the presence of the high-velocity body affects stress orientation outside of the impact structure.

The pattern of stress change correlates with the pattern of velocity anomalies determined from 3D tomography and clustering of seismicity along rift-related faults of the St. Lawrence rift zone. This suggests that the seismicity and the observed stress rotations of the CSZ are controlled by velocity heterogeneity and rock stiffness, including the impact structure, and pre-existing fault structures within a stress field generated by both plate tectonic forces and glacial rebound.

Acknowledgments

This material is based upon work supported by the U.S. Geological Survey under Grant No. G19AP00052. The views and conclusions contained in this document are those of the authors and should not be interpreted as representing the opinions or policies of the U.S. Geological Survey. Mention of tradenames or commercial products does not constitute their endorsement by the U.S. Geological Survey. We acknowledge the Center of Earthquake Research and Information (CERI) at the University of Memphis, TN for providing the computer resources for this research. Waveform data used in this work is openly available from Natural Resources Canada AutoDRM website at: https://earthquakescanada.nrcan.gc.ca/stndon/AutoDRM/autodrm_req-en.php (last accessed August 2021).

References

- Altmann, S. L. (1986). Rotations, quaternions and double groups, Clarendon Press, Oxford.
- Anglin, F. M. (1984). Seismicity and faulting in the Charlevoix Zone of the St. Lawrence Valley. *Bulleting of the Seismological Society of America*, 74(2), 595–603.
- Adams, J. (1991). New focal mechanisms for Eastern Canadian, Geological Survey of Canada. Open File, OF2430.
- Baird, A. F., McKinnon, S. D., & Godin, L. (2010). Relationship between structures, stress and seismicity in the Charlevoix Seismic Zone revealed by 3-D geomechanical models: Implications for the seismotectonics of continental interiors. *Journal of Geophysical Research: Solid Earth*, 115(11), 1–16. <https://doi.org/10.1029/2010JB007521>.
- Bent, A. L. (1992). A re-examination of the 1925 Charlevoix, Québec, earthquake. *Bulletin of the Seismological Society of America*, 82 (5): 2097–2113.
- Bent, A. L., Drysdale, J., & Perry, H. K. C. (2003). Focal mechanisms for Eastern Canadian Earthquakes, 1994-2000. *Seismological Research Letters*, 74(4), 452–468. <https://doi.org/10.1785/gssrl.74.4.452>.
- Bott, M. (1959). The mechanics of oblique slip faulting. *Geological Magazine*, 96(2), 109–117. doi:10.1017/S0016756800059987.
- Bullen, K. E. (1963). An introduction to the theory of seismology, Third Edition, Cambridge Uni. Press, Cambridge, 1-381.
- Crotwell, H. P., Owens, T. J., & Ritsema, J. (1999). The TauP Toolkit: Flexible seismic travel-time and ray-path utilities, *Seismological Research Letters* 70(2), 154–160. doi: <https://doi.org/10.1785/gssrl.70.2.154>.
- Dahal, N.R. & Ebel, J.E. (2020). Method for Determination of Focal Mechanisms of Magnitude 2.5–4.0 Earthquakes Recorded by a Sparse Regional Seismic Network. *Bulletin of the Seismological Society of America*, XX, 1-12, doi: <https://doi.org/10.1785/0120190170>.
- D’Amico, S., B. Orecchio, D. Presti, A. Gervasi, L. Zhu, I. Guerra, G. Neri, & R. B. Herrmann (2011). Testing the stability of moment tensor solutions for small earthquakes in the Calabro-Peloritan Arc region (southern Italy), *Boll. Geo. Teor. Appl.* 52, 283–298, doi: 10.4430/bgta0009.
- Ebel, J. E. (2011). A new analysis of the magnitude of the February 1663 earthquake at Charlevoix, Quebec. *Bulletin of the Seismological Society of America*, 101(3), 1024–1038. <https://doi.org/10.1785/0120100190>.
- Fadugba, O. I., Choi, E., & Powell, C. A. (2019). Effects of preexisting structures on the seismicity of the Charlevoix Seismic Zone. *Journal of Geophysical Research: Solid Earth*, 124, 7370–7386. <https://doi.org/10.1029/2019JB017831>.
- Gardner, G. H. F., Gardner, L. W., & Gregory, A. R. (1974). Formation velocity and density—The diagnostic basics for stratigraphic traps. *Geophysics*, 39(6), 770–780. <https://doi.org/10.1190/1.1440465>.
- Gephart, J. W., & Forsyth, D. W. (1984), An improved method for determining the regional stress tensor using earthquake focal mechanism data: Application to the San Fernando Earthquake Sequence, *Journal of Geophysical Research*, 89(B11), 9305–9320, doi:[10.1029/JB089iB11p09305](https://doi.org/10.1029/JB089iB11p09305).
- Hardebeck, J. L. and Hauksson, E. (2001). Stress Orientations Obtained from Earthquake Focal Mechanisms: What Are Appropriate Uncertainty Estimates? *Bulletin of the Seismological Society of America*, 91 (2). pp. 250-262.

- Hardebeck, J. L., and Hauksson, E. (2001), Crustal stress field in southern California and its implications for fault mechanics, *J. Geophys. Res.*, 106 (B10), 21859–21882, doi:[10.1029/2001JB000292](https://doi.org/10.1029/2001JB000292).
- Hardebeck, J. L., & Shearer, P. M. (2002). A new method for determining first-motion focal mechanisms. *Bulletin of the Seismological Society of America*, 92(6), 2264–2276. <https://doi.org/10.1785/0120010200>.
- He, X., Zhang, P., Ni, S., & Zheng, W. (2019). Resolving focal depth in sparse network with local depth phase sPL: A case study for the 2011 Mineral, Virginia, earthquake sequence. *Bulletin of the Seismological Society of America*, 109(2), 745–755. <https://doi.org/10.1785/0120180221>.
- Kagan, Y. Y. (1991). 3-D rotation of double-couple earthquake sources. *Geophysical Journal International*, 106(3), 709–716. <https://doi.org/10.1111/j.1365-246X.1991.tb06343.x>.
- Kraft, T., Wassermann, J., & Igel, H. (2006). High-precision relocation and focal mechanism of the 2002 rain-triggered earthquake swarms at Mt Hochstaufen, SE Germany. *Geophysical Journal International*, 167(3), 1513–1528. <https://doi.org/10.1111/j.1365-246X.2006.03171.x>.
- Kubo, A., Fukuyama, E., Kawai, E., & Nonomura, K. (2002). NIED seismic moment tensor catalogue for regional earthquakes around Japan: quality test and application. *Tectonophysics* 356(1):23-48. doi:[10.1016/S0040-1951\(02\)00375-X](https://doi.org/10.1016/S0040-1951(02)00375-X).
- Lamontagne, M. (1998). New and revised earthquake focal mechanisms for the Charlevoix Seismic Zone, Canada. Geological Survey of Canada. Open File, OF3556.
- Lamontagne, M. (1999). Rheological and geological constraints on the earthquake distribution in the Charlevoix Seismic Zone, Quebec, Canada. Geological Survey of Canada. Open File, D3778.
- Levandowski, W., Herrmann, R.B., Briggs, R., Boyd, O.S., and Gold, R. (2018). An revised stress map of the continental United States reveals evidence for heterogeneous intraplate stress: *Nature Geoscience*, v. 11, doi:10.1038/s41561-018-0120-x.
- Lund, B., & Slunga, R. (1999), Stress tensor inversion using detailed microearthquake information and stability constraints: Application to Ölfus in southwest Iceland, *Journal of Geophysical Research*, 104(B7), 14947– 14964, doi:[10.1029/1999JB900111](https://doi.org/10.1029/1999JB900111).
- Mazzotti, S., James, T. S., Henton, J., & Adams, J. (2005). GPS crustal strain, postglacial rebound, and seismic hazard in eastern North America: The Saint Lawrence Valley example. *Journal of Geophysical Research*, 110, B11301. <https://doi.org/10.1029/2004JB003590>.
- Mazzotti, S., & Townend, J. (2010). State of stress in central and eastern North American seismic zones. *Lithosphere*, 2(2), 76–83. <https://doi.org/10.1130/l65.1>.
- Michael, A.J. (1984). Determination of stress from slip data: faults and folds, *Journal of Geophysical Research*, 89, 11 517–11 526.
- Pondrelli, S., S. Salimbeni, G. Ekström, A. Morelli, P. Gasperini, & G. Vannucci (2006). The Italian CMT dataset from 1977 to the present, *Phys. Earth Planet. In.* 159, 286–303, doi: 10.1016/j.pepi.2006.07.008.
- Powell, C. A., & Lamontagne, M. (2017). Velocity models and hypocenter relocations for the Charlevoix Seismic Zone. *Journal of Geophysical Research: Solid Earth*, 122, 6685–6702. <https://doi.org/10.1002/2017jb014191>.
- Rondot, J. (1971). Impactite of the Charlevoix structure Quebec, Canada. *Journal of Geophysical Research*, 76(23), 5414–5423. <https://doi.org/10.1029/jb076i023p05414>
- Rondot, J. (1994). Recognition of eroded astroblemes. *Earth-Science Reviews*, 35(4), 331–365. [https://doi.org/10.1016/0012-8252\(94\)90001-9](https://doi.org/10.1016/0012-8252(94)90001-9).

- Shearer, P. (2009). *Introduction to Seismology*. Cambridge: Cambridge University Press. 1
[doi:10.1017/CBO9780511841552](https://doi.org/10.1017/CBO9780511841552).
- Solomon, S. C., & Duxbury, E. D. (1987). A test of the longevity of impact-induced faults as preferred sites for later tectonic activity, *Journal of Geophysical Research*, 92(B4), E759– E768, doi:10.1029/JB092iB04p0E759.
- Thomas, W. A., & Powell, C. A. (2017). Necessary conditions for intraplate seismic zones in North America. *Tectonics*, 36, 2903-2917. <https://doi.org/10.1002/2017TC004502>.
- Valley, B., & Evans, K.F. (2009). Stress orientation to 5 km depth in the basement below Basel (Switzerland) from borehole failure analysis. *Swiss J. Geosci.* **102**, 467.
<https://doi.org/10.1007/s00015-009-1335-z>.
- Vavryčuk, V. (2014). Iterative joint inversion for stress and fault orientations from focal mechanisms. *Geophysical Journal International*, 199(1), 69–77.
<https://doi.org/10.1093/gji/ggu224>.
- Vlahovic, G., Powell, C., & Lamontagne, M. (2003). A three-dimensional P wave velocity model for the Charlevoix Seismic Zone, Quebec, Canada. *Journal of Geophysical Research: Solid Earth*, 108(B9), 2439. <https://doi.org/10.1029/2002jb002188>.
- Wallace, R.E., 1951. Geometry of shearing stress and relation to faulting, *J. Geol.*, 59, 118–130.
<https://doi.org/10.1086/625831>.
- Wesson, R. L. (1988). Predicted variation of stress orientation with depth near an active fault: Application to the Cajon Pass Scientific Drillhole, southern California. *Geophysical Research Letters*. 15 (9), 0094-8276. <https://doi.org/10.1029/GL015i009p01009>.
- Wu, Q., Chapman, M. C., & J. N. Beale (2015). The Aftershock Sequence of the 2011 Mineral, Virginia, Earthquake: Temporal and Spatial Distribution, Focal Mechanisms, Regional Stress, and the Role of Coulomb Stress Transfer. *Bulletin of the Seismological Society of America*; 105 (5): 2521–2537. <https://doi.org/10.1785/0120150032>.
- Zakharova, N. V., and Goldberg, D. S. (2014). In situ stress analysis in the northern Newark Basin: Implications for induced seismicity from CO₂ injection, *J. Geophys. Res. Solid Earth*, 119, 2362– 2374, doi:[10.1002/2013JB010492](https://doi.org/10.1002/2013JB010492).
- Zoback, M. L. (1992). First- and second-order patterns of stress in the lithosphere: The world stress map project. *J. of Geophysical Research*, 97(B8), 11703. <https://doi.org/10.1029/92jb00132>.

Supporting Information to “Focal Mechanisms of Relocated Earthquakes and Stress Orientation in the Charlevoix Seismic Zone”

Proof for the relation between the trace of \mathbf{T} and the dot product of all observed and calculated amplitude ratio vectors

The weighted observed amplitude ratios using the observed amplitude ratio and the weighting matrix is:

$$\begin{aligned}\mathbf{V}'_{\text{obs}} &= \mathbf{V}_{\text{obs}} \mathbf{W}_{\text{obs}} \\ &= \begin{bmatrix} v_{11} & \cdots & v_{1s} \\ v_{21} & \cdots & v_{2s} \end{bmatrix} \begin{bmatrix} w_{11} & \cdots & 0 \\ \vdots & \ddots & \vdots \\ 0 & \cdots & w_{ss} \end{bmatrix} \\ &= \begin{bmatrix} w_{11}v_{11} & w_{22}v_{12} & \cdots & w_{ss}v_{1s} \\ w_{11}v_{21} & w_{22}v_{22} & \cdots & w_{ss}v_{2s} \end{bmatrix}\end{aligned}\quad (\text{S1})$$

Also, using the theoretical amplitude ratio vectors (\mathbf{V}_{calc}), Take:

$$\begin{aligned}\mathbf{T} &= \mathbf{V}'_{\text{obs}} \mathbf{V}_{\text{calc}}^T \\ &= \begin{bmatrix} w_{11}v_{11} & w_{22}v_{12} & \cdots & w_{ss}v_{1s} \\ w_{11}v_{21} & w_{22}v_{22} & \cdots & w_{ss}v_{2s} \end{bmatrix} \begin{bmatrix} v''_{11} & v''_{21} \\ v''_{12} & v''_{22} \\ \vdots & \vdots \\ v''_{1s} & v''_{2s} \end{bmatrix}\end{aligned}\quad (\text{S2})$$

$$= \begin{bmatrix} w_{11}v_{11}v''_{11} + w_{22}v_{12}v''_{12} + \cdots + w_{ss}v_{1s}v''_{1s} & w_{11}v_{11}v''_{21} + \cdots + w_{ss}v_{1s}v''_{2s} \\ w_{11}v_{21}v''_{11} + \cdots + w_{ss}v_{2s}v''_{1s} & w_{11}v_{21}v''_{21} + \cdots + w_{ss}v_{2s}v''_{2s} \end{bmatrix}\quad (\text{S3})$$

The trace of \mathbf{T} will be:

$$\text{tr } \mathbf{T} = w_{11}(v_{11}v''_{11} + v_{21}v''_{21}) + w_{22}(v_{12}v''_{12} + v_{22}v''_{22}) + \cdots + w_{ss}(v_{1s}v''_{1s} + v_{2s}v''_{2s}) \quad (\text{S4})$$

Therefore, the trace of \mathbf{T} ($\text{tr } \mathbf{T}$) will be related to the dot product of all observed and calculated amplitude ratio vectors.

Effect of the free surface on the displacement of an incident SV wave

The mathematical background of this problem is well-known by many seismologists (e.g., Helmberger, 1968), we present here a quick review of the effect of free surface receiver function on the displacement of an incident SV wave as a function of incident angle using synthetic seismograms (radial component). Figure S1 shows the schematic diagram of the problem and the ray geometry for an incident SV wave interacting with the free surface with the solution evaluated at some field point (x_1, x_3).

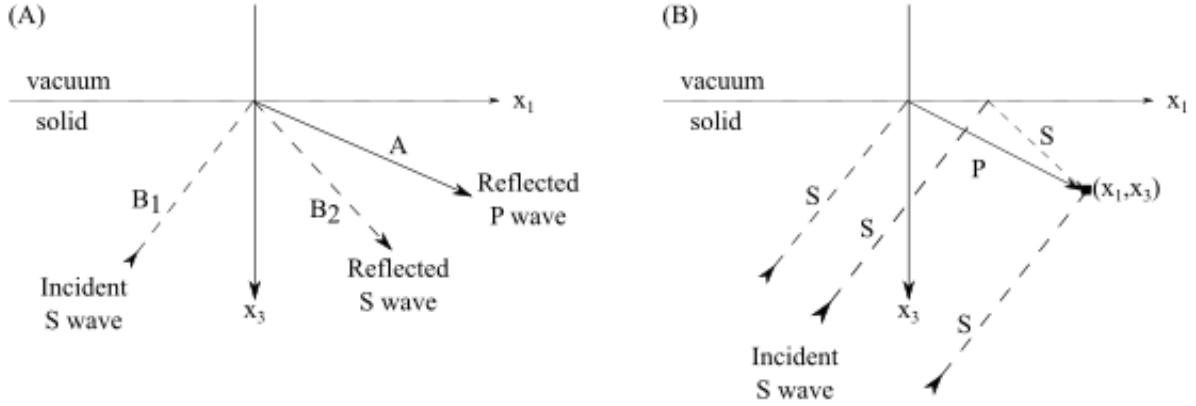


Figure S1: (A) Schematic and (B) Ray geometry of an incident S plane wave interacting with the free surface. The solutions are evaluated at some field point (x_1, x_3) .

The P and SV wave potentials are given as

$$\hat{\phi}(\omega) = A(\omega)e^{-i\omega(px_1 + \eta_\alpha x_3)} \quad (S5)$$

$$\hat{\psi}(\omega) = B_1(\omega)e^{-i\omega(px_1 - \eta_\beta x_3)} + B_2(\omega)e^{-i\omega(px_1 + \eta_\beta x_3)} \quad (S6)$$

Define the SV wave reflection (R_{SS}) and the SV-to-P conversion (R_{SP}) coefficients as

$$R_{SS} = \frac{B_2(\omega)}{B_1(\omega)}; \quad R_{SP} = \frac{A(\omega)}{B_1(\omega)}; \quad (S7)$$

Therefore,

$$\hat{\phi}(\omega) = B_1(\omega)R_{SP}e^{-i\omega(px_1 + \eta_\alpha x_3)} \quad (S8)$$

$$\hat{\psi}(\omega) = B_1(\omega)e^{-i\omega(px_1 - \eta_\beta x_3)} + B_1(\omega)R_{SS}e^{-i\omega(px_1 + \eta_\beta x_3)} \quad (S9)$$

The potentials can be converted to displacements (\hat{u}_1 and \hat{u}_3) using

$$\begin{aligned} \hat{u}_1 &= \frac{\partial \hat{\phi}}{\partial x_1} - \frac{\partial \hat{\psi}}{\partial x_3} \\ &= -i\omega p B_1(\omega) R_{SP} e^{-i\omega(px_1 + \eta_\alpha x_3)} - i\omega \eta_\beta B_1(\omega) e^{-i\omega(px_1 - \eta_\beta x_3)} \\ &\quad + i\omega \eta_\beta B_1(\omega) R_{SS} e^{-i\omega(px_1 + \eta_\beta x_3)} \end{aligned} \quad (S10)$$

Also,

$$\begin{aligned} \hat{u}_3 &= \frac{\partial \hat{\phi}}{\partial x_3} + \frac{\partial \hat{\psi}}{\partial x_1} \\ &= -i\omega \eta_\alpha B_1(\omega) R_{SP} e^{-i\omega(px_1 + \eta_\alpha x_3)} - i\omega p B_1(\omega) e^{-i\omega(px_1 - \eta_\beta x_3)} \\ &\quad - i\omega p B_1(\omega) R_{SS} e^{-i\omega(px_1 + \eta_\beta x_3)} \end{aligned} \quad (S11)$$

Letting $x_3=0$,

$$\begin{aligned}\hat{u}_1|_{x_3=0} &= -i\omega B_1(\omega)[pR_{SP} + \eta_\beta - \eta_\beta R_{SS}]e^{-i\omega p x_1} \\ &= -i\omega B_1(\omega)R_{SX}e^{-i\omega p x_1}\end{aligned}\quad (S12)$$

$$\begin{aligned}\hat{u}_3|_{x_3=0} &= -i\omega B_1(\omega)[\eta_\alpha R_{SP} + p + pR_{SS}]e^{-i\omega p x_1} \\ &= -i\omega B_1(\omega)R_{SZ}e^{-i\omega p x_1}\end{aligned}\quad (S13)$$

The quantities R_{SX} and R_{SZ} are the free surface receiver functions for an incident SV wave.

Applying a stress-free boundary condition at the vacuum and solid interface (i.e., at $x_3 = 0$) using zero normal and shear stress:

$$\tau_{33} = \tau_{31} = 0 \quad (S14)$$

the receiver functions are given as

$$R_{SX} = \frac{2\eta_\beta b - pc}{a + b} \quad (S15)$$

$$R_{SZ} = \frac{-2pa + \eta_\alpha c}{a + b} \quad (S16)$$

where

$$a = 4p^2\eta_\alpha\eta_\beta; b = (\eta_\beta^2 - p^2)^2; \text{ and } c = -4p\eta_\alpha(\eta_\beta^2 - p^2)$$

The R_{SX} is used as the receiver function since we used the radial component SV wave. We determined R_{SX} at different incident angles using V_p , V_s and density values of 6.1 km/s, 3.53 km/s and 2.74 km/m³ for the near surface of the CSZ, and used a Gaussian function as the input SV wave given as

$$g(t) = e^{-\alpha^2(t-t_0)^2}; \alpha = 3.0 \text{ and } t_0 = 5.0 \quad (S17)$$

And determine synthetic seismograms (radial component) showing the effect of free surface receiver function on the displacement of an incident SV wave as a function of incident angle (Fig. S2).

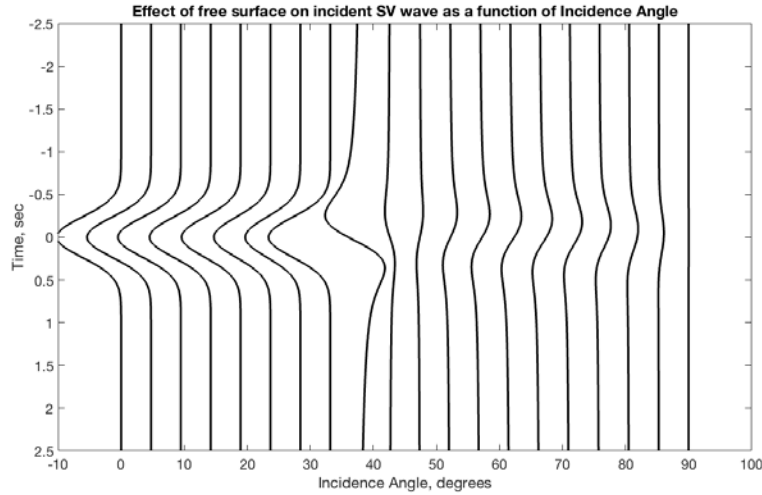


Figure S2: Synthetic seismograms (radial component) showing the effect of free surface receiver function on the displacement of an incident SV wave as a function of incident angle (Helmberger, 1968).

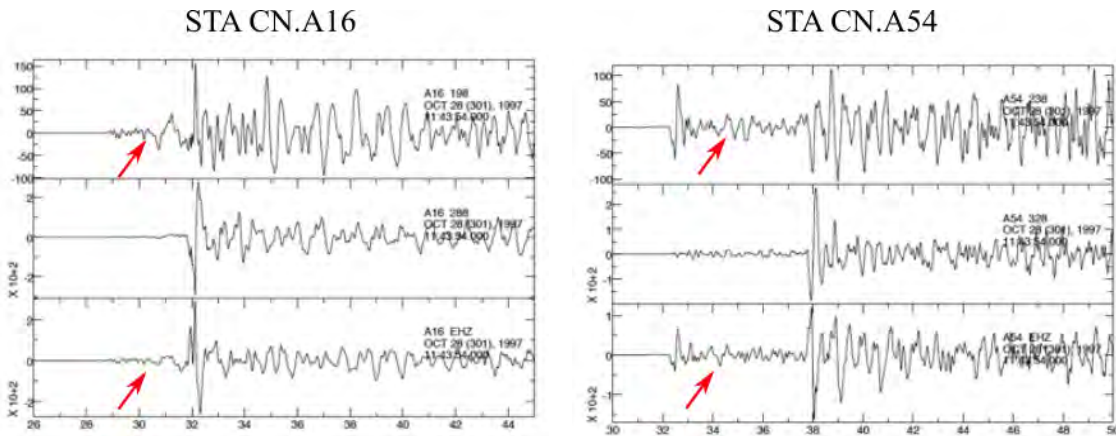


Figure S3: Observation of a large secondary P-wave arrival before S-wave arrival on stations A16 and A54 for the October 28, 1997 earthquake. The stations are at distance 23.5 km and 44.4 km from the epicenter. The red arrow shows the SP headwave prominent on both radial and vertical components.

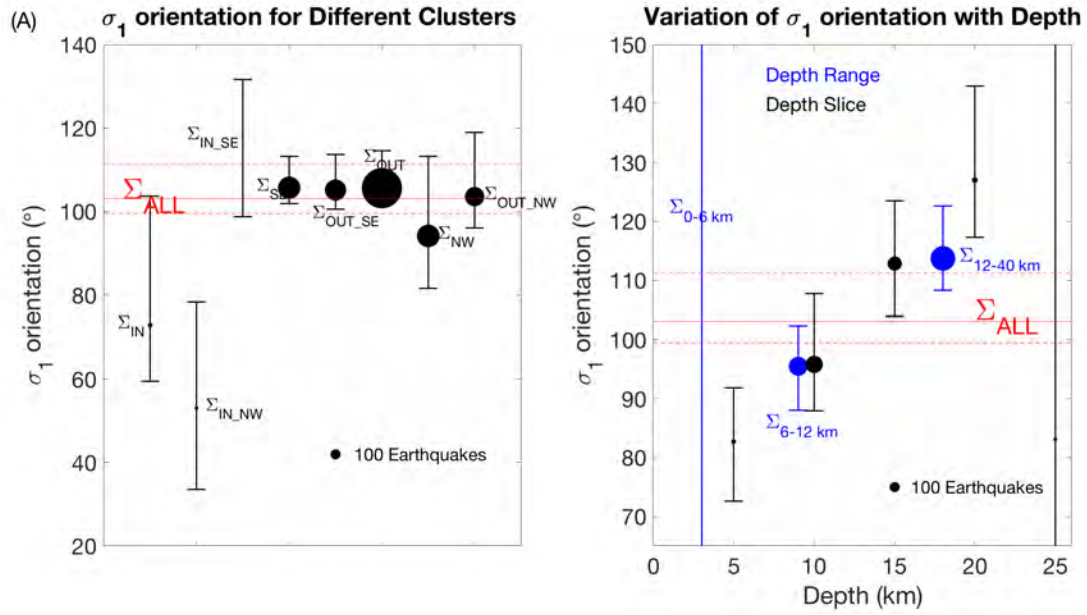


Figure S4: Variation of σ_1 orientation with (left) different clusters and (right) depth slice and depth range showing the effect of using a mean deviation value of 15 in the error bars. The observed spatial and depth variations in σ_1 orientation are still significant despite the larger error bars.

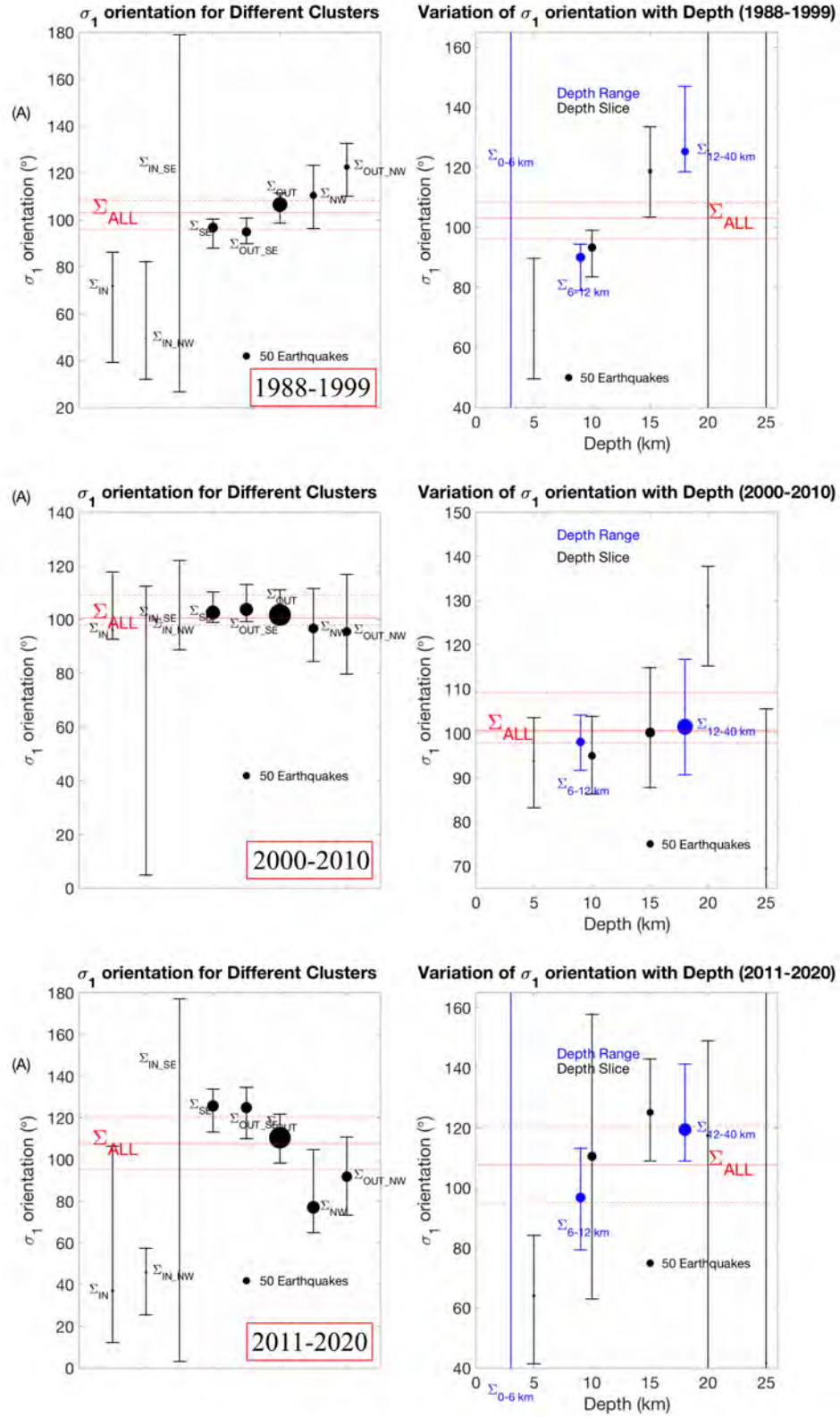


Figure S5: Same as Fig. S4 but showing temporal variations of the spatial and depth stress orientation for (top) 1988-1999, (middle) 2000-2010 and (bottom) 2011-2020.

Table S1: Station parameters for generating synthetic datasets.

SN	1	2	3	4	5	6	7	8	9	10	11	12	13
Distance (km)	3.5	20.0	38.6	60.3	10.7	28.5	20.0	32.0	50.3	11.5	14.0	20.0	24.0
Azimuth (°)	10	15	25	50	80	105	130	125	158	190	210	250	333

Table S2: Summary of the preferred solutions of the synthetic data using different constraints.

SN	Constraints	Strike	Dip	Rake	RMS (1σ)	Kagan Angle	Number of acceptable solutions
1	P_{pol}	40°	72°	80°	15.5°	11.8°	154
2	$(P, SH)_{pol}$	43°	70°	77°	9.48°	12.5°	68
3	$(P, SH, SV)_{pol}$	46°	71°	85°	5.5°	5.4°	16
4	$(P, SH)_{pol}$ + $\left(\frac{ SV }{SH}\right)_{ratio}$	50°	70°	90°	0°	0°	1

Table S3: All relocated earthquakes ($M \geq 2$) and their focal mechanisms.

SN	Date	HH:MM:SS	Latitude	Longitude	depth	mag	Strike1	Dip1	Rake1	Accuracy (%)	Strike aux	Dip aux	Rake aux	No of stations
1	10/28/1997	11:44:19	47.67	-69.91	9.14	4.70	310	52	24	98	205	71	139	6
2	12/8/1991	3:00:30	47.78	-69.87	23.12	4.30	354	46	52	94	222	55	123	6
3	9/25/1994	0:53:29	47.76	-69.97	16.83	4.30	82	60	114	99	220	38	55	7
4	12/30/1993	23:01:48	47.45	-70.36	6.82	3.80	108	84	16	99	16	74	174	7
5	8/20/1997	9:12:04	47.54	-70.29	7.09	3.70	136	40	124	98	275	58	65	5
6	11/22/1989	23:02:52	47.45	-70.34	8.04	3.40	204	68	124	99	323	40	36	6
7	7/14/1996	18:46:49	47.69	-69.99	6.72	3.40	280	6	8	97	182	89	96	7
8	3/10/1992	5:45:33	47.72	-69.86	9.65	3.30	118	64	26	97	16	67	152	6
9	10/13/1989	14:04:43	47.39	-70.13	22.07	3.20	180	46	62	96	37	51	116	6
10	3/13/1990	19:10:39	47.53	-70.13	14.67	3.20	52	64	84	99	245	27	102	6
11	1/10/1997	19:27:28	47.51	-70.19	16.32	3.20	146	24	74	96	343	67	97	7
12	4/21/1990	1:23:04	47.55	-70.08	8.64	3.10	340	56	98	98	146	35	78	6
13	10/26/1990	9:13:51	47.57	-69.99	10.37	3.10	172	36	110	98	328	56	76	6
14	5/12/1996	11:53:22	47.52	-70.03	13.90	3.10	200	52	80	99	36	39	103	7
15	6/7/1996	9:41:43	47.53	-69.94	12.40	3.10	28	28	96	97	201	62	87	7
16	9/24/1996	23:41:03	47.55	-70.24	12.31	3.10	256	58	96	99	65	32	81	7
17	1/14/1997	4:47:33	47.65	-69.88	13.29	3.10	156	74	130	98	264	43	24	7
18	4/23/1990	0:28:05	47.41	-70.17	7.53	3.00	50	72	160	99	146	71	19	5
19	10/2/1999	9:45:37	47.42	-70.12	8.50	3.00	38	64	82	91	236	27	106	7
20	9/13/1989	14:55:24	47.57	-70.04	13.80	2.90	256	48	110	98	47	46	69	6
21	4/4/1992	12:30:29	47.43	-70.17	17.93	2.90	268	28	68	99	113	64	101	6
22	4/24/1993	6:45:24	47.66	-69.91	7.12	2.90	192	72	164	98	287	75	19	7
23	12/26/1995	14:51:10	47.40	-70.18	11.32	2.90	180	12	226	99	45	81	278	5
24	12/18/1989	14:55:36	47.39	-70.15	17.85	2.80	34	54	108	98	185	40	67	5
25	10/18/1990	6:03:29	47.48	-70.08	14.42	2.80	70	36	114	97	221	58	74	5

26	11/25/1991	17:08:59	47.41	-70.17	9.41	2.80	236	30	126	98	16	66	71	6
27	4/23/1993	0:07:50	47.63	-69.83	11.40	2.80	160	68	138	93	269	52	29	7
28	6/9/1999	1:35:02	47.70	-69.90	8.61	2.80	18	38	102	98	183	53	81	7
29	10/28/1999	1:52:09	47.70	-69.87	14.11	2.80	212	28	72	92	52	63	99	7
30	8/30/1989	8:25:49	47.66	-70.05	19.94	2.70	234	26	88	97	56	64	91	6
31	12/2/1993	9:03:18	47.46	-70.04	7.70	2.70	164	44	22	97	58	75	132	7
32	6/15/1995	15:59:17	47.71	-69.93	25.37	2.70	184	54	68	100	39	41	117	6
33	1/17/1996	0:42:24	47.48	-70.14	11.09	2.70	214	36	152	99	327	74	57	6
34	12/8/1989	17:20:35	47.70	-70.06	9.86	2.60	30	46	126	96	164	54	59	6
35	9/19/1991	11:06:53	47.54	-69.94	12.70	2.60	22	34	44	99	253	67	116	4
36	6/5/1993	4:49:41	47.49	-70.11	10.52	2.60	248	20	150	99	6	80	73	7
37	9/30/1995	0:01:20	47.42	-70.26	16.36	2.60	36	68	14	99	301	77	157	5
38	7/26/1999	17:35:19	47.48	-70.11	18.89	2.60	180	46	60	98	40	51	117	7
39	9/21/1990	9:11:43	47.55	-70.26	12.94	2.50	244	34	108	99	43	58	78	6
40	8/12/1995	17:42:56	47.67	-69.91	9.31	2.50	6	42	70	98	212	51	107	6
41	1/1/1997	17:14:16	47.44	-70.11	21.81	2.50	216	30	102	100	22	61	83	7
42	9/3/1997	15:52:28	47.48	-70.06	7.60	2.50	38	54	84	99	228	36	98	5
43	10/28/1997	16:54:03	47.67	-69.92	7.80	2.50	352	28	92	99	170	62	89	5
44	3/13/1990	18:49:41	47.53	-70.13	14.52	2.40	36	58	88	99	220	32	93	5
45	12/30/1990	16:33:55	47.67	-70.02	24.34	2.40	68	58	94	95	240	32	84	6
46	5/18/1993	0:17:42	47.54	-70.03	7.08	2.40	2	46	68	98	212	48	111	6
47	3/16/1994	7:23:05	47.44	-70.04	9.31	2.40	188	56	72	97	38	38	115	6
48	6/2/1994	14:45:37	47.72	-69.95	24.91	2.40	202	52	74	99	47	41	109	7
49	11/4/1995	9:32:58	47.60	-69.99	16.70	2.40	4	64	166	99	100	77	27	7
50	4/4/1996	15:13:02	47.57	-70.10	18.11	2.40	244	48	72	98	90	45	109	7
51	7/30/1997	15:56:13	47.58	-70.20	4.40	2.40	166	24	50	99	29	72	106	4
52	8/6/1997	1:32:29	47.58	-69.95	13.38	2.40	50	62	110	99	192	34	57	5
53	10/31/1997	15:41:21	47.54	-70.04	7.57	2.40	160	40	38	99	39	67	123	5

54	11/28/1997	10:56:35	47.67	-69.92	7.94	2.40	346	30	84	98	173	60	93	5
55	9/4/1998	15:42:04	47.56	-70.22	10.87	2.40	162	20	50	99	24	75	103	5
56	3/31/1990	6:05:34	47.62	-70.16	9.09	2.30	328	56	82	97	162	35	102	6
57	1/24/1992	1:37:03	47.53	-70.09	7.86	2.30	238	36	98	97	48	54	84	5
58	6/16/1992	20:11:47	47.41	-70.34	7.48	2.30	312	32	70	98	155	60	102	7
59	2/23/1993	9:51:51	47.49	-69.99	11.26	2.30	32	62	86	99	220	28	97	7
60	6/2/1993	22:00:02	47.45	-70.17	21.45	2.30	42	76	76	99	268	20	134	7
61	8/23/1995	12:30:19	47.43	-70.32	10.77	2.30	312	48	32	99	199	67	133	7
62	9/24/1995	14:27:06	47.64	-69.96	6.85	2.30	162	38	36	96	42	69	122	5
63	7/26/1996	14:38:45	47.61	-69.95	10.05	2.30	60	74	290	98	187	25	220	7
64	10/28/1996	2:45:39	47.55	-70.04	10.46	2.30	332	16	352	98	70	88	254	6
65	12/22/1996	0:30:32	47.51	-70.06	10.15	2.30	118	26	30	99	1	77	113	5
66	1/11/1997	7:50:49	47.54	-70.04	10.93	2.30	62	40	82	90	252	50	97	7
67	12/28/1997	20:39:58	47.78	-69.93	26.02	2.30	260	28	124	99	43	67	73	6
68	5/15/1998	22:17:37	47.63	-70.06	22.65	2.30	342	42	178	99	73	89	48	6
69	8/12/1999	3:09:29	47.57	-70.00	14.07	2.30	142	40	22	99	35	76	128	6
70	4/7/1990	13:30:57	47.57	-69.96	10.63	2.20	42	30	154	90	155	77	63	5
71	10/20/1990	3:46:47	47.39	-70.15	11.29	2.20	124	56	108	96	274	38	65	5
72	7/22/1992	23:07:31	47.56	-69.94	11.92	2.20	120	60	50	98	359	48	138	6
73	4/15/1993	9:02:58	47.61	-69.84	19.95	2.20	26	54	52	98	259	50	130	6
74	2/16/1995	17:09:39	47.41	-70.26	13.66	2.20	356	72	304	99	111	38	210	5
75	7/14/1996	7:15:03	47.48	-70.05	13.10	2.20	22	64	158	98	122	70	28	5
76	8/14/1996	21:10:54	47.38	-70.13	13.97	2.20	16	72	112	97	143	28	41	5
77	9/13/1996	23:55:36	47.50	-70.21	11.55	2.20	264	30	134	100	36	69	68	4
78	9/23/1996	5:26:54	47.66	-69.90	12.60	2.20	132	58	66	98	352	39	123	7
79	8/9/1997	18:00:35	47.46	-70.06	17.20	2.20	306	18	46	99	171	77	103	5
80	1/3/1998	9:57:00	47.44	-70.16	9.09	2.20	224	28	10	97	125	85	118	7
81	3/2/1998	1:52:57	47.44	-70.37	8.75	2.20	218	22	20	99	109	83	111	6

82	8/1/1998	16:29:35	47.50	-70.22	21.78	2.20	172	32	52	98	35	65	111	7
83	8/15/1998	7:46:17	47.65	-70.10	13.60	2.20	88	64	174	95	181	85	26	7
84	10/21/1998	18:53:55	47.49	-70.04	14.75	2.20	20	24	70	96	222	68	99	5
85	2/8/1999	20:48:49	47.44	-70.17	20.27	2.20	164	28	84	99	351	62	93	7
86	5/30/1990	2:50:54	47.53	-69.97	10.84	2.10	214	28	88	99	36	62	91	6
87	12/28/1990	6:32:23	47.40	-70.22	13.10	2.10	150	68	60	98	27	37	141	6
88	6/3/1992	3:58:58	47.41	-70.32	10.37	2.10	150	52	38	99	34	61	135	5
89	7/22/1992	22:33:06	47.57	-70.21	10.41	2.10	82	50	308	99	211	53	234	5
90	1/6/1994	15:58:23	47.43	-70.11	9.77	2.10	120	18	22	99	9	83	107	7
91	10/19/1995	3:16:08	47.58	-70.00	8.19	2.10	194	54	88	98	17	36	93	6
92	8/19/1996	17:06:10	47.30	-70.24	5.57	2.10	182	18	80	98	13	72	93	5
93	2/22/1997	1:38:50	47.62	-69.95	7.65	2.10	178	74	68	97	54	27	143	6
94	5/9/1997	14:57:47	47.55	-70.07	19.47	2.10	290	34	130	99	65	65	67	4
95	10/27/1997	15:04:51	47.59	-69.99	8.13	2.10	156	58	98	98	321	33	77	6
96	11/8/1997	11:51:34	47.44	-70.05	13.87	2.10	20	44	78	99	216	47	101	4
97	12/1/1997	22:31:02	47.72	-70.00	13.98	2.10	44	78	128	100	149	40	19	5
98	2/4/1998	18:15:12	47.62	-70.15	10.45	2.10	240	34	80	98	72	57	97	7
99	4/30/1998	15:18:06	47.58	-69.93	11.45	2.10	18	42	82	98	209	49	97	6
100	5/6/1998	7:46:11	47.68	-69.92	8.19	2.10	164	44	14	98	64	80	133	5
101	5/21/1998	15:59:51	47.67	-69.91	6.81	2.10	10	42	154	98	120	73	51	6
102	7/19/1999	21:18:07	47.58	-69.90	14.40	2.10	14	62	116	96	148	37	50	6
103	6/1/1991	4:49:27	47.47	-70.20	7.84	2.00	194	42	82	98	25	49	97	5
104	2/7/1994	6:09:01	47.59	-70.00	7.37	2.00	172	70	64	99	47	32	140	7
105	7/23/1994	9:46:41	47.38	-70.13	13.92	2.00	28	72	130	97	138	43	27	7
106	5/3/1995	14:31:54	47.68	-69.85	9.73	2.00	16	50	150	90	126	67	44	6
107	8/24/1996	2:45:08	47.40	-70.32	11.68	2.00	190	12	52	99	49	81	97	4
108	9/24/1996	6:44:46	47.59	-70.15	20.59	2.00	36	78	114	99	151	27	28	7
109	1/4/1997	12:14:22	47.62	-70.13	8.50	2.00	162	26	82	97	351	64	94	6

110	10/20/1997	16:27:07	47.67	-69.91	12.50	2.00	354	50	42	99	234	59	132	5
111	12/25/1997	5:58:56	47.56	-69.92	11.64	2.00	48	38	102	99	213	53	81	6
112	12/29/1997	9:27:39	47.74	-70.00	9.77	2.00	226	84	168	97	317	78	6	6
113	2/13/1998	20:44:54	47.46	-70.13	9.75	2.00	248	28	130	100	24	69	71	4
114	2/20/1998	22:06:32	47.44	-70.16	21.09	2.00	192	30	64	99	41	63	104	7
115	3/21/1998	23:01:49	47.52	-70.27	6.69	2.00	334	76	258	99	195	18	310	5
116	7/12/1998	3:38:22	47.52	-70.02	13.63	2.00	230	60	94	99	42	30	83	6
117	8/3/1998	2:20:22	47.63	-70.15	11.90	2.00	162	22	90	98	342	68	90	6
118	12/4/1998	8:02:26	47.45	-70.13	13.81	2.00	72	58	120	99	205	43	51	5
119	9/25/1994	5:03:37	47.59	-70.21	12.40	4.30	78	40	62	99	293	55	112	5
120	1/6/2000	18:56:30	47.39	-70.22	12.60	2.00	244	40	12	94	145	82	129	6
121	6/15/2000	9:25:54	47.67	-69.80	11.40	3.70	14	44	140	98	135	63	54	7
122	5/22/2001	0:33:29	47.65	-69.92	11.43	3.50	44	42	64	89	257	53	112	7
123	1/3/2008	9:37:56	47.38	-70.31	13.50	3.40	218	22	96	98	32	68	88	6
124	2/28/2003	9:40:47	47.50	-70.03	8.62	3.30	128	64	72	91	345	31	122	7
125	5/29/2004	21:21:16	47.44	-70.17	6.50	3.30	324	80	24	98	230	66	169	7
126	4/12/2009	6:48:26	47.52	-70.06	12.60	3.20	28	76	80	99	244	17	125	7
127	5/22/2001	0:36:47	47.65	-69.92	10.86	3.10	228	54	54	98	99	49	129	7
128	5/14/2002	7:26:40	47.66	-69.97	14.08	3.10	148	72	126	98	261	40	29	7
129	6/12/2002	17:14:18	47.51	-70.02	7.78	3.10	164	48	86	96	350	42	94	7
130	5/5/2010	22:19:18	47.58	-70.09	19.12	3.10	262	30	118	100	50	64	75	6
131	9/27/2000	12:42:02	47.47	-70.04	8.12	3.00	50	58	116	90	187	40	55	7
132	10/31/2006	2:41:41	47.62	-70.18	14.37	3.00	202	36	88	99	24	54	91	6
133	10/7/2010	23:10:53	47.41	-70.33	13.96	3.00	118	40	322	99	239	67	237	5
134	8/17/2003	6:00:04	47.56	-70.04	8.50	2.90	2	38	66	99	211	56	108	7
135	1/15/2000	4:50:52	47.45	-70.23	24.05	2.80	302	48	40	92	183	61	130	7
136	6/10/2001	15:59:33	47.29	-70.21	16.75	2.80	46	74	40	90	303	52	159	6
137	8/8/2006	3:09:44	47.69	-70.01	19.42	2.80	210	22	78	95	43	69	95	6

138	6/20/2002	6:10:08	47.44	-70.05	7.27	2.70	164	42	78	96	360	49	101	7
139	6/9/2003	19:32:55	47.58	-69.92	17.06	2.70	156	52	52	95	28	52	128	7
140	6/8/2006	9:38:00	47.59	-69.98	7.89	2.70	46	66	116	90	176	35	45	7
141	12/25/2006	18:13:14	47.52	-70.02	14.80	2.70	174	56	38	99	60	59	139	7
142	10/18/2010	1:58:22	47.71	-69.96	24.36	2.70	214	28	60	100	67	66	105	6
143	1/10/2000	16:55:01	47.69	-69.88	14.61	2.60	354	46	32	98	241	68	131	5
144	1/19/2002	1:18:05	47.48	-70.11	22.93	2.60	154	62	70	99	12	34	123	7
145	12/18/2002	2:32:12	47.60	-69.97	15.75	2.60	176	68	302	98	297	38	217	6
146	10/24/2005	21:10:44	47.54	-70.27	13.19	2.60	254	42	110	99	48	51	73	6
147	4/28/2009	13:07:13	47.79	-69.89	19.39	2.60	104	70	182	98	13	88	340	5
148	7/3/2000	11:01:43	47.43	-70.16	11.56	2.50	194	48	30	95	83	68	134	7
149	8/16/2000	11:52:26	47.79	-69.93	15.71	2.50	252	12	94	99	68	78	89	5
150	9/8/2001	5:31:22	47.79	-69.86	23.04	2.50	66	74	86	98	260	16	104	5
151	6/18/2003	18:54:57	47.45	-70.07	9.59	2.50	162	78	74	95	36	20	142	6
152	12/19/2003	12:40:17	47.47	-70.13	12.94	2.50	20	72	78	99	235	22	123	6
153	2/3/2005	10:12:19	47.57	-70.23	6.48	2.50	240	38	140	98	3	67	59	7
154	8/31/2005	23:37:50	47.46	-70.13	14.80	2.50	32	48	104	99	192	44	75	6
155	11/14/2005	4:55:16	47.40	-70.19	6.73	2.50	206	30	118	98	354	64	75	7
156	2/4/2006	4:39:48	47.49	-69.98	7.17	2.50	222	54	106	98	16	39	69	7
157	8/17/2006	13:29:31	47.51	-70.30	10.80	2.50	160	22	50	99	22	73	105	7
158	2/20/2010	4:41:17	47.44	-70.39	6.31	2.50	290	64	352	93	24	83	206	6
159	8/11/2010	13:03:22	47.42	-70.31	12.90	2.50	242	38	198	100	138	79	307	5
160	4/17/2000	22:30:16	47.34	-70.20	15.80	2.40	280	20	42	98	150	77	105	7
161	6/21/2000	12:16:44	47.65	-69.91	13.10	2.40	150	76	84	93	353	15	113	6
162	12/1/2000	2:50:16	47.52	-70.21	13.29	2.40	228	38	104	98	30	53	79	6
163	12/4/2000	6:44:54	47.40	-70.17	10.30	2.40	238	22	100	98	47	68	86	6
164	10/26/2001	12:57:42	47.39	-70.11	17.51	2.40	162	42	52	95	28	58	119	7
165	12/5/2001	18:48:27	47.55	-70.25	9.21	2.40	32	68	92	99	207	22	85	7

166	11/24/2002	16:24:23	47.51	-69.96	12.28	2.40	124	28	68	96	329	64	101	6
167	12/21/2002	8:30:16	47.51	-70.21	13.47	2.40	238	26	102	99	45	65	84	7
168	8/25/2003	8:53:31	47.63	-69.94	15.47	2.40	128	36	342	99	233	80	235	5
169	11/20/2003	19:54:47	47.47	-70.11	11.04	2.40	208	28	86	98	33	62	92	6
170	2/4/2004	15:01:53	47.66	-70.12	6.52	2.40	130	66	14	99	34	77	155	6
171	4/25/2004	20:41:17	47.62	-70.18	12.49	2.40	318	76	84	97	161	15	113	7
172	12/15/2004	19:17:26	47.60	-70.03	26.64	2.40	258	22	34	98	136	78	109	7
173	10/3/2005	7:21:45	47.56	-70.01	14.67	2.40	264	54	26	96	158	69	141	7
174	6/9/2006	14:51:32	47.51	-70.19	18.14	2.40	264	12	136	99	37	82	81	7
175	11/1/2006	9:29:36	47.61	-70.17	13.85	2.40	150	58	66	99	10	39	123	6
176	3/12/2009	22:20:38	47.42	-70.33	12.20	2.40	344	66	158	97	83	70	26	6
177	7/23/2010	15:28:17	47.55	-70.25	13.08	2.40	274	46	124	98	50	53	60	6
178	9/30/2010	3:45:54	47.49	-70.14	7.70	2.40	66	90	170	98	156	80	0	5
179	1/2/2011	15:55:34	47.66	-69.81	11.65	2.40	32	74	140	98	135	52	21	7
180	8/16/2011	14:08:29	47.61	-70.07	18.67	2.40	18	38	128	99	153	61	64	6
181	3/14/2000	0:37:21	47.62	-69.89	14.75	2.30	132	38	38	95	10	68	122	6
182	4/29/2000	1:51:08	47.48	-70.14	21.75	2.30	46	58	126	92	172	47	47	7
183	11/3/2000	17:21:03	47.42	-70.06	11.56	2.30	262	34	158	98	11	78	58	5
184	12/12/2000	13:48:25	47.57	-70.20	16.00	2.30	290	12	138	100	61	82	81	5
185	8/19/2001	17:20:02	47.43	-70.16	12.10	2.30	58	50	120	98	196	48	59	7
186	10/25/2001	8:12:00	47.34	-70.20	23.60	2.30	296	56	46	97	176	53	136	7
187	10/26/2001	5:08:31	47.36	-70.23	12.94	2.30	88	46	134	93	214	59	54	6
188	1/15/2002	4:31:50	47.55	-70.03	8.47	2.30	224	84	190	99	133	80	354	6
189	10/5/2002	9:34:35	47.45	-70.39	21.93	2.30	6	40	66	99	216	54	109	7
190	12/5/2003	4:59:21	47.43	-70.13	8.56	2.30	318	70	84	98	155	21	106	7
191	8/9/2004	16:47:22	47.72	-69.87	17.25	2.30	322	46	346	98	62	80	225	5
192	8/6/2005	1:17:59	47.56	-70.06	11.22	2.30	42	36	232	93	266	62	294	6
193	9/15/2006	4:42:09	47.46	-70.03	10.61	2.30	2	60	154	97	106	68	33	7

194	11/26/2006	19:19:30	47.59	-69.94	11.68	2.30	254	58	282	85	52	34	252	7
195	7/3/2007	3:28:33	47.58	-70.24	7.09	2.30	140	48	56	91	5	52	122	7
196	7/25/2008	1:40:37	47.55	-69.92	14.20	2.30	14	38	70	95	219	55	105	6
197	9/14/2009	22:09:22	47.60	-70.10	24.43	2.30	100	40	114	98	250	54	71	7
198	12/1/2009	1:44:42	47.65	-69.87	14.37	2.30	126	40	100	95	293	51	82	7
199	12/5/2009	23:31:23	47.55	-70.03	13.40	2.30	210	18	74	99	47	73	95	7
200	2/27/2010	16:36:48	47.60	-70.15	14.45	2.30	234	36	250	97	78	56	284	5
201	2/9/2011	14:25:06	47.45	-70.37	6.93	2.30	16	68	178	99	107	88	22	6
202	6/20/2000	20:12:06	47.41	-70.09	8.52	2.20	30	26	20	89	282	81	115	6
203	3/6/2001	2:09:03	47.49	-70.08	7.91	2.20	218	24	108	99	18	67	82	6
204	5/3/2001	20:07:45	47.43	-70.16	11.28	2.20	40	56	110	99	187	39	63	6
205	7/10/2001	12:30:20	47.43	-70.06	18.05	2.20	334	36	40	99	210	68	119	7
206	11/9/2001	10:23:48	47.51	-69.96	7.16	2.20	6	28	92	96	184	62	89	5
207	2/25/2002	6:09:15	47.52	-70.19	17.36	2.20	264	34	130	99	39	65	67	7
208	10/23/2002	8:05:31	47.57	-70.04	10.52	2.20	188	44	78	99	24	47	101	6
209	8/21/2003	7:59:41	47.67	-69.90	9.46	2.20	8	30	86	95	193	60	92	6
210	5/20/2004	3:24:39	47.48	-70.06	6.82	2.20	340	54	70	98	192	41	115	7
211	6/12/2004	12:05:27	47.53	-70.03	14.17	2.20	30	54	82	99	223	37	101	6
212	7/5/2004	14:54:49	47.51	-69.95	9.65	2.20	230	86	132	93	324	42	6	6
213	9/15/2004	1:53:02	47.50	-70.06	11.97	2.20	188	20	80	98	19	70	94	5
214	1/24/2005	10:00:34	47.58	-69.96	10.82	2.20	148	22	146	94	270	78	71	6
215	10/4/2006	8:52:23	47.41	-70.34	18.56	2.20	220	40	160	99	326	77	52	7
216	1/24/2008	14:16:47	47.42	-70.11	9.75	2.20	36	68	74	98	253	27	124	7
217	3/12/2008	1:59:38	47.56	-69.98	15.91	2.20	46	68	82	100	247	23	109	6
218	4/8/2010	1:19:18	47.58	-70.00	7.65	2.20	50	54	92	86	227	36	87	5
219	5/18/2010	22:41:27	47.59	-69.89	16.25	2.20	160	22	54	99	18	72	103	5
220	5/25/2010	14:09:47	47.55	-70.16	19.45	2.20	50	58	142	100	162	59	38	6
221	6/19/2010	23:59:33	47.72	-69.77	27.45	2.20	162	80	58	100	56	33	162	4

222	11/11/2010	13:07:21	47.46	-70.14	9.77	2.20	324	30	40	99	198	71	114	7
223	2/13/2011	13:05:21	47.49	-70.20	17.48	2.20	154	24	80	95	345	66	94	7
224	4/17/2000	6:44:00	47.49	-70.09	14.28	2.10	164	64	60	92	37	39	136	5
225	1/31/2001	13:52:30	47.53	-70.13	14.90	2.10	270	30	106	98	72	61	81	7
226	2/15/2001	7:47:20	47.59	-69.98	9.85	2.10	32	42	114	99	181	52	70	6
227	4/28/2001	7:10:44	47.41	-70.30	13.40	2.10	10	66	132	99	124	47	34	5
228	6/6/2001	5:51:58	47.54	-70.11	10.54	2.10	334	84	144	98	68	54	7	7
229	7/27/2001	23:12:42	47.69	-69.86	14.41	2.10	170	10	70	100	10	81	93	5
230	9/20/2001	22:33:11	47.41	-70.08	21.60	2.10	52	46	124	98	188	53	60	6
231	10/20/2001	1:29:01	47.43	-70.30	15.43	2.10	198	66	112	98	333	32	50	6
232	12/24/2001	2:36:23	47.49	-70.16	15.08	2.10	38	58	128	92	162	48	45	7
233	2/13/2002	22:48:35	47.46	-70.05	12.32	2.10	222	10	116	98	16	81	86	6
234	2/15/2002	11:00:11	47.50	-70.04	11.87	2.10	190	86	130	98	285	40	6	6
235	4/19/2002	21:54:50	47.43	-70.17	9.80	2.10	216	28	76	95	52	63	97	6
236	10/16/2002	14:07:33	47.43	-70.38	6.48	2.10	34	48	58	99	257	51	120	5
237	12/24/2002	9:40:43	47.60	-69.96	9.50	2.10	260	34	136	90	29	67	64	6
238	8/5/2003	18:41:38	47.50	-70.01	16.11	2.10	22	46	138	98	144	61	52	5
239	9/5/2003	3:50:42	47.39	-70.25	9.49	2.10	288	22	358	99	20	89	248	4
240	9/14/2003	22:48:21	47.73	-69.76	20.83	2.10	52	50	82	99	244	41	99	6
241	2/2/2004	7:41:40	47.55	-70.25	13.90	2.10	254	40	106	90	53	52	77	7
242	5/7/2004	14:37:34	47.44	-70.03	10.13	2.10	24	32	78	97	218	59	97	5
243	10/6/2004	18:59:48	47.32	-70.15	7.46	2.10	236	40	116	99	24	55	70	5
244	10/13/2004	17:49:19	47.59	-70.13	25.17	2.10	240	26	98	99	51	64	86	6
245	11/9/2005	8:52:54	47.38	-70.14	14.84	2.10	266	36	72	98	108	56	103	7
246	1/15/2006	9:01:22	47.39	-70.29	15.14	2.10	300	22	132	97	76	74	75	5
247	2/6/2006	11:40:49	47.50	-69.99	6.69	2.10	224	54	132	98	347	53	47	6
248	11/2/2006	3:57:50	47.55	-70.17	17.26	2.10	40	64	94	99	211	26	82	6
249	9/22/2009	22:07:38	47.71	-69.93	25.68	2.10	152	54	60	99	16	46	125	4

250	3/1/2010	0:01:46	47.60	-70.18	10.60	2.10	36	82	136	99	134	47	11	5
251	8/13/2010	0:05:47	47.44	-70.30	13.92	2.10	304	34	84	100	131	56	94	5
252	8/31/2010	2:10:16	47.45	-70.34	14.17	2.10	2	64	76	99	212	29	116	5
253	11/5/2010	7:02:18	47.42	-70.29	15.07	2.10	108	88	4	99	18	86	178	6
254	7/5/2011	17:37:29	47.42	-70.10	7.92	2.10	198	72	284	99	339	23	233	6
255	8/15/2011	0:07:03	47.58	-70.00	9.82	2.10	34	34	162	96	139	80	57	5
256	2/24/2000	2:01:05	47.51	-70.04	12.06	2.00	214	28	118	99	3	66	76	6
257	2/24/2000	2:19:14	47.51	-70.04	12.08	2.00	172	18	64	96	19	74	98	6
258	3/8/2000	14:33:58	47.60	-69.94	12.23	2.00	162	68	114	98	292	32	45	5
259	6/19/2000	3:02:44	47.55	-70.05	13.96	2.00	14	48	74	99	217	44	107	6
260	10/19/2000	20:02:14	47.61	-69.97	9.40	2.00	244	54	100	99	47	37	77	4
261	6/22/2001	3:29:03	47.39	-70.13	16.04	2.00	314	22	98	97	125	68	87	5
262	12/2/2001	8:38:30	47.59	-70.05	24.92	2.00	150	56	88	98	334	34	93	6
263	1/19/2002	13:32:48	47.44	-70.04	14.73	2.00	202	72	110	96	332	27	44	6
264	8/22/2002	4:19:14	47.55	-70.22	17.23	2.00	228	18	282	96	35	72	266	6
265	11/25/2002	12:29:23	47.33	-70.17	12.74	2.00	20	50	100	98	185	41	78	5
266	11/27/2002	9:00:56	47.52	-70.07	12.90	2.00	184	30	112	99	339	62	78	6
267	6/17/2003	10:56:08	47.70	-70.07	11.76	2.00	62	62	76	97	270	31	114	6
268	6/20/2003	11:21:04	47.69	-70.08	12.55	2.00	30	26	168	100	131	85	64	5
269	11/8/2003	10:50:06	47.65	-69.94	16.29	2.00	142	36	42	99	16	67	118	6
270	2/13/2004	2:22:18	47.44	-70.39	6.89	2.00	174	20	68	98	17	72	98	7
271	4/24/2004	21:30:36	47.40	-70.31	16.40	2.00	22	48	266	95	208	42	274	4
272	6/30/2004	12:07:23	47.55	-70.17	18.00	2.00	36	88	84	99	288	6	162	7
273	8/19/2004	21:51:37	47.43	-70.38	12.57	2.00	202	34	112	100	356	59	76	5
274	11/19/2004	20:44:06	47.58	-69.91	13.09	2.00	174	30	28	97	59	76	117	5
275	11/27/2004	12:45:31	47.62	-70.01	27.09	2.00	128	36	80	92	320	55	97	6
276	12/10/2004	21:36:41	47.62	-69.99	7.98	2.00	180	44	114	98	328	51	69	6
277	3/28/2005	23:50:17	47.58	-70.13	18.66	2.00	198	32	76	99	34	59	99	7

278	6/5/2005	9:22:12	47.63	-69.98	27.07	2.00	218	64	56	99	95	42	139	7
279	11/1/2005	23:56:04	47.55	-70.16	18.70	2.00	148	50	108	99	301	43	70	5
280	11/9/2005	5:02:11	47.49	-70.13	8.55	2.00	26	80	70	100	270	22	153	4
281	12/22/2005	20:21:39	47.59	-69.90	14.22	2.00	260	44	144	94	18	66	52	6
282	4/7/2006	2:35:15	47.52	-70.21	14.42	2.00	226	34	116	98	16	60	74	6
283	8/12/2006	0:33:21	47.44	-70.12	13.19	2.00	52	50	98	99	220	41	81	7
284	1/9/2007	17:06:58	47.39	-70.23	12.79	2.00	332	18	94	97	148	72	89	6
285	1/15/2007	8:36:22	47.55	-70.15	22.86	2.00	210	52	116	99	352	45	61	6
286	8/17/2009	6:30:23	47.69	-70.05	10.89	2.00	262	54	158	99	5	72	38	5
287	9/9/2009	18:05:50	47.78	-69.82	21.66	2.00	116	46	124	99	252	53	60	6
288	2/20/2010	16:46:48	47.72	-69.92	25.50	2.00	174	56	68	100	30	40	119	4
289	3/6/2010	19:03:25	47.48	-70.14	14.52	2.00	272	34	130	99	47	65	67	5
290	5/7/2010	21:23:12	47.43	-70.33	19.40	2.00	308	60	202	98	207	71	328	5
291	11/5/2010	10:41:58	47.66	-69.81	20.97	2.00	234	34	104	99	37	57	81	4
292	12/4/2010	4:37:42	47.66	-69.83	18.33	2.00	264	40	114	91	54	54	71	5
293	1/10/2011	18:31:03	47.57	-69.90	15.32	2.00	240	48	112	97	29	46	67	6
294	5/3/2011	8:13:04	47.66	-70.10	11.97	2.00	250	26	138	99	19	73	70	6
295	7/11/2013	20:16:07	47.81	-70.06	14.52	4.00	26	56	108	99	176	38	65	6
296	7/29/2016	19:55:21	47.43	-70.11	18.27	3.00	186	10	58	98	38	82	95	7
297	8/2/2014	18:38:40	47.58	-70.18	13.80	3.00	140	56	64	99	1	42	123	6
298	4/29/2020	18:43:12	47.25	-70.25	17.54	2.90	192	36	62	99	45	59	109	6
299	3/25/2012	11:30:49	47.26	-70.27	24.05	2.90	276	42	46	98	148	61	122	6
300	7/12/2015	4:17:38	47.46	-70.07	10.57	2.80	26	38	100	99	193	53	82	5
301	7/11/2013	20:58:10	47.81	-70.06	14.47	2.80	4	46	98	96	173	45	82	6
302	5/12/2016	23:31:10	47.53	-70.05	18.84	2.70	44	50	100	99	209	41	78	7
303	11/15/2013	0:13:33	47.62	-69.83	16.39	2.70	120	16	248	99	323	75	276	6
304	9/5/2015	7:01:17	47.69	-70.07	15.91	2.70	314	44	44	97	189	61	125	5
305	8/1/2019	17:12:19	47.33	-70.35	10.51	2.60	124	4	90	94	304	86	90	7

306	5/1/2019	17:04:35	47.29	-70.29	10.43	2.60	196	10	288	98	358	80	267	7
307	9/20/2016	15:12:06	47.80	-69.84	23.39	2.60	300	64	56	98	177	42	139	7
308	5/28/2016	12:10:38	47.56	-70.07	23.83	2.60	332	28	56	100	189	67	107	7
309	6/17/2015	11:12:51	47.37	-70.26	9.34	2.60	264	44	56	99	127	55	118	6
310	1/14/2014	19:23:04	47.57	-70.00	12.45	2.60	28	46	278	99	197	45	262	6
311	2/28/2014	20:28:36	47.49	-70.03	8.38	2.60	8	60	112	98	149	37	57	7
312	10/5/2019	15:51:41	47.69	-69.86	12.88	2.50	20	56	120	96	154	44	53	7
313	2/3/2019	21:53:55	47.80	-69.92	18.33	2.50	244	32	114	99	36	61	76	6
314	5/22/2018	8:52:01	47.79	-69.70	21.18	2.50	316	24	140	95	83	75	71	5
315	5/23/2017	21:20:24	47.41	-70.27	10.44	2.50	178	64	148	98	283	62	30	7
316	3/25/2017	8:36:59	47.47	-70.12	12.70	2.50	34	38	104	99	196	53	79	7
317	10/27/2016	23:26:03	47.49	-70.03	14.04	2.50	238	32	126	98	17	65	70	6
318	2/16/2016	5:13:40	47.57	-69.97	13.42	2.50	260	52	88	97	83	38	93	7
319	2/4/2016	12:38:28	47.24	-70.36	8.24	2.50	196	30	226	88	64	69	292	5
320	7/3/2014	15:02:06	47.57	-69.85	12.57	2.50	0	58	98	97	165	33	77	6
321	10/9/2013	19:24:12	47.55	-70.03	0.72	2.50	176	76	8	96	84	82	166	6
322	10/4/2013	13:13:02	47.65	-69.90	11.81	2.50	36	46	106	92	194	46	74	7
323	9/2/2013	5:15:15	47.79	-69.84	24.61	2.50	8	30	116	99	159	63	76	5
324	5/15/2012	4:41:26	47.40	-70.38	8.29	2.50	132	70	44	99	24	49	153	7
325	3/23/2019	7:57:10	47.46	-70.05	8.08	2.40	150	22	64	98	358	70	100	5
326	2/7/2019	2:23:51	47.71	-70.07	8.38	2.40	222	18	80	99	53	72	93	7
327	9/11/2018	4:26:01	47.72	-69.93	24.64	2.40	14	38	102	99	179	53	81	6
328	6/18/2018	13:15:02	47.47	-69.98	13.16	2.40	228	34	102	96	34	57	82	6
329	5/6/2018	7:59:37	47.39	-70.13	15.67	2.40	58	32	144	96	180	72	63	6
330	6/25/2017	13:28:50	47.60	-70.18	3.13	2.40	140	76	204	98	44	67	345	7
331	11/20/2016	14:20:14	47.48	-70.09	13.19	2.40	260	22	82	99	89	68	93	7
332	10/31/2015	4:18:20	47.39	-70.12	15.61	2.40	312	36	136	97	80	66	62	7
333	9/26/2014	2:36:35	47.23	-70.38	8.84	2.40	292	76	72	94	165	23	141	4

334	3/22/2014	4:54:02	47.24	-70.59	5.95	2.40	222	48	98	99	30	43	81	6
335	2/24/2013	15:52:29	47.40	-70.44	6.42	2.40	18	18	226	89	243	77	283	6
336	11/29/2012	19:20:38	47.79	-69.96	19.93	2.40	254	28	110	99	52	64	80	5
337	6/18/2012	9:37:54	47.58	-70.18	11.89	2.40	144	40	6	98	49	86	130	7
338	7/16/2013	5:04:02	47.81	-70.05	14.56	2.40	48	28	112	99	203	64	79	6
339	8/8/2020	1:22:58	47.51	-70.07	11.37	2.30	14	88	72	98	278	18	174	7
340	1/22/2020	4:36:59	47.65	-69.90	12.41	2.30	16	38	74	91	216	54	102	7
341	7/31/2019	23:36:30	47.85	-69.95	21.46	2.30	54	62	112	100	193	35	55	6
342	6/8/2019	22:41:09	47.76	-69.94	21.81	2.30	294	40	158	99	41	76	52	7
343	4/19/2019	8:48:02	47.32	-70.19	17.32	2.30	208	38	92	99	25	52	88	6
344	1/9/2019	10:07:31	47.39	-70.13	15.50	2.30	112	10	268	96	294	80	270	7
345	6/5/2018	3:30:05	47.42	-70.42	5.60	2.30	342	30	106	99	144	61	81	5
346	12/8/2016	22:39:46	47.55	-70.24	12.16	2.30	262	24	118	99	52	69	78	6
347	8/20/2016	19:53:40	47.59	-70.37	16.15	2.30	102	52	54	99	332	50	127	4
348	11/11/2015	14:49:20	47.78	-70.13	12.16	2.30	8	32	86	100	193	58	92	6
349	5/2/2015	6:43:51	47.48	-70.30	12.52	2.30	24	68	204	99	285	68	336	5
350	1/25/2015	10:01:31	47.59	-70.18	5.34	2.30	234	18	80	90	65	72	93	6
351	1/1/2015	16:40:01	47.48	-70.14	19.28	2.30	320	84	42	97	225	48	172	7
352	3/28/2014	8:58:55	47.52	-70.14	16.94	2.30	18	50	90	90	198	40	90	7
353	4/9/2013	20:14:11	47.81	-69.81	23.38	2.30	10	50	62	99	230	47	119	5
354	9/12/2012	9:55:08	47.59	-70.17	8.69	2.30	152	40	28	98	40	72	127	7
355	2/11/2012	2:57:37	47.70	-70.02	16.94	2.30	180	32	56	96	38	64	109	7
356	7/11/2013	21:00:29	47.81	-70.06	14.31	2.30	52	72	102	99	197	22	57	5
357	10/28/2019	0:48:29	47.82	-69.76	23.54	2.20	252	34	114	98	44	59	75	5
358	2/18/2019	6:39:04	47.80	-69.91	18.83	2.20	238	46	110	90	30	47	70	6
359	1/14/2019	8:09:42	47.82	-70.03	8.11	2.20	12	80	80	99	237	14	135	7
360	3/8/2018	7:40:07	47.61	-70.17	13.82	2.20	260	40	130	99	32	61	62	7
361	10/6/2017	2:21:28	47.60	-70.23	10.64	2.20	36	50	72	98	243	43	110	5

362	9/1/2017	21:23:45	47.44	-70.14	15.16	2.20	252	46	114	100	39	49	67	5
363	3/18/2017	10:07:21	47.74	-70.00	14.79	2.20	154	46	18	99	51	77	135	7
364	12/5/2016	17:29:31	47.34	-70.16	19.74	2.20	296	48	80	92	131	43	101	6
365	10/31/2016	0:30:14	47.59	-70.00	7.68	2.20	26	36	100	99	194	55	83	6
366	10/17/2016	22:49:32	47.39	-70.11	16.73	2.20	40	70	56	98	283	39	147	5
367	10/10/2016	22:10:19	47.61	-69.93	10.64	2.20	194	30	70	99	37	62	101	5
368	9/23/2016	15:01:58	47.62	-70.13	13.51	2.20	36	56	66	99	255	41	121	7
369	7/31/2016	22:06:11	47.48	-70.14	19.81	2.20	234	16	110	99	33	75	84	7
370	7/4/2016	9:04:32	47.42	-70.07	15.02	2.20	32	36	110	98	188	56	76	6
371	6/19/2015	21:41:09	47.78	-69.98	24.66	2.20	296	54	118	99	74	44	57	6
372	6/16/2015	14:35:26	47.47	-70.11	7.55	2.20	278	46	136	98	42	60	53	5
373	11/23/2014	15:28:53	47.39	-70.45	13.98	2.20	58	32	114	91	210	61	76	7
374	10/26/2014	17:03:54	47.83	-69.81	23.89	2.20	12	52	162	100	113	76	39	4
375	5/20/2014	21:01:04	47.75	-69.86	20.96	2.20	22	38	128	99	157	61	64	6
376	2/28/2014	4:20:32	47.39	-70.25	11.92	2.20	90	16	110	98	249	75	84	6
377	11/6/2013	22:12:01	47.42	-70.41	5.83	2.20	300	52	48	99	176	54	131	7
378	5/29/2013	12:50:23	47.78	-70.05	3.60	2.20	10	12	242	100	219	79	276	4
379	5/5/2013	14:31:35	47.54	-69.94	12.67	2.20	16	38	78	99	211	53	99	6
380	2/28/2013	13:04:48	47.36	-70.18	12.56	2.20	34	42	108	98	190	50	74	5
381	4/11/2012	8:07:37	47.51	-70.05	9.36	2.20	0	64	112	99	137	34	52	5
382	7/22/2013	0:26:46	47.53	-70.37	10.50	2.20	206	22	68	99	50	70	99	6
383	5/26/2014	0:29:41	47.68	-70.20	5.96	2.20	198	16	88	97	20	74	91	6
384	10/7/2014	0:52:51	47.58	-70.21	6.55	2.20	98	54	18	98	357	76	143	7
385	3/12/2014	10:36:17	47.48	-70.34	4.43	2.20	280	40	140	98	43	66	57	5
386	5/13/2020	9:16:13	47.39	-70.13	17.22	2.10	138	52	110	91	287	42	66	5
387	2/18/2019	4:18:34	47.48	-70.20	11.50	2.10	226	44	154	98	335	72	49	6
388	2/5/2019	6:52:14	47.60	-69.95	10.85	2.10	340	14	48	98	203	80	99	6
389	9/20/2018	13:18:11	47.46	-70.05	11.26	2.10	40	26	322	99	165	74	249	5

390	9/9/2018	21:44:14	47.47	-70.10	15.23	2.10	42	60	86	94	230	30	97	7
391	5/26/2018	14:12:41	47.64	-69.87	8.75	2.10	298	80	110	94	54	22	27	4
392	4/25/2018	23:36:01	47.47	-70.06	14.43	2.10	220	32	82	99	49	58	95	6
393	3/2/2018	7:14:26	47.64	-69.91	11.82	2.10	94	26	236	97	311	69	285	5
394	10/25/2017	13:04:04	47.28	-70.38	8.14	2.10	16	42	124	100	154	56	63	4
395	8/28/2017	11:54:08	47.49	-70.09	13.17	2.10	232	54	88	100	55	36	93	5
396	7/24/2017	9:35:59	47.62	-70.22	11.22	2.10	122	40	140	99	245	66	57	7
397	3/9/2017	6:49:52	47.41	-70.08	6.53	2.10	218	32	132	97	351	67	67	6
398	10/30/2016	23:02:10	47.59	-70.00	7.71	2.10	212	44	96	99	24	46	84	5
399	10/15/2016	17:17:19	47.45	-70.34	13.86	2.10	306	42	54	99	170	57	118	6
400	9/25/2016	11:20:11	47.58	-70.19	12.00	2.10	232	76	280	99	16	17	235	6
401	7/13/2016	20:00:35	47.53	-70.14	12.65	2.10	38	8	276	100	212	82	269	6
402	5/4/2016	14:39:28	47.49	-69.99	11.46	2.10	174	20	58	99	28	73	101	6
403	2/16/2016	7:58:43	47.56	-69.97	13.42	2.10	62	40	78	98	258	51	100	7
404	2/15/2016	16:13:43	47.47	-70.00	11.78	2.10	36	28	118	97	185	66	76	6
405	12/20/2015	21:25:04	47.41	-70.14	10.42	2.10	16	78	36	97	277	55	165	4
406	12/1/2014	21:03:13	47.78	-69.83	20.64	2.10	268	56	40	97	153	58	139	6
407	8/31/2014	10:33:04	47.38	-70.50	5.95	2.10	266	46	32	95	153	68	131	7
408	1/22/2014	4:02:22	47.47	-70.10	8.56	2.10	316	40	110	98	111	53	74	5
409	1/31/2013	19:34:02	47.77	-70.11	9.75	2.10	230	28	106	97	32	63	82	5
410	6/30/2012	17:29:20	47.72	-70.12	9.04	2.10	272	24	84	99	99	66	93	6
411	9/11/2020	12:43:26	47.60	-70.01	9.13	2.00	272	76	130	92	18	42	21	7
412	4/2/2020	5:44:22	47.88	-70.26	20.66	2.00	36	44	66	98	248	51	111	7
413	2/9/2020	3:55:15	47.69	-69.80	22.78	2.00	262	64	120	92	29	39	44	6
414	12/17/2019	19:24:51	47.54	-70.01	6.08	2.00	86	58	202	99	344	71	326	4
415	12/13/2019	23:00:20	47.51	-69.96	9.09	2.00	18	42	104	96	179	50	78	5
416	9/1/2019	4:38:51	47.29	-70.36	3.57	2.00	176	16	168	99	278	87	74	5
417	7/29/2019	9:50:55	47.81	-69.82	21.86	2.00	14	32	98	98	185	58	85	7

418	11/18/2018	18:21:27	47.39	-70.26	10.93	2.00	272	24	54	98	130	71	105	6
419	9/22/2018	18:52:05	47.78	-70.03	7.48	2.00	140	16	14	99	37	86	106	6
420	8/16/2018	23:26:48	47.71	-70.12	6.64	2.00	170	64	146	98	276	60	30	6
421	4/8/2018	9:12:06	47.50	-70.16	14.91	2.00	268	28	154	99	21	78	64	7
422	3/23/2018	6:47:38	47.45	-70.06	6.83	2.00	160	20	48	90	24	75	104	6
423	3/15/2018	15:22:00	47.44	-70.13	11.87	2.00	184	84	310	99	281	40	189	7
424	8/28/2017	11:55:24	47.58	-70.41	20.56	2.00	208	22	94	98	24	68	88	5
425	2/24/2017	0:40:30	47.31	-70.52	14.19	2.00	172	4	28	99	54	88	94	5
426	6/6/2016	21:23:40	47.80	-69.96	24.00	2.00	242	32	120	98	28	63	73	5
427	5/26/2016	13:26:38	47.64	-69.91	11.96	2.00	60	70	72	94	284	27	130	7
428	4/16/2016	0:44:56	47.54	-70.25	13.44	2.00	20	42	126	99	156	57	62	7
429	8/26/2015	21:43:25	47.76	-69.78	26.79	2.00	240	48	54	100	107	53	123	4
430	7/21/2015	2:44:57	47.44	-70.12	22.02	2.00	236	32	66	99	84	61	104	6
431	4/27/2015	19:35:38	47.46	-70.16	22.22	2.00	182	46	56	97	46	53	120	4
432	4/9/2015	21:18:29	47.46	-70.03	10.71	2.00	34	30	114	87	187	63	77	6
433	2/7/2015	18:59:07	47.73	-70.13	8.02	2.00	328	60	128	100	91	47	43	5
434	2/3/2015	6:21:11	47.56	-70.27	9.68	2.00	270	52	52	99	142	52	128	6
435	1/22/2015	23:04:42	47.70	-69.91	7.46	2.00	176	68	76	98	30	26	121	5
436	11/1/2014	2:29:20	47.68	-70.03	22.58	2.00	176	32	56	98	34	64	109	6
437	8/2/2014	21:49:03	47.60	-70.27	2.55	2.00	332	42	72	99	176	50	106	6
438	6/27/2014	18:05:43	47.54	-69.98	15.08	2.00	228	40	116	99	16	55	70	6
439	4/22/2014	5:26:33	47.40	-70.28	15.88	2.00	66	38	326	96	184	70	237	5
440	4/7/2014	2:33:00	47.47	-70.08	11.18	2.00	308	32	78	93	142	59	97	7
441	3/27/2014	14:33:05	47.67	-69.90	13.94	2.00	252	28	108	99	52	63	81	5
442	3/19/2014	7:17:54	47.61	-69.92	11.51	2.00	20	48	66	100	234	47	114	6
443	2/20/2014	17:28:06	47.55	-69.98	9.43	2.00	136	58	80	97	334	33	106	7
444	10/31/2013	16:42:02	47.75	-70.00	6.25	2.00	132	60	268	92	316	30	273	4
445	10/12/2013	0:16:04	47.64	-70.11	11.59	2.00	78	30	134	99	210	69	68	4

446	8/23/2013	11:55:07	47.59	-69.89	15.34	2.00	204	26	88	100	26	64	91	5
447	8/11/2013	15:20:28	47.66	-69.87	13.25	2.00	34	14	272	98	212	76	270	5
448	7/23/2013	13:36:41	47.43	-70.06	9.06	2.00	210	18	112	98	7	73	83	3
449	5/18/2013	12:28:54	47.46	-70.05	7.78	2.00	222	24	110	98	20	68	81	4
450	5/10/2013	1:19:14	47.83	-70.03	23.26	2.00	18	66	96	99	184	25	77	5
451	10/13/2012	21:22:45	47.82	-69.96	21.18	2.00	258	30	132	90	32	68	69	6
452	9/26/2012	8:17:06	47.52	-70.13	19.95	2.00	216	50	64	100	73	46	118	6
453	9/15/2012	23:10:39	47.51	-70.05	10.64	2.00	44	84	102	99	160	13	27	6
454	8/10/2012	9:27:30	47.31	-70.39	8.69	2.00	0	36	70	99	204	56	104	4
455	8/4/2012	6:29:21	47.44	-70.34	8.38	2.00	262	72	40	99	157	52	157	4
456	1/31/2012	7:21:09	47.52	-69.95	9.68	2.00	258	26	116	98	50	67	78	5

Fault Geometry for the Charlevoix Seismic Zone

Oluwaseun Idowu Fadugba¹, Charles A. Langston¹ and Christine A. Powell¹

¹Center for Earthquake Research and Information, The University of Memphis, Memphis, TN 38152.

Submitted to
Journal of Geophysical Research: Solid Earth

Key Points

- We apply a modified version of the OADC algorithm to model fault geometry for the CSZ.
- Our fault model shows dips of 65°, 39° and 47°SE for the three-fault system, from north to south, respectively, near the impact structure.
- The dips of the three-faults system change to 65°, 69° and 64° dipping fault geometry in the NE end of the CSZ.

Abstract

We apply a modified version of the Optimal Anisotropic Dynamic Clustering (OADC) algorithm to model realistic but simplified fault geometry for the Charlevoix Seismic Zone (CSZ). The CSZ is located along the Late Proterozoic-Early Cambrian St. Lawrence rift zone in southeastern Quebec at the location of a major Devonian impact structure. The impact structure is superimposed on three major rift faults trending approximately N35°E. Previous work suggests two sets of geometries for the rift faults. One set has a uniform dip of 70°SE for all three faults while the other has 65°, 40°, and 40°SE, from north to south, respectively. Visual estimation of fault planes from over 1600 relocated hypocenters in the CSZ suggests more complex fault geometry. We remove diffuse hypocenters from the catalog by examining the cumulative probability density function of tetrahedra volumes defined by closest neighbor events. We extend the OADC method by incorporating focal mechanisms to specify seed planes rather than using randomly seeded planes. Our fault model shows a 65°-39°-47° dipping fault system in the CSZ near the impact but changes to a 65°-69°-64° dipping fault geometry in the NE end of the CSZ. Our model also shows the geometry of some bounding faults associated with the damage zone of the impact structure. This study presents a realistic but simplified fault geometry of the CSZ and suggests a combination of the two fault geometries found in previous studies.

Plain Language Summary

We used the locations of well-located local earthquakes to determine possible fault planes within the Charlevoix Seismic Zone (CSZ). This was done by detecting clusters of earthquakes that could be represented by a single planar feature. A progressive and random process of testing candidate fault planes was initiated using a computer algorithm called Optimal Anisotropic Dynamic Clustering that we modified to include information about fault geometry from well-studied individual earthquakes. We created a large number of fault network models from the data. Common features of these models included near-vertical faults on the northwestern edge of the CSZ changing to faults that dip more gradually to the southeast. Irregular fault orientations are observed within the Malbaie impact structure suggesting that faulting is related to impact damage

to the crust. The size and extent of faults within the CSZ support the possibility of future large earthquakes of M7.2.

1.0 Introduction

The Charlevoix Seismic Zone (CSZ) is located along the Late Proterozoic-Early Cambrian St. Lawrence rift zone in southeastern Quebec at a major Devonian impact structure (Fig. 1; Rondot, 1994). The CSZ is the most active seismic zone in southeastern Canada (e.g., Anglin, 1984), and it poses a high risk to the surrounding region due to its history of generating large (M4+) earthquakes compared to the other seismic zones in the area and its proximity to densely

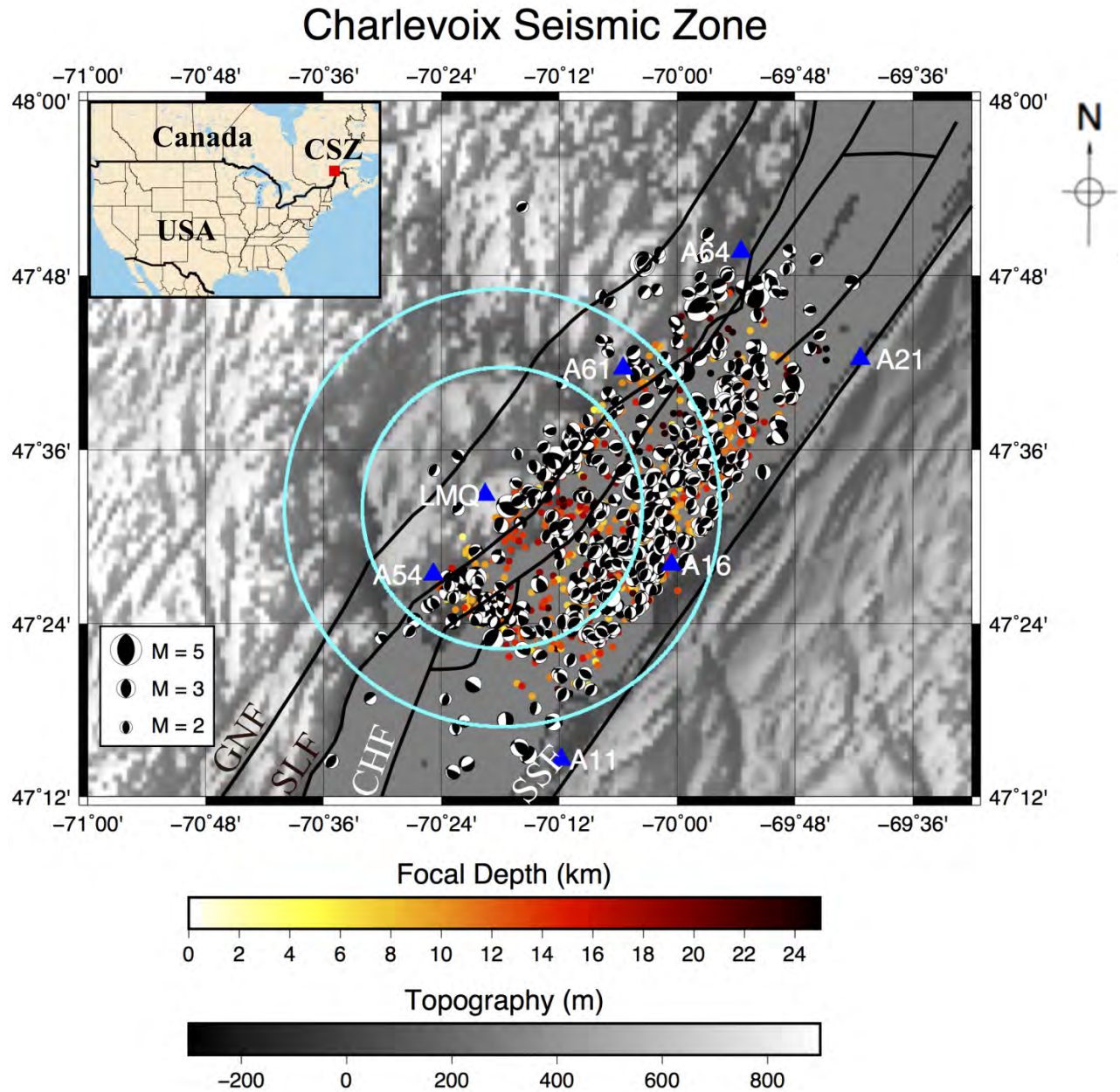


Figure 1: Topography and seismicity of the Charlevoix Seismic Zone (CSZ), locations of the impact structure (outer cyan circle), the more damaged inner impact structure (inner cyan circle), and the seismic stations (blue triangles). Small circles are the relocated epicenters for the years 1988–2020 from Powell & Lamontagne (2017) and additional relocated earthquakes, and their colors represent the focal depths. The focal mechanisms are from Fadugba et al. (2021). Solid black lines mark the rift faults known in the region: GNF, Gouffre Northwest fault; SLF, Saint-Laurent fault; CHF, Charlevoix fault; and SSF, South Shore fault (Lamontagne, 1999; Rondot, 1971). The inset shows the location of the CSZ in eastern Canada. The original earthquake data set is from the National Resources Canada catalog for the years 1988–2020.

populated cities (e.g., Quebec City, Ottawa, and Montreal).

The CSZ geologic structure was formed by a series of tectonic events including the Grenville orogeny (1100-990 Ma) reflected in amphibolite to granulite facies metamorphic basement rocks (Rondot, 1971, 1994; Anglin, 1984). The Grenville orogeny was followed by the breakup of the basement terrains by major rift faults trending approximately N35°E to form the Iapetus Ocean and then the Appalachian orogeny by the closing of the Iapetus ocean. The CSZ is located along a set of three rift-parallel faults, inboard from the rifted continental margin (Thomas and Powell, 2017). An impact structure was superimposed on the three major basement faults in the Devonian (Rondot, 1971; Anglin, 1984).

The three major rift faults in the CSZ are the Gouffre Northwest fault, Saint-Laurent fault, and Charlevoix fault (Fig. 1; Powell and Lamontagne, 2017; Fadugba et al., 2019). Previous studies suggest two sets of geometries for the rift faults in the CSZ. One set has a uniform dip of 70°SE for all three faults (e.g., Baird et al., 2010), while the second set has dips of 65°, 40°, and 40°SE, from north to south, respectively (Powell and Lamontagne, 2017). Visual estimation of fault planes from over 1600 relocated hypocenters in the CSZ (Powell and Lamontagne, 2017) suggests a more complex fault geometry.

Powell and Lamontagne (2017) determined three-dimensional (3-D) Vp and Vs velocity models of the CSZ and relocated the local earthquakes using the 3-D velocity model. Visual estimation of the epicenters in the CSZ shows two major earthquake clusters: the northwestern (NW) and southeastern (SE) clusters. The NW cluster has earthquakes on the Gouffre Northwest fault and in the impact structure region, while the SE cluster comprises the earthquakes on the Saint-Laurent and Charlevoix faults and the impact structure (Fig. 1). Powell and Lamontagne (2017) observed circular arcs of seismicity that follow the edge of the impact structure and a mid-crustal high-velocity body in the seismic zone, similar to the high-velocity body imaged by Vlahovic et al. (2003).

Earlier studies noted an asymmetry in the magnitude distribution of the earthquakes and stress rotations in the CSZ (e.g., Zoback, 1992; Mazzotti and Townend, 2010). The M4+ earthquakes in the CSZ are concentrated outside of the impact structure, on the major rift faults, while the earthquakes with $m_N \leq 3$ are generally concentrated on the rift faults within and beneath the impact structure (Lamontagne, 1999; Baird et al., 2010; Anglin, 1984). Numerical stress modeling gives insight into the earthquake distribution and stress rotation in the CSZ (e.g., Baird et al., 2010; Fadugba et al., 2019). However, numerical stress models require a realistic fault geometry due to the sensitivity of the stress model to fault structure. Fadugba et al. (2019) used the two fault geometries mentioned above to model the stress state of the CSZ and suggested along-strike variations in the dip angles of the rift faults.

Pattern recognition algorithms have been used to determine fault planes from clouds of hypocenters (e.g., Ouillon et al., 2008; Hardebeck, 2013; Wang et al., 2013). For example, Ouillon et al. (2008) developed the Optimal Anisotropic Dynamic Clustering (OADC) analysis technique to delineate fault planes within the aftershocks of the Parkfield earthquake sequences. The OADC method is a pattern recognition method that reconstructs fault networks using the covariance of the spatial distribution of earthquakes from seismic catalogs. Wang et al. (2013) extended the OADC method to develop Anisotropic Clustering of Location Uncertainty Distributions (ACLU) by incorporating some validation steps to give the best agreement between the derived fault planes and the observed focal mechanisms. They also incorporated the uncertainty in the location of each hypocenter instead of the uniform allowable cloud thickness assumed in Ouillon et al. (2008). Ouillon and Sornette (2011) used the Gaussian kernel in an Expectation-Maximization algorithm

to identify fault planes in intersecting clouds of seismicity, hence intersecting fault planes.

In this study, we used the relocated earthquakes of Powell and Lamontagne (2017) in the CSZ from 1988-1999 and additional relocated earthquakes ($M \geq 2$) from 2000-2020 to determine realistic but simplified fault geometries using a modified version of the OADC algorithm. Among other modifications (discussed in section 2.2), we incorporated available focal mechanisms of relocated earthquakes (Fadugba et al., 2021) to determine focal mechanism seeded planes rather than randomly seeded planes in the original OADC algorithm. We also set a minimum dip angle for the faults to address the limitation of OADC in generating subhorizontal fault planes.

Our first hypothesis is that modern seismicity in the CSZ illuminates active faults, and seismicity can be used to determine fault geometries and the interconnectivity of the complex fault system. The second hypothesis is that earthquake source mechanisms and seismicity clusters define coherent fault surfaces if modern earthquakes occur on active faults (Powell and Lamontagne, 2017). The derived fault geometry from this study will be incorporated in future geodynamic models to revise numerical simulations that investigate the observed stress variations in the CSZ. The interconnectivity of these faults is important for seismic hazard analyses to estimate the maximum magnitude earthquake in the CSZ (Harris et al., 1991; Harris and Day, 1993).

2.0 Materials and Methods

We use a total of 1669 relocated earthquakes in this study: 1329 relocated hypocenters determined by Powell and Lamontagne (2017) and an additional 340 relocated earthquakes ($M \geq 2$). Despite the high precision in the hypocenter location, the seismicity shows unclustered hypocenters, probably due to the damaged crustal rocks in the impact structure (Fig. 1).

We determine fault models of the CSZ using several steps. We first perform declustering analysis on the relocated hypocenters using the cumulative tetrahedra volume method of Ouillon and Sornette (2011) to highlight the rift faults by separating clustered and diffuse seismicity. We then apply a modified version of the OADC algorithm on the clustered seismicity to generate realistic fault planes (Ouillon et al., 2008). We create several fault models by running the OADC model using different random-number generator seeds and determine the distribution of the strike and dip angles of the faults in all the fault models to generate a unified fault model for the CSZ. In instances where the cluster exceeds the allowable thickness, we split the cluster using focal mechanism seeded planes.

2.1 Declustering Analyses

We determine the volume (V) of tetrahedra formed with quadruplets of nearest neighbor events for each hypocenter for both observed (V) and randomized (V_0) catalogs using equation 1 (Ouillon and Sornette, 2011).

$$V = \frac{1}{6} \times \begin{vmatrix} x_1 & y_1 & z_1 & 1 \\ x_2 & y_2 & z_2 & 1 \\ x_3 & y_3 & z_3 & 1 \\ x_4 & y_4 & z_4 & 1 \end{vmatrix} \dots\dots\dots (1)$$

where x_i , y_i and z_i are the coordinates of the i^{th} hypocenters of the tetrahedra ($i = 1, 2, 3$ and 4). The x_1 , y_1 and z_1 are the coordinates of the object earthquake.

We then determine the cumulative distributions of the volumes of the observed and randomized catalogs, i.e., $N(V)$ and $N_0(V_0)$, and separate the diffuse earthquakes from the observed earthquakes by removing all hypocenters in the observed catalog with volumes above a certain volume threshold (V_{thresh}), noting that the calculated tetrahedra volume for clustered

earthquakes is generally less than the tetrahedra volume for diffuse earthquakes. Following Ouillon and Sornette (2011), we assume that the 5% quantile (i.e., probability of 0.05) of the volume distribution of the randomized catalog corresponds to V_{thresh} and can be used to model the diffuse earthquakes expected for the CSZ. We remove all hypocenters in the observed catalog with $V > V_{\text{thresh}}$ to determine a clustered subset of the observed earthquakes. The resulting clustered earthquakes will be used as input to a modified version of the OADC algorithm to generate a fault geometry model for the CSZ.

2.2 Modified OADC Algorithm

The OADC method is a generalization of the k-means method to iteratively partition hypocenters into planar clusters that minimize the global variance (Ouillon et al., 2008). The algorithm determines the associated fault planes for each cluster using principal component analyses to generate optimal fault geometries for the dataset. We give a brief description of the technique here, but readers are referred to Ouillon et al. (2008) for further description with synthetic tests.

According to Ouillon et al. (2008), the hypocenters are partitioned into different clusters based on their proximity to the initial random fault(s). Eigenvalue-eigenvector analysis of the covariance matrix (C , equation 2) of each cluster is used to determine the eigenvalues ($\lambda_1^2 \geq \lambda_2^2 \geq \lambda_3^2$) and associated eigenvectors.

$$\text{Covariance matrix, } C = \begin{pmatrix} \sigma_x^2 & \text{cov}(x, y) & \text{cov}(x, z) \\ \text{cov}(x, y) & \sigma_y^2 & \text{cov}(y, z) \\ \text{cov}(x, z) & \text{cov}(y, z) & \sigma_z^2 \end{pmatrix} \dots\dots\dots (2)$$

Under the assumption that earthquakes are uniformly distributed over a fault plane, Ouillon et al., (2008) estimated the length (L) and width (W) of the fault plane using $\lambda_1\sqrt{12}$ and $\lambda_2\sqrt{12}$, respectively. The value of λ_3 gives information about the thickness of the cluster while the strikes and dips of the fault planes can be determined from their corresponding eigenvectors. After the first iteration, the hypocenters are partitioned again into different clusters using the updated fault geometries in the spirit of the k-means method. The algorithm is repeated for the initial number of faults until the algorithm converges to a fixed geometry. The computation will stop when the maximum value of λ_3 in all the clusters is less than the allowable thickness of a cluster (Δ).

If the maximum λ_3 in the stable fault geometry is greater than Δ , the fault with the largest λ_3 is replaced by two faults with random orientations within the ‘thick’ cluster, hence increasing the number of faults by one. The lengths of the two faults are one-half that of the original ‘thick’ fault. The partitioning and covariance matrix analyses of each cluster are repeated until a fixed geometry is obtained. Clusters with less than 4 events are discarded from further analyses.

The conventional algorithm described above has some limitations in its application to the CSZ due to the complexity of the fault geometry revealed in the clustered hypocenter distribution. Splitting the ‘thick’ fault with randomly seeded planes requires several runs to get a geologically feasible fault geometry due to the closeness of the faults. Therefore, we split the fault within the ‘thick’ cluster using focal mechanism seeded planes within the cluster instead of the randomly seeded planes. We generate the focal mechanism seeded planes using the strike and dip of the average focal mechanism of the earthquakes (Hardebeck and Shearer, 2002) within the ‘thick’ cluster. We use assign a high-quality focal mechanism that is closest to an earthquake with no focal mechanism, but the focal mechanism must be within Δ of the earthquake. We determine the average focal mechanism by averaging the normal and slip vectors of the available focal

mechanisms and iteratively remove the mechanisms that are more than 30° from the average focal mechanism (Hardebeck and Shearer, 2002). We determine the average focal mechanism for the nodal faults and the auxiliary faults and use the average mechanism with the smaller root-mean-squared value of the angles between the focal mechanisms and the average focal mechanism (Kraft et al., 2006; Fadugba et al., 2021). In a case where there is no focal mechanism with the cluster, we use randomly seeded planes similar to the conventional OADC algorithm. Wang et al. (2013) and Hardebeck (2013) also incorporate focal mechanisms to OADC, but as a validation step after determining several OADC-type algorithm results.

The OADC method tends to fit the hypocenters with a subhorizontal plane when the depth extent of the earthquakes in a cluster is far less than the areal extent of the cluster (Ouillon et al., 2008; Hardebeck, 2013). To avoid subhorizontal fault planes, we set a minimum dip angle allowed at each increment in the number of fault planes to determine geologically feasible fault configurations. At a given number of fault planes, we repeat the simulation several times by placing the two focal mechanism seeded planes at different locations within the ‘thick’ cluster until we get a stable configuration that satisfies the minimum dip angle. The simulation will be terminated if a subhorizontal plane cannot be avoided.

When the faults are very close, as we observed in the CSZ, one or both of the two focal mechanism seeded planes of a ‘thick’ fault occasionally intersect the neighboring cluster, inhibiting the convergence to a realistic fault geometry. To avoid interference of these two new faults on other clusters, we determine a stable 2-fault geometry for the ‘thick’ cluster before determining a global stable fault geometry.

We estimate the thickness of each fault using $\lambda_3\sqrt{12}$ to give a conceptual thickness of the cluster in the unit of length for easy comparison with the input maximum cluster thickness (Δ). We set the maximum number of faults (N_{\max}) in our algorithm and stop the simulation when the maximum value of thicknesses for all clusters is less than the value of Δ , or the N_{\max} is reached. Similar to Hardebeck (2013)’s modifications to the OADC algorithm, we combined coplanar faults and removed clusters with ≤ 4 events in the final fault geometry. We identify coplanar planes by iteratively combining two neighboring clusters with minimum distance $\leq \Delta$ whose combined earthquakes give thickness $\leq \Delta$. We did not include the confidence ellipsoid in our study. The tunable parameters in our algorithm are the minimum (N_0) and maximum (N_{\max}) number of faults, the maximum cluster thickness (Δ) and the minimum fault dip angle allowed in the algorithm.

3.0 Results

3.1 Declustering Analyses

We generate the randomized catalog by randomly varying the latitude, longitude, and depth of each hypocenter in the observed catalog within a 3-D domain similar to the dimension of the CSZ (Fig. 2). The CSZ can be characterized as an approximately rectangular zone of seismicity with a dimension of about 20 x 60 km oriented along the St. Lawrence valley in a NE direction (Fig. 2A). We randomized the hypocenter in depth, contrary to Ouillon and Sornette (2011), due to the high density of the hypocenters in the upper 15 km in the CSZ. The ranges of tetrahedra volumes for the observed and randomized catalogs are similar, but the cumulative distribution functions (CDF) are quite different (Fig. 2C). The volumes of the tetrahedra for the observed hypocenters range from 1.8×10^{-5} to about 137.1 km^3 while those of the randomized catalog range from 1.8×10^{-4} to 22.5 km^3 . The volume at 5 percent probability (V_{05}) in the random catalog is 0.0652 km^3 , and it corresponds to the probability of 0.5716 in the observed catalog ($N(V_{05})$) (Fig. 2C).

We classify and remove 715 diffuse earthquakes (42.84% of the original catalog) with volumes above 0.0652 km^3 (Fig. 3A and B). The 954 clustered hypocenters reveal clearer and more identifiable alignments than the original relocated hypocenters of Powell and Lamontagne (2017) (Fig. 3C and D). We removed the isolated clustered earthquakes within the blue dash circle from further analyses (Fig. 3D). In addition to the rift faults, the clustered earthquakes reveal some hypocenters related to the impact structure. Hence, the clustered earthquakes properly

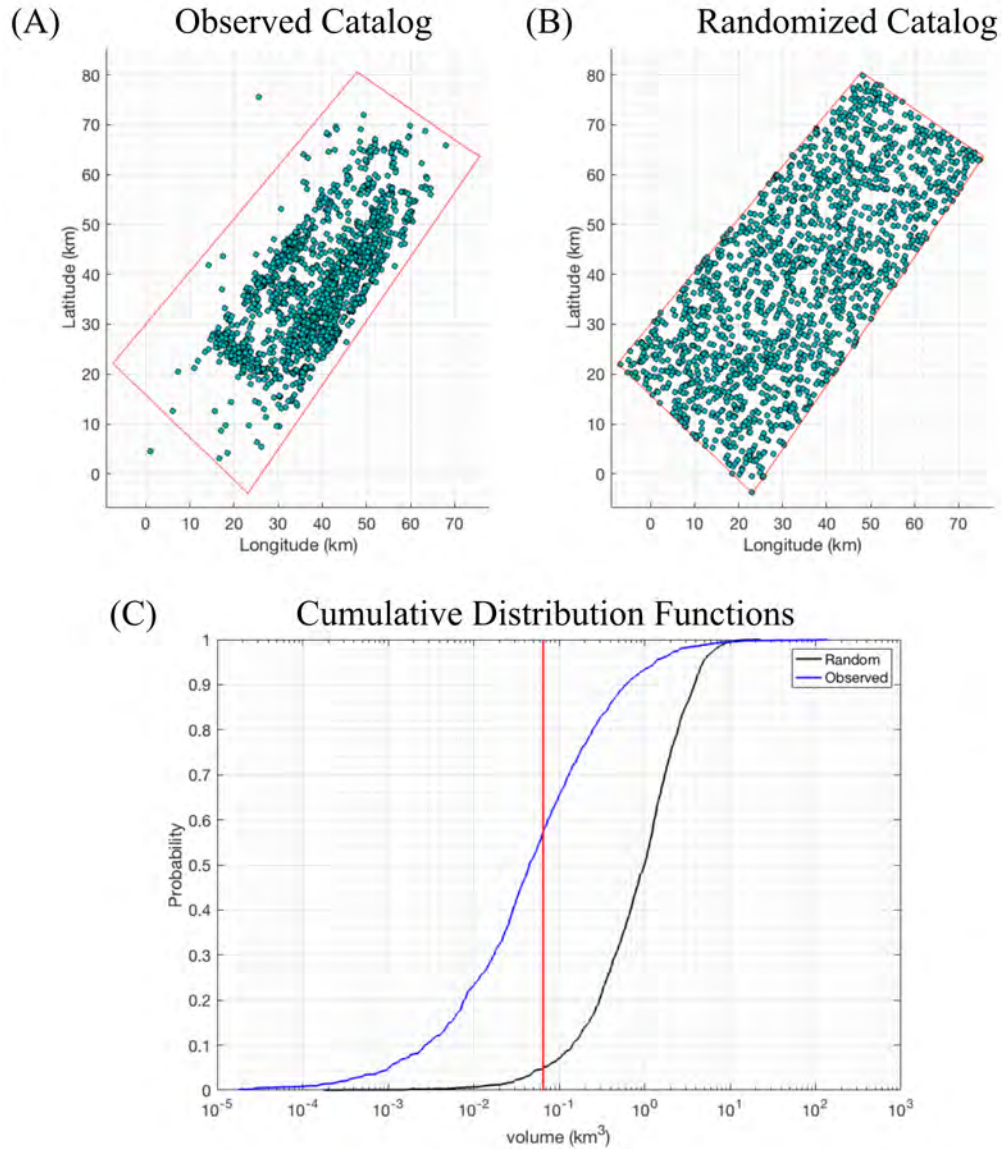


Figure 2: (A) Natural (relocated) and (B) Randomized catalog for the declustering method. The red box in (A) and (B) is used to generate the randomized catalog showing an approximately rectangular zone of seismicity with a dimension of about $20 \times 60 \text{ km}$ oriented along the St. Lawrence valley in a SW to NE orientation. (C) Cumulative distribution curve for the natural (blue) and randomized (red) catalogs of the CSZ. The thick red vertical line shows the volume ($V_0 = 0.0652 \text{ km}^3$) at 5% quantile (i.e., 0.05 probability) of the randomized catalog (Ouillon and Sornette, 2011). All earthquakes above V_0 are classified as diffuse.

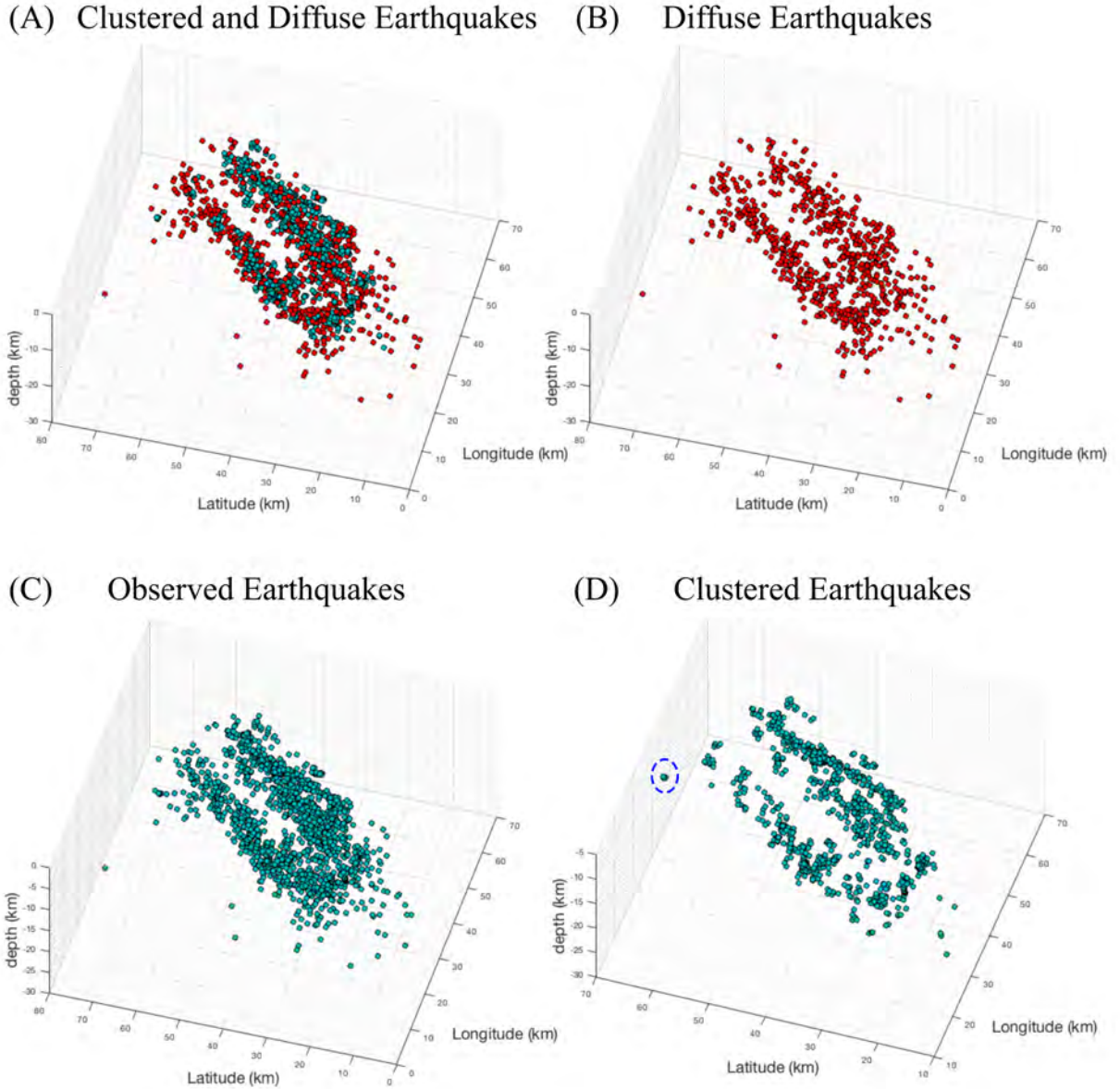


Figure 3: Declustering analyses results using the cumulative distribution method of Ouillon and Sornette (2011) showing the (A) clustered (green) and diffuse (red) earthquakes of the CSZ, (B) diffuse earthquakes only. (C) and (D) compare natural (relocated) earthquakes and the clustered earthquakes, respectively. We removed the isolated clustered earthquakes within the blue dash circle in (D) from further analyses.

highlight the fault structure and can be used to generate a fault model for the CSZ.

3.2 Fault Plane Geometry of the CSZ using the Clustered Hypocenters

We set the minimum number of faults to 1, the maximum number of faults to 100, and the fault thickness threshold (Δ) to 2.5 km. We set the minimum fault dip angle to 10° to avoid subhorizontal faults and used 455 focal mechanisms of $M \geq 2$ earthquakes from 1988-2020 to generate focal

mechanism seeded planes (Fadugba et al., 2021). We ran 501 fault models using MATLAB random seed generators initialized with different positive integer seeds to generate several fault models of the CSZ. The positive integer seed in our study is equivalent to the fault model number e.g., 300 for the 300th fault model. The non-negative integer random seed generator is used to ensure the repeatability of the models. The outputs of each model are the fault strike and dip angles, fault length, width and thickness, coordinates of the fault corners, fault centers, and the associated earthquakes. In this study, we use the right-hand rule for the strike and dip angles of the faults.

Out of the 501 models, 305 fault models (61%) converged to within error, thus providing insight into the complexity of the fault geometry in the CSZ. Figures 4A and 4B show the OADC fault models for Models 17 and 119 as examples. The observed fault traces and the impact structure outlines are superimposed on the surface of the model results for geographical reference (Lamontagne, 1999). The inner (damaged zone) and outer rings of the impact structure have diameters of 36 and 56 km, respectively (Rondot, 1994). The histogram of the strike angles of all the faults from the 305 models shows bimodal strike angles of about N40° and N220° (Fig. 4C). The two strike angles are similar, but the angles are plotted from 0 to 360 degrees because the faults dip either towards the southeast or northwest. The rose diagram of the dip angles shows four modes at about 40°, 65°, 75° and 90° further suggesting faults with similar strike azimuths can have varying dip angles. Some of the faults fit an alignment of earthquakes that crosscut two

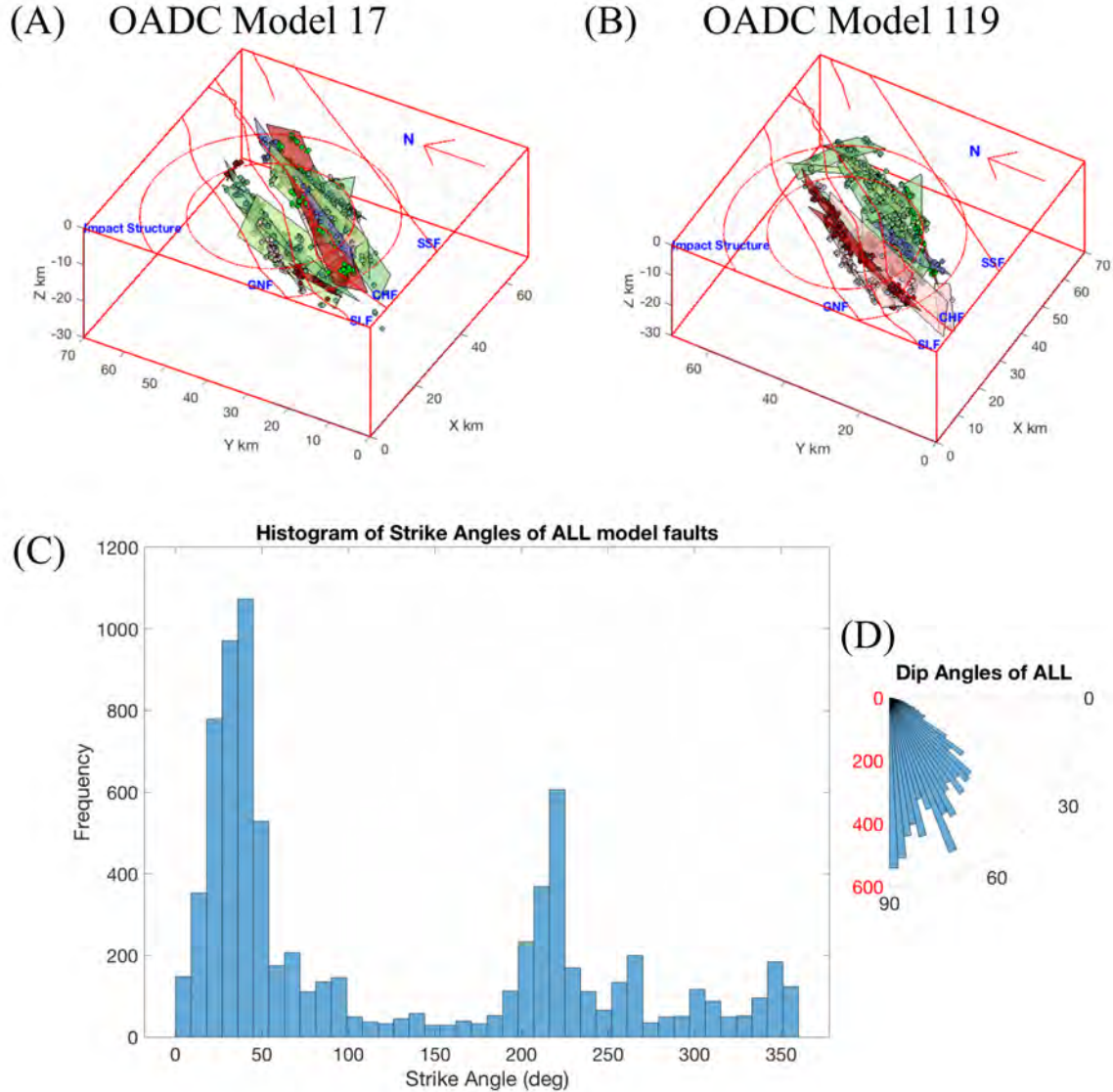


Figure 4: The OADC fault model results of the Charlevoix Seismic Zone for (A) Model 17 and (B) Model 119 using different starting random numbers equivalent to the model number. Figure (C) shows the histogram of the strike angles of all the faults from all the 305 models and (D) shows the rose diagram of the dip angles. We superimpose the observed fault traces and the impact structure outlines on the surface of the model results for geographical reference (Lamontagne, 1999). The inner (damaged zone) and outer rings of the impact structure have diameters of 36 and 56 km, respectively (Rondot, 1994).

or more earthquake alignments in a seemingly spurious way. In this study, we performed statistical analyses on all the faults from all the models without removing any seemingly spurious faults

under the assumption that realistic faults will be coherent in all the models while the seemingly spurious faults will be incoherent.

We perform a statistical analysis on the fault parameters of each model to build a combined fault model for the CSZ. To do this, we plot the fault centers for all of the faults in our 305 fault models to investigate coherent faults and study the spatial distribution of the faults (Fig. 5A). The coherent fault centers show the tendency of the seismicity to cluster into faults. We use the spatial location of the fault centers to partition the faults into different clusters (Fig. 5B). We discuss them in terms of the faults associated with the (1) Gouffre Northwest Fault, (2) Saint-Laurent Fault, (3) Charlevoix fault, and the (4) impact structure. We determine the histogram of the strike angles and the rose diagram of the dip angles for each fault cluster. When a fault group shows distinct peaks in the strike angle distribution, we partition the fault cluster into different zones based on the distribution of the peaks and determine the average strike and dip values and their associated one standard deviation for each zone. In our analyses, we further partition the faults based on the peaks in the dip angles, suggestive of faults with similar strike angles but different dip angles. The length, width and the fault centers and their associated one standard deviation are for the faults within 1° of the average strike angle in their earthquake partition. Table 1 contains the strikes and dips, lengths and widths, and the coordinates of the fault centers for all the fault groups and zones, and the number of planes we use for each fault parameter.

3.2.1 Faults Associated with the Gouffre Northwest Fault (GNF)

The distribution of the fault centers (Fig. 5) reveals three distinct fault groups associated with the GNF. We labeled the three fault groups GNF_A, GNF_B and GNF_C (red boxes in Fig.

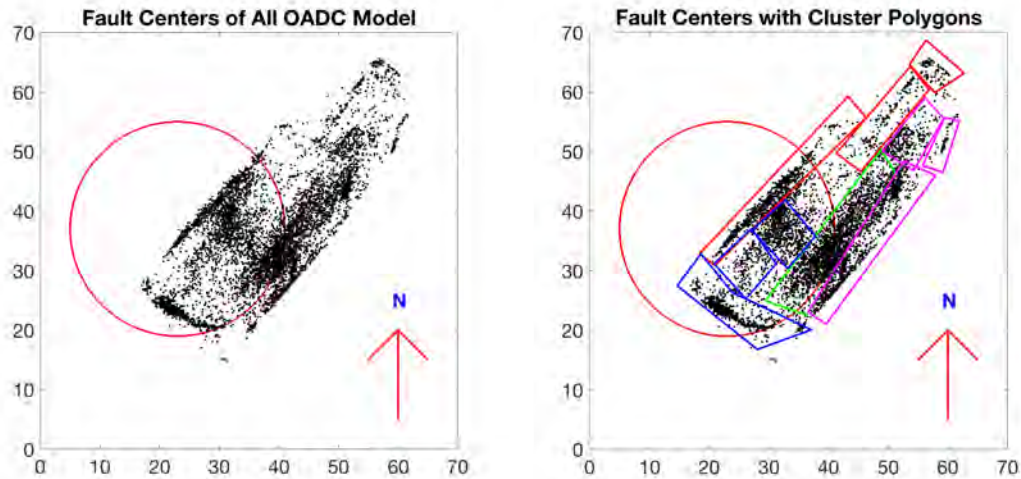


Figure 5: Fault clusters using fault centers based on known locations of rift faults in the CSZ. (A) The fault centers for all the faults in our 305 fault models to investigate coherent faults showing the tendency of the seismicity to cluster into faults. (B) The fault clusters are based on the coherence and spatial location of the fault centers. The rectangles in (B) show the fault clusters and they are associated with Gouffre Northwest Fault (red), Saint-Laurent Fault (green), Charlevoix fault (purple), and the impact structure (blue).

5B). The fault centers associated with GNF_A shows a distinct linear trend signifying a consistent delineation of the faults by most of the models. Fault groups GNF_B and GNF_C appear to be laterally offset from the GNF_A because they are located at a greater depth, but the amount of lateral offset reveals that they are distinct fault groups from GNF_A (Fig. 5B).

The histogram of the strike angles of all the faults in the GNF_A group reveals three distinct strike peaks (Fig. 6A), and the rose diagram of the dip angles shows two distinct peaks (Fig. 6B). We partition the faults associated with GNF_A into three groups based on the strike peaks (Fig. 6A) and determine the rose diagram of the dip angles for each zone (Fig. 6C-E). A significant number of the models show a shallower-dipping fault group (GNF_B) located deeper than the faults in GNF_A. The histogram of the strike angles shows two main peaks (Fig. S1A) while the dip angles show three distinct peaks (Fig. S1B-D). We also observe a cluster of fault

Table 1: Average OADC fault parameters of the fault clusters and zones for the CSZ.

SN	Possible Faults	Associated Fault	Zone (°)	Subzones based on dip (°)	Strike (°)	Dip (°)	L (km)	W (km)	Fault Centers			Number of planes
									X (km)	Y (km)	Z (km)	
1	Gouffre Northwest Fault (GNF)	GNF_A	0-80		39.5 ± 7.7	65.0 ± 10.6	25.2 ± 6.5	7.2 ± 2.6	29.7	41.6	11.7 ± 0.7	680
2			190-240		218.4 ± 6.8	73.2 ± 13.4	25.2 ± 4.2	6.2 ± 0.7	32.5	45.0	11.6 ± 0.3	180
3			240-285		262.0 ± 5.3	83.7 ± 7.3	4.7 ± 0.0	3.1 ± 0.0	40.4	54.2	10.8 ± 0.0	78
		GNF_B	0-55	All dips	36.3 ± 8.8	45.9 ± 8.5	26.6 ± 1.9	9.2 ± 0.9	46.8	51.9	25.0 ± 0.3	264
4				30-45	41.4 ± 4.7	38.6 ± 2.9	33.1 ± 1.9	6.5 ± 1.5	50.5	56.8	24.5 ± 0.3	125
5				45-60	31.4 ± 8.9	52.7 ± 3.8	26.9 ± 10.2	9.9 ± 3.1	46.8	52.0	24.6 ± 0.5	131
6			55-100	All dips	70.7 ± 8.6	62.3 ± 22.5	29.0 ± 4.0	6.5 ± 3.5	45.0	50.8	15.1 ± 2.2	103
7				60-90	67.7 ± 3.6	79.2 ± 4.4	6.0 ± 5.4	3.2 ± 1.3	45.4	46.8	26.0 ± 2.0	64
	Saint-Laurent Fault (SLF)	SLF	0-70		261.3 ± 5.8	62.5 ± 9.7	10.6 ± 6.7	4.6 ± 2.6	57.6	63.7	22.4 ± 0.2	219
				All dips	36.3 ± 11.2	62.0 ± 19.4	27.8 ± 9.4	9.0 ± 2.4	40.7	34.5	11.5 ± 1.6	995
8				0-55	40.4 ± 12.6	38.6 ± 10.6	32.7 ± 11.1	8.5 ± 1.7	41.1	35.3	11.3 ± 1.2	336
9				60-75	34.8 ± 9.0	68.5 ± 3.8	22.7 ± 9.8	7.8 ± 3.3	41.5	34.7	12.7 ± 3.7	307
10				75-90	33.4 ± 9.9	82.9 ± 4.5	29.7 ± 8.4	8.9 ± 1.8	43.2	38.3	10.3 ± 1.1	293
11			160-260		213.6 ± 16.4	63.0 ± 19.8	29.6 ± 12.0	8.7 ± 3.4	41.1	35.5	10.7 ± 2.1	855
	Charlevoix Fault (CHF)	CHF_A	0-80	All dips	29.1 ± 13.8	58.3 ± 18.8	29.0 ± 12.4	8.8 ± 2.4	43.9	33.6	10.3 ± 2.4	637
12				30-60	22.0 ± 11.0	46.5 ± 5.6	19.9 ± 8.3	7.7 ± 2.1	49.6	42.0	10.7 ± 0.9	367
13				75-90	40.4 ± 7.0	84.0 ± 4.3	29.4 ± 8.3	9.0 ± 2.1	42.7	29.5	12.1 ± 0.7	182
14			180-250		215.1 ± 10.0	76.0 ± 14.8	33.4 ± 9.9	10.2 ± 2.8	48.0	35.7	12.2 ± 1.1	388
		CHF_B	0-60	All dips	32.9 ± 14.9	70.4 ± 16.5	11.6 ± 0.0	8.9 ± 0.0	52.6	52.7	9.1 ± 0.0	134
15				50-75	29.1 ± 15.6	64.3 ± 5.0	12.0 ± 4.1	7.1 ± 1.4	52.5	51.4	9.6 ± 0.7	55
16				75-90	40.1 ± 8.5	83.6 ± 3.3	22.2 ± 5.9	9.1 ± 2.6	51.0	51.7	10.6 ± 0.4	65
17			60-100		80.3 ± 8.6	71.0 ± 16.6	16.6 ± 7.9	6.0 ± 1.5	51.3	50.7	11.4 ± 1.3	63
18		CHF_C	0-50	50-75	13.8 ± 8.6	71.6 ± 1.7	3.6 ± 0.0	2.5 ± 0.0	59.8	51.8	10.5 ± 0.0	31
19				75-90	32.6 ± 3.4	87.2 ± 2.2	11.0 ± 0.1	6.3 ± 0.0	60.8	55.2	21.7 ± 0.0	83
20			185-225		203.7 ± 5.5	85.8 ± 5.6	19.3 ± 2.9	9.7 ± 0.8	59.7	51.8	15.1 ± 1.1	82
21	Impact Structure Boundary (IM)	IM_ABC	330-30		357.1 ± 15.5	55.7 ± 13.0	15.8 ± 7.0	6.8 ± 3.9	21.7	23.7	12.0 ± 2.1	437
22			70-110		90.6 ± 6.6	71.6 ± 14.1	10.4 ± 5.2	4.6 ± 2.0	28.0	20.7	12.4 ± 0.3	146
23			280-330		308.5 ± 10.4	64.6 ± 12.1	11.5 ± 2.5	6.5 ± 1.8	23.8	23.0	12.2 ± 1.0	157
		IM_D	0-70	All dips	27.7 ± 11.4	50.1 ± 15.3	33.5 ± 3.4	11.2 ± 2.9	26.6	31.8	12.6 ± 0.8	169
24				0-60	25.7 ± 9.7	42.4 ± 7.9	31.5 ± 4.4	13.1 ± 2.7	26.3	31.0	12.2 ± 1.1	126
25				60-90	33.5 ± 14.0	72.6 ± 7.6	39.8 ± 8.3	9.3 ± 2.7	29.2	31.6	15.4 ± 0.1	43
26		IM_E	0-70		31.0 ± 15.1	54.8 ± 15.3	27.8 ± 12.2	9.6 ± 3.5	31.8	39.1	13.7 ± 1.8	441

centers, GNF_C, at the NE end of GNF_B (Fig. S2). GNF_C is at greater depth than GNF_B. We identify seven individual faults associated with the GNF (1-7 Table 1).

3.2.2 Faults Associated with the Saint-Laurent Fault (SLF)

The fault models show a more complicated fault system associated with the SLF than the faults associated with the GNF. The histogram of the strike angles of SLF faults shows two main peaks (Fig. 7A) and the rose diagram of the dip angles shows three distinct groups (Fig. 7B). We partition the faults into two zones which have the same azimuth but different dip directions (Fig. 7 C and D).

The dip angle distribution of the fault planes in zone 1 (i.e., SLF_Z1) also shows the three distinct dip angles (Fig. 7C). We determine four individual faults, three in zone 1 and one in zone 2, associated with the SLF (8-11 Table 1).

3.2.3 Faults Associated with the Charlevoix Fault (CHF)

Almost all the fault models contain the faults associated with CHF_A. The histogram of the strike angles shows two peaks defining two zones (CHF_A_Z1 and CHF_A_Z2). The azimuths for the two zones are similar but faults that are not vertical in zone 1 dip to the SE while those in zone 2 dip to the NW (Fig. 8A). The rose diagram of the dip angles also shows two distinct dip angles: one at about 45° and one near-vertical (Fig. 8B). Faults in zone CHF_A_Z2 are mostly near-vertical or dip at high angle to the NW (Fig. 8D).

Fault group CHF_B is as considered the NE continuation of CHF_A (Fig. 5B). The histogram of the strike angles varies, but we consider two main zones (Fig. S3A). The dip angles are generally greater than 60°, but some faults have dip angles of about 30° (Fig. S3B). The fault dips at a higher angle at the NE end of CHF_A.

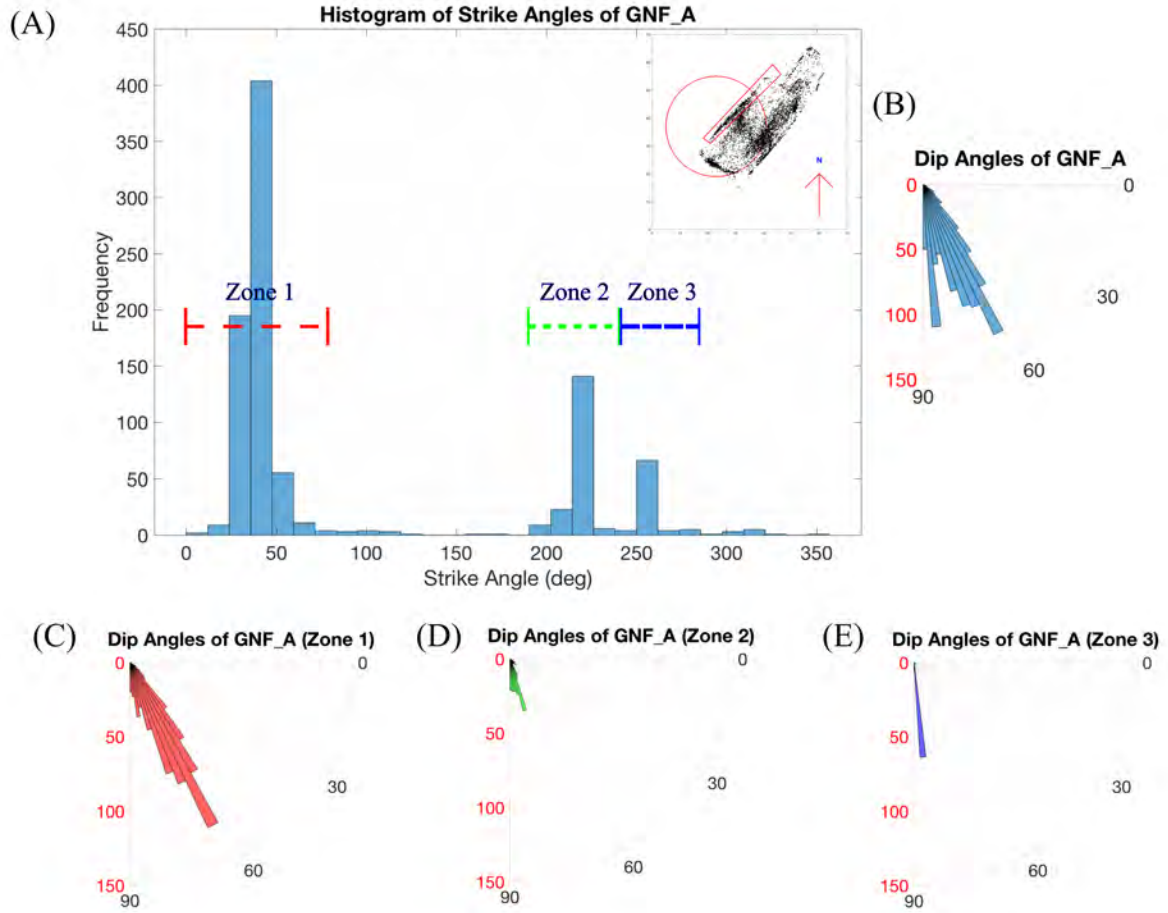


Figure 6: (A) The histogram of the strike angles and (B) the rose diagram of the dip angles of one of the fault groups associated with the Gouffre Northwest fault (GNF_A). In cases when a fault group shows distinct peaks strike angles, we partition the fault cluster into different zones (i.e., Zones 1 to 3) based on the distribution of the peaks. The dotted horizontal line in (A) corresponds to the range of the strike angle in each zone. The inset plot in (A) shows the location of the fault cluster in the fault center map. (C - E) show the rose diagrams of the dip angle of the different zones in (A). We determine the strike and dip angles for each partition. The fault length, width and fault centers, and their associated one standard deviation are for the faults within 1° of the average strike angle in their earthquake partition.

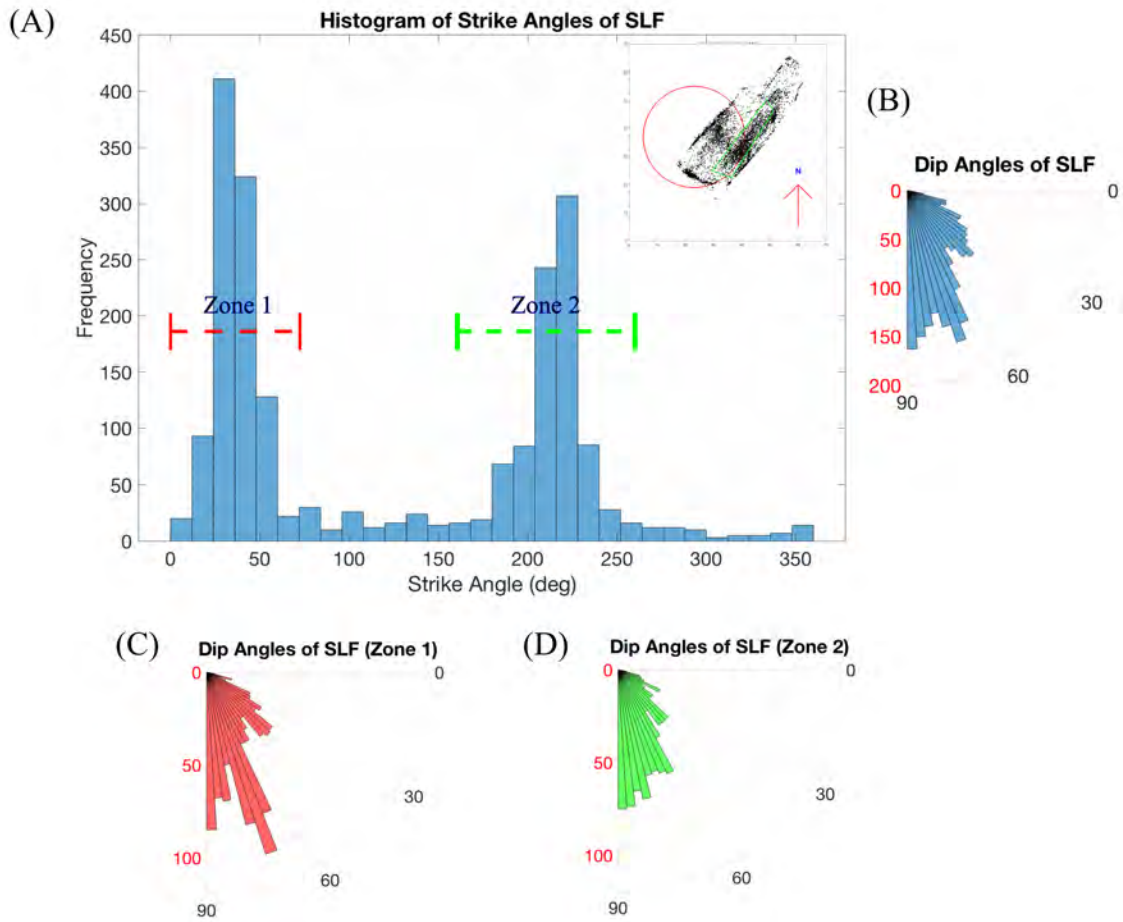


Figure 7: Same as Fig. 6 but for faults associated with one of the fault groups associated with the Saint-Laurent fault (SLF). The rose diagram of zone 1 shows different peaks for the group. We further partition the faults based on the dip angles' peaks and determine the fault parameters for each subset. The partitioning suggesting faults with similar strike angles but different dip angles.

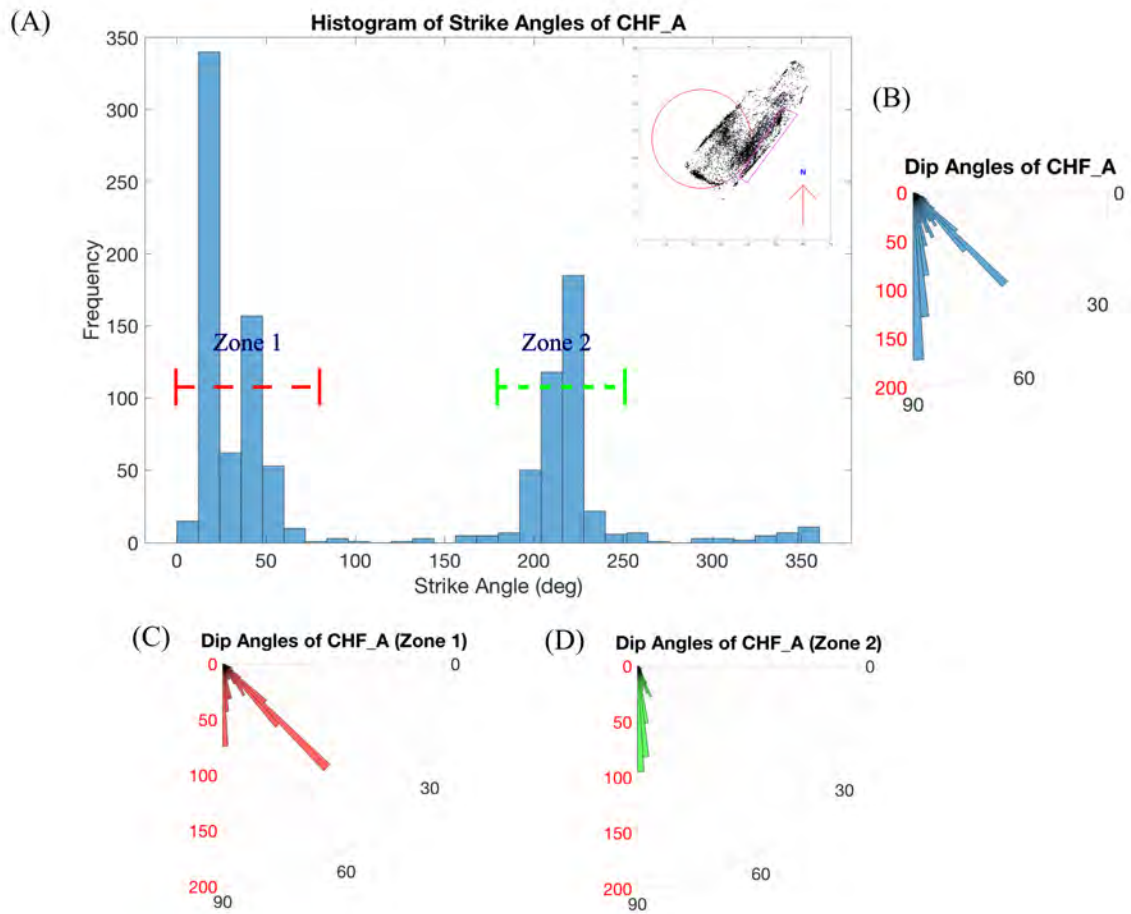


Figure 8: Same as in Fig. 6 and 7 but for faults associated with one of the Charlevoix Fault (CHF_A).

Some of the models delineated a smaller fault group (CHF_C) offset to the NE of CHF_A (Fig. 5B). The histogram of strike angles shows two distinct groups (Fig. S4A). The dip angles are mostly near-vertical but some of the faults have dip angles of about 70° (Fig. S4B). All together, we determine nine individual faults associated with the CHF (12-20 Table 1).

3.2.4 Faults Associated with the Impact Structure (IM)

The histogram of the strike angle of IM_ABC shows several peaks and can be partitioned into three zones (Fig. 9A). The rose diagram of the dip angles shows two main peaks at about 60° and 80° (Fig. 9B). The strike peaks indicate the presence of three faults that dip either NE or SW. For example, zone 1 strikes roughly N-S (Fig. 9C). Zone 2 strikes roughly E-W (Fig. 9D), and zone 3 strikes NW-SE (Fig. 9E).

The histogram of the strike angles of fault group IM_D has one peak between $N0^\circ$ - 70° (Fig. S5A) and the dip angle distribution shows two peaks near 50° and 70° (Fig. S5C). The histogram of strike angles for faults associated with IM_E also peaks between $N0^\circ$ - 70° (Fig. S6A) and the dip angle also centers around 50° (Fig. S4C). We identify six individual faults associated with the impact structure (21-26 Table 1).

3.2.5 Combined Fault Model for the CSZ

We plot the traces of the OADC faults to discuss a combined fault model for the CSZ (Fig. 10). The parameters of these faults are presented in Table 1, including the average fault centers. A combined fault model in 3D is shown in Figure 11 determined using the average fault parameters for the identified fault groups (Fig. 11 and S7).

There are two main faults associated with GNF_A (1 and 2 in Fig. 10). Both have a strike azimuth of about $N40^\circ$ but the dip angles are 65° SE and 73.2° NW. There is also a smaller fault located to the NE of the GNF_A fault group with an oblique strike angle (3 in Fig. 10). The

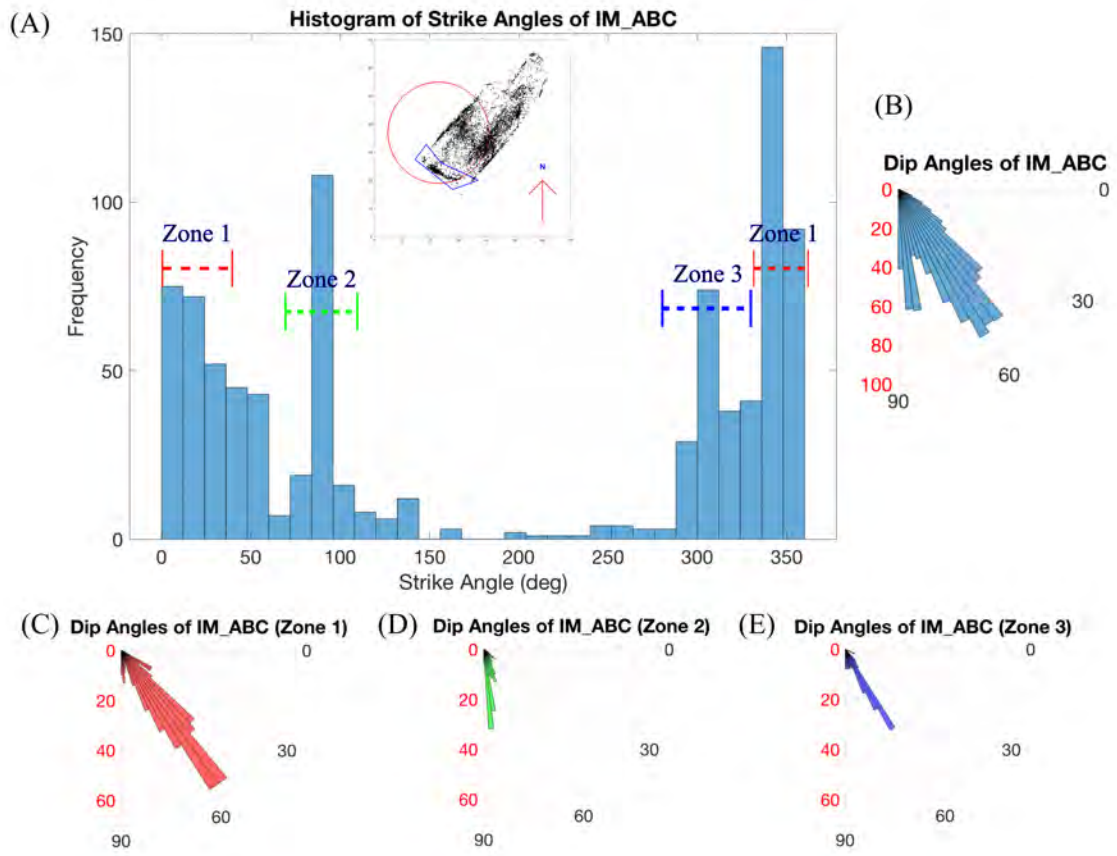


Figure 9: Same as in Fig. 6 and 7 but for faults associated with one of the boundary faults of the impact structure (IM_ABC).

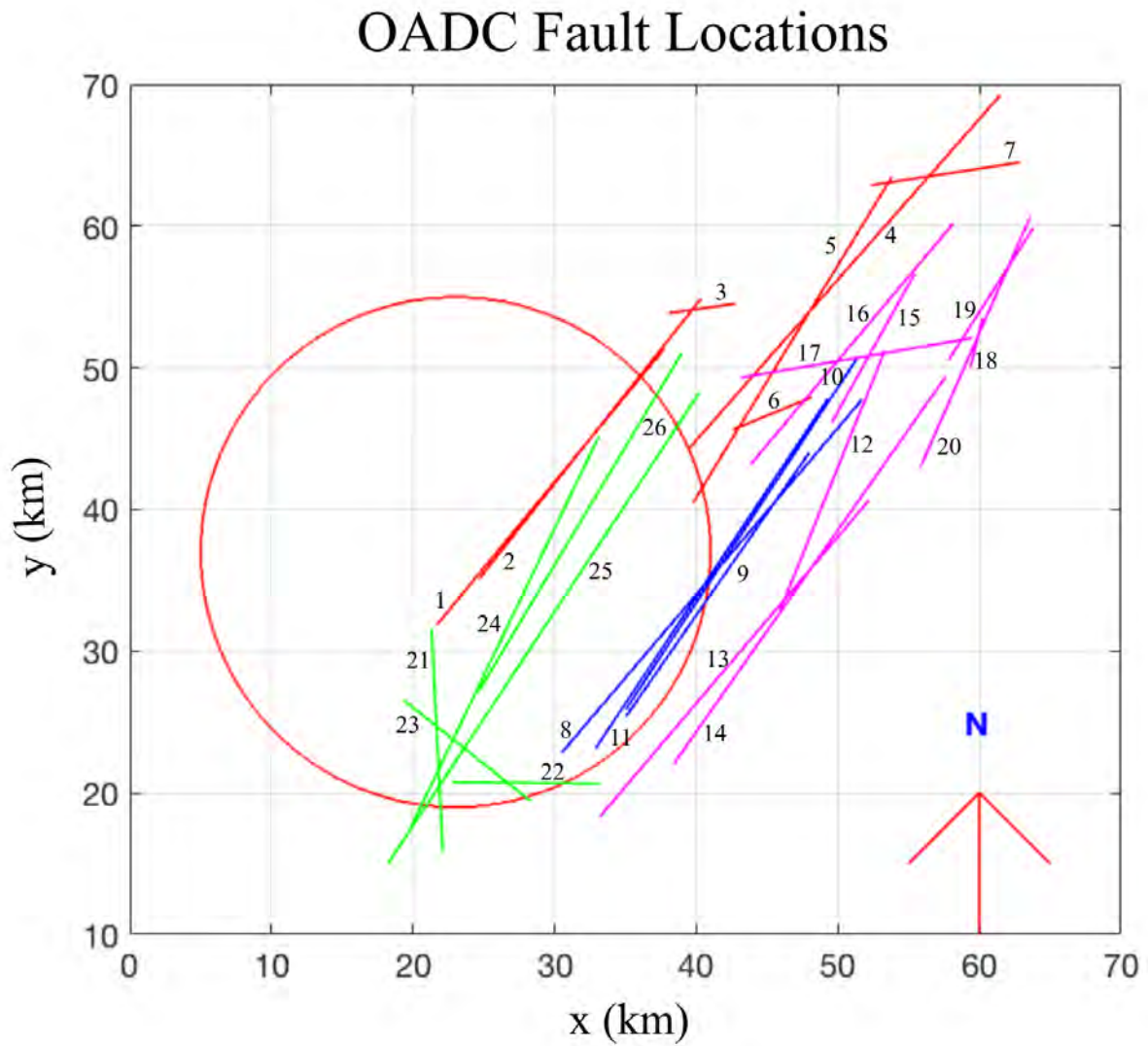


Figure 10: A pseudo-fault traces of the average OADC faults from all the 305 fault models. The different colors are for the faults associated with the different fault clusters in Fig. 5. The numbers assigned to each fault trace correspond to the serial number of the fault parameters in Table 1. The red circle is the outline of the damage zone of the impact structure corresponding to the inner circle in Figure 1.

Fault Model of the Charlevoix Seismic Zone

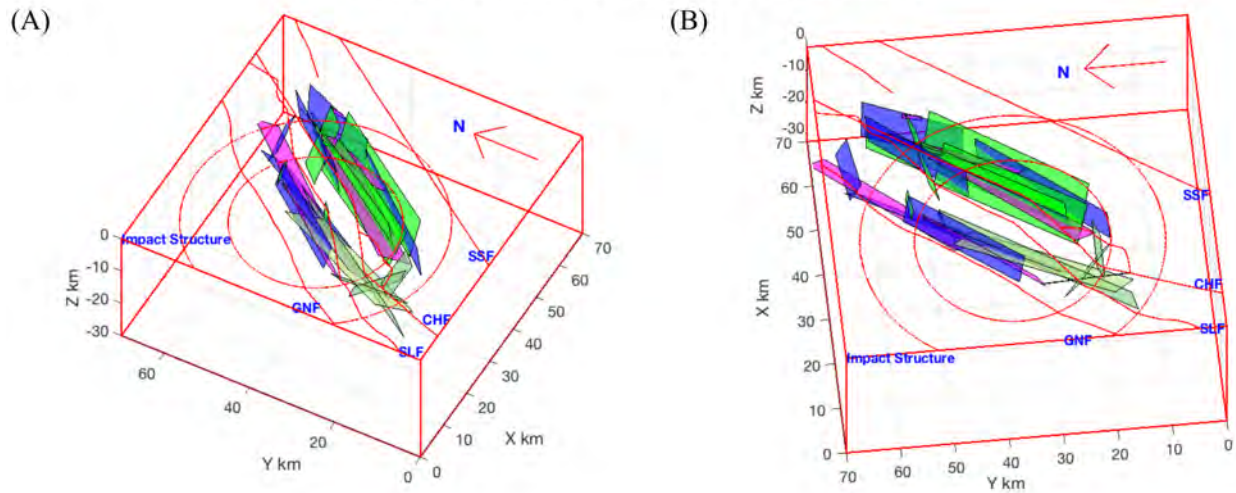


Figure 11: The fault model of the Charlevoix Seismic Zone using the average fault parameters. (A-B) show different views of the fault model. We superimposed fault traces and the outline of the impact structure.

GNF_B fault group (4-6 in Fig. 10) has a similar strike as the GNF_A group but is located at a greater depth and dips at a generally shallower angle. A third fault, GNF_C, is a smaller cross-cutting fault located at a greater depth than GNF_A but with a similar dip magnitude (7 in Fig. 10). The strike, dip angle magnitudes and dimension of GNF_C are similar to those of GNF_B zone 2 (6 in Fig. 10) and both of these faults strike at a greater angle than the general strike direction of the majority of the CSZ faults ($N33^{\circ}$ - 40°). The decrease in the dip angle of the GNF segments with increasing depth supports the possibility that GNF is listric (Baird et al., 2010; Fadugba et al., 2019).

The four faults associated with the SLF have similar strike directions but varying dip angles (8-11 in Fig. 10). Visual inspection of the earthquake distribution suggests the presence of at least two parallel 38.6° dipping faults in this group (Fig. 3).

The faults associated with CHF_A have a wide distribution of strike and dip angles. The strike angle of the main fault in this group, CHF_A_Z1 (12 in Fig. 10), is $N22^{\circ}$ which is smaller than the usual strike angle for the CSZ faults. Two near-vertical faults (13 and 14 in Fig. 10) have strike azimuths that are similar to the general strike angle of most faults in the CSZ. The fault associated with CHF_A_Z2 has a near-vertical dip (14 in Fig. 10), and it is located at the SW end of CHF_A (Fig. 8D).

The faults in CHF_B (15-17 in Fig. 10) are considered the NE continuation of CHF_A. However, the faults dip at a greater angle than those in CHF_A. CHF_B has a strike angle of $N29.1^{\circ}$ similar to CHF_A_Z1 but dips at an angle of 64.3° (15 in Fig. 10). The fault group also has a near-vertical fault that strikes at an angle of about $N40.1^{\circ}$ (16 in Fig. 10), similar to the general strike angle for the CZS. Another fault is present with an oblique strike angle (17 in Fig. 10; Fig. S3D).

The faults associated with CHF_C_Z1 fit earthquakes in the upper 12 km and earthquakes located below 15 km. The fault in the upper 12 km has a small strike angle of $N13.8^{\circ}$ with a dip angle of 71.6° (18 in Fig. 10). However, the fault below 15 km has a strike angle of $N32.6^{\circ}$, similar to the general strike angles of CSZ faults, with a dip angle of 87.2° (19 in Fig. 10).

The fault models indicate five fault groups (IM_A to IM_E) associated with the impact structure (Fig. 5B). Faults IM_A, IM_B and IM_C are located on the SW end of the damaged zone (21-23 in Fig. 10; Fig. 5B) and display variable strike and dip angles. In contrast, faults IM_D and IM_E (24-26 in Fig. 10) are located near the GNF_A faults and have strikes that are more compatible with the general strike direction of the CSZ faults. Two of the faults, 24 and 26, dip at shallower angles than the GNF_A faults and all three faults are associated with earthquakes beneath the impact structure.

The identified fault planes demonstrate a high degree of variability in strike and dip, providing an explanation for the observed varying focal mechanisms. Figure 12 shows the plane of each identified OADC fault and the observed nodal planes for focal mechanisms within 1.0 km of the fault. We observe a good first-order agreement between the observed focal mechanisms and the OADC fault parameters except for the faults that strike in the opposite direction of the general strike azimuth for the CSZ.

We estimate the maximum magnitude earthquake expected in the CSZ from the fault dimensions using the different moment magnitude-fault area relations (Table S1; Leonard, 2010; Wells and Coppersmith, 1994; Somerville et al., 1999; and Wyss, 1979). We did not consider any stress transfer between the faults which will increase the maximum magnitude. We estimate the moment magnitude for the two largest rift faults delineated in this study to be 6.63 and 6.62, respectively, while an extreme deep-crustal fault with a length of 40 km and 25-km width would have a moment magnitude of 7.19.

4.0 Discussion

4.1 Clustered Seismicity

The cumulative distribution method of Ouillon and Sornette (2011) proves effective in removing diffuse earthquakes in the CSZ, thereby highlighting identifiable planes that reveal the three major rift faults in the CSZ. The alignment of the earthquakes on identifiable planes supports the results of Powell and Lamontagne (2017) that the earthquakes in the CSZ occurred on the faults rather than concentrating within the fault volume (e.g., Baird et al. 2010; Anglin, 1984; Lamontagne, 1999).

The declustering method also helps remove the randomness of the seismicity within the impact structure revealing the continuation of the rift faults within the impact structure, and highlights the faults bounding the damaged zone. The results show that most earthquakes occurring within the impact structure are diffuse (Fig. 3), suggesting that they occur in highly faulted rocks with varying strikes and dips. We can use the clustered earthquakes to delineate the bounding

OADC Fault Planes and Observed Focal Mechanisms

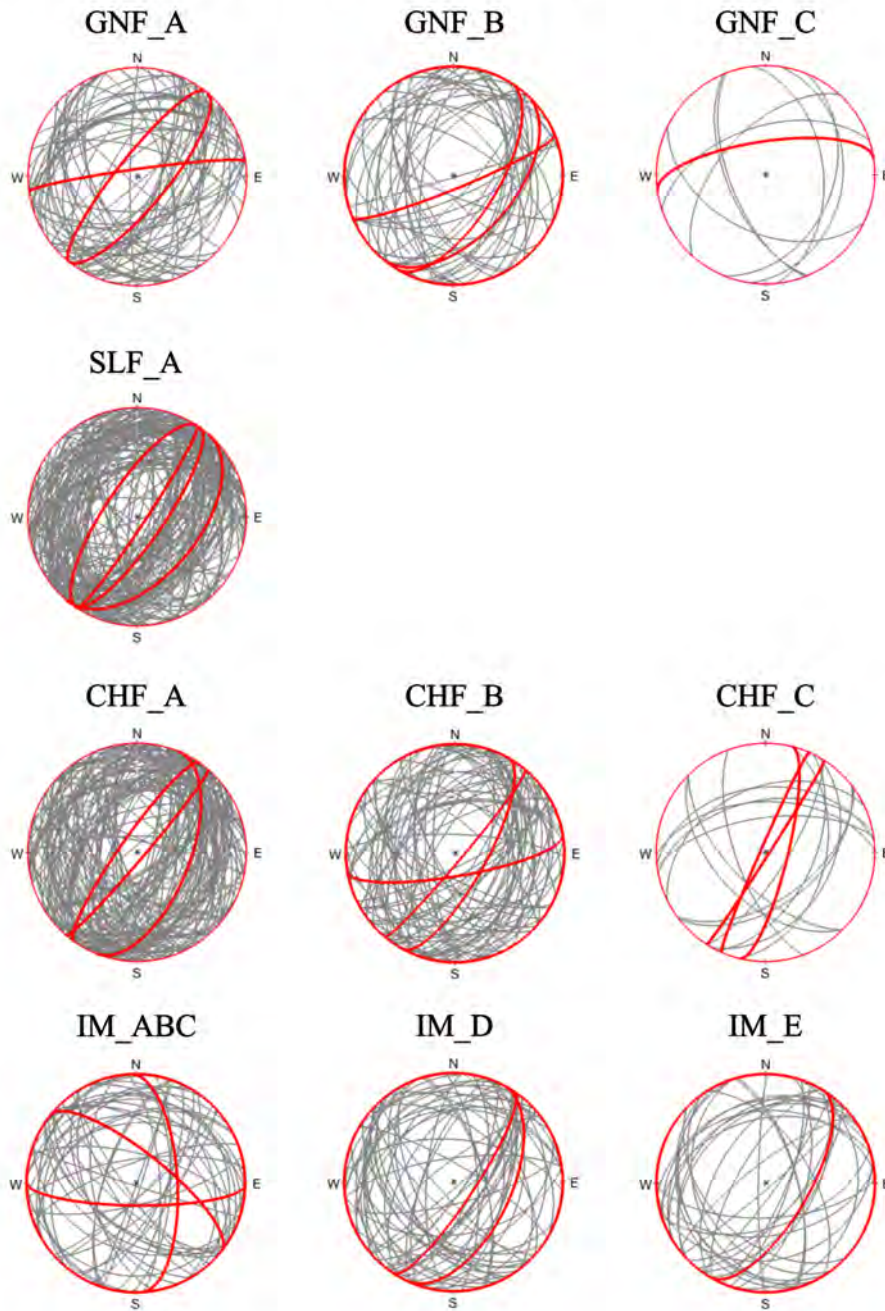


Figure 12: The nodal plane for each OADC fault group (red) and the observed focal mechanisms (grey) within 1.0 km of the OADC faults.

faults of the impact structure damage zone (e.g., the inner circle in Figures 1 and 11).

4.2 Fault Planes of the Modified OADC Algorithm

The rift faults show a more complicated geometry than the simple three-fault model determined in previous studies, especially near the impact structure region and the faults associated with the SLF (e.g., Fadugba et al., 2019; Baird et al. 2010; Anglin, 1984; Lamontagne, 1999). The alignment of the clustered earthquakes supports our first hypothesis that modern seismicity in the CSZ illuminates active faults (Powell and Lamontagne, 2017) and the seismicity can be used to determine fault geometries and the interconnectivity of the fault system. The average strike angle for all of the faults (except those associated with the impact structure) is $N42^\circ$ supporting the average strike angle of $N35^\circ$ used for the rift faults in previous studies (e.g., Fadugba et al., 2019; Baird et al., 2010).

Our modified version of the OADC algorithm ensures the repeatability of the fault model results. The conventional OADC algorithm fault model changes for every run because the results depend on the initial seed of the random seed generator. As a result, the repeatability of the model is not guaranteed. Getting fault models from OADC generally requires running the model several times to get a geologically feasible fault geometry. The random number sequence can be repeated in MATLAB using a non-negative integer seed. Hence, the inclusion of a positive integer seed corresponding to the fault model number for the random number generator (e.g., 300 for the 300th fault model) in our study helps the repeatability of the model results. However, the procedure still requires computing multiple models because the use of repeatable random numbers does not guarantee geologically feasible fault models.

Our fault model reveals a change in the dip angles of the rift faults supporting observations from Powell and Lamontagne (2017). The GNF dips at an angle of about 65° while the other two main rift faults, SLF and CHF (represented by 8 and 12 in Fig. 10) dip at 39° and 47° , respectively (Table 1; Fig. 11). Therefore, our model shows a 65° - 39° - 47° dipping fault system in the CSZ. However, the presence of a 65° - 69° - 64° dipping fault geometry delineated in the NE end of the CSZ rift faults and the near-vertical faults beneath the impact structure and on most of the CHF suggests a combination of a 65° - 40° - 40° and a 70° - 70° - 70° dipping fault geometry.

Our fault model reveals some segmented faults associated with the boundary of the damaged zone of the impact structure, especially in the southwestern part. Based on the location of these boundary faults, the model highlights the extent of the damaged zone of the impact structure. The bounding faults to the SW end of the impact structure have an average dip of 64.0° . The shallower dipping fault (IM_D_Z1), dipping at about 42.4° , is probably associated with earthquakes wrapping around the impact structure region. These bounding faults support the observation of Powell and Lamontagne (2017) that some earthquakes occur around the rim of the impact structure. The presence of diffuse earthquakes within the impact structure supports the presence of highly fractured rock due to the meteor impact (Lamontagne and Ranalli, 1997). Our model also reveals faulting beneath the impact structure, in agreement with the results of Powell and Lamontagne (2017). The compatibility of the strikes of these faults with those of faults outside of the impact structure indicates continuity of the rift faults below the damage zone.

The presence of faults in our model with varying strike and dip angles and the first-order correlation between the modeled fault parameters and the proximal focal mechanisms could explain the observed variability in the strike and dip angles in the CSZ focal mechanisms. This observation also supports the suggestion that the majority of the seismicity in the CSZ occurs on the identifiable faults and faults associated with the impact structure (Powell and Lamontagne, 2017; Lamontagne and Ranalli, 1997) rather than concentrating within the fault volume (e.g., Baird et al. 2010; Anglin, 1984; Lamontagne, 1999). Our fault model also supports our second

hypothesis that earthquake source mechanisms and seismicity clusters define coherent fault surfaces.

Our study shows that the simplified and realistic fault geometry of the CSZ, after removing diffuse earthquakes, can reveal local variations in the dip and strike of the regional faults. This provides some insight into the problems of correlating seismicity only with the faults of regional extent, such as the rift faults of the CSZ (Lamontagne and Ranalli, 1997); the observed seismicity can also be due to other active faults such as the bounding faults of the impact structure.

The modified version of the OADC algorithm used in this study for generating fault geometry for the CSZ shows the benefits of the improvements in the OADC algorithm. The inclusion of focal mechanisms, minimum dip angles, and local splitting of faults within the ‘thick’ cluster helps resolve complicated fault geometry involving systems of closely spaced, parallel, and listric faults. Our modified version of the OADC algorithm also avoids overfitting by combining coplanar faults with a combined thickness less than the specified thickness threshold. Improvements to the method would involve using only high confidence focal mechanisms to generate focal mechanism seeded planes and incorporating the earthquake location ellipsoid into the algorithm.

There are several uses for the realistic fault model determined in our study. The model can be used in a revised numerical simulation to investigate observed stress variations and the observed stress rotations in the CSZ. Knowledge of the fault system can be used to better assess the seismic hazard of the CSZ and better understand wave propagation of earthquakes, thereby allowing determination of the largest magnitude earthquakes expected in the CSZ (Harris et al., 1991; Harris and Day, 1993). Using the fault dimensions in this study and without considering interactions between the rift faults, we estimate the maximum magnitude earthquake expected in the CSZ to be 6.63 while an extreme deep-crustal fault with a length of 40 km and 25-km width would have a moment magnitude of 7.19. The two notable historical earthquakes in the CSZ have magnitude (M) 6.5 in 1925 (Bent, 1992) and a M7.5 in 1663 (Ebel, 2011). The fault model can also be used to develop a scenario map of ground shaking due to a large earthquake that originates on any of the identified faults.

5.0 Conclusions

This study demonstrates the use of declustering analysis to highlight the faults of the CSZ and uses a modified version of the OADC algorithm to determine realistic but simplified fault geometry of the CSZ. The original OADC algorithm is modified by the implementation of focal mechanism seeded planes in splitting clusters with thickness greater than a threshold value (i.e., the ‘thick’ faults) instead of the original randomly seeded planes. Other modifications provide solutions to the problem of generating subhorizontal faults and ensuring repeatability of the fault model from the OADC algorithm.

The rift faults of the CSZ show a more complicated geometry than the simple three-fault model determined in previous studies, especially near the impact structure region. We observe a variation in the strike and dip angle of the three rift faults, providing a possible explanation for the variety of focal mechanisms in the CSZ (Lamontagne and Ranalli, 1997). For example, the GNF dips at an angle of 65° but also shows evidence of being listric (i.e., shallower dipping fault of about 45.9° at greater depth). The model also contains a complicated fault system associated with the SLF involving two parallel 38.6° dipping faults and a fault dipping at about 68.5° . The CHF strikes at a relatively smaller angle of $N22.0^\circ$, evident in the outline of the mapped fault traces

(Fig. 1). The fault generally dips at 46.5° , but the models also show a high angle dipping fault of about 64.3° at the NE end of the CHF, similar to the dip variations along the SLF fault system.

Our fault model reveals some segmented faults dipping at an average angle of 66° associated with the SW end of the impact structure boundary. Faults are also detected below the impact structure that align with the major rift faults.

Our model indicates a 65° - 39° - 47° dipping rift fault system in the CSZ near the impact structure, similar to fault dips determined by Powell and Lamontagne (2017). However, the presence of a 65° - 69° - 64° dipping rift fault geometry in the NE end of the rift faults is similar to the 70° - 70° - 70° dipping fault model used in previous studies involving stress reorientation (Baird et al. 2010). Hence, our study suggests a combination of 65° - 40° - 40° dipping rift fault geometry near the impact structure and the 70° - 70° - 70° dipping fault geometry away from the impact structure. The presence of faults in our model with varying strike and dip angles and the first-order correlation between the model fault parameters and the proximal focal mechanisms could explain the observed focal mechanisms with highly variable strike and dip angles in the CSZ.

Acknowledgments

This material is based upon work supported by the U.S. Geological Survey under Grant No. G19AP00052. The views and conclusions contained in this document are those of the authors and should not be interpreted as representing the opinions or policies of the U.S. Geological Survey. Mention of tradenames or commercial products does not constitute their endorsement by the U.S. Geological Survey. We acknowledge the Center of Earthquake Research and Information (CERI) at the University of Memphis, TN, provides the computing time for this research. The original earthquake hypocenters are available from Earthquakes Canada, GSC, Earthquake Search (On-line Bulletin), <https://earthquakescanada.nrcan.gc.ca/stdon/NEDB-BNDS/bulletin-en.php>, Natural Resources Canada (last accessed August 2021).

References

- Anglin, F. M. (1984). Seismicity and Faulting in the Charlevoix Zone of the St. Lawrence Valley. *Bulletin of the Seismological Society of America*, 74(2), 595–603.
- Baird, A. F., McKinnon, S. D., & Godin, L. (2010). Relationship between structures, stress and seismicity in the Charlevoix seismic zone revealed by 3-D geomechanical models: Implications for the seismotectonics of continental interiors. *Journal of Geophysical Research: Solid Earth*, 115(11), 1–16. <https://doi.org/10.1029/2010JB007521>.
- Fadugba, O. I., Choi, E., & Powell, C. A. (2019). Effects of preexisting structures on the seismicity of the Charlevoix Seismic Zone. *Journal of Geophysical Research: Solid Earth*, 124, 7370–7386. <https://doi.org/10.1029/2019JB017831>.
- Fadugba, O.I., Langston, C.A. and Powell, C.A. (2021). Focal Mechanisms of Relocated Earthquakes and Stress Orientation in the Charlevoix Seismic Zone (submitted).
- Hardebeck, J. L., & Shearer, P. M. (2002). A new method for determining first-motion focal mechanisms. *Bulletin of the Seismological Society of America*, 92(6), 2264–2276. <https://doi.org/10.1785/0120010200>.
- Hardebeck, J. L. (2013). Geometry and Earthquake Potential of the Shoreline Fault, Central California. *Bulletin of the Seismological Society of America* 2013; 103 (1): 447–462. <https://doi.org/10.1785/0120120175>.

- Harris R. A., Archulets R. J. and S. M. Day (1991). Fault steps and the dynamic rupture processes: 2-D numerical simulations of a spontaneously propagating shear fracture. *GRL*, vol. 18, No. 5, pp. 893-896.
- Harris R. A. and S. M. Day (1993). Dynamic of fault interaction: Parrallel strike-slip faults. *JGR*, vol. 98, No. B3, pp. 4461-4472.
- Kraft, T., Wassermann, J., & Igel, H. (2006). High-precision relocation and focal mechanism of the 2002 rain-triggered earthquake swarms at Mt Hochstaufen, SE Germany. *Geophysical Journal International*, 167(3), 1513–1528. <https://doi.org/10.1111/j.1365-246X.2006.03171.x>
- Lamontagne, M. (1999). Rheological and geological constraints on the earthquake distribution in the Charlevoix Seismic Zone, Quebec, Canada. Geological Survey of Canada. Open File, D3778.
- Lamontagne, M. and G. Ranalli (1997). Faults and Spatial Clustering of Earthquakes Near La Malbaie, Charlevoix Seismic Zone, Canada. *Seismological Research Letters* 1997; 68 (2): 337–352. <https://doi.org/10.1785/gssrl.68.2.337>.
- Leonard, M. (2010). Earthquake fault scaling: Relating rupture length, width, average displacement, and moment release, *Bulletin of the Seismological Society of America*, 100, 5A, 1971–1988.
- Mazzotti, S., & Townend, J. (2010). State of stress in central and eastern North American seismic zones. *Lithosphere*, 2(2), 76–83. <https://doi.org/10.1130/l65.1>.
- Ouillon G. C., C. Ducorbier and D. Sornette (2008). Automatic reconstruction of fault networks from seismicity catalogs: Three dimensional optimal anisotropic dynamic clustering. *Journal of Geophysical Research*, Vol 113, No. B01306, <https://doi.org/10.1029/2007B005032>.
- Ouillon G. and D. Sornette (2011). Segmentation of fault networks determined from spatial clustering of earthquakes. *Journal of Geophysical Research*, Vol. 116, No. B02306, <https://doi.org/10.1029/2010JB007752>.
- Powell, C. A., & Lamontagne, M. (2017). Velocity models and hypocenter relocations for the Charlevoix Seismic Zone. *Journal of Geophysical Research: Solid Earth*, 122, 6685–6702. <https://doi.org/10.1002/2017jb014191>.
- Rondot, J. (1971). Impactite of the Charlevoix structure Quebec, Canada. *Journal of Geophysical Research*, 76(23), 5414–5423. <https://doi.org/10.1029/jb076i023p05414>.
- Rondot, J. (1994). Recognition of eroded astroblemes. *Earth-Science Reviews*, 35(4), 331–365. [https://doi.org/10.1016/0012-8252\(94\)90001-9](https://doi.org/10.1016/0012-8252(94)90001-9).
- Somerville, P., K. Irikura, R. Graves, S. Sawada, D. Wald, N. Abrahamson, Y. Iwasaki, T. Kagawa, N. Smith, and A. Kowada (1999). Characterizing crustal earthquake slip models for the prediction of strong ground motion, *Seismological Research Letters* 70, no. 1, 59–80.
- Vlahovic, G., Powell, C., & Lamontagne, M. (2003). A three-dimensional P wave velocity model for the Charlevoix Seismic Zone, Quebec, Canada. *Journal of Geophysical Research: Solid Earth*, 108(B9), 2439. <https://doi.org/10.1029/2002jb002188>.
- Wang Y, G. Ouillon, J. Woessner, D. Sornette, S. Husen (2013). Automatic reconstruction of fault networks from seismicity catalogs including location uncertainty. *Journal of Geophysical Research*, VOL. 118, 5956–5975, <https://doi.org/10.1002/2013JB010164>.
- Wells, D. L., and K. J. Coppersmith (1994). New empirical relationships among magnitude, rupture length, rupture width, rupture area, and surface displacement, *Bulletin of the Seismological Society of America*, 84, no. 4, 974–1002.
- Wyss, M. (1979). Estimating maximum expectable magnitude of earthquakes from fault dimensions, *Geology* 7, no. 7, 336–340.

Zoback, M. L. (1992). First- and second-order patterns of stress in the lithosphere: The world stress map project. *Journal of Geophysical Research*, 97(B8), 11703.
<https://doi.org/10.1029/92jb00132>.

Supporting Information for “Fault Geometry for the Charlevoix Seismic Zone”

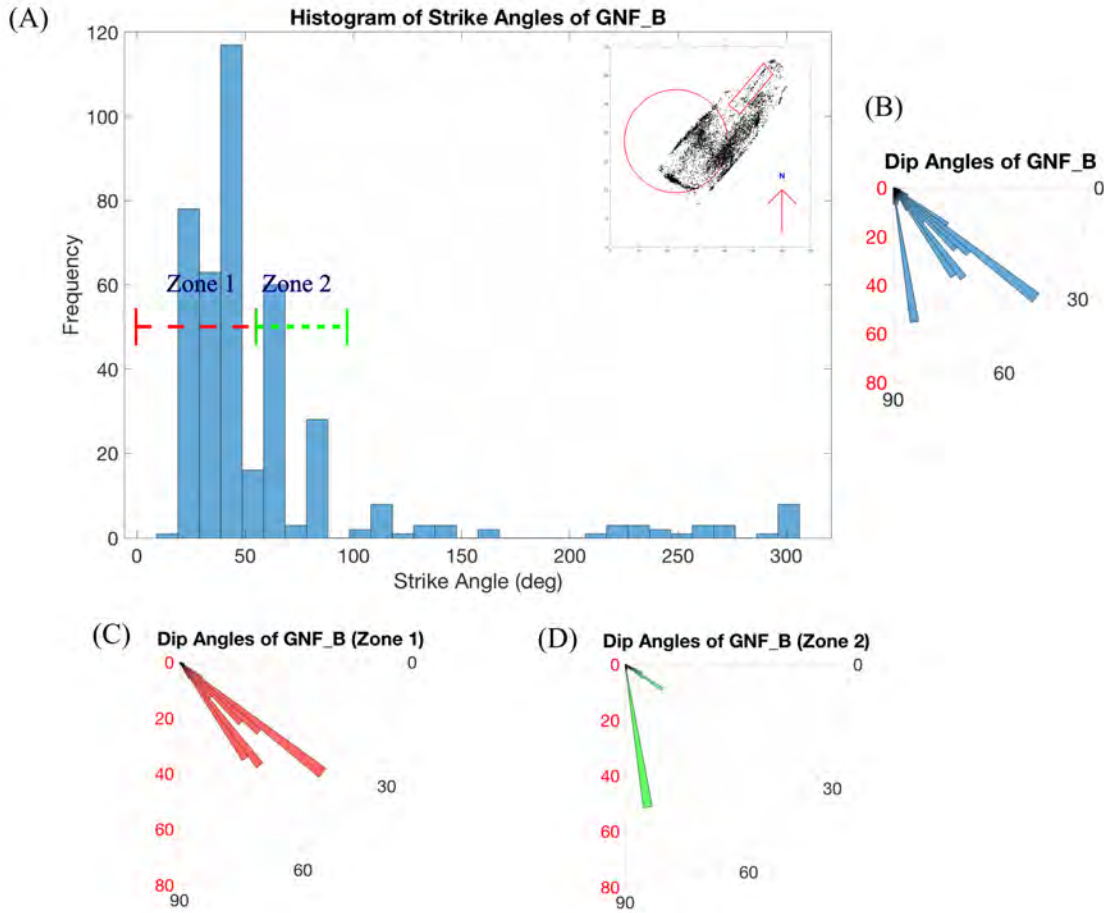


Figure S1: (A) The histogram of the strike angles and (B) the rose diagram of the dip angles of one of the fault groups associated with the Gouffre Northwest fault (GNF_B). In cases when a fault group shows distinct peaks strike angles, we partition the fault cluster into different zones (i.e., Zones 1 and 2) based on the distribution of the peaks. The dotted horizontal line in (A) corresponds to the range of the strike angle in each zone. The inset plot in (A) shows the location of the fault cluster in the fault center map. (C - D) show the rose diagrams of the dip angle of the different zones in (A). We determine the strike and dip angles for each partition. The rose diagram of zone 1 shows different peaks for the group. We further partition the faults based on the dip angles' peaks and determine the fault parameters for each subset. The partitioning suggesting faults with similar strike angles but different dip angles. The fault length, width and fault centers, and their associated one standard deviation are for the faults within 1° of the average strike angle in their earthquake partition.

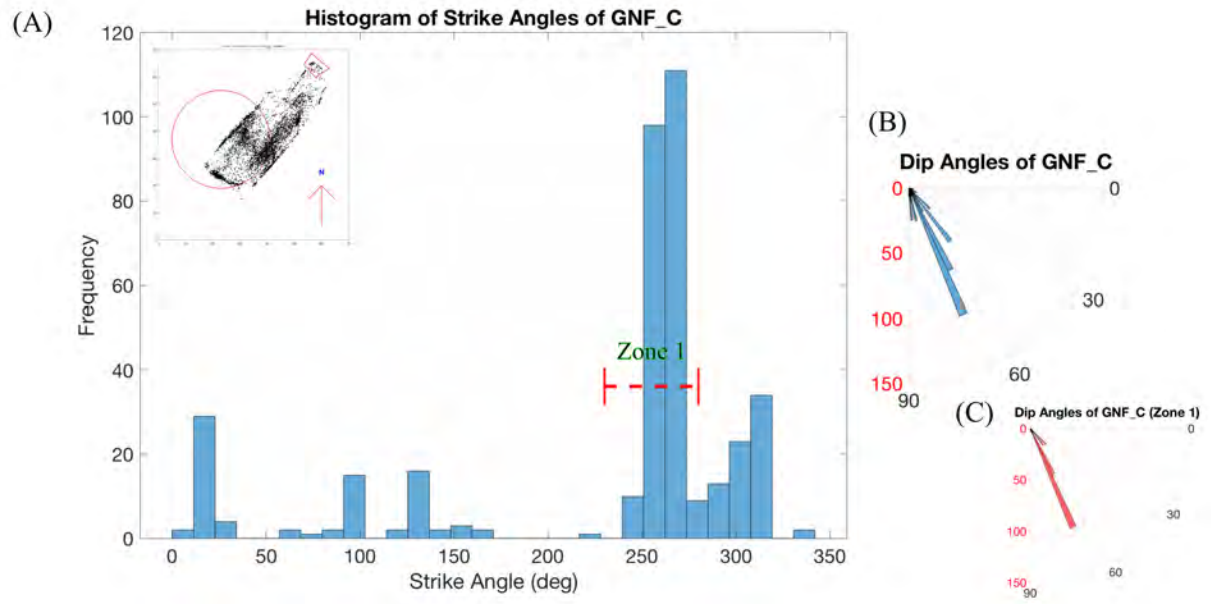


Figure S2: Same as Fig. S1 but for one of the fault groups associated with the Gouffre Northwest Fault (GNF_C).

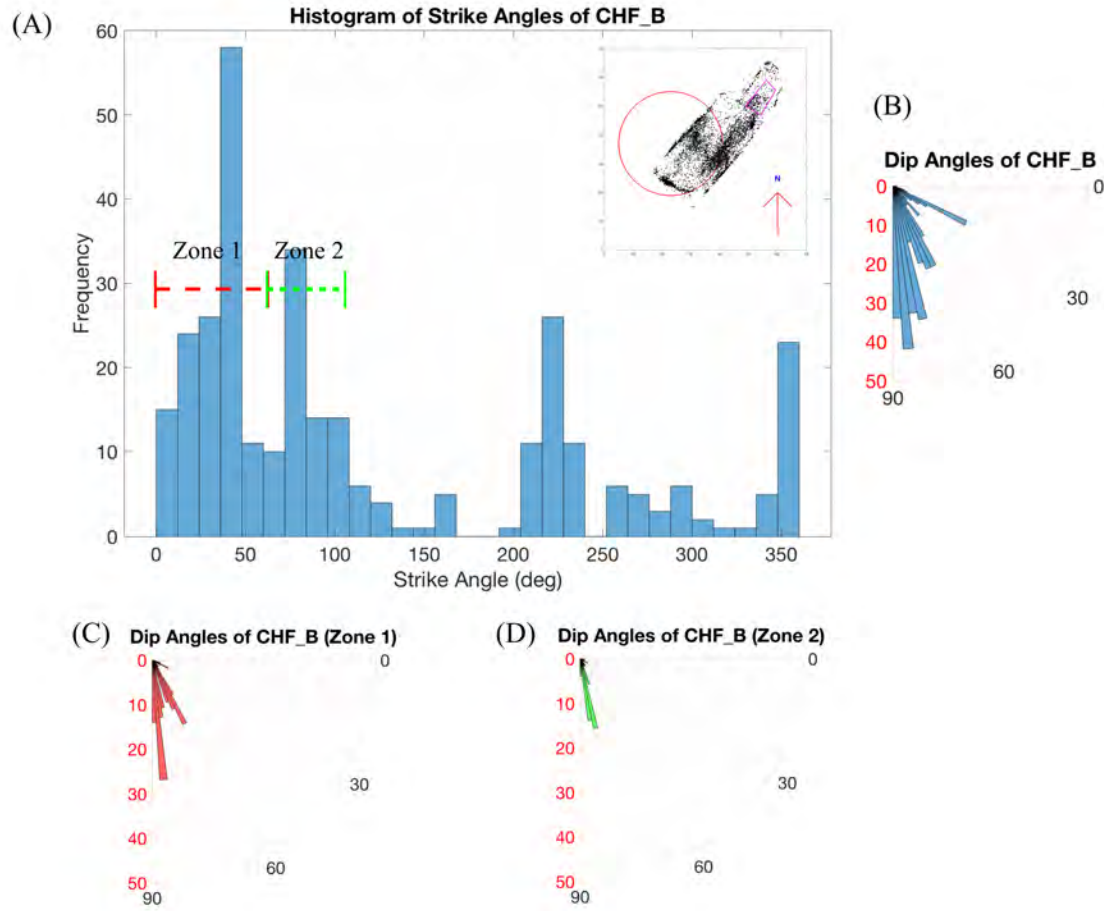


Figure S3: Same as Fig. S1 but for one of the fault groups associated with the Charlevoix Fault (CHF_B).

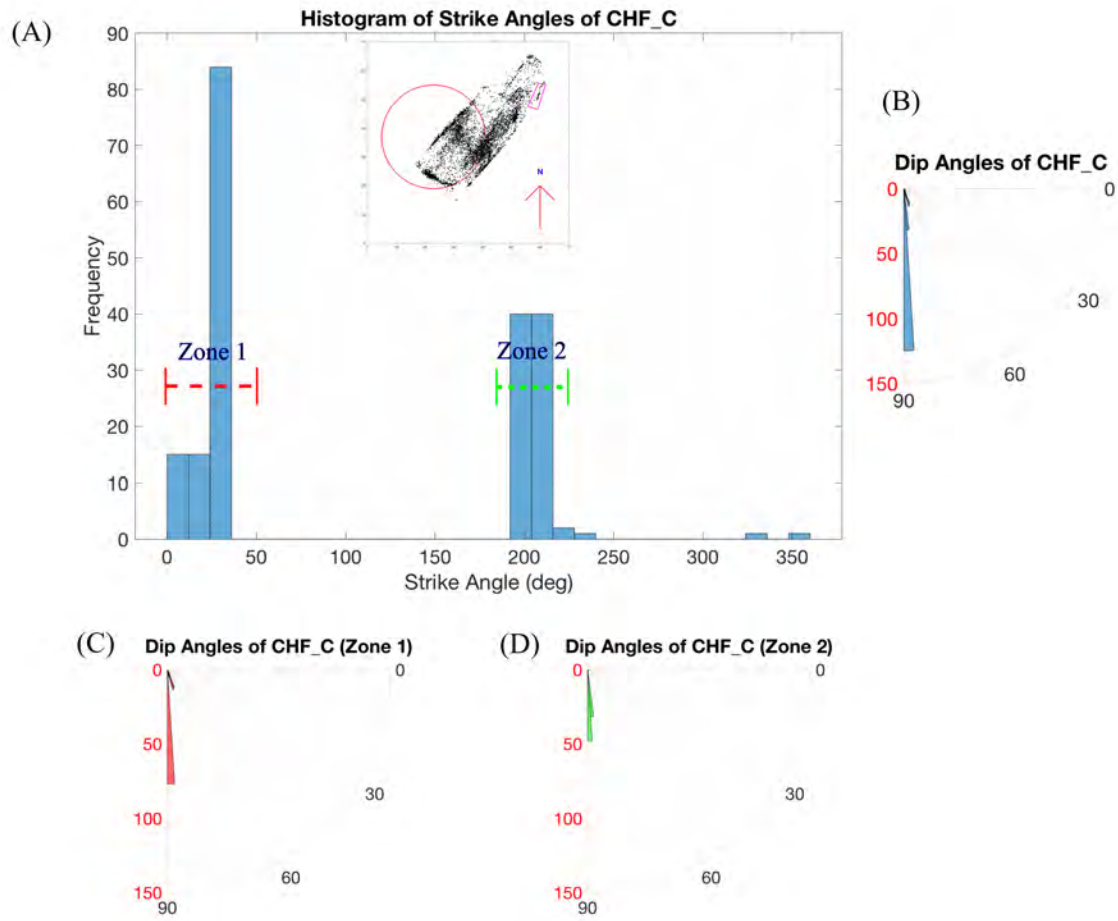


Figure S4: Same as Fig. S1 but for one of the fault groups associated with the Charlevoix Fault (CHF_C).

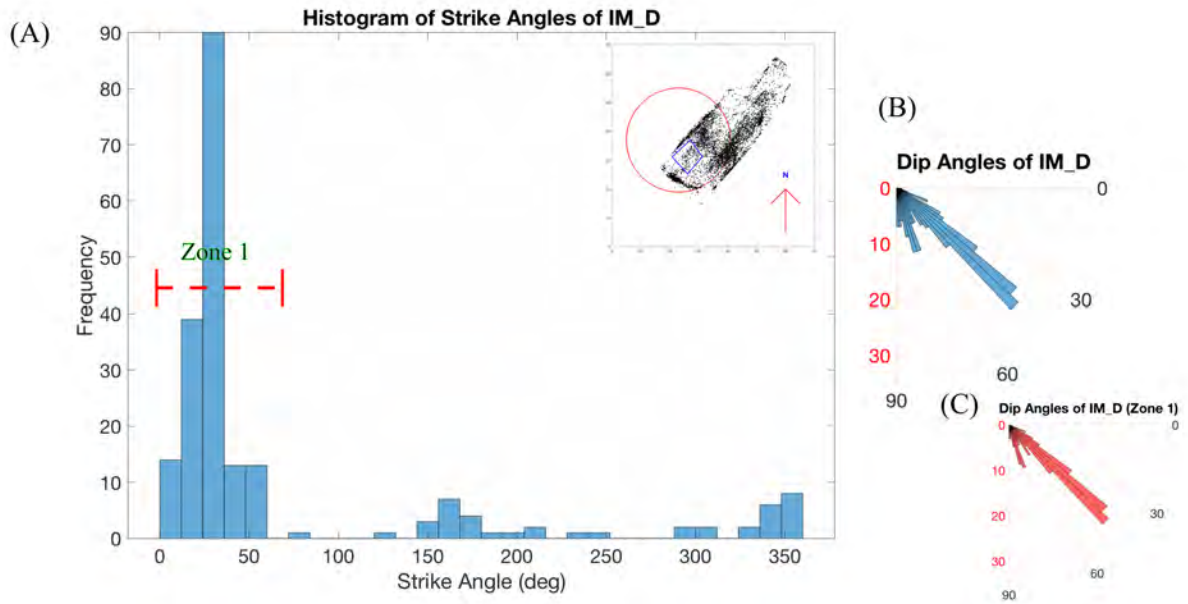


Figure S5: Same as Fig. S1 but for one of the fault groups associated with the impact structure boundary (IM_D).

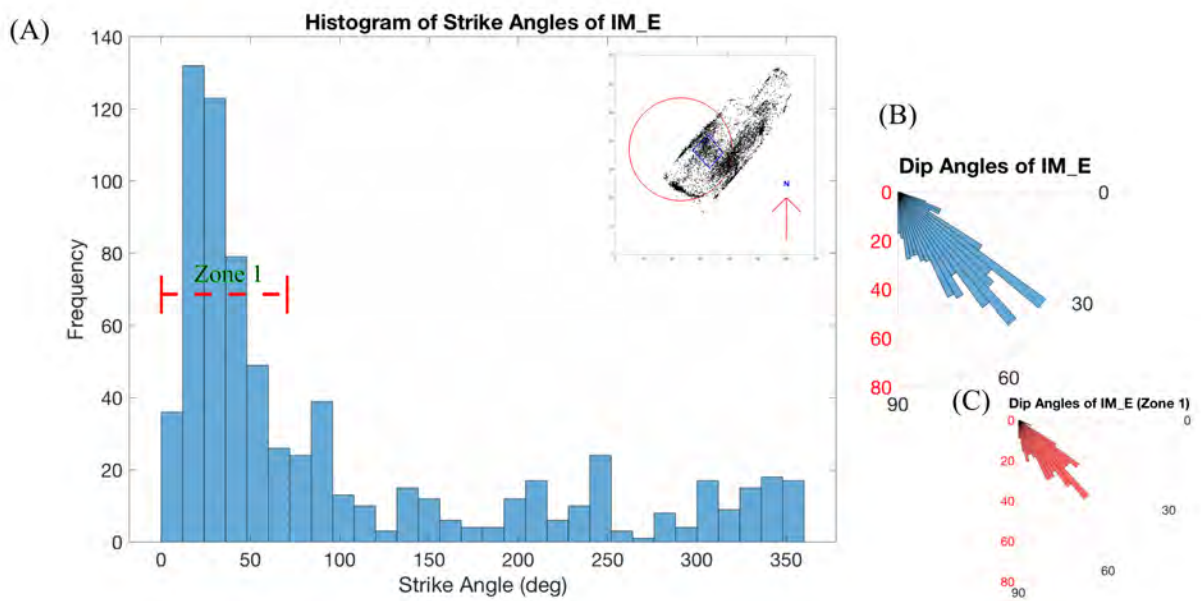


Figure S6: Same as Fig. S1 but for one of the fault groups associated with the impact structure boundary (IM_E).

Fault Model of the Charlevoix Seismic Zone

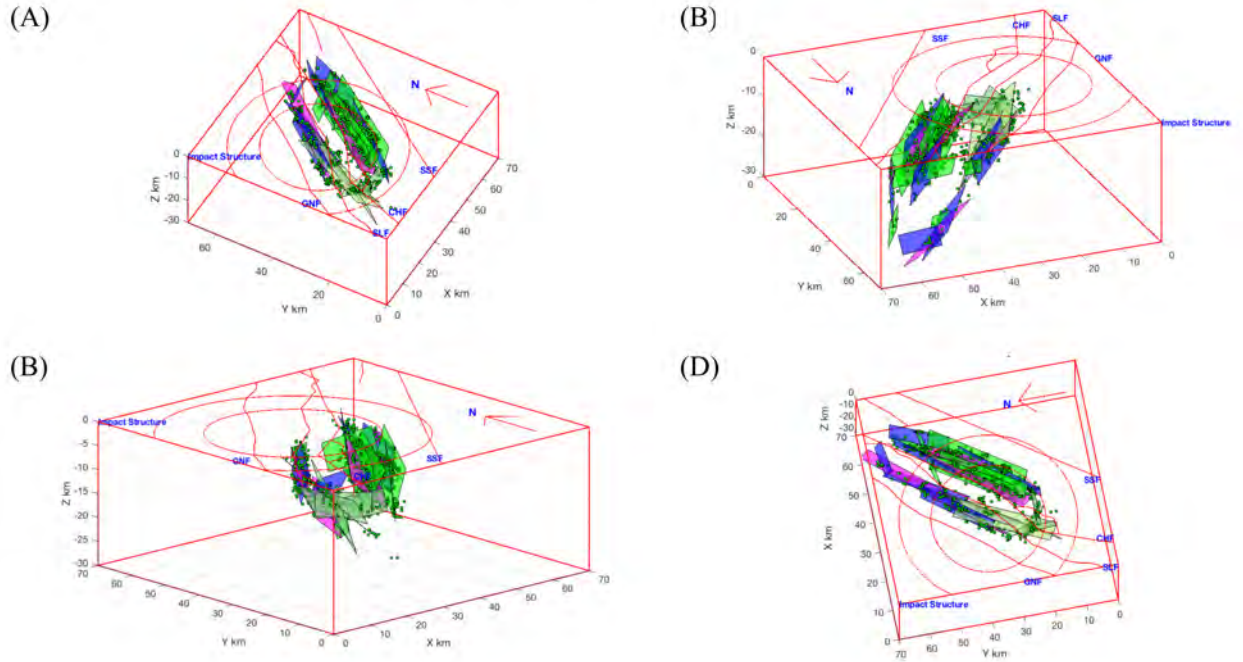


Figure S7: The fault model of the Charlevoix Seismic Zone using the average fault parameters and showing the clustered earthquakes. (A-D) show different views of the fault model. We superimposed fault traces and the outline of the impact structure.

Table S1: Estimation of maximum earthquake moment magnitude using the fault dimension.

	Cases	Length (km)	Width (km)	M_w^a	M_w^b	M_w^c	M_w^d
1	Largest fault	32.7	8.5	6.63	6.47	6.39	6.59
2	Second Largest fault	26.9	9.9	6.62	6.45	6.34	6.58
3	Deep-crustal fault	40.0	25.0	7.19	7.01	6.95	7.15

^a $M_w = \log A + 4.19$ (Stable continental region; Leonard, 2010);

^b $M_w = 0.98 \log A + 4.07$ (all slip types; Wells and Coppersmith, 1994);

^c $M_w = \log A + 3.95$ (Somerville et al., 1999); ^d $M_w = \log A + 4.15$ (for $M_w > 5.6$; Wyss, 1979).

A New Madrid Seismic Zone Fault System Model from Relative Event Locations and Application of Optimal Anisotropic Dynamic Clustering

Yixin Zhang¹, Oluwaseun Fadugba¹, Christine Powell¹, Stephen Horton¹, and Charles A. Langston¹

¹Center for Earthquake Research and Information, The University of Memphis, Memphis, TN

Corresponding author: Yixin Zhang (yzhang22@memphis.edu)

Key Points:

- New Madrid seismic zone hypocenters for the years 2000-2019 are relocated and have a median location error of 64.63m.
- Planes are fit to the relocated hypocenters producing a detailed three-dimensional model of fault structure.
- The Reelfoot fault is continuous along its entire length.

Abstract

A new model of fault structure in the active New Madrid Seismic Zone (NMSZ) is presented based on relocated hypocenters and application of a statistical clustering method to determine fault planes. Over 200 earthquakes are recorded in the NMSZ every year, but the three-dimensional (3-D) fault structure is difficult to determine because the zone is covered by thick, Mississippi Embayment sediment. The distribution of earthquakes in the NMSZ indicates four major arms of seismicity, suggesting the presence of a northeast-southwest trending strike-slip fault system with a major northwest trending, contractional stepover fault. The most seismogenic faults are the strike-slip Axial fault and the Reelfoot thrust fault. Developing an accurate, 3-D fault model is important for dynamic modeling of the fault system and better specification of the seismic hazard. We relocated 4131 hypocenters for earthquakes occurring between 2000 and 2019 using the HypoDD double difference relocation technique. HypoDD is appropriate for the NMSZ because the earthquakes are tightly clustered, and the network stations are dense. The Optimal Anisotropic Dynamic Clustering technique is used to develop the fault structure for the NMSZ using the relocated hypocenters. The 3-D fault model provides a clear indication of the continuity of the Reelfoot fault and suggests a structural relationship between the northern and southern part of the Axial fault.

Plain Language Summary

A new fault model is determined for the active New Madrid seismic zone using earthquakes that occurred from 2000 to 2020. The seismic zone is located in the central United States and poses a hazard to critical infrastructure and numerous population centers. The first step in constructing the improved fault model involved relocation the earthquakes to decrease location error. The

second step involved fitting planes to the relocated earthquakes under the assumption that the earthquakes cluster along fault segments. The resulting model provides a three-dimensional representation of the fault structure. The major fault, the Reelfoot thrust fault, is continuous along its entire length but changes orientation where it is intersected by the strike-slip Axial fault. The northern part of the Axial fault is very well defined. Earthquakes are more scattered along the southern part of the Axial fault but three fault planes are resolved that suggest continuity between the southern and northern parts of the Axial fault. The fault model can be used in studies involving possible rupture length and magnitude of large earthquakes.

1 Introduction

The intraplate New Madrid Seismic Zone (NMSZ) is located in the northern Mississippi Embayment (ME) (Figure 1). Over 200 NMSZ earthquakes are recorded every year but the zone is most noted for three large earthquakes ($M > 7$) that occurred in 1811-1812 (Johnston, 1996; Hough et al., 2000). A recent study indicates that the present seismicity is not a prolonged aftershock sequence from the 1811-1812 events (Page and Hough, 2014); present-day seismicity is being driven by ongoing strain accumulation. Determining the reason for the buildup of strain is hampered by very low deformation rates on the order of 10^{-9} indicated by global positioning studies (GPS) (Calais and Stein, 2009; Frankel et al. 2012, Boyd et al. 2015). The 1811-1812 sequence was not unique; paleoseismic evidence suggests that large NMSZ earthquakes occur roughly every 500 years (Tuttle et al., 2002; 2019). A few models for strain accrual, particularly those involving relaxation of a weak lower crust or upper mantle (Kenner and Segall, 2000; Zhan et al, 2016) and dislocation creep on the lower portion of the major thrust fault (Frankel et al., 2012) reproduce the GPS observations with a high degree of fidelity. Geological observations suggest that slip rates on NMSZ faults have increased in the Holocene, reaching 4.4-6.2 mm/yr (Mueller et al., 1999; Van Arsdale, 2000).

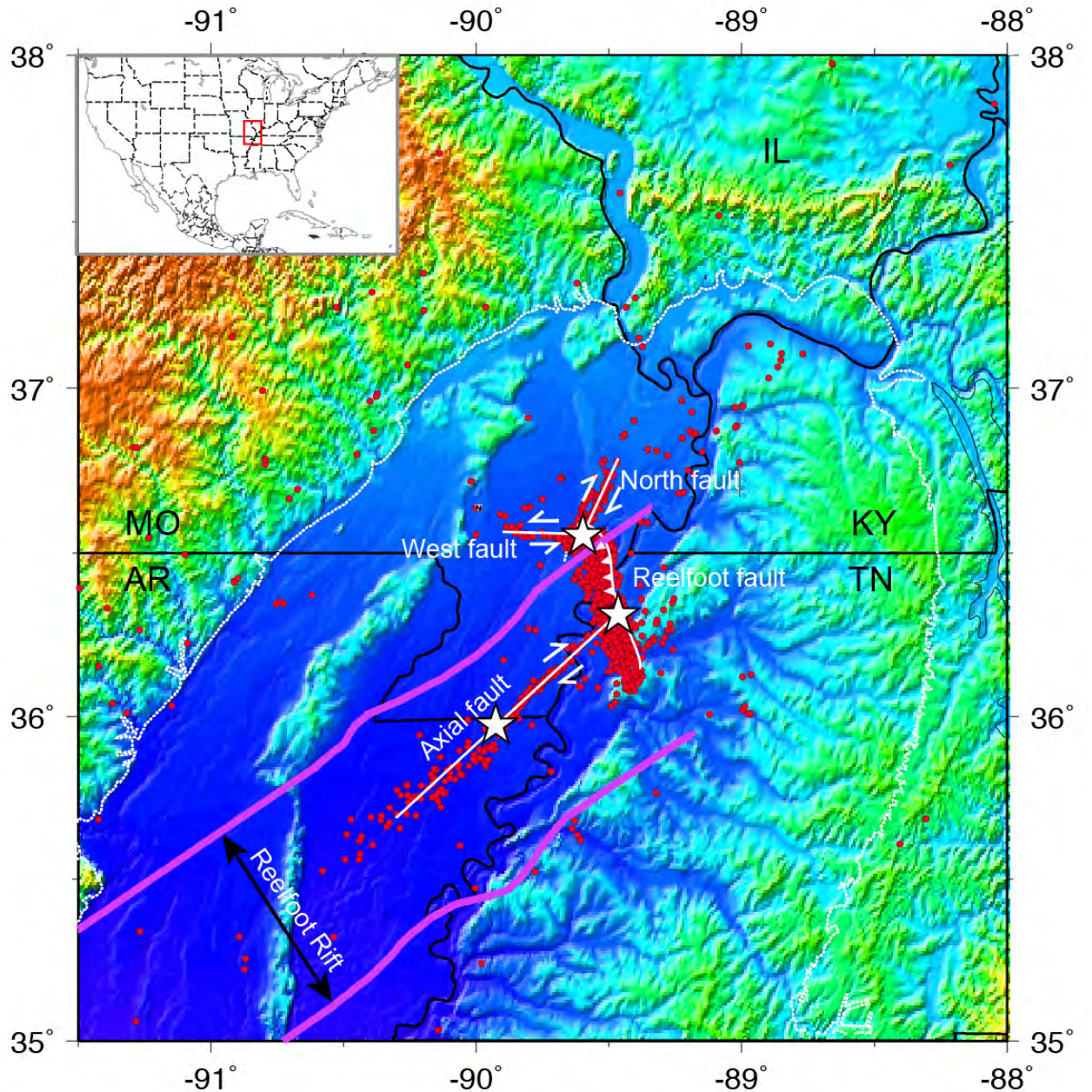


Figure 1. Seismicity (red circles) in the NMSZ and nearby areas compiled by the Center for Earthquake Research and Information catalogs from April 1974 to December 2012. Three white stars are paleo-earthquakes with a magnitude over M 6.0 (Johnston and Schweig, 1996; Hough et al., 2003). Magenta lines indicate the boundary of the Reelfoot Rift. White dashed line is the boundary of the Mississippi Embayment. The inset map shows the location of the present study area (red box). Basic NMSZ fault geometry and offsets are indicated by white lines. MO: Missouri; IL: Illinois; KY: Kentucky; TN: Tennessee; AR: Arkansas. (modified from Dunn et al., 2013).

Four major fault arms in the NMSZ are illuminated by the distribution of seismicity (Figure 1), a vertical left-lateral strike-slip fault (West fault, WF) with a strike of about 270° to 280°, a vertical right-lateral strike-slip fault (North fault, NF) with a strike of about 25° to 30°, a

vertical right-lateral strike-slip fault (Axial fault, AF) with a strike of about 40° to 50° and an approximately northwest-southeast trending thrust fault (Reelfoot fault, RF). The RF is divided into northern and southern parts near the intersection with the AF (Figure 1). The northern segment is interpreted as a compressive stepover between the right lateral AF and NF strike slip faults (e.g. Pratt, 2012). The presence of the southern segment of the RF is difficult to define in terms of a simple structural model and this segment is cut by at least one northeast trending fault (Csontos and Van Arsdale, 2008). The northern and southern RF segments have different strike and dip angles.

Accurate fault models are needed to properly assess the hazard that the NMSZ poses to the central United States. The most detailed three-dimensional (3-D) fault model was developed by Mueller and Pujol (2001) based on the distribution of about 550 relocated NMSZ hypocenters. This study centered on the RF and divided the fault into northern, central, and southern segments. Structural contours of the thrust surface were determined by dividing the fault into strips oriented perpendicular to the local fault strike, projecting the earthquakes in each strip to the center line and fitting the fault surface by hand. The resulting model captured the change in strike and dip along the RF from about $N28^{\circ}W$ in the south, to NS in the center, to $N10^{\circ}$ to $20^{\circ}W$ in the north. The dip on the southern portion of the fault is steeper than on the northern portion.

In this study, we will determine a more complete fault model for the NMSZ that includes the strike-slip arms of seismicity as well as the RF. HypoDD (Waldhauser and Ellsworth, 2000) will be used to relocate NMSZ earthquakes recorded between 2000 and 2019. Optimal Anisotropic Dynamic Clustering (OADC) will be used to generate three-dimensional (3-D) fault structure, under the assumption that hypocenters cluster along fault surfaces. Ouillon et al. (2008) applied OADC to the 1992 Landers California earthquake aftershock sequence and arrived at a successful match between modeled fault structure and known faults based on geological mapping (Ouillon et al., 2008). The technique was used by Hardebeck (2013) to investigate the geometry of the Shoreline fault near San Luis Obispo, California and most recently by Fadugba (2021) to delineate fault structure in the Charlevoix seismic zone. The large number of earthquakes and the high station density make the NMSZ an excellent candidate for OADC analysis. We will use OADC to cluster the relocated hypocenters and create a reasonable fault model for the NMSZ that specifies fault locations, dimensions, and strike and dip angles.

1.1 Tectonic History

During the supercontinent Rodinia fragmentation in the early Paleozoic, several grabens, including the Reelfoot Rift, were generated in Precambrian basement rock, inboard of the rifted margin (Thomas, 1991; Thomas, 2006). The extension thinned and weakened the ME lithosphere possibly leading to mafic intrusions in the lower crust. The rift was compressed during the late Paleozoic Ouachita orogeny. Uplifts, including the Pascola arch roughly coincident with the RF, occurred and some intrusions may have been emplaced along the rift axis and margins. The thinned lithosphere below the rift allowed upwelling of high-temperature fluid during passage of the Bermuda hotspot in the Cretaceous (Cox and Van Arsdale, 1997; 2002). Intrusions along the axis and margins of the rift were also emplaced during this time and passage of the hotspot may have resulted in formation of the ME (Cox and Van Arsdale, 1997; 2002). Thick, unconsolidated Upper Cretaceous and younger sediments cover the ME (Cox and Van Arsdale, 2002; Hildenbrand and Hendricks, 1995) and make it difficult to determine the faulting kinematics.

The only surface expression of faulting in the NMSZ is the Reelfoot scarp, a 32km long uplift that is associated with the RF thrust. The scarp has up to 9m of structural relief due to monoclinial flexure (Mueller et al., 1999). Widespread sandblows attest to the occurrence of strong, repeating earthquakes in the zone (e.g. Tuttle et al., 2002; 2019). Uplift rates may have increased in the Holocene in the NMSZ and along the eastern rift margin based on seismic reflection interpretations (Van Arsdale, 2000; Hao et al., 2013).

2 Methods

2.1 Double-Difference (DD) Relocation

The velocity structure associated with the NMSZ is complex and the double difference inversion method of Waldhauser and Ellsworth (2000) will minimize the effects of unmodeled velocity heterogeneity when determining earthquake relocations. HypoDD takes advantage of dense earthquake and station distributions which makes the NMSZ an excellent candidate for the method.

We used the HypoDD program (Waldhauser, 2000) to determine the relative relocations. Each input event was linked with at least 8 neighbor events within a 10 km radius. The double-difference travel time residuals were calculated for each pair of events and minimized in the inversion process using either the conjugate gradient method (LSQR, Paige, 1982) or singular value decomposition (SVD). For both inversion approaches, HypoDD minimizes the residuals between the observed arrival time differences from paired stations and the calculated differences by updating the hypocenters and reweighting the data iteratively, until the residual becomes lower than the noise level or until the number of iterations reaches a preset limit (Waldhauser, 2001).

2.1.1 LSQR inversion

LSQR is efficient when dealing with a large number of sparsely located events; it can be used to analyze a large hypocentral system by solving the damped least-square problem. HypoDD uses damping to regularize the solution. A condition number (CND), representing the stability of the system, is returned as well as a root-mean-squared residual (RMS) time for the solution in milliseconds. The damping factor should be in the range 1 to 100 and reasonable CND values should lie between 40 and 80 (Waldhauser, 2001).

To improve the LSQR results, we partitioned the NMSZ events into 8 clusters according to their probable kinematic structure (Figure 2). Clusters 1, 2 and 6 represent the three strike-slip faults, the WF, NF and the AF. Events in cluster 7 are more scattered than those in cluster 6 and they are therefore placed into a separate cluster. Clusters 3, 4 and 5 together cover the main RF. We separated the RF into 3 clusters because prior research indicates that the three segments have different strike and dip angles (Mueller and Pujol, 2001; Parrish and Van Arsdale, 2004; Csontos and Van Arsdale, 2008; Pratt, 2012; Greenwood et al., 2016; Delano et al., 2018). Cluster 8 contains events at the intersection of clusters 1, 2 and 3, that cannot be placed into any of the other clusters.

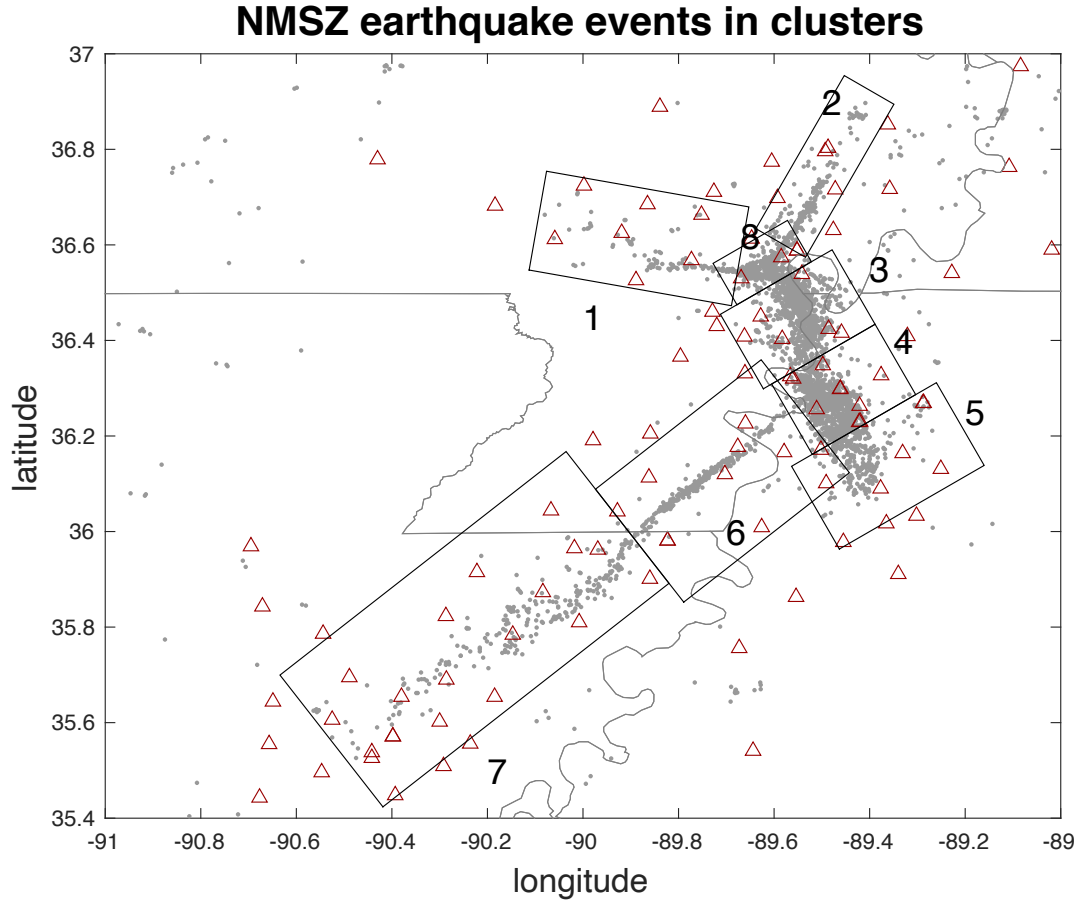


Figure 2. Partitioning used for the HypoDD relocation analysis. Grey dots are the NMSZ earthquakes. Red triangles are NM seismic stations. State boundaries are indicated. Black boxes separate earthquakes into 8 clusters based on fault type and prior studies indicating segmentation along the RF.

The HypoDD program can use any combination of original phase-picked earthquake catalog times and waveform cross-correlated differential times (Waldhauser and Ellsworth 2001). Users can set different weights for each dataset in any iteration. Original phase-picked catalog data (catalog data; CT) are more numerous than the waveform cross-correlated catalog data (cross-correlation data; CC), while the CC data are more accurate. To test the stability and quality of the NMSZ data, we ran HypoDD with LSQR using the CT data only and then using CC data only. For both datasets, we ran the inversion for the 8 separate clusters shown in Figure 2 and then combined the results. This produced 4422 event relocations with a median RMS residual of 60 milliseconds for the CT data and 2647 event relocations with a median RMS residual of 38 milliseconds for the CC data (see Supporting Information Figures S1 and S2).

Based on both the CT and CC data results using HypoDD with LSQR, we tested several sets of data weights and determined the appropriate weights as indicated in Table 1. For the first 2 iterations, we weighted CT data higher to include more event information. For the following iterations, we increased the weights for the more accurate CC data. S waves are generally less accurate than P waves, thus we lowered the weights of the S waves for both data types (CT and

CC). After applying the weights in Table 1 and adjusting damping parameters for the 8 clusters, a set of CND numbers and RMS residual times for both types of data were generated and listed in Table 2. With one small exception for cluster 3, the CND numbers are within the reasonable range (40 to 80, Waldhauser, 2001). The damping values used for clusters 3, 4 and 8 are high, which may indicate low stability for these clusters. Supporting Information Figure S3 indicates that relocation using both types of data (CT and CC) results in a much smaller RMS residual than using CT data alone.

TABLE 1. WEIGHTING VALUES FOR INPUT DATA

Iteration	CC P wave weight	CC S wave weight	CT P wave weight	CT S wave weight
1-2	0.01	0.008	1	0.8
3-5	1	0.8	1	0.8
5-8	1	0.5	0.2	0.1

TABLE 2. RELOCATION PARAMETERS AND RESULTS

Cluster	Event # before relocation	Event # after relocation	CND	Damping	RMS CT (ms)	RMS CC (ms)
1	115	111	53	40	42	13
2	218	209	59	45	45	14
3	1251	1192	81	100	39	13
4	1421	1156	79	100	32	7
5	286	286	56	50	33	10
6	357	335	61	55	32	10
7	321	306	69	55	44	9
8	865	839	70	90	39	9

2.1.2 SVD inversion

The SVD method can only process a small number of events (we used 50 in our study) but gives more accurate solutions than LSQR along with relocation errors. The SVD approach is more efficient when examining small hypocenter datasets. To use SVD, we first roughly partitioned events by their locations into a by a ($a=0.2$ rad degree) sized blocks. To make sure each block has less than 50 events, we continuously partitioned blocks which have more than 50 events into 4 equally sized blocks. The smallest blocks have a size of $a/64$ by $a/64$. Then,

HypoDD was run using SVD for each block to obtain event relocations and the associated errors in meters. The process of event partitioning can cut off events from their linked neighbor events and prohibit them from pairing with other events in adjacent blocks. To compensate for the loss, we shifted the starting point of the partitions to the northeast at lengths of $\frac{\sqrt{2}}{2}a$, $\frac{\sqrt{2}}{4}a$, $\frac{\sqrt{2}}{8}a$, $\frac{\sqrt{2}}{16}a$, $\frac{\sqrt{2}}{32}a$, $\frac{\sqrt{2}}{64}a$, $\frac{\sqrt{2}}{128}a$ and ran the inversion 7 more times. All blocks are overlapped by different blocks at least once. In the end, we used the location with the smallest error for each event. A comparison between the LSQR and SVD results is presented in the Supplemental Material. The SVD results are used for the OADC analysis.

2.2 Optimal Anisotropic Dynamic Clustering

OADC (Ouillon et al., 2008) is a planar fault recognition technique to determine 3-D fault structure from the spatial distribution of hypocenters in a region with elevated seismicity. It is a generalization of the dynamic clustering method (or k -means clustering method (Likas et al., 2003)) which partitions n observations into k clusters using the variance of the observations about their center of mass (barycenter) as a global minimization criterion. Specifically, the k -means method involves first setting k initial centroid points randomly and then calculating the distances between each observation and each initial point. The n observations are then clustered into k groups where, in each group, the observations share the same nearest centroid. A new set of centroid points are appointed by using the calculated mean point of each cluster. The clustering will run iteratively until a configuration is reached that produces the smallest variance (Likas et al., 2003).

Ouillon et al. (2008) develop a minimization criterion that takes into account the whole covariance tensor of each cluster, leading to the concept of 3-D dynamic clustering. The fault planes for each cluster are determined using principal component analysis of the covariance tensor to develop optimal fault geometries. Following the k -means approach, the hypocenters are partitioned into different clusters based on their proximity to an initial, random fault(s). Eigenvalue-eigenvector analysis of the covariance matrix of each cluster is used to determine the dimensions and orientation of the optimal fault plane. The whole covariance matrix of a cluster is

$$C = \begin{pmatrix} \sigma_x^2 & cov(x, y) & cov(x, z) \\ cov(x, y) & \sigma_y^2 & cov(y, z) \\ cov(x, z) & cov(y, z) & \sigma_z^2 \end{pmatrix}.$$

Assume $\lambda_1, \lambda_2, \lambda_3, u_1, u_2, u_3$ are eigenvalues and eigenvectors, respectively, obtained by diagonalizing the covariance matrix C . The largest eigenvalue λ_1 , refers to the length of the 3-D cluster (i.e. fault plane length), λ_2 , refers to the width of the fault plane and λ_3 , refers to the thickness.

If earthquakes are uniformly distributed over a fault of length L and width W then $L = \lambda_1 \sqrt{12}$ and $W = \lambda_2 \sqrt{12}$ (Ouillon et al., 2008). The square root of λ_3 is the standard deviation of the location of the earthquakes perpendicular to the fault plane and should be on the order of the location uncertainty. In addition, u_3 is the pole to the plane and specifies the strike and dip of the fault. Following the k -means method, the hypocenters are partitioned again after the first iteration into different clusters using the updated fault geometries. The algorithm is repeated for

the initial number of faults until the faults converge to a fixed geometry (i.e. the maximum value of λ_3 is smaller than an allowable thickness). The objective is to partition the hypocenters by minimizing the sum of all λ_3 values obtained for each clustering so that the partition will converge to a set of clusters that tends to be as thin as possible in one direction while being arbitrary in the other directions. A maximum number of clusters is set to account for the possibility that the program will fail to converge. The OADC method tends to find a near horizontal plane for a cluster that consists of hypocenters in a small depth range relative to the horizontal area (Ouillon et al., 2008; Ouillon and Sornette, 2011; Hardebeck, 2013). Thus, a constraint is placed on the dip angle to avoid modeling subhorizontal planes.

The OADC program we used was developed by Fadugba et al. (2019). Hypocenter errors from the original catalog were used to set the maximum thickness of the fault planes, λ_3 , to 1.2 km. Using smaller errors determined by the HypoDD analysis prevented the program from converging. A similar problem was encountered by Ouillon et al. (2008) in the analysis of the Landers, California earthquake aftershocks and the original catalog error was used in that study. The program output includes the spatial dimensions, orientation and location for each fault plane. We set the maximum number of possible planes to 100 and we set a minimum dip angle of 10° to avoid generating subhorizontal planes. The simulation ran 5 times for each increment in the number of fault planes to improve the convergence success rate and we chose the result that has the minimum λ_3 .

2.3 Declustering Analysis

We removed outlying hypocenters from clustered hypocenters prior to the OADC analysis to facilitate identifying accurate fault planes. We used a declustering program developed by Fadugba (2021) that is based on the cumulative tetrahedra volume method of Ouillon and Sornette (2011). A detailed description is presented in Fadugba (2021). Briefly, a randomized catalog of events for a particular portion of the NMSZ was generated. We determined the volume of tetrahedra formed with quadruplets of nearest neighbor events for each hypocenter for both the observed and randomized catalogs. After determining the cumulative distributions of the volumes of the observed and randomized catalogs, we separated the diffuse earthquakes from the observed earthquakes by removing all hypocenters in the observed catalog with volumes above a certain volume threshold. Following Fadugba (2021), we use the 5% quantile as the maximum threshold of the tetrahedra volume distribution to model the diffuse earthquakes

3 Data

Broadband data were obtained from the Center for Earthquake Research and Information (CERI) earthquake catalog. We used earthquakes recorded from Jan 1st, 2000 to Dec 31st, 2019 within an area from $35.5^\circ N$ to $36.9^\circ N$ and from $90.6^\circ W$ to $89.2^\circ W$ (Figure 2). This dataset includes 4568 earthquakes recorded by 314 stations.

Waveform cross-correlated data were generated using a program developed by Horton et al. (2005). We set the threshold for the cross-correlation coefficient to 0.7 and developed a cross-correlation catalog containing 4486 earthquakes.

4 Results

4.1 Relocation

Relocations determined using HypoDD with SVD are shown in Figure 3. As is indicated in the histogram (Figure 3b), the mode of the residual time is located in the 10 to 15 ms range. About 1800 events have an RMS residual below 15 ms. A comparison between original catalog hypocenters and relocated hypocenters for each group in Figure 3 is presented in Supporting Information Figure S4. The SVD solution also returns the error in meters for event relocations. The accuracy of earthquake locations in the NMSZ is significantly improved using HypoDD as can be seen in Supporting Information Figure S5, showing the original event errors and the relocated event errors. Relocated events in the NMSZ have a minimum error of 10.63m, a median error of 64.63m, and a mean error of 109.99m. This is a significant reduction of hypocenter uncertainties from the original uncertainties averaging about 1 km. The RMS residuals for the HypoDD solution for each cluster shown in Figure 2 are plotted in Figure 4. Clusters 4, 5 and 6 contain the smallest RMS residuals, indicating more stable hypocentral relocations than in the other clusters.

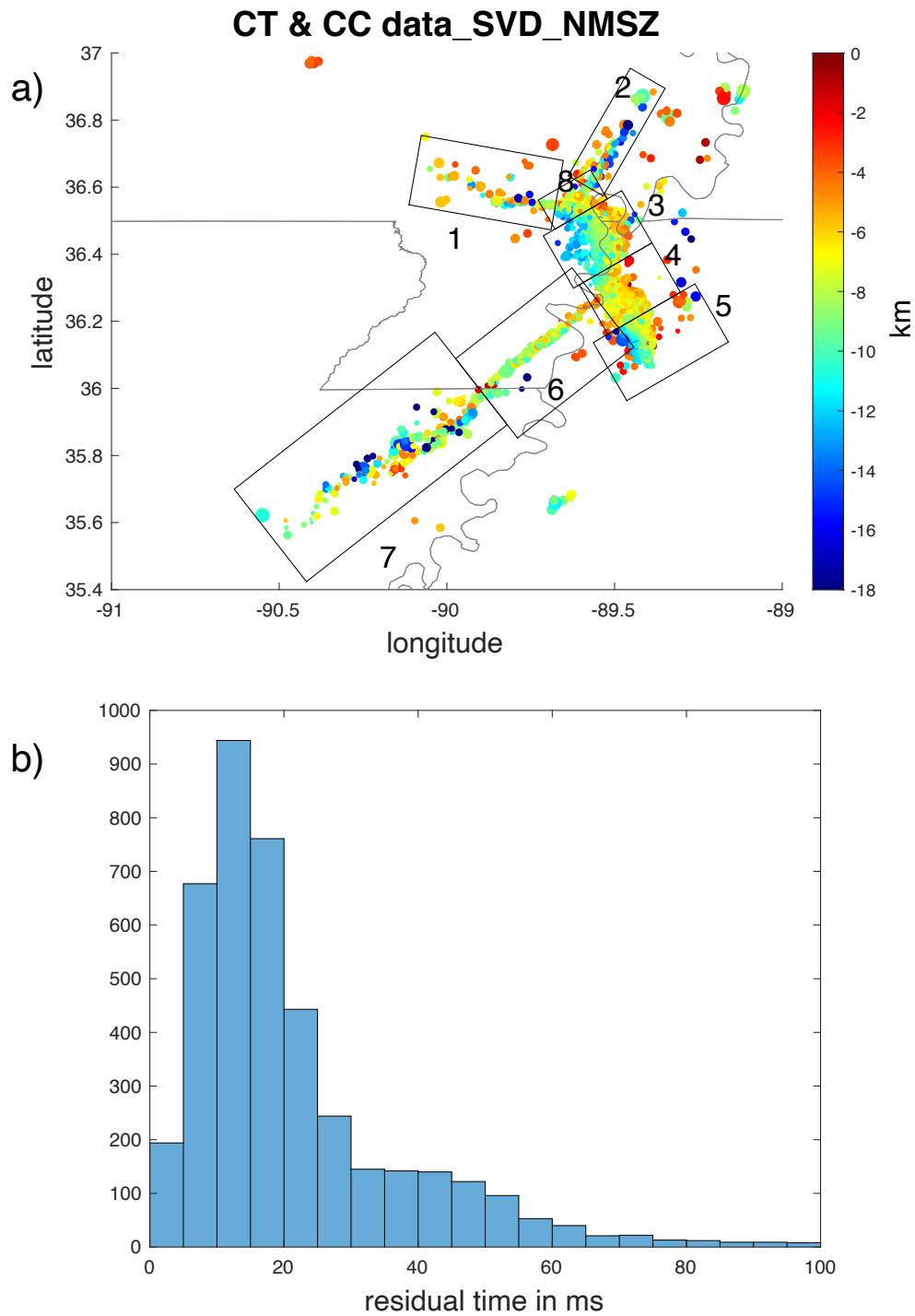


Figure 3. (a) NMSZ event locations determined using HypoDD using both catalog data and cross-correlated data. Circles represent earthquakes; the size of circles is proportional to the earthquake

magnitude, ranging from 0.1 to 3.9. The color scale shows the hypocenter depth. (b) Histogram of the residual times for the 4131 events.

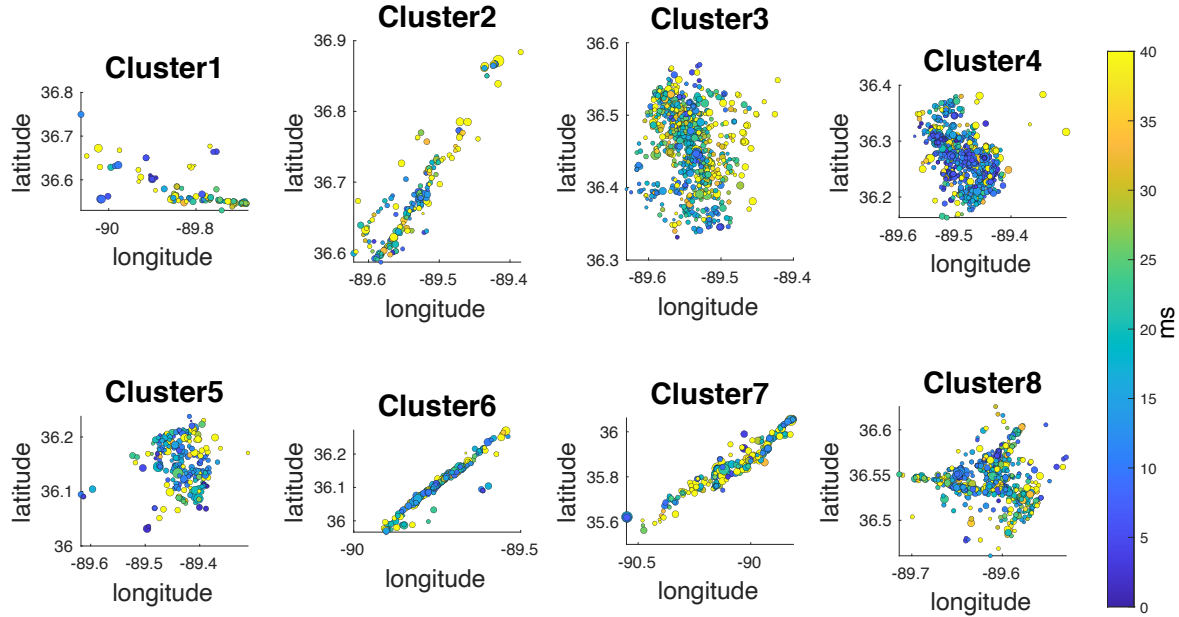


Figure 4. NMSZ event relocations determined using HypoDD using both catalog data and cross-correlated data in each cluster. The color scale is the RMS time residual.

The relocated hypocenters in Figure 3 provide a detailed view of structure on the RF. The northern and southern parts of the fault (clusters 3 and 5) have the least complicated structure and are clearly dipping to the southwest. The dip on the southern part is steeper than the dip on the northern part, in agreement with the assessment by Mueller and Pujol (2001). Structure in the middle part of the RF (cluster 4) is more complex and the fault is not as deep as the northern and southern parts. A shallow, crosscutting, northeast-trending fault is present in this cluster as indicated by the orange band of seismicity. The northern part of the AF (cluster 6) is very well defined and does not extend deeper than about 10 km. The fault is shallower near the intersection with the RF, possibly indicating more structural complexity.

4.2 OADC fault models

The spatial dimensions of the NMSZ fault system make it difficult to use OADC modeling for the whole NMSZ; the horizontal extent of the seismic zone is much larger than the vertical extent, giving it a flat shape and OADC will tend to model this as a flat fault. To avoid this problem, we separated the NMSZ into 3 areas, the northern part (NP) containing the WF and NF and the intersection of WF and NF and RF, the remaining RF part (RFP), and the AF part (AFP). The separate parts are shown in Figure 5 along with the results of the declustering analysis.

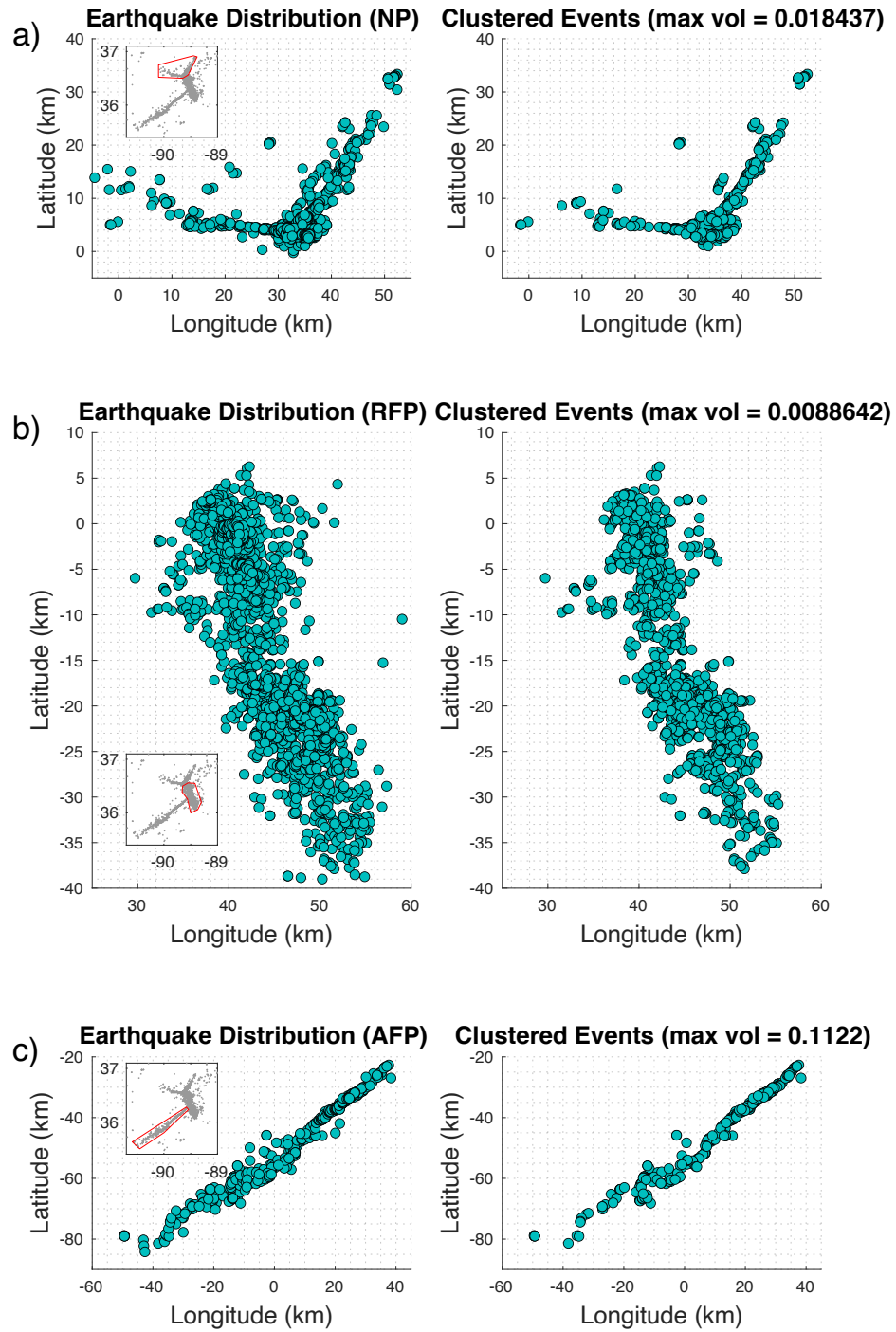


Figure 5. a) b) c) are the Northern Part (NP), Reelfoot Part (RFP), and the Axial Fault Part (AFP) of the NMSZ, respectively. For each area, the relocated hypocenter distribution is shown on the left and the remaining hypocenters after declustering are shown on the right. For each area, we use 5% quantile as the maximum threshold of the tetrahedra volume distribution to model the diffuse earthquakes (see Fadguba

2021). The maximum tetrahedra volume value for each area is labeled in the top of the figures on the right in km^3 (Ouillon and Sornette, 2011).

Since the starting plane and added planes in each increment of the OADC modeling are random, the resulting fault models will be different for each run. Two runs for the RFP are shown in Figure 6 as an example. Both models have the main fault plane indicating a northwest trending, southwest dipping thrust fault. However, the sizes of the thrust fault planes in the two models are different, as well as their locations and their strike and dip angles. Some minor faults that pass through the main faults are present in both models, and some are quite different from each other. Due to the complexity of the NMSZ, we ran 500 models for each of the three parts shown in Figure 5. There were 208, 383, and 218 models that converged within the threshold thickness $\lambda_3 = 1.2 \text{ km}$ for the NP, RF, and AF parts, respectively. For faults that appear in several successful model results, we calculate their average plane strike and dip angles (all strike and dip angles follow the right-hand rule), location, width, length and thickness. We remove randomly distributed faults that just occur in a few models. We also plot the centers of the acceptable fault planes to examine the tendency of the hypocenters to cluster into faults (Figure 7).

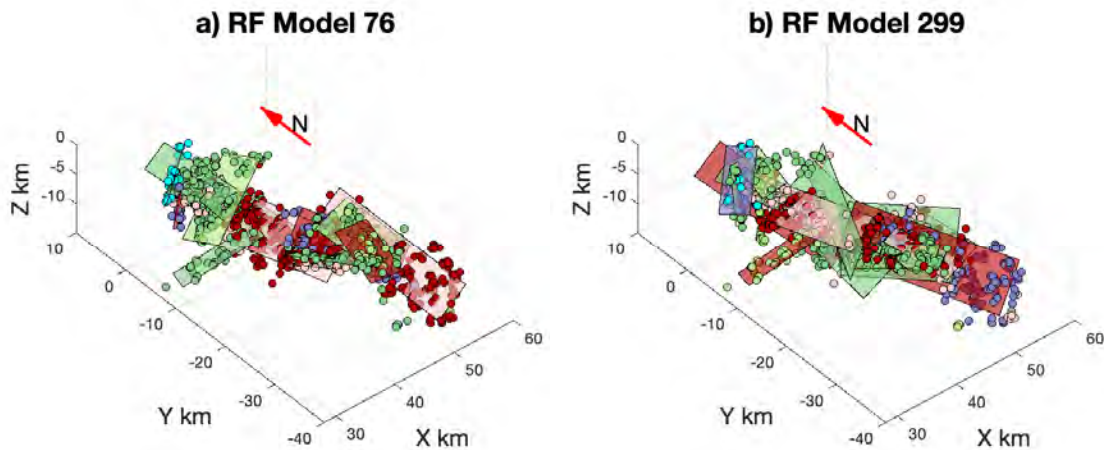


Figure 6. Two fault models for the RF area. The main RF thrust fault shows up striking to northwest and dipping to the southwest in both models, as well as some minor faults, such as the long-narrow fault intersecting the north RF area.

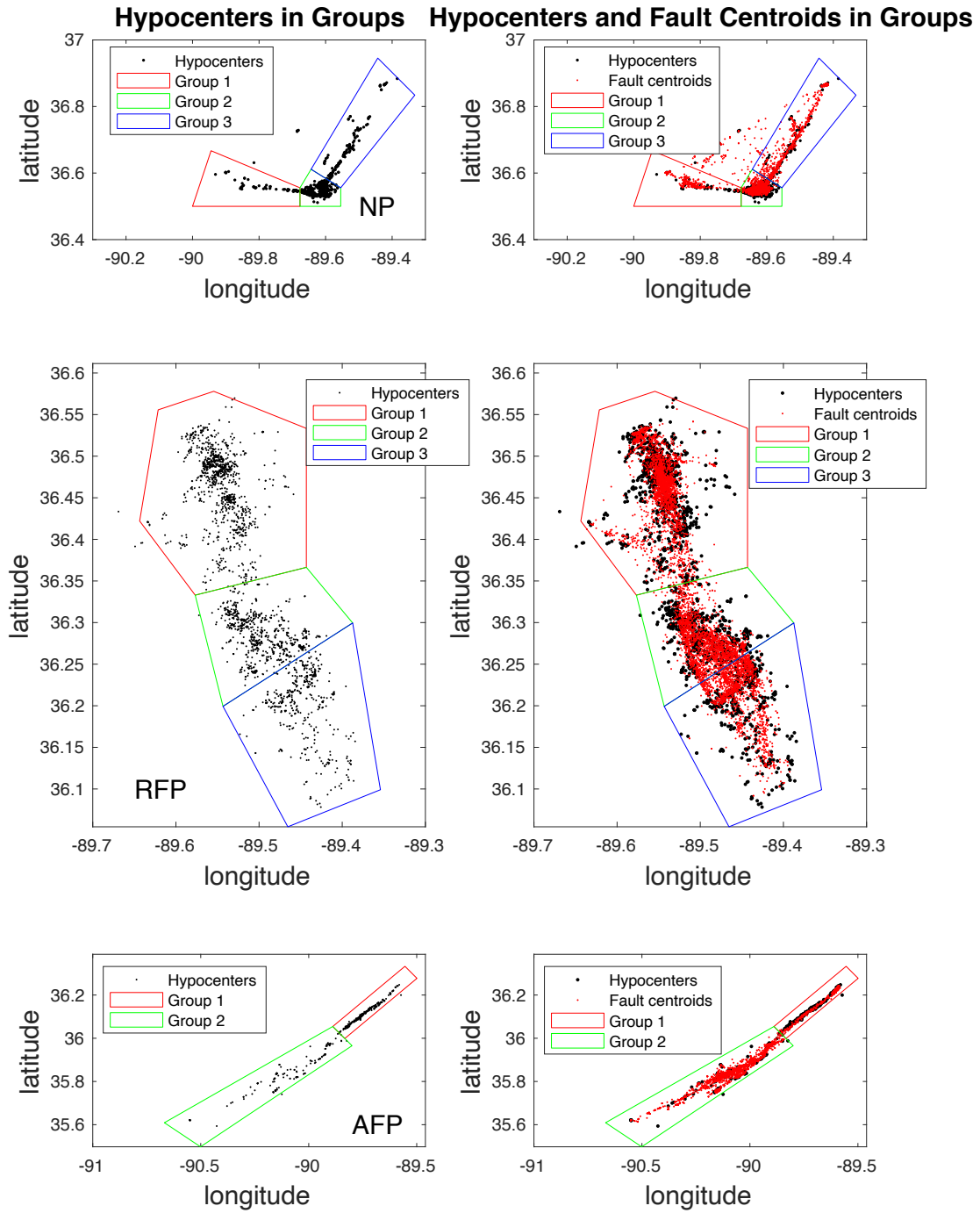


Figure 7. Left) The three areas for OADC analysis and how they are subdivided into groups. Right) black dots are earthquakes; red dots are the central points on all resolved fault planes.

We subdivide each area in Figure 5 into groups based on the distribution of seismicity (Figure 7). The analysis of the RFP, the most seismogenic part of the NMSZ is presented in Figures 8-10 and is discussed in detail below. OADC analysis for the NP and AFP areas are in the Supporting Information (Figures S6 – S10). As indicated in Figures 8–10, we plot the results from all of the successful models and show a histogram of fault strikes and a rose diagram of dip angles for each group. We determine the mean strike for any peak in the histogram with more than 40 values within a range of clustered strikes and the mean dip angle. This analysis produced 31 fault planes total for the three areas (RFP, NP and AF). Fault parameters for the 31 planes are given in Supplementary Table S1. A final fault model is determined by using only those faults with 200 or greater modeled planes, as indicated in Table 3.

Table 3. PARAMETERS OF MODELED FAULT PLANES

Part name	Group #	Fault ID	Strike range	Dip range	Strike mean value	Dip mean value	Length mean value	Width mean value	Lambda 3 mean value	# of modeled planes
Northern	2	8	80~125	75~90	95.69	85.75	11.36	4.03	0.89	242
	3	10	30~50	75~90	33.96	83.26	18.01	5.05	0.88	288
RF	1	18	140~230	15~45	172.30	30.89	15.76	5.76	0.94	1513
	2	19	100~135	0~30	119.48	17.77	12.23	6.08	0.97	215
		20	135~165	30~60	150.31	43.53	14.73	5.96	0.89	312
		21	165~205	15~45	184.76	30.36	13.46	5.51	0.85	464
	3	23	20~65	30~75	43.61	52.04	8.19	4.23	0.82	207
		24	100~170	30~60	148.46	44.79	15.80	6.17	0.95	682
AF	1	26	40~70	75~90	52.48	84.25	21.16	3.86	0.90	296
	2	28	10~90	50~65	50.04	57.04	10.79	2.66	0.47	218
		29		70~90	49.00	82.30	13.82	3.95	0.70	547
		30	210~270	75~90	239.20	85.28	16.72	4.43	0.55	681

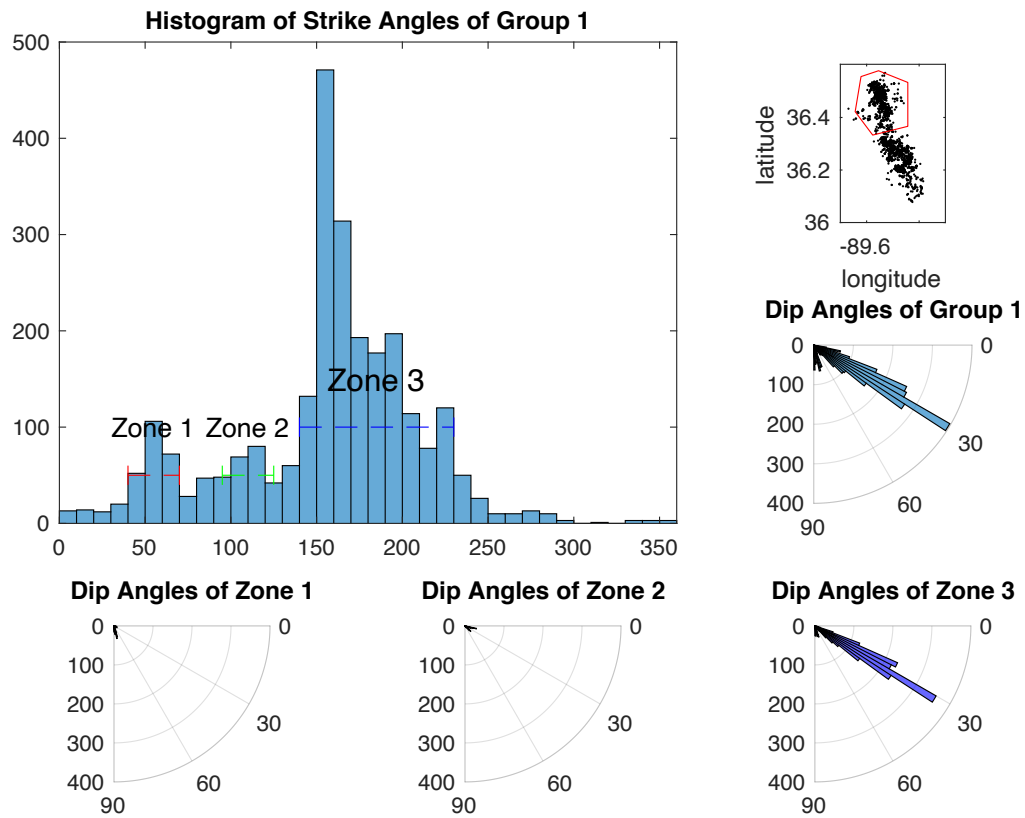


Figure 8. OADC analysis for RFP group 1 (upper right). Three zones are labeled with bin values over 40. The dashed lines indicate the strike range for each zone. Rose diagrams are determined for each zone. Fault parameters for these zones are given in Table S1. Only zone 3 is used in the final fault model.

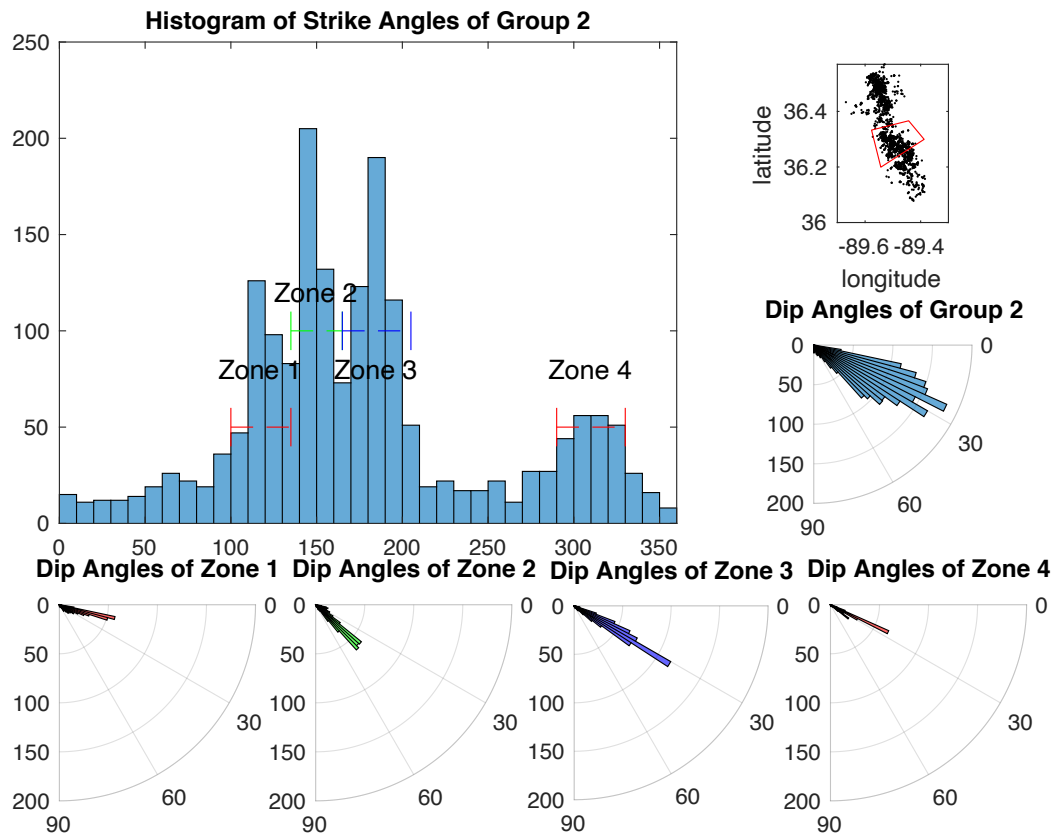


Figure 9. OADC analysis for RFP group 2 (upper right). Four zones are labeled with bin values over 40. The dashed lines indicate the strike range for each zone. Rose diagrams are determined for each zone. Fault parameters for these zones are given in Table S1. Zones 1-3 are used in the final model.

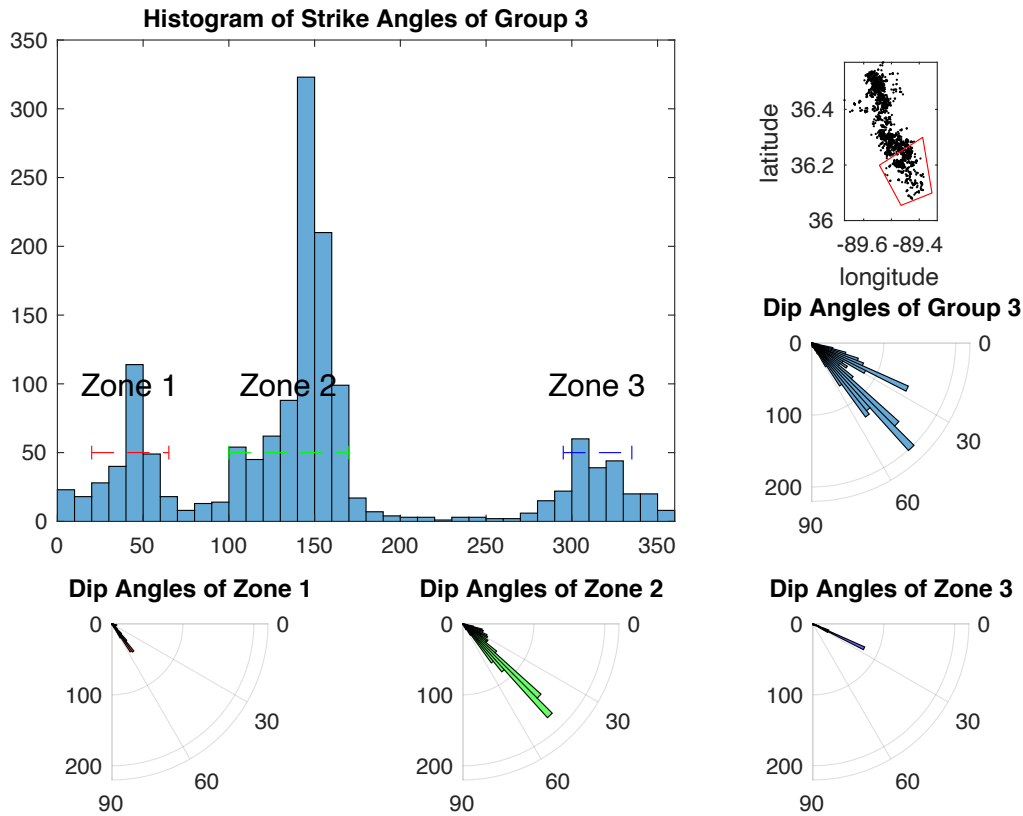


Figure 10. OADC analysis for RFP group 3 (upper right). Three zones are labeled with bin values over 40. The dashed lines indicate the strike range for each zone. Rose diagrams are determined for each zone. Fault parameters for these zones are given in Table S1. Zones 1 and 2 are used in the final model.

RFP Group 1 (Figure 8) contains the northern part of the RF. The modeled average fault for zone 3 has a strike of N172° and a dip angle of 31°, in agreement with a strike of N160° to 170° determined in previous studies (Parrish and Van Arsdale, 2004; Csontos and Van Arsdale, 2008; Greenwood et al., 2016). Strikes and dips of the planes in zone 1 suggest the presence of steeply dipping faults that crosscut the trend of the northern RF. However, only the average fault plane from zone 3 in group 1 is used in the final fault model (fault 18 in Table 3).

Group 2 (Figure 9) has the most complex fault structure in the NMSZ. The strike distribution is broader than the distribution found for group1 but the pattern is similar. The major exception is the presence of zone 4 in group 2. The strike directions for most planes in zone 4 are the same as those for zone 2 but the dip directions are different. This suggests the presence of backlimb or kink bend faults as suggested in previous studies (e.g. Mueller et al., 1999). Fault planes representing zones 1 – 3 (faults 19, 20, and 21 in Table 3) are used in the final model.

The main fault in group 3 (Figure 10) has a mean strike of N148° and a mean dip of about 45°. This corresponds to strikes of N150°~160° determined for the southern RF in previous studies (Mueller and Pujol, 2001; Parrish and Van Arsdale, 2004; Csontos and Van Arsdale,

2008; Greenwood et al., 2016; Delano et al., 2018). The mean strike direction angle is 24 degrees smaller than the mean strike angle for the northern RF. This change in fault orientation is also observed in the prior studies. As is the case for the northern RF, zone 1 fault planes in Figure 10 suggest the presence of crosscutting faults. In this case, the faults are shallower than those that crosscut the northern RF and have a greater number of planes. Fault planes representing zones 1 and 2 (faults 23 and 24 in Table 3) are used in the final model.

4.2.1 Final Fault Model for the NMSZ

Faults with more than 200 modeled planes constitute the final fault model and are plotted in Figure 11. Figure 12 shows the fault model in different orientations. The fault parameters for the model are given in Table 3 and information for all modelled planes is presented in the Supporting Information (Table S1).

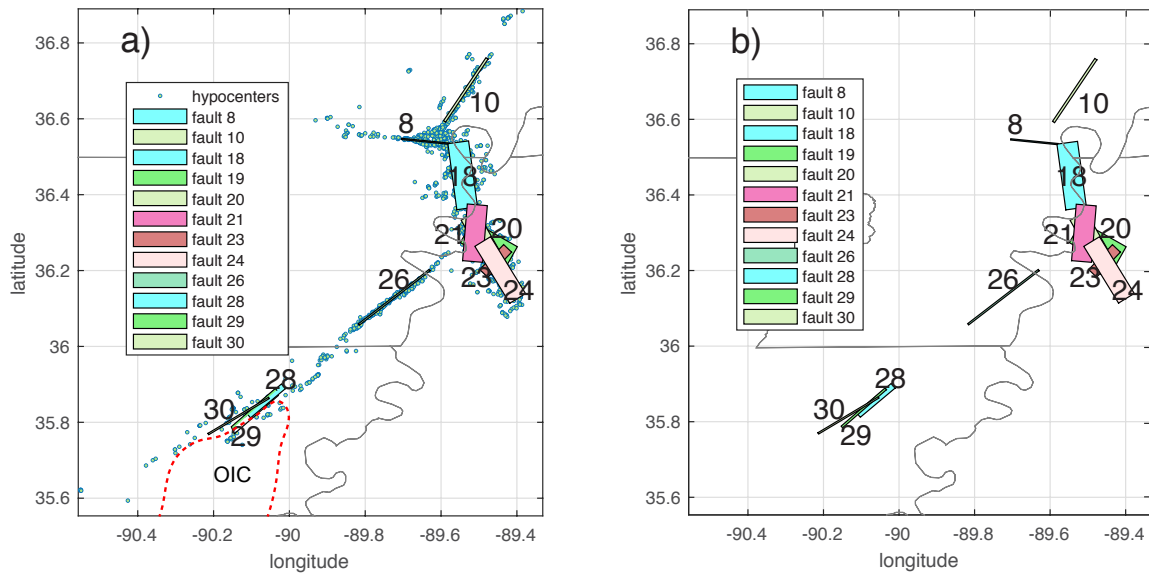


Figure 11. a) Final fault model for the NMSZ. Earthquakes are removed from the model in b). Identified faults have more than 200 modeled planes. The fault numbers refer to the list in Table S1 and in Table 3. Dashed contour is the outline of the Osceola intrusive complex (OIC) taken from Hildenbrand et al.(2001).

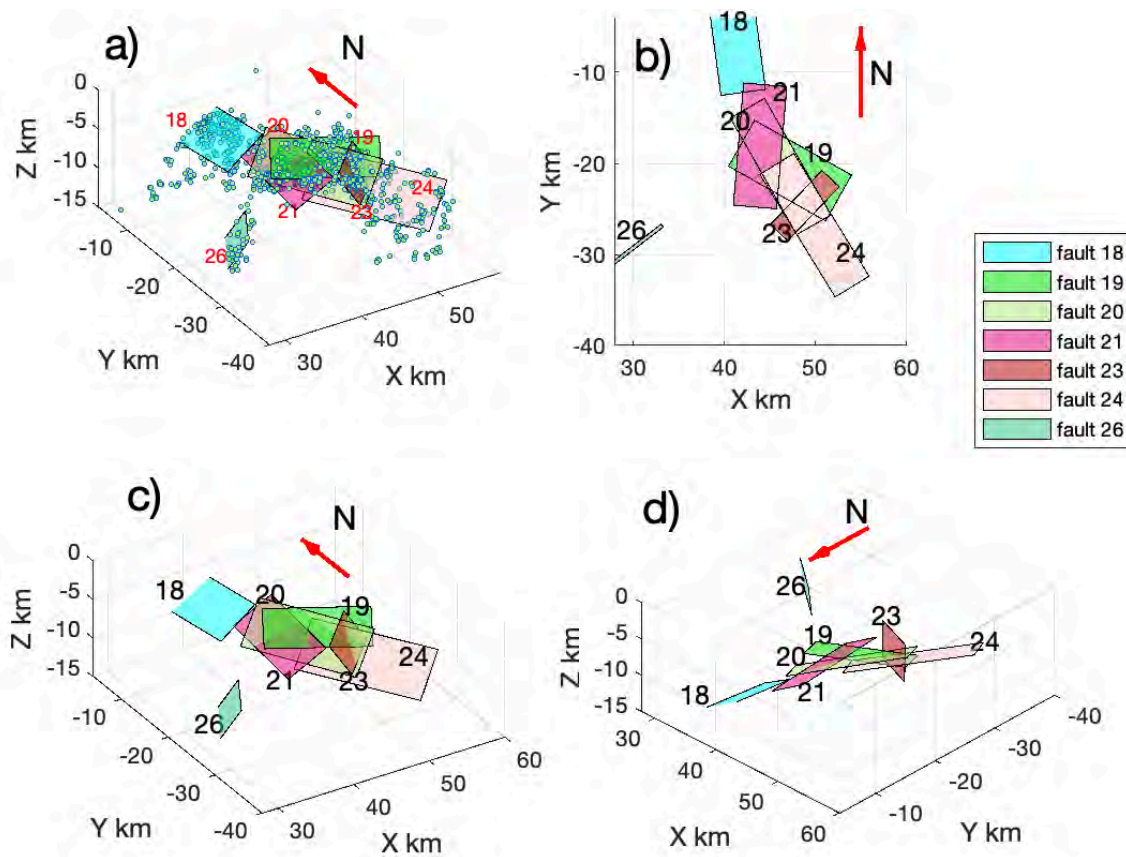


Figure 12. Blowup of the fault model for the RF. a) shows the distribution of hypocenters. b) is a map view. c) is a view looking toward the NE. Fault 26 is the AF. d) is a view looking up.

Planes representing the strike-slip faults, WF, NF and AF, are clearly represented and are labeled 8, 10, and 26, respectively. Planes 18 and 24 represent the northern and southern RF thrust, respectively. The middle part of the RF has a complicated structure containing 4 planes labeled 19, 20, 21, and 23. Fault 21 connects with fault 18. These planes have strike angles that differ by about 13° but the same dip angles (Figure 12c). Plane 20 is the deepest fault in the central RF and is parallel to and overlaps plane 24 representing the southern RF. The strike and dip angles of planes 20 and 24 differ by less than 2° and, from their orientation and dip angles, we suggest that they represent the main RF thrust surface (Figure 12 a, c, d). The continuity of faults 18, 21, 20 and 24 indicate a continuous thrust fault extending along the entire RF. Fault 23 has a strike angle of $N44^\circ$ and a dip angle of 52° and this shallow fault crosscuts the southern RF.

5 Discussion

The availability of a much larger dataset in our study resulted in a more precise image of the NMSZ fault structure than was possible in the hypoDD study by Dunn et al. (2010). Figure S11 provides a direct comparison between the hypoDD relocation results in Figure 3 and those

determined by Dunn et al. (2010). Major improvements are better definition of the deeper structure on the RF and a very clear, vertical alignment of hypocenters along the northern segment of the AF. Additional earthquakes in our study closed the gap in seismicity near the intersection of the AF and the RF (Figure 3 cluster 6). Most of these earthquakes are aligned along the same trend as the well-defined portion of the AF but have shallower hypocenters, suggesting a change in fault structure near the intersection with the RF.

Modeled fault planes along the major strike-slip arms of the NMSZ (Figure 11) agree with previous published fault models. Our results confirm that these faults are near vertical and the fault strikes we determine lie within or just outside of the range of strikes found previously for these faults (Mueller & Pujol, 2001; Parrish and Van Arsdale, 2004; Csontos & Van Arsdale, 2008; Dunn et al., 2010; Pratt, 2012; Greenwood et al., 2016; Delano et al., 2018).

Our results for the southern part of the AF are revealing. Seismicity in the southern part of the AF is more diffuse than in the northern part but we have detected the presence of three distinct faults (28, 29 and 30 in Figure 11). Two of these faults strike roughly parallel to the northern part of the AF and one, fault 30, is oriented further east by about 10° . Two of the faults have near-vertical dips and one (fault 28) has a shallower dip. The similarity of these faults with the northern part of the AF suggests that the southern part of the AF is continuous with the northern part. The reason for the reduced amount of seismic activity in between the northern and southern segments of the AF is enigmatic. According to Hildenbrand et al. (2001), seismicity in the southern part of the AF is strongly affected by a major axial intrusion called the Osceola intrusive complex (OIC in Figure 11). According to Hildenbrand et al. (2001), the presence of the OIC produces scattered seismicity offset to the northwest from the trend of the northern AF and clustering of earthquakes near the northern end of the intrusion. Our results indicate that seismicity is less scattered than previously thought and that distinct faults with roughly the same orientation and dip as the northern part of the AF are present along the upper, northwestern side of the intrusion. These faults are located along the trend of the northern AF and are not offset to the northwest. The relative age of the faulting and the intrusion is difficult to assess. The intrusion may have followed preexisting faults or, faults may have developed along the side of the intrusion in response to a concentration of differential stress produced by the stronger, more rigid OIC. The latter explanation is favored by Hildenbrand et al. (2001) and is compatible with other studies involving stress concentration around large igneous intrusions (e.g. Ravat et al., 1987; Campbell, 1978).

The central portion of the RF has the most complicated fault structure, as has been noted in previous studies (e.g. Muller and Pujol, 2001). Despite this complexity, there is a continuity of SW dipping planes from the northern RF to the southern RF (Figure 12) that indicates a continuous rather than a segmented RF. A continuous fault implies that rupture could continue unimpeded along its entire length. Fault plane 23 in the central RF strikes at high angle to the trend of the RF. Fault 23 corresponds to the Ridgely fault (Csontos and Van Arsdale, 2008; Greenwood et al., 2016). Our results depicting the vertical extent of the Ridgely fault indicate that it does not cut the RF into different segments. This result is in agreement with Greenwood et al. (2016) based on seismic reflection and geological surveys.

Our final depiction of the NMSZ fault structure is an approximation, limited by our inability to model curved fault surfaces. This limitation did not affect our ability to model the straight, strike-slip segments of the NMSZ and our results add better defined fault dimensions for these segments. The RF is curved, as is obvious from Figure 3. Our plotted fault centers capture

the curvature of the RF (Figure 7) but planes fit to the hypocenters produce the approximation indicated in Figure 11. Nonetheless, our model for the RF indicates continuity of the fault through the intersection with the AF and the Ridgely fault and can serve as a useful approximation of the RF in studies involving seismotectonics and rupture dynamics.

6 Conclusions

Relocation of 4568 earthquakes using HypoDD resulted in major improvement in the depiction of fault structure in the NMSZ. Three-dimensional structural variations along the Reelfoot fault are apparent. The northern portion of the Axial fault is very well defined; hypocenters do not exceed 10km and become shallower near the intersection with the Reelfoot fault, indicating structural complexity.

OADC analysis of the relocated hypocenters produced a fault model consisting of 12, well resolved planes. The model indicates that the Reelfoot fault is not segmented but continuous along strike from the northern to the southern end. There are no obvious barriers to rupture propagation along the entire fault. The southern end of the fault has a smaller strike angle and a greater dip than the northern portion of the fault, in agreement with prior studies. A cross cutting fault, corresponding to the Ridgely fault, is present in the hanging wall of the southern part of the Reelfoot fault. The strike-slip arms of the NMSZ are well resolved and correspond to near vertical planes. Three planes are resolved in the seismicity comprising the southern part of the Axial fault. These faults trend close to the same direction as the northern part of the fault, suggesting that the southern and northern parts of the fault are probably continuous but separated by a fault segment experiencing little present-day seismic activity. The southern part of the Axial fault does not appear to be disrupted by a major axial intrusion, as postulated in prior studies.

Data and Resources

All earthquake data are available at the U.S. Geological Survey Advanced National Seismic System (ANSS) Comprehensive Earthquake Catalog (ComCat) and the Center for Earthquake Research and Information (CERI) earthquake catalog.

Acknowledgments

This material is based upon work supported by the U.S. Geological Survey under Grant Number G19AP00052. The views and conclusions contained in this document are those of the authors and should not be interpreted as representing the opinions or policies of the U.S. Geological Survey. Mention of trade names or commercial products does not constitute their endorsement by the U.S. Geological Survey.

References

- Boyd, O.S., Smalley, R., Jr., & Zeng, Y. (2015). Crustal deformation in the New Madrid seismic zone and the pore of postseismic stress. *Journal of Geophysical Research: Solid Earth*, 120, doi:10.1002/2015HB012049..
- Braile, L. W., Keller, G. R., Hinze, W. J., & Lidiak, E. G. (1982). An ancient rift complex and its relation to contemporary seismicity in the New Madrid seismic zone. *Tectonics*, 1(2), 225-237.

- Chen, C., Zhao, D., & Wu, S. (2014). Crust and upper mantle structure of the New Madrid Seismic Zone: Insight into intraplate earthquakes. *Physics of the Earth and Planetary Interiors*, 230, 1-14.
- Campbell, D. L. (1978). Investigation of the stress-concentration mechanism for intraplate earthquakes. *Geophysical Research Letters*, 5(6), 477-479.
- Calais, E., & Stein, S. (2009). Time-variable deformation in the New Madrid seismic zone. *Science*, 323(5920), 1442-1442.
- Csontos, R., & Van Arsdale, R. (2008). New Madrid seismic zone fault geometry. *Geosphere*, 4(5), 802-813.
- Cox, R. T., & Van Arsdale, R. B. (2002). The Mississippi Embayment, North America: a first order continental structure generated by the Cretaceous superplume mantle event. *Journal of Geodynamics*, 34(2), 163-176.
- Cox, R. T., & Van Arsdale, R. B. (1997). Hotspot origin of the Mississippi embayment and its possible impact on contemporary seismicity. *Engineering Geology*, 46(3-4), 201-216.
- Craig, T. J., & Calais, E. (2014). Strain accumulation in the New Madrid and Wabash Valley seismic zones from 14 years of continuous GPS observation. *Journal of Geophysical Research: Solid Earth*, 119(12), 9110-9129.
- Delano, J. E., Gold, R. D., Briggs, R. W., & Jibson, R. W. (2018). Coseismic sackungen in the New Madrid seismic zone, USA. *Geophysical Research Letters*, 45(24), 13-258.
- Dunn, M., DeShon, H. R., & Powell, C. A. (2013). Imaging the New Madrid Seismic Zone using double-difference tomography. *Journal of Geophysical Research: Solid Earth*, 118(10), 5404-5416.
- Dunn, M., Horton, S., DeShon, H., & Powell, C. (2010). High-resolution earthquake relocation in the New Madrid seismic zone. *Seismological Research Letters*, 81(2), 406-413.
- Frankel, A., Smalley, R., & Paul, J. (2012). Significant motions between GPS sites in the New Madrid region: Implications for seismic hazard. *Bulletin of the Seismological Society of America*, 102(2), 479-489.
- Fadugba, O. I. (2021). *Waveform and Geodynamic Modeling of Seismicity Associated with the Charlevoix Seismic Zone* (Doctoral dissertation, The University of Memphis).
- Fadugba, O. I., Langston, C. A., & Powell, C. A. (2019). Better Constraining the Geometry of Faults in the Charlevoix Seismic Zone. *AGUFM*, 2019, S52C-08.
- Greenwood, M. L., Woolery, E. W., Van Arsdale, R. B., Stephenson, W. J., & Patterson, G. L. (2016). Continuity of the Reelfoot Fault across the Cottonwood Grove and Ridgely Faults of the New Madrid Seismic Zone. *Bulletin of the Seismological Society of America*, 106(6), 2674-2685.
- Geng, Y., Powell, C. A., & Saxena, A. (2020). Joint local and teleseismic tomography in the central United States: exploring the mantle below the upper Mississippi Embayment and the Illinois Basin. *Journal of Geophysical Research: Solid Earth*, 125(10), e2020JB020625.
- Hough, S. E., Seeber, L., & Armbruster, J. G. (2003). Intraplate triggered earthquakes: Observations and interpretation. *Bulletin of the Seismological Society of America*, 93(5), 2212-2221.
- Hough, S. E., & Martin, S. (2002). Magnitude estimates of two large aftershocks of the 16 December 1811 New Madrid earthquake. *Bulletin of the Seismological Society of America*, 92(8), 3259-3268.

- Hough, S. E., Armbruster, J. G., Seeber, L., & Hough, J. F. (2000). On the modified Mercalli intensities and magnitudes of the 1811–1812 New Madrid earthquakes. *Journal of Geophysical Research: Solid Earth*, 105(B10), 23839–23864.
- Horton, S. P., Kim, W. Y., & Withers, M. (2005). The 6 June 2003 Bardwell, Kentucky, earthquake sequence: Evidence for a locally perturbed stress field in the Mississippi embayment. *Bulletin of the Seismological Society of America*, 95(2), 431–445.
- Hildenbrand, T. G., Stuart, W. D., & Talwani, P. (2001). Geologic structures related to New Madrid earthquakes near Memphis, Tennessee, based on gravity and magnetic interpretations. *Engineering Geology*, 62(1–3), 105–121.
- Hildenbrand, T. G., & Hendricks, J. D. (1995). *Geophysical setting of the Reelfoot rift and relations between rift structures and the New Madrid seismic zone* (No. 1538-E).
- Hao, Y., McIntosh, K., & Magnani, M. B. (2015). Long-lived deformation in the southern Mississippi Embayment revealed by high-resolution seismic reflection and sub-bottom profiler data. *Tectonics*, 34(3), 555–570.
- Hildenbrand, T.G., & Hendricks, J.D. (1995). Geophysical setting of the Reelfoot rift and relations between rift structures and the New Madrid seismic zone, U.S. Geological Survey Professional Paper 1538-E, 30 pp.
- Hildenbrand, T.G., Stuart, W.D., & Talwani, P. (2001) Geologic structures related to New Madrid earthquakes near Memphis, Tennessee, based on gravity and magnetic interpretations, *Engineering Geology*, 62, 105–121.
- Johnston, A. C. (1996). Seismic moment assessment of stable continental earthquakes, III: 1811–1812 New Madrid, 1886 Charleston and 1755 Lisbon. *Geophys. J. Int.*, 126, 314–344.
- Johnston, A. C., & Schweig, E. S. (1996). The enigma of the New Madrid earthquakes of 1811–1812. *Annual Review of Earth and Planetary Sciences*, 24(1), 339–384.
- Kenner, S. J., & Segall, P. (2000). A mechanical model for intraplate earthquakes: Application to the New Madrid seismic zone. *Science*, 289(5488), 2329–2332.
- Likas, A., Vlassis, N., & Verbeek, J. J. (2003). The global k-means clustering algorithm. *Pattern recognition*, 36(2), 451–461.
- Liu, L., Gurnis, M., Seton, M., Saleeby, J., Müller, R. D., & Jackson, J. M. (2010). The role of oceanic plateau subduction in the Laramide orogeny. *Nature Geoscience*, 3(5), 353–357.
- MacQueen, J. (1967, June). Some methods for classification and analysis of multivariate observations. In *Proceedings of the fifth Berkeley symposium on mathematical statistics and probability* (Vol. 1, No. 14, pp. 281–297).
- Mueller, K., & Pujol, J., (2001). Three-dimensional geometry of the Reelfoot blind thrust: implications for moment release and earthquake magnitude in the New Madrid seismic zone. *Bulletin of the Seismological Society of America*, 91(6), 1563–1573.
- Mueller, K., Champion, J., Guccione, M., & Kelson, K. (1999). Fault slip rates in the modern New Madrid seismic zone. *Science*, 286(5442), 1135–1138.
- Ouillon, G., & Sornette, D. (2011). Segmentation of fault networks determined from spatial clustering of earthquakes. *Journal of Geophysical Research: Solid Earth*, 116(B2).
- Ouillon, G., Ducorbier, C., & Sornette, D. (2008). Automatic reconstruction of fault networks from seismicity catalogs: Three-dimensional optimal anisotropic dynamic clustering. *Journal of Geophysical Research: Solid Earth*, 113(B1).
- Page, M. T., & Hough, S. E. (2014). The New Madrid seismic zone: Not dead yet. *Science*, 343(6172), 762–764.

- Paige, C. C. (1982). LSQR: Sparse linear equations and least squares problems. *ACM Trans. Math. Software*, 8(1), 195-209.
- Parrish, S., & Van Arsdale, R. (2004). Faulting along the southeastern margin of the Reelfoot Rift in northwestern Tennessee revealed in deep seismic-reflection profiles. *Seismological Research Letters*, 75(6), 784-793.
- Ravat, D. N., Braile, L. W., & Hinze, W. J. (1987). Earthquakes and plutons in the midcontinent-Evidence from the Bloomfield pluton, New Madrid rift complex. *Seismological Research Letters*, 58(2), 41-52.
- Santosh, M., Zhao, D., & Kusky, T. (2010). Mantle dynamics of the Paleoproterozoic North China Craton: a perspective based on seismic tomography. *Journal of Geodynamics*, 49(1), 39-53.
- Sigloch, K. (2011). Mantle provinces under North America from multifrequency P wave tomography. *Geochemistry, Geophysics, Geosystems*, 12(2).
- Tavakoli, B., Pezeshk, S., & Cox, R. T. (2010). Seismicity of the New Madrid seismic zone derived from a deep-seated strike-slip fault. *Bulletin of the Seismological Society of America*, 100(4), 1646-1658.
- Tuttle, M. P., Wolf, L. W., Starr, M. E., Villamor, P., Lafferty III, R. H., Morrow, J. E., ... & Haynes, M. L. (2019). Evidence for large New Madrid earthquakes about AD 0 and 1050 BC, central United States. *Seismological Research Letters*, 90(3), 1393-1406.
- Tuttle, M. P., Schweig, E. S., Sims, J. D., Lafferty, R. H., Wolf, L. W., & Haynes, M. L. (2002). The earthquake potential of the New Madrid seismic zone. *Bulletin of the Seismological Society of America*, 92(6), 2080-2089.
- Thomas, W. A. (2006). Tectonic inheritance at a continental margin. *GSA today*, 16(2), 4-11.
- Thomas, W. A. (1991). The Appalachian-Ouachita rifted margin of southeastern North America. *Geological Society of America Bulletin*, 103(3), 415-431.
- Tian, Y., & Zhao, D. (2011). Destruction mechanism of the North China Craton: insight from P and S wave mantle tomography. *Journal of Asian Earth Sciences*, 42(6), 1132-1145.
- Van Arsdale, R., & Cupples, W. (2013). Late Pliocene and Quaternary deformation of the Reelfoot rift. *Geosphere*, 9(6), 1819-1831.
- Van Arsdale, R. (2000). Displacement history and slip rate on the Reelfoot fault of the New Madrid seismic zone. *Engineering Geology*, 55(4), 219-226.
- Waldhauser, F. (2001). hypoDD--A program to compute double-difference hypocenter locations.
- Waldhauser, F., & Ellsworth, W. L. (2000). A double-difference earthquake location algorithm: Method and application to the northern Hayward fault, California. *Bulletin of the Seismological Society of America*, 90(6), 1353-1368.
- Zhang, Q., Sandvol, E., & Liu, M. (2009). Lithospheric velocity structure of the New Madrid Seismic Zone: A joint teleseismic and local P tomographic study. *Geophysical research letters*, 36(11).
- Zhan, Y., Hou, G., Kusky, T., & Gregg, P. M. (2016). Stress development in heterogeneous lithosphere: Insights into earthquake processes in the New Madrid Seismic Zone. *Tectonophysics*, 671, 56-62.

Supporting Information for

A New Madrid Seismic Zone Fault System Model from Relative Event Locations and Application of Optimal Anisotropic Dynamic Clustering

Yixin Zhang¹, Oluwaseun Fadugba¹, Christine Powell¹, Stephen Horton¹, and Charles A. Langston¹

¹Center for Earthquake Research and Information, The University of Memphis, Memphis, TN

Contents of this file

Figure S1. Relocations using CT data only

Figure S2. Relocations using CC data only

Figure S3. Relocations using CC and CT compared to CT alone

Figure S4. Comparison between original locations and relocated hypocenters for the 7 partitions of the NMSZ.

Figure S5. Original event errors and relocated event errors

Figures S6 – S8. OADC analysis for the NP area

Figures S9 and S10. OADC results for AP area

Figure S11. Direct comparison of results obtained here and those by Dunn et al. (2010)

Table S1 fault parameters for the 31 resolved planes

Introduction

The supporting information provides details on performing event relocations with catalog data only, cross correlation data only, and the improvement in event locations when both datasets are used. A comparison between the original event locations and the relocations is given as well as the reduction in location errors produced by relocation. The OADC analyses used to select fault planes for the North and the Axial Parts of the NMSZ are presented. Fault parameters for all 31 modeled fault planes are listed in Table S1. Finally, the improvement in locations over the model obtained in the prior hypoDD study by Dunn et al., (2010) is indicated.

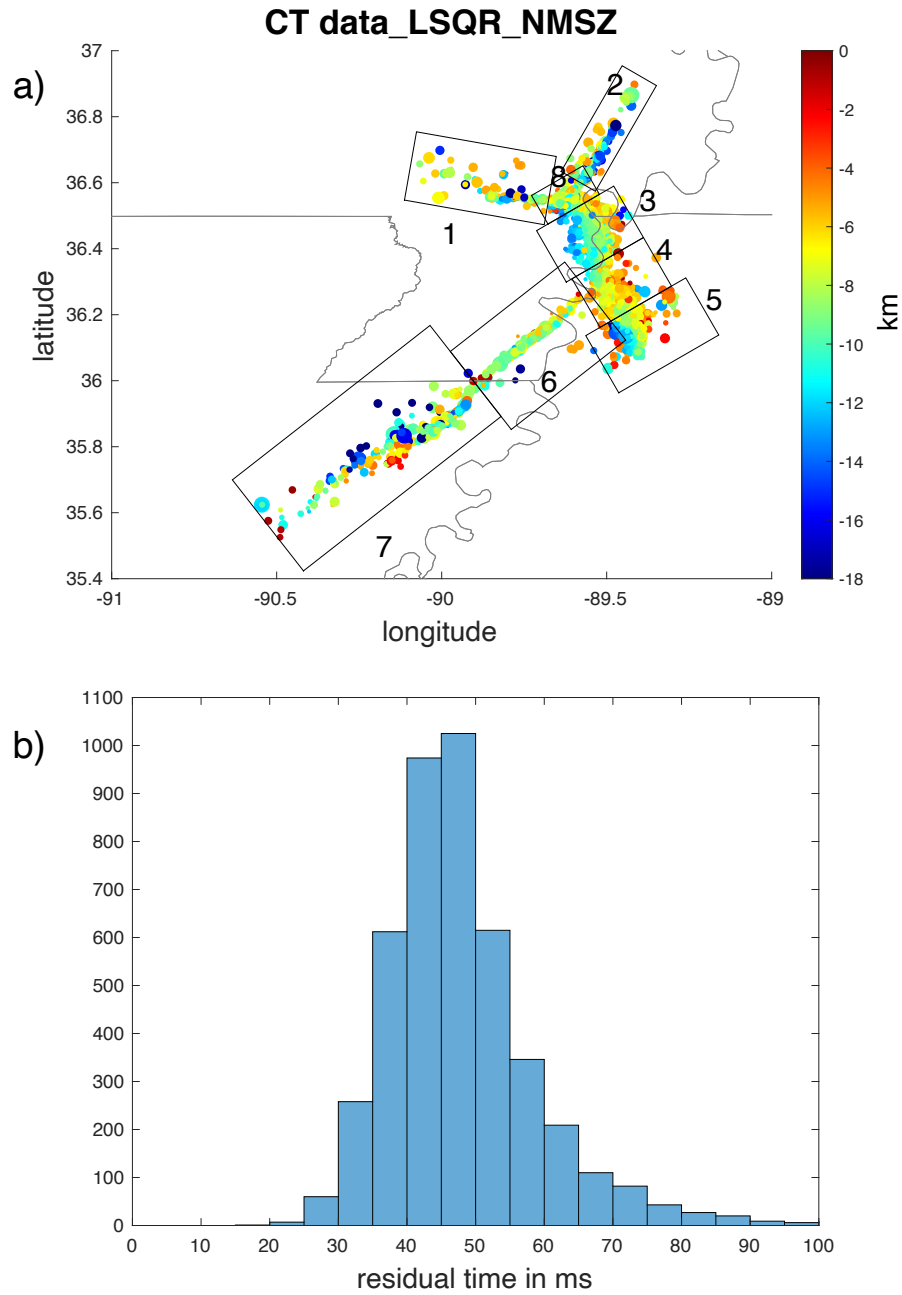


Figure S1. a) NMSZ event locations determined using HypoDD_LSQR using only catalog data. Circles represent earthquakes; the size of circles is proportional to the earthquake magnitude, **ranging from 0.1 to 3.9**. The color scale shows the hypocenter depth. b) Histogram of the residual times for the 4422 events.

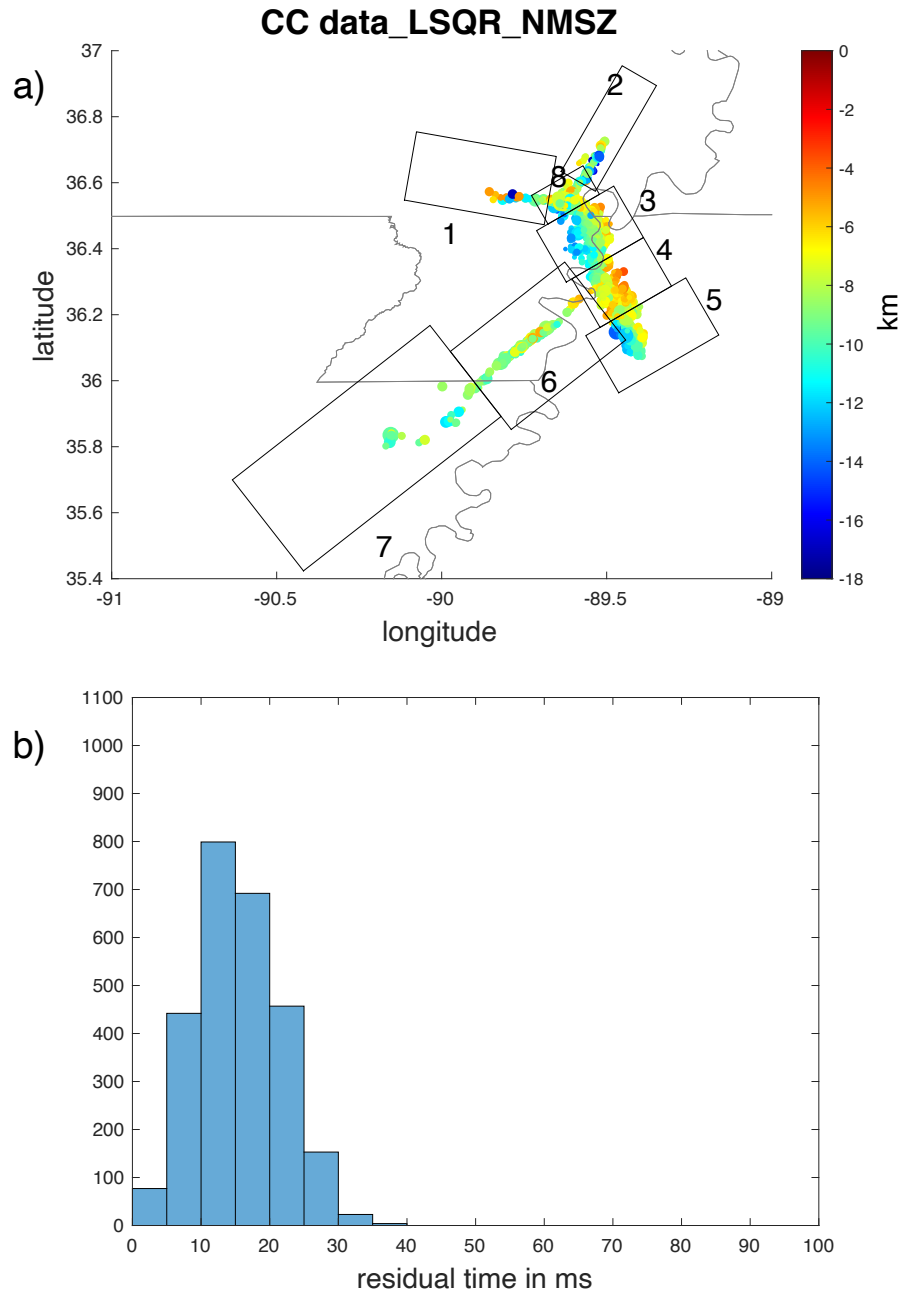


Figure S2. a) NMSZ event locations determined using HypoDD_LSQR using only cross-correlation data. Circles represent earthquakes; the size of circles is proportional to the earthquake magnitude, **ranging from 0.1 to 3.9**. The color scale shows the hypocenter depth. b) Histogram of the residual times for the 2647 events.

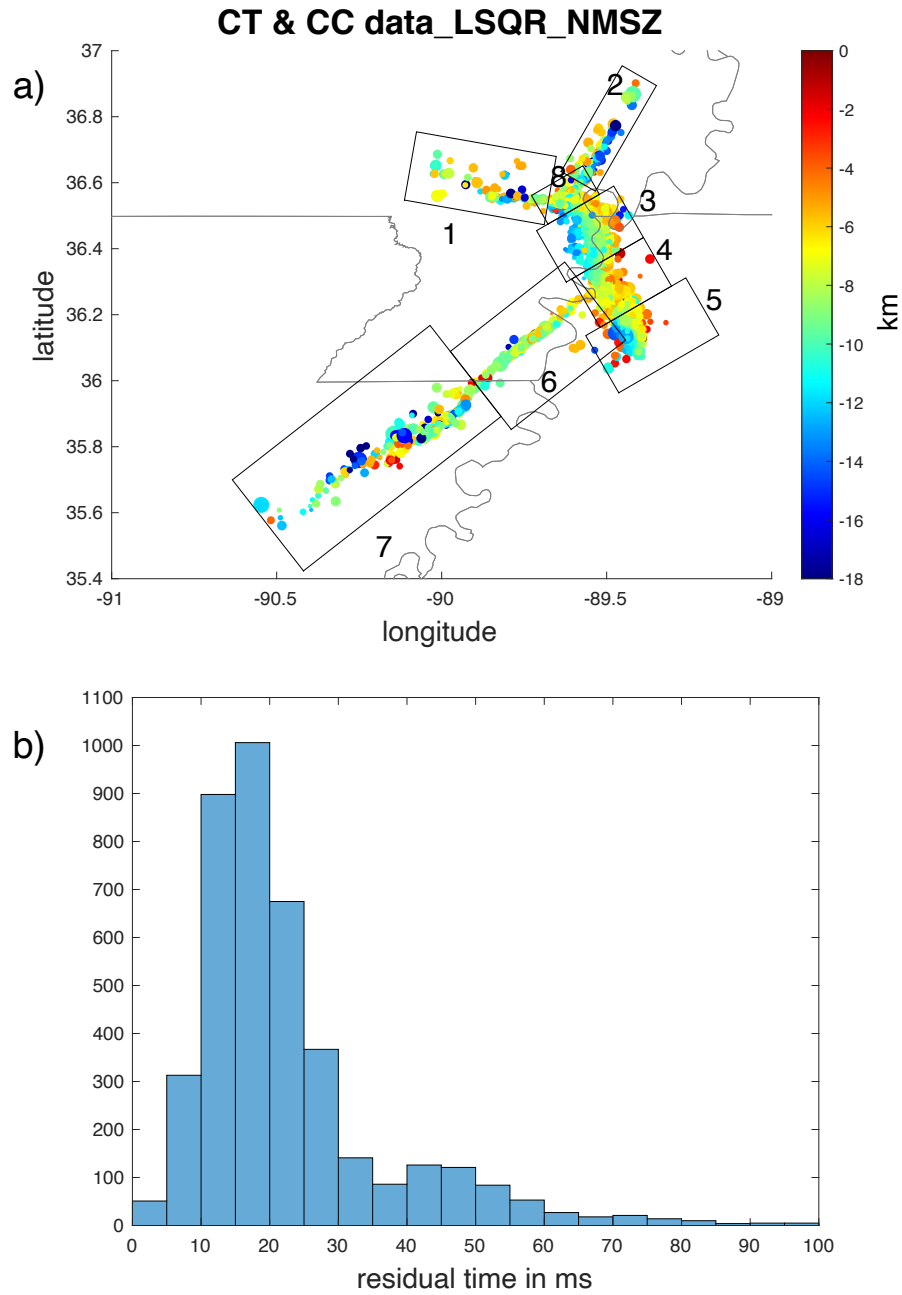


Figure S3. a) NMSZ event locations determined using HypoDD_LSQR using both catalog and cross-correlation data. Circles represent earthquakes; the size of circles is proportional to the earthquake magnitude, ranging from 0.1 to 3.9. The color scale shows the hypocenter depth. b) Histogram of the residual times for the 4032 events.

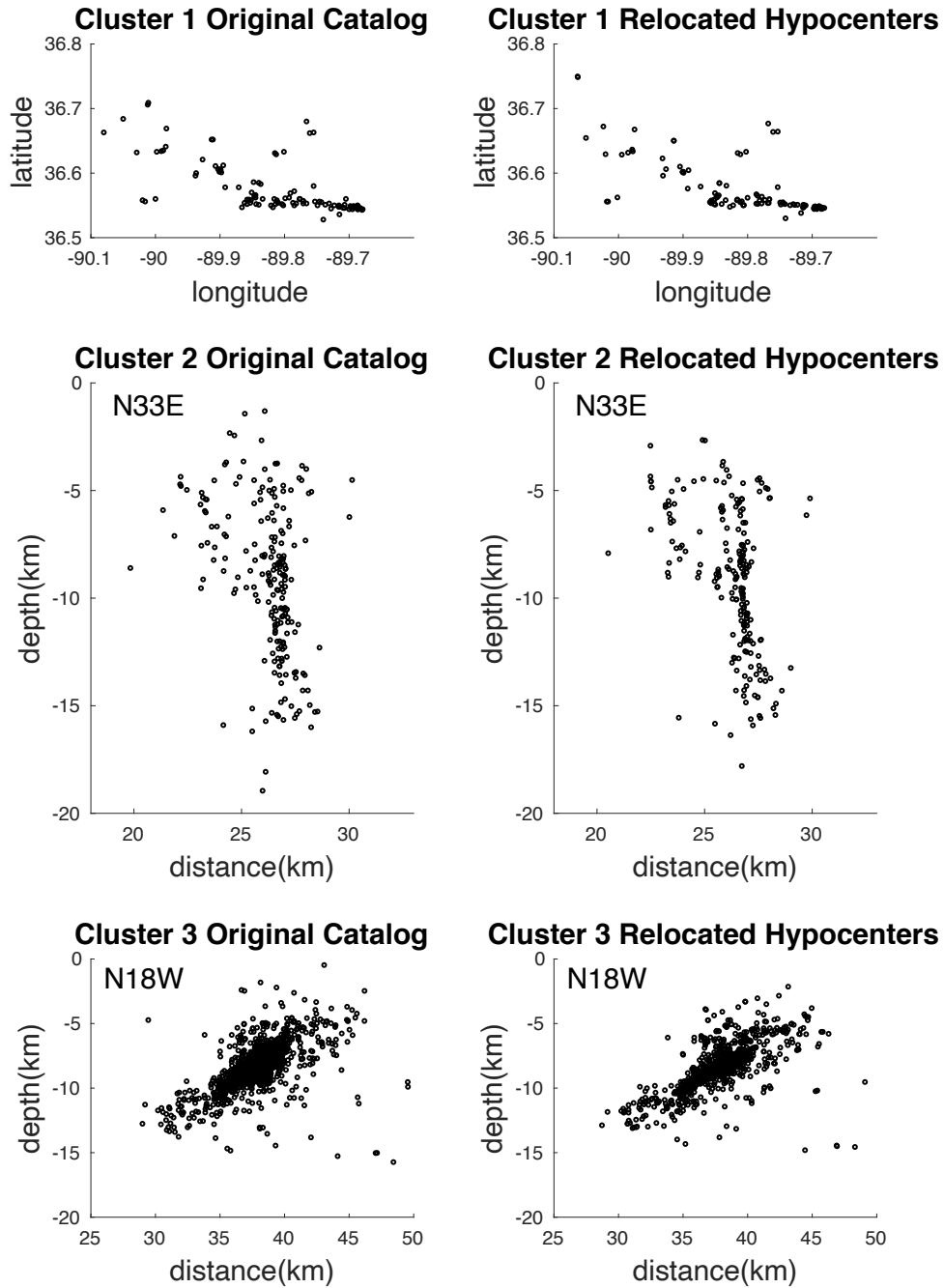


Figure S4. Comparison between the original and relocated catalog hypocenters for the clusters shown in Figure 2. For each cluster, we use the same view angle as in Dunn et al., (2010). We also use a similar way of partitioning clusters, except we separate the RF area into 3 clusters and Dunn et al. (2010) separate the area into northern and southern segments. Cluster 1 shown in map view. All other clusters shown in cross section. Cross section orientation indicated.

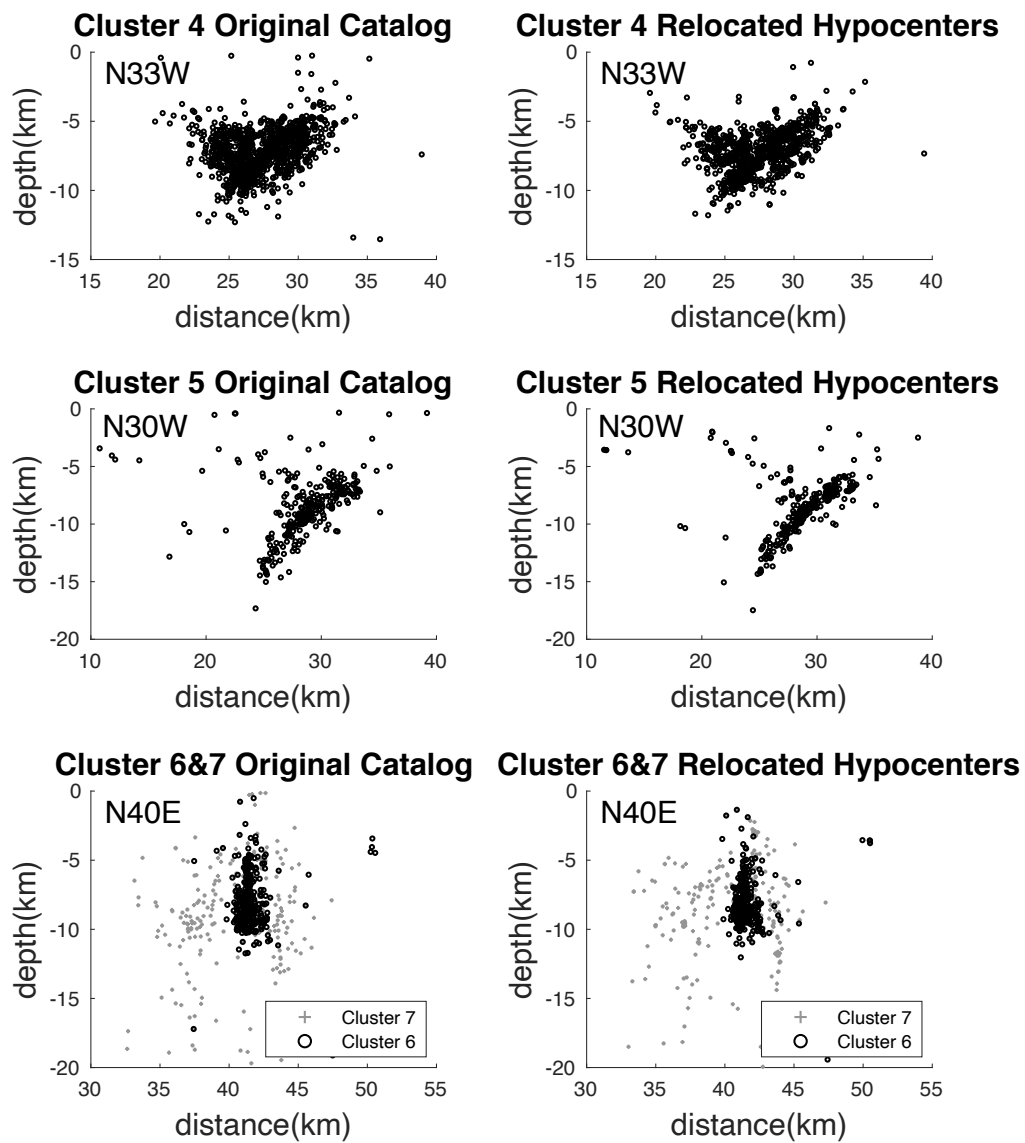


Figure S4. Continued.

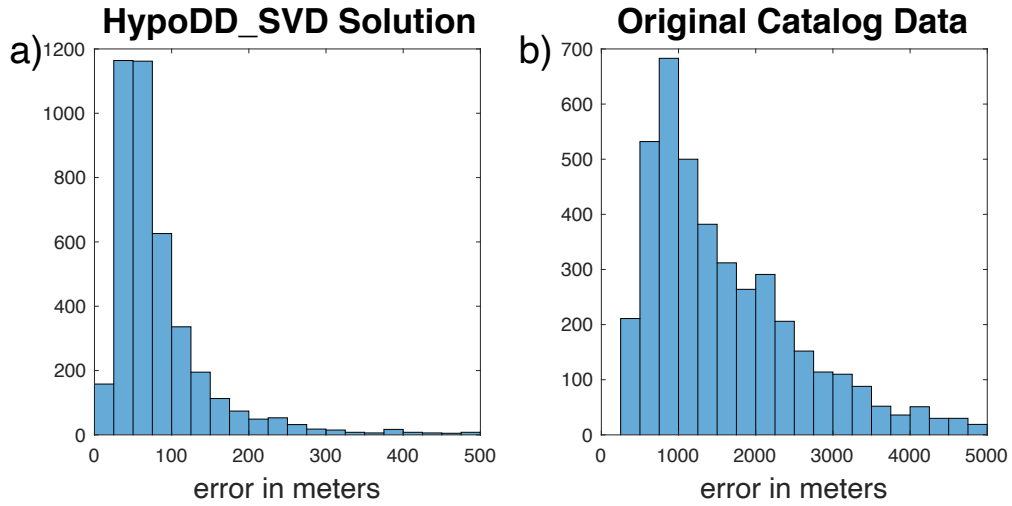


Figure S5. Histograms of earthquake location errors. a) our solution errors in meters. Most events have an error less than 150 meters. b) original catalog data errors; errors are larger than 250 meters.

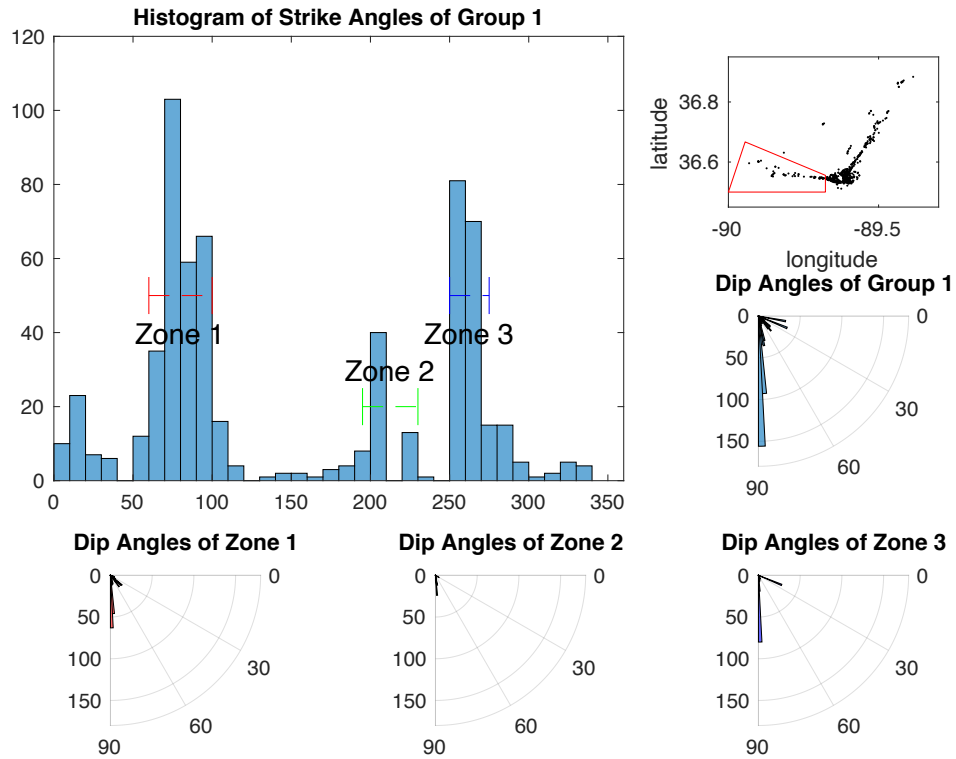


Figure S6. OADC analysis for NP group 1 (upper right). Three zones are labeled with bin values over 40. The dashed lines indicate the strike range for each zone. Rose diagrams are determined

for each zone. Fault parameters for these zones are given in Table S1. No zones are used in the final fault model.

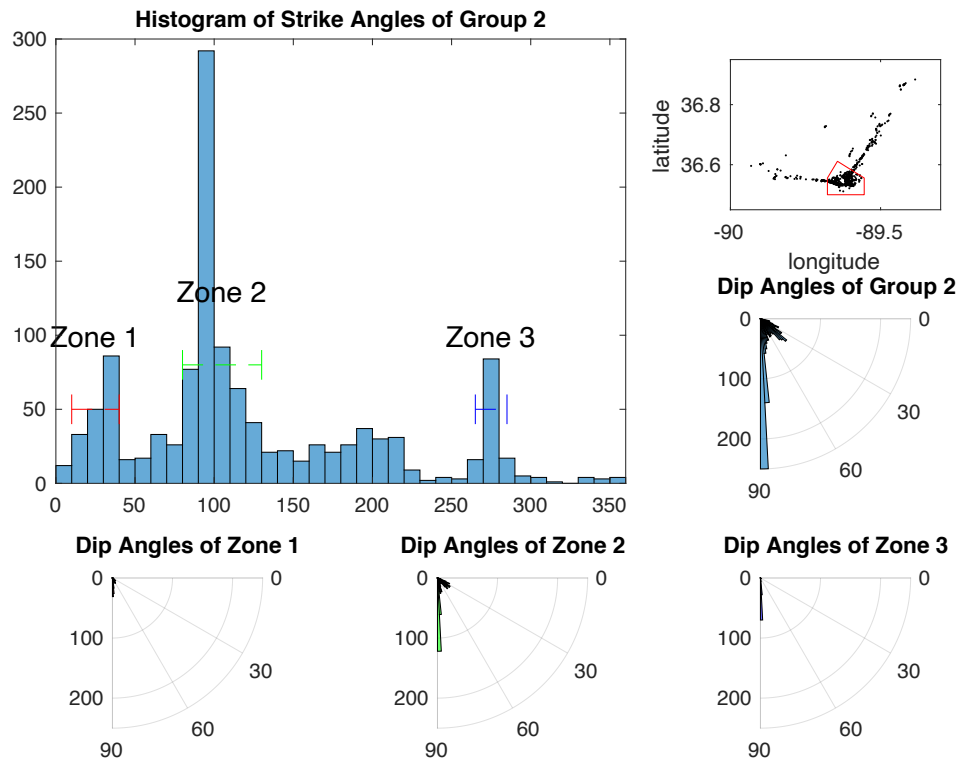


Figure S7. OADC analysis for NP group 2 (upper right). Three zones are labeled with bin values over 40. The dashed lines indicate the strike range for each zone. Rose diagrams are determined for each zone. Fault parameters for these zones are given in Table S1. Only zone 2 are used in the final model.

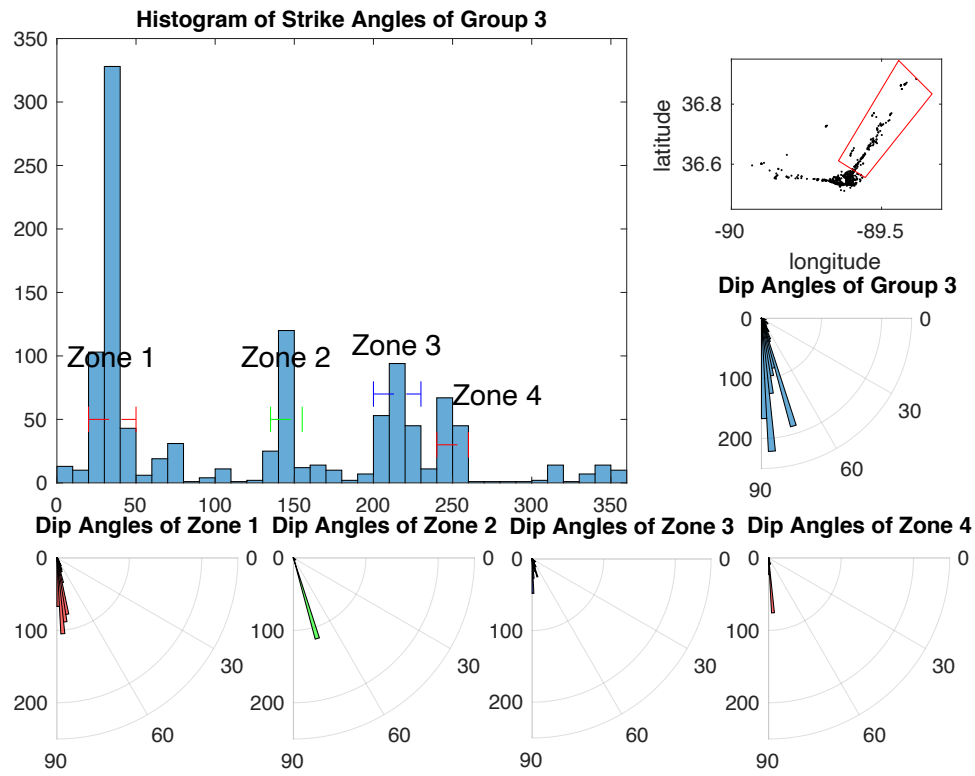


Figure S8. OADC analysis for NP group 3 (upper right). Four zones are labeled with bin values over 40. The dashed lines indicate the strike range for each zone. Rose diagrams are determined for each zone. Fault parameters for these zones are given in Table S1. Only zone 1 are used in the final model.

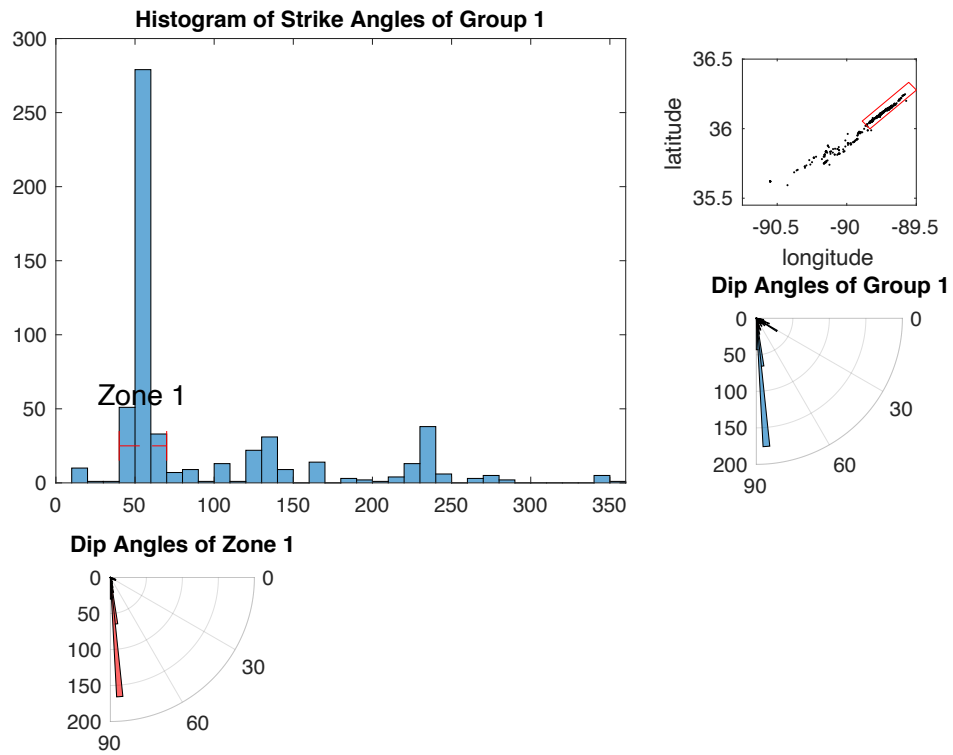


Figure S9. OADC analysis for AFP group 1 (upper right). Only one zone is labeled with bin value over 40. The dashed line indicates the strike range for the zone. Rose diagram is determined. Fault parameters for this zone are given in Table S1. The zone is used in the final model.

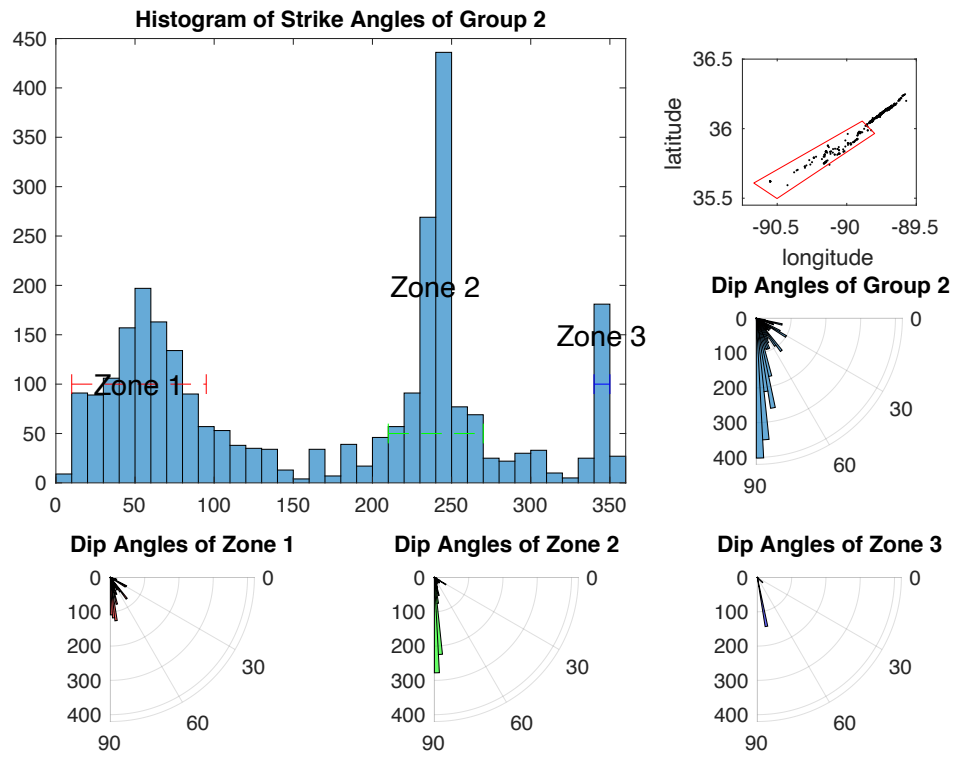


Figure S10. OADC analysis for AFP group 2 (upper right). Three zones are labeled with bin values over 40. The dashed lines indicate the strike range for each zone. Rose diagrams are determined for each zone. Fault parameters for these zones are given in Table S1. Zones 1 and 2 are used in the final mode.

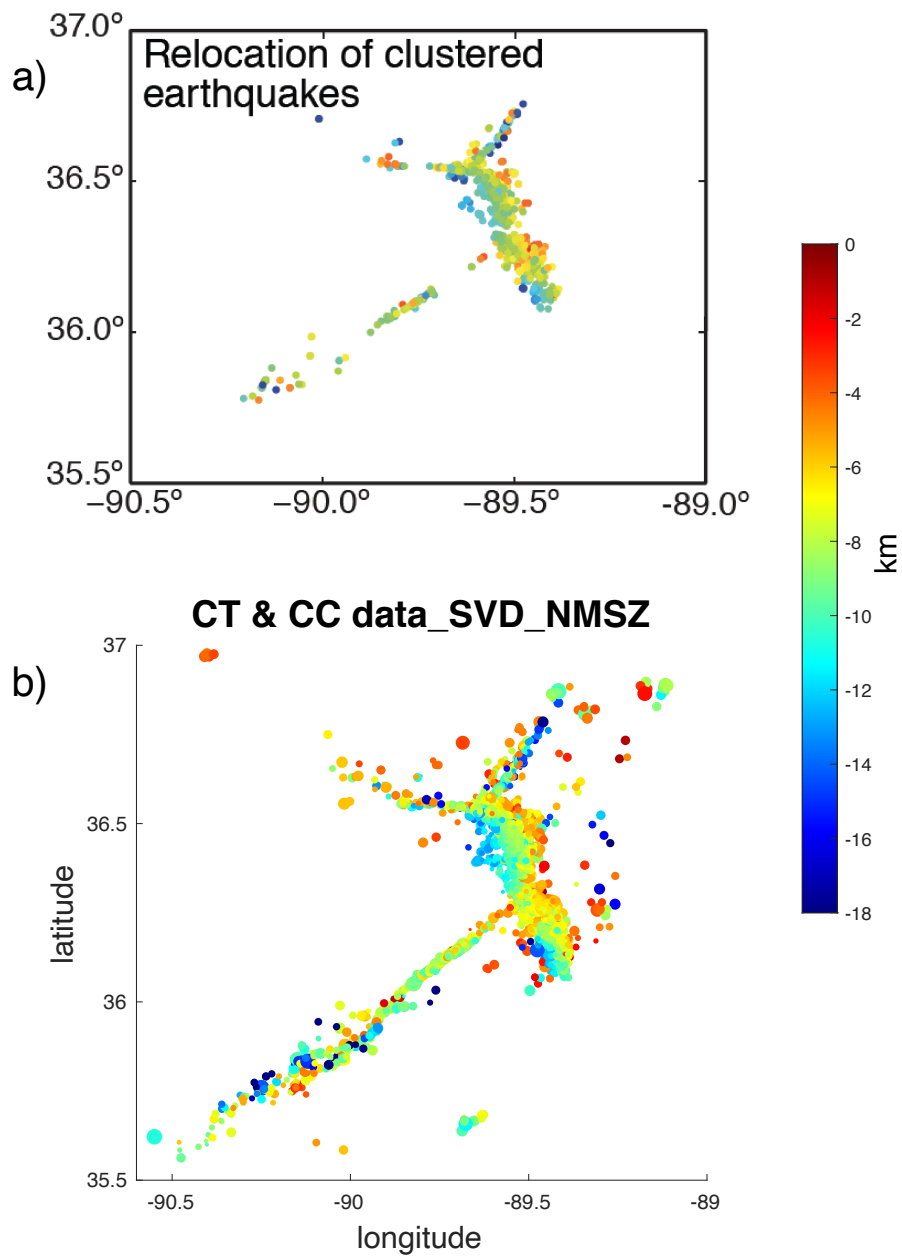


Figure S11. A comparison between the HypoDD results obtained by Dunn et al. (2010) a) and our results b). The availability of a larger dataset has sharpened the fault structure in the NMSZ here.

Table S1. PARAMETERS of MODELED FAULT PLANES										
Part name	Group #	Fault ID	Strike range	Dip range	Strike mean value	Dip mean value	Length mean value	Width mean value	Lambda 3 mean value	# of modeled planes
Northern	1	1	60~100	30~60	73.15	46.39	12.47	3.04	0.58	93
		2		75~90	82.72	85.39	11.88	4.01	0.71	140
		3	195~210	75~90	204.31	84.79	4.87	2.09	0.80	35
		4	250~275	0~30	265.98	22.84	5.94	2.09	0.07	35
		5		75~90	262.02	86.10	6.78	2.62	0.38	119
	2	6	10~40	45~75	29.77	60.84	11.15	3.93	0.79	57
		7	80~125	30~60	102.25	43.17	6.65	3.67	0.90	172
		8		75~90	95.69	85.75	11.36	4.03	0.89	242
		9	265~285	75~90	275.50	87.48	8.95	3.36	0.72	105
	3	10	30~50	75~90	33.96	83.26	18.01	5.05	0.88	288
		11	135~155	60~90	143.76	73.02	4.53	2.03	1.07	124
		12	200~230	70~80	218.59	74.89	14.69	2.70	0.40	56
		13		80~90	212.43	86.62	17.89	4.64	0.92	93
		14	240~260	75~90	248.82	85.69	6.45	2.25	0.27	110
RF	1	15	40~70	60~90	54.83	77.27	8.15	2.69	0.84	153
		16	95~125	0~30	109.64	18.40	14.79	4.66	0.84	102
		17		30~60	110.88	42.69	8.15	4.37	0.75	82
		18	140~230	15~45	172.30	30.89	15.76	5.76	0.94	1513
	2	19	100~135	0~30	119.48	17.77	12.23	6.08	0.97	215
		20	135~165	30~60	150.31	43.53	14.73	5.96	0.89	312
		21	165~205	15~45	184.76	30.36	13.46	5.51	0.85	464
		22	290~330	15~45	310.73	29.28	13.11	4.85	0.85	190
	3	23	20~65	30~75	43.61	52.04	8.19	4.23	0.82	207
24		100~170	30~60	148.46	44.79	15.80	6.17	0.95	682	
25		295~335	15~45	313.65	25.51	9.66	4.80	0.90	154	
AF	1	26	40~70	75~90	52.48	84.25	21.16	3.86	0.90	296
	2	27	10~90	20~40	71.86	30.76	14.83	3.56	0.48	129
		28		50~65	50.04	57.04	10.79	2.66	0.47	218
		29		70~90	49.00	82.30	13.82	3.95	0.70	547
		30	210~270	75~90	239.20	85.28	16.72	4.43	0.55	681
	31	340~350	60~90	344.16	77.64	1.43	0.37	0.20	151	

Table S1. Parameters of modeled fault planes.

References:

Dunn, M., Horton, S., DeShon, H., & Powell, C. (2010). High-resolution earthquake relocation in the New Madrid seismic zone. *Seismological Research Letters*, 81(2), 406-413.